

University of Nottingham
UK | CHINA | MALAYSIA

Faculty of Engineering
Mechanical Engineering Department

Numerical and experimental investigation of boiling nanofluids in vapour absorption refrigeration

Hayder Ibrahim Mohammed

A thesis submitted to the University of Nottingham for the degree of Doctor of Philosophy

July 2018

[This page intentionally left blank]

Abstract

To achieve decreasing power demands across several industries, improving the heat transfer of vapour absorption refrigeration system (VARS) based on flow boiling heat transfer have been proposed. Nanofluid, a fairly new class of coolants formed by suspending 1-100 nm sized particles in a base fluid which in this thesis was presented by a salt - fluid (acetone / $ZnBr_2$), has been shown to improve a fluid's thermal properties. Previous researches concentrate on water based fluids or commonly found refrigerants and heat transfer fluids. This research focuses on developing a new method to simulate flow boiling of a novel fluid, we define it as a nano-salt-fluid, numerically. A model was generated using commercial CFD code with additional user defined function, (UDF) for the case of determining the heat and mass transfer in a boiler duct for a vapour absorption refrigerator. The simulations were performed to assess the effect of varying nanoparticle concentrations, fluid velocity and boiler temperature on the boiling and phase change characteristics of the system. The fluid was treated as four separate phases: liquid acetone; vapour acetone; liquid Acetone / $ZnBr_2$ solution; solid nanoparticles cloud. Graphene nanoparticles were represented as a cloud-like phase in the mixture to calculate the viscosity. This study evaluates the key characteristics of the nanofluid system, and how the different components and phases behave when the liquid acetone evaporates. The process was modelled using ANSYS® Fluent V.15 using the mixture multiphase flow model, however, the volume of fluid (VoF) method is also used to show the behaviour of the vapour phase.

To validate the modelling method, an experimental work examines the improvement of the heat transfer and investigates the performance of the working

fluid. The high pressure part of the VARS is built as the test rig. The rig evaluated the heat transfer improvement in the boiler side of VAR system by use of nanofluid instead of the normal binary fluid only, which is acetone/$ZnBr_2$ in this case. Various values of flow rate, temperature and the concentration of the nanoparticles were used and the effects observed on the heat transfer and the fluid flow. These tests had acceptable accuracy, for example, the heat flux and the heat transfer coefficient are 8704±85W/m^2 and 104±0.5W/m^2.K, respectively, when the boiler temperature is 180 ^oC. The tests validated the results of the numerical modelling part of this work, which simulated the boiling of the salt-nanofluids, in order to justify the use of the CFD on a design tool for VARS.

Nanofluid in CFD are represented as multiphase and single-phase. To model the boiling process, a comparison between these models was assessed to discover which model represents the nano-particles as a distinct fluid phase used in the boiling process. The cases of laminar and turbulent flow regimes were explored numerically for a wide range of acetone and nanoparticles concentrations. The velocity was varied between 1.5 – 6 $m.s^{-1}$, representing typical heat exchanger conditions. Reynolds number depended significantly on the solution concentration.

The novel working fluid solution consisted of dissolved salt in refrigerant mixed with nanoparticles, called have a nano-binary fluid (NBF) or nano-salt-fluid (NSF). The study covered the properties of the acetone/ $ZnBr_2$ as a binary (base) fluid and nanofluid by adding Zinc Oxide (ZnO) and Graphene, separately. The overall results show that the nanoparticle enhances the thermal properties of the fluid.

Acknowledgements

I feel that the words alone are not enough to show the great gratitude and praise that I owe for the unlimited support of my supervisors Dr Donald Giddings, Prof Gavin S. Walker and the late Prof Henry Power. Throughout the whole period of the study, their continuous help and guidance were invaluable without which this research would not have come to light.

The special thanks should go for my lovely family Bayan, Helin, Kardo and Maria, who lately jumped to our world during the writing period, without whom the life would be difficult in Nottingham. I acknowledge the overwhelmed love and support that they have given to me.

I am also grateful for my Mum, brothers and friends who have never stopped wishing me the best in my study and life through their support and prayers.

I feel very grateful for the Higher Committee for Education Development in Iraq (HCED) for funding me over the course of my study.

My thanks also go to the technician staff in laboratory of Wolfson building, ETB and the Nanoscale and Microscale Research Centre (nmRC) who are the hidden army that is behind the success in any experimental research.

I would also like to express my thanks and love to my great friends and colleagues Aram Afrasiaw, Hasanain Attiah, Monkith Mohammed, Ali Jamil, Mohammed Said, Emad Kaky, and my friend David Devadason.

Affirmation

With the exception of the following publication, this work presented in this Thesis has not been published elsewhere:

Conference Paper: Hayder I. Mohammed, Donald Giddings, Gavin S. Walker, Henry Power. CFD multiphase modelling for the nanofluid boiling of the salt solution in a symmetric rectangular boiler. *Proceedings of* 2^{nd} *International Conference on Multiphase Flow and Heat Transfer* (ICMFHT'17), Napoly-Italy, 2017.

Journal Paper: Hayder I. Mohammed, Donald Giddings, Gavin S. Walker, Henry Power. CFD assessment of the effect of nanoparticles on the heat transfer properties of $acetone/ZnBr_2$ solution. *Applied Thermal Engineering* 128 (2018) 264–273.

Journal Paper: Hayder I. Mohammed, Donald Giddings, Gavin S. Walker. CFD simulation of a concentrated salt nanofluid flow boiling in a rectangular tube. *International Journal of Heat and Mass Transfer* 125 (2018) 218–228.

Journal Paper: Hayder I. Mohammed, Donald Giddings, Gavin S. Walker. Experimental investigation of flow boiling heat transfer characteristics of a nano-salt-fluid in a rectangular duct.*International Journal of Heat and Mass Transfer* 130 (2019) 710–721.

Under review with a Journal: Hayder I. Mohammed, Donald Giddings, Gavin S. Walker. Flow boiling heat transfer of a nano-binary-fluid in a rectangular tube: an experimental and numerical study.

Technical note under review with a Journal: Hayder I. Mohammed, Donald Giddings, Gavin S. Walker. Thermo-physical properties of the nano-binaryfluid (acetone–zinc bromide-ZnO) as a low temperature operating fluid for using in absorption refrigeration machine.

Contents

Contents v

List of Figures ix

List of Tables xxiii

Nomenclature xxvi

1 INTRODUCTION 1

1.1 Context 1

1.2 Aims and Objectives 4

1.3 Structure of the thesis 6

2 LITERATURE REVIEW 8

2.1 Development of Absorption Refrigeration 8

2.1.1 The Basic principles of absorption cycle 10

2.1.2 Types of absorption system 13

2.1.3 Working fluid for absorption refrigeration systems 16

2.2 Nanofluids 18

2.2.1 Applications of nanofluids 20

2.2.2 The synthesis and nature of Nanofluids 23

2.2.3 Properties of the nanofluid (analytical expressions and experimental observation) . . . 27
2.2.3.1 Density . . . 27
2.2.3.2 Viscosity . . . 29
2.2.3.3 Specific heat capacity . . . 32
2.2.3.4 Thermal conductivity . . . 34
2.2.3.5 Parameters influencing thermal conductivity . . . 38
2.3 Modelling Review . . . 46
2.4 Numerical Modelling . . . 48
2.4.1 Boiling . . . 49
2.4.2 Single and two phase models for nanoparticles simulations 55
2.5 Summary . . . 58

3 PREPARATION AND PROPERTIES OF NANOFLUID 59

3.1 Introduction . . . 59
3.2 Sources of the materials . . . 60
3.3 Preparation . . . 60
3.3.1 Zinc Oxide (ZnO)(Suspension stability study) . . . 61
3.3.2 Graphene (G)(Suspension stability study) . . . 65
3.3.3 Transmission Electron Microscope (TEM) analyzer: . . . 74
3.4 Properties Investigations . . . 80
3.4.1 Density . . . 80
3.4.2 Viscosity . . . 85
3.4.3 Thermal Conductivity . . . 91
3.4.4 Specific heat capacity . . . 96
3.4.5 The size of the nanoparticles . . . 102
3.4.6 Do the nanoparticles transfer with the vapour during the boiling? . . . 106

3.4.7 Summary 109

4 EXPERIMENTAL STUDY OF FLOW BOILING IN THE VARS 111

4.1 Introduction 111

4.2 Rig description 112

4.3 Experimental procedure 117

4.3.1 Controlling the boiler temperature 120

4.3.2 Calculation and measurement of the flow rate and heat transfer parameters 122

4.4 Error Analysis: 126

4.5 Effects of the nanoparticles volume fraction with constant boiler temperature and flow rate: 129

4.6 Effects of the boiler temperature at constant flow rate on basefluid: 137

4.7 Effect of the flow rate at constant boiler temperature on basefluid: 143

4.8 Summary 148

5 EVALUATION OF SINGLE AND TWO PHASE MODELS FOR THE NANOFLUID HEAT TRANSFER 150

5.1 Introduction 150

5.2 Geometry and assumptions 152

5.3 Single phase model 152

5.4 Two phase CFD methodology 154

5.5 Boundary condition for the novel refrigerant simulation 157

5.6 Results and discussion 158

5.6.1 Justification of mesh structure 158

5.6.2 Validation of the CFD Modelling 159

5.6.3 Effects on the centreline velocity for the novel nanofluid . 162

5.6.4 Effects on the turbulence intensity 165

5.6.5 Effects on the wall shear stress and skin friction 166
5.6.6 Effect on the heat transfer coefficient 170
5.7 Summary 174

6 NUMERICAL STUDY OF FLOW BOILING OF THE NANO-SALT-FLUID IN THE BOILER 176

6.1 Introduction 176
6.2 Summary of related literature and justification for research . . . 177
6.3 Method 179
6.4 Mathematical model 182
6.5 Geometry and boundary condition 187
6.6 Mesh independence study: 189
6.7 Validation of mixture method applied to boiling flow 190
6.8 Quantifying the flow with the mixture model 194
6.8.1 Effect of nanoparticle concentrations 194
6.8.2 Effects of the boiler temperature 201
6.8.3 Effects of the flow rate 203
6.9 Visualising the flow 206
6.10 Summary 212

7 CONCLUSIONS AND RECOMMENDATIONS 215

7.1 Conclusions 215
7.2 Recommendations 221

REFERENCES 223

Appendices i

A DATA USED TO FIND THE UNCERTAINTY i

B UDF SOURCE CODE vii

List of Figures

2.1 Absorption refrigeration machine sketch by Ferdinand Carre . . 9

2.2 a) VCRS and b)VARS, where C: condenser; E:evaporater; G:generator; A: absorber; Q_c:condenser heat transfer; Q_E:evaporater heat transfer; Q_a:absorber heat transfer; Q_G: generator heat transfer; SHX: solution heat exchangeer and MC: compressor motor . 12

2.3 Single effect absorption cycle with two heat exchangers: refrigerant heat exchanger RHX and solution heat exchanger SHX . . 14

2.4 Two-step preparation method of nanofluids. 23

2.5 Effects of a) volume fraction and b) temperature on the density of the nanofluid. 28

2.6 a) Influence of nanoparticle volume concentration on relative viscosity of ZnO–EG, nanofluids; viscosity increases with Φ, when $\Phi \leq 0.25\%$, and decreases when $\Phi \geq 0.25\%$. b) Influence of nanoparticle volume concentration on relative viscosity of ZnO–EG/water, nanofluids; viscosity decrease with increasing Φ for any range of concentration. c) Influence of small concentration of ZnO nanoparticles in EG; viscosity ratio increase with increasing Φ 31

2.7 Comparison between experimental data of Zhou and Ni. 33

2.8 (a). Measured thermal conductivities of Al_2O_3–EG at different volume fraction (experimentally and theoretically). (b) Measured the TC of $ZnO - EG$ for different nanoparticles concentrations 39

2.9 a) The effect of (ZnO) nanoparticle size on the TC of water. b) Effect of (Al_2O_3) nanoparticle size on the TC 42

2.10 The shape factor of (Al) effects on the thermal conductivity. . . 43

2.11 Thermal conductivity enhancement with Temp. for Al_2O_3 (80 $nm)/EG$ and Al (80 $nm)/EO$ base nanofluid. 45

2.12 Effect of parameters on the properties of nanofluid. 46

2.13 Regimes of pool boiling in water at atmospheric pressure. 50

2.14 Nanoparticle materials used in the experimental investigations of nanofluid flow boiling. 54

2.15 Working fluid used in the experimental investigations of nanofluid flow boiling. 54

3.1 The sonication bath used to prepare the nanofluid Ac-$ZnBr_2 - ZnO$. 63

3.2 Sedimentation of different concentration of ZnO nanoparticles in acetone - $ZnBr_2$. 1- 0.3 vol. % 24 hrs Sonication. 2- 0.5 vol. %(without sonication). 3- 0.1 vol. % (2 hrs Sonication). 4- 0.5 vol. % (2 Hrs Sonication). 5- 1 Vol. % (2 Hrs Sonication). 6- 1.2 Vol. % (2 hrs Sonication). 64

3.3 Settling of nanoparticles ZnO in the base fluid (Acetone / $ZnBr_2$) nanofluid for different times, using different surfactants. 65

3.4 Cole-Parmer 750-Watt Ultrasonic Homogenizer with Temp Controller; 115V. Item number: EW-04711-40. 66

3.5 A sample of a nanofluid acetone/$ZnBr_2$-Graphene ($ZnBr_2$=50 wt. % and Graphene=0.05 vol. %), sonication time= 2 hrs and amplitude= 45%. 67

3.6 Samples of a nanofluid acetone/$ZnBr_2$-Graphene ($ZnBr_2$=50 wt. % and Graphene =0.05 vol. %), Right sample had sonication time= 4 hrs and amplitude= 65%. and acetone added to compensate the evaporated acetone. Left sample had sonication time= 2 hrs with amplitude= 45%. 67

3.7 Samples of a nanofluid acetone/$ZnBr_2$-Graphene ($ZnBr_2$=50 wt. %), the two samples on right had concentrations=0.05 and 0.2 vol. % with sonication time= 2 hrs, amplitude= 45%. and acetone added to compensate the evaporated acetone. Left sample had sonication time= 2 hrs, amplitude= 45%. Without adding acetone. 69

3.8 Samples of a nanofluid acetone/$ZnBr_2$-Graphene ($ZnBr_2$=50 wt. %, graphene=0.05 vol. %), a) prepared without sonication, b) sonicated with amplitude= 45% probe sonication for 1 hr, c) sonicated for 2 hrs, d) sonicated for 2 hr and centrifuged, e) has a concentration of $ZnBr_2$ =60 wt. %. and f) sonicated for 2 hours with 70% power of the sonication and centrifuged for 30 minutes 72

3.9 Samples of a nanofluid acetone/$ZnBr_2$-Graphene. With different concentration of $ZnBr_2$ (40 wt. % (far left) – 65 wt. % (far right)) with 5 % increase steps. The sonication time is 1 hour with 45 % of the probe total power. The graphene concentration=0.05 vol. %). 73

3.10 a- Copper mesh holey Carbon film. b- Holes in the carbon film. 74

3.11 Different TEM images of graphene from suspension in the pure acetone on the Copper mesh holey Carbon film, a) shows a distribution of graphene from acetone/graphene sample on the Carbon film, b) shows a particle stuck on the film, c) show particles stuck on the film and d) shows the surface of the nanoplate view. 75

3.12 Different TEM images of graphene suspend in the acetone / $ZnBr_2$ on the Copper mesh holey Carbon film, a) nanoparticles distribute on the film between the holes, b) single particle on the film and crystallization of the $ZnBr_2$ (appears as a black part), c) shows grains of the non crystallized $ZnBr_2$, and d) shows some particles on the film in different scale. 76

3.13 Different TEM images of ZnO suspension in the acetone / $ZnBr_2$ on the Copper mesh holey Carbon film, a & b) show a random star shape of the $ZnBr_2$ crystallization and c & d) show grains appear between the hole of the carbone film. 78

3.14 TEM images of ZnO suspension in the acetone/$ZnBr_2$ on the Copper mesh holey Carbon film. 78

3.15 STEM image of ZnO nanoparticles suspension in acetone/$ZnBr_2$. 79

3.16 Density of acetone / $ZnBr_2$ with different concentration of $ZnBr_2$ as measured experimentally at 20 ^oC and those based on the data from literature 81

3.17 Effect of the ZnO nanoparticle volume fraction on the density of nanofluid experimentally at 20 ^oC and theortically based on equation 2.3. 84

3.18 Effect of the graphene nanoparticle volume fraction on the density of nanofluid at 20 ^oC. 84

3.19 hts-VROC Viscometer Rheometer On a Chip. 85

3.20 Cell or "chip" which contains a rectangular slit flow channel constructed of borosilicate glass, with a uniform cross-sectional area and multiple pressure sensors. 86

3.21 Relation of the viscosity with the volume fraction of ZnO nanoparticles in acetone / 50% $ZnBr_2$ at 20 ^oC. 87

3.22 Relation between the shear stress and the shear rate of the acetone / 50% $ZnBr_2$ based on different concentration of ZnO at 20 ^oC. 88

3.23 Relation between the viscosity and the shear rate of the acetone / 50% $ZnBr_2$ based on different concentration of ZnO at 20 ^oC. 89

3.24 Relation between the viscosity of the nanofluid and the temperature for the different volume fraction of the ZnO nanoparticles. 89

3.25 Three dimensional surface explain the relation between the viscosity (in m.Pa s), temperature (in Celsius) and the volume fraction. 90

3.26 Modified transient plane source (MTPS) sensor a)taken from C-therm company website and b) lab instrument. 91

3.27 Illustration of how C-therm operation. 92

3.28 Relation between the thermal conductivity and the concentration of the $ZnBr_2$ in the acetone / $ZnBr_2$ solution at 20 ^oC. . . 93

3.29 Experimental and theoretical (based on Suganthi and Maxwell's Models) relation between thermal conductivity of the acetone / 50% $ZnBr_2$ with different concentrations of ZnO nanoparticles at 20 ^oC. 95

3.30 Experimental and theoretical (based on Suganthi model) relation between thermal conductivity of the acetone / 50% $ZnBr_2$ with different concentrations of Graphene nanoparticles at 20 ^oC. 96

3.31 Differential Scanning Calorimetry DSC, which used to find a Cp for the acetone/$ZnBr_2$ based ZnO nanofluid. 97

3.32 Crucibles (Al) (bottom) and DSC-lid (Al) (top). 98

3.33 The DSC output graph of the relation of heat transfer and the temperature for the empty pan, standard sample sapphire and the test sample ($ZnBr_2$). This Figure should be printed in colour. 98

3.34 Relation between the specific heat capacity of acetone / $ZnBr_2$ with different concentrations of $ZnBr_2$ experimentally and compare with results from literature. 100

3.35 Relation between the specific heat capacity and nanoparticles concentration experimentally and theoretically (using equation 3.13) for the solution acetone/ 50% $ZnBr_2$ based ZnO. 101

3.36 Relation between the specific heat capacity and nanoparticles concentration experimentally and theoretically (using equation 3.13) for the solution acetone/ 50% $ZnBr_2$ based Graphene. . . 101

3.37 Schematic representation of the speckle pattern. 103

3.38 The observed signal bases on the phase pattern of the scattered light falling. A) two beams with opposite phase makes the outcome zero intensity detector. B) two beams with the same phase and enhance each other resulting in the sum of the intensity detector. 104

3.39 Typical intensity fluctuations for the large and small particles. . 105

3.40 Rig of evaporation and condensation of nanofluid, used to check the possibility of transferring a nanoparticles with a vapour during the boiling. 108

3.41 A clear acetone collected from the condensation of acetone vapour, which confirm that there are no nanoparticles transfer with a vapour during the evaporation or boiling processes of nanofluid. 108

4.1 Equipment schematic of the high pressure side of the VARS. . . 114

4.2 Photo of the high pressure part of the vapour absorption refrigeration system experimental test rig. 115

4.3 The feeding system of the absorption refrigerator experimental test rig, shows the power supply, the Micropump (R400BL) and the flow controller. 116

4.4 The flow controller provided by TCS Micropumps Company. Input Voltage 12-30 V(dc), Flow can be controlled via an on-board Potentiometer. Or a 0-5 V signal and Operating Temperature 0 - 80 ^oC. 116

4.5 Strip heater and boiler used in this experiment. Type Caloritech, 250 W. 117

4.6 The temperature of the condenser and the pressure of the system as a function of time. In case (flow rate 3.6 ml/s, 180 ^oC and 0 concentration of nanoparticles). 119

4.7 Temperature difference between the bottom and the inner surface of the boiler. 121

4.8 Difference between the temperatures of the controlled surface in the boiler inner surface (adjacent with the solution) in the specific time (PID set on 180 ^oC). 121

4.9 Consumption the electric power by the heater controlled by the PID controller. 125

4.10 Temperature of the pump at different concentration of nanoparticles. 131

4.11 Developing the pressure of the system at different nanoparticles concentrations. 132

4.12 Developing the saturation temperature (at the entrance of the condenser) of the system at different concentration of nanoparticles. 133

4.13 Relationship between the heat flux and the heat transfer coffi-cient in the boiler with the different concentration of nanoparticles. 134

4.14 Relationship between the $ZnBr_2$ concentration in SSR and the condensed acetone flow rate in the condenser with the different concentration of nanoparticles. 135

4.15 Relationship between the saturation temperature of acetone in the condenser, the average boiler temperature and the temperature recorded at thermocouple 5 (closest to the outlet section) with the different concentration of nanoparticles. 136

4.16 The P-T chart of the acetone in the salt solution acetone / $ZnBr_2$. 136

4.17 The characteristic boiling curves of water / Al_2O_3 nanofluid, (a) the film boiling, (b) the minimum heat flux (MHF) point, (c) the transient boiling, (d) the maximum heat flux point or critical heat flux (CHF), and (e) the nucleate boiling 138

4.18 Developing the pressure of the system at different boiler temperature at 3.35 ml/s. 139

4.19 Developing the saturation temperature (at the entrance of the condenser) of the system at different boiler temperature. 140

4.20 Relationship between the saturation temperature of acetone in the condenser, the average boiler temperature and the temperature recorded at thermocouple 5 (closest to the outlet section) with the different controlled temperature of the boiler. 141

4.21 Relationship between the heat flux and the heat transfer coefficient in the boiler with the different controlled temperature of the boiler. 142

4.22 Relationship between the $ZnBr_2$ concentration in SSR and the condensed acetone flow rate in the condenser with the different controlled temperature of the boiler. 142

4.23 Developing the pressure of the system at different flow rate at the boiler temperature 180 ^oC. 144

4.24 Developing the saturation temperature (at the entrance of the condenser) of the system at different flow rate. 145

4.25 Relationship between the saturation temperature of acetone in the condenser, the average boiler temperature (average temperatures which measured from the thermocouples (1-5) of the boiler) and the temperature recorded at thermocouple 5 (closest to the outlet section) with the magnitude of the boiler flow rate. 146

4.26 Relationship between the $ZnBr_2$ concentration in SSR and the condensed acetone flow rate in the condenser with the magnitude of the boiler flow rate. 147

4.27 Relationship between the heat flux and the heat transfer coefficient in the boiler with the magnitude of the flow rate. 147

5.1 Dimensions of the symmetric flat tube in this study in mm (Not to scale). 153

5.2 Mesh #2 used in this study. 158

5.3 Comparison between the experimental Nu from (Peyghamberzadeh 2011) and the predicted Nu from (Yimin and Li 2003). Horizontal error bars are experimental uncertainty (18%) (Peyghamberzadeh 2011); vertical error bars are error of analytical prediction (7%) (Yimin and Li 2003). This Figure is reproduced by permission from (Peyghamberzadeh 2011). 159

5.4 Comparison between the enhancement in the Nusselt number as a function of a nanoparticle volume fraction in water at 308 K for different Re in the cases of two phase, single phase of the current study and the previous experiment results. 161

5.5 Comparison between Nusselt number as a function of a flow rate at the nanoparticles volume concentration of 1 % for different Re in the cases of two phase, single phase of the current study and the previous experiment results. 161

5.6 Comparison between Nu as function of volume fraction in present study and the numerical study of literature for a- single phase and b- two models using water mixed with ZnO nanoparticles. . 162

5.7 Centreline velocity along the tube with different concentration of ZnO nanoparticles and 60 wt.% & 70 wt.% of acetone at Re of 25000.(Present in colour). 164

5.8 Centreline velocities as function of nanoparticles volume fraction at distance 0.15m from the inlet of the tube, for the both cases the acetone concentrations 60wt.% and 70wt.%. 164

5.9 Turbulence intensity along the tube with different concentration of ZnO nanoparticles and 60% & 70% of acetone at Re of 30000. 165

5.10 Turbulence intensity along the tube with different Re at mass concentration of acetone 50% and concentration of ZnO nanoparticles 0.015. 166

5.11 Relation between wall shear stress and the acetone concentration at different velocity and 0.01 volume fractions of nanoparticles. 167

5.12 Relation between wall shear stress and Re different concentration of ZnO nanoparticles and 60 wt.% & 70 wt.% of acetone. . 167

5.13 Skin friction along the tube with different concentration of a nanoparticles at Re=20000 and for acetone 60wt.% and 70wt.%. 169

5.14 Skin friction along the tube with different concentration of a nanoparticles for acetone 40wt.% with Re=2500 and 50wt.% with Re of 12000. 169

5.15 Variation of the heat transfer coefficient along the tube wall in both of single and two phase approaches for the same values of Re.(Presents in colour) 171

5.16 Variations of the numerical results of $h_{nf}/h_{bf}$with different concentration of nanoparticles in single and two phase approach (at acetone concentration of 50%).(Presents in colour) 171

5.17 Relation between heat transfer coefficient and acetone mass fraction with different velocity of fluid and volume fraction of nanoparticles of 0.01. 172

5.18 Nusselt number as function of the volume fraction for different Re and for the H_2O/Al_2O_3 case and acetone $/ZnBr_2$ (acetone 60%)/ ZnO for a two phase model flow. 173

6.1 Geometry and the boundary conditions of the symmetric boiler used to boil the solution acetone/$ZnBr_2$ with graphene nanoparticles. 187

6.2 Cross-sectional view of the $151 \times 51 \times 51$ grids, a- regular hexahedral grid b- hexahedral bias grid. 190

6.3 Comparison between the experimental and numerical model for varying concentration of nanoparticles, a) heat flux and heat transfer coefficient, b) centreline temperature and c) average temperature at the out section. 192

6.4 Comparison for base fluid between the experimental and the numerical model, a) heat flux and heat transfer coefficient vs. boiler temperature and b) centreline temperature vs. axial position. 193

6.5 Comparison for base fluid between the experimental and the numerical model, a) heat flux and heat transfer coefficient vs. flow rate and b) centreline temperature vs. axial position. . . . 193

6.6 Relation between the produced acetone vapour mass flux and the nanoparticle volume fraction for different velocity and temperature and 50 wt. % $ZnBr_2$ in the solution. 195

6.7 Relation between the average heat transfer coefficient and heat flux with nanoparticle volume fraction for different velocity and temperature and 50 wt. % $ZnBr_2$ in the solution. 196

6.8 The effect of volume fraction of particles on the centreline temperature along the pipe at 50 wt. % $ZnBr_2$ concentration, $T_h = 426K$, and flow rate = $3.66ml/s$. (present in colour). . . . 197

6.9 The effect of the concentration of the nanoparticles, surface temperature and the flow rate on the average outlet temperature of the mixture solution in the boiler. 198

6.10 The effect of the concentration of the nanoparticles, surface temperature and the flow rate on the turbulent intensity of the mixture solution in the boiler. 199

6.11 Developing of acetone vapour in the boiler with a time during the boiling of nanofluid (T_h= 426 K and flow rate = 3.66 ml/s). 199

6.12 Relation between the heat flux and heat transfer coefficient and the boiler temperature for different velocity and particles concentrations with 50 wt. % $ZnBr_2$ in the solution. 201

6.13 Relation between the productions of acetone vapour mass flux and vapour volume fraction and the boiler temperature for different velocity and particles concentrations with 50 wt. % $ZnBr_2$ in the solution. 202

6.14 The effect of the boiler temperatures on the turbulent intensity of the mixture solution in the boiler at different particles concentration and the flow rate. 202

6.15 The effect of the boiler temperature on the outlet temperature of the mixture solution in the boiler with different surface temperatures and the flow rates. 203

6.16 Relation of the heat flux and heat transfer coefficient with the flow rate variation for different boiler temperature and particles concentrations with 50 wt. % $ZnBr_2$ in the solution. 204

6.17 Relation of the productions of acetone vapour mass flux and vapour volume fraction with the flow rate variations for different boiler temperature and particles concentrations with 50 wt. % $ZnBr_2$ in the solution. 204

6.18 The effect of the solution flow rate on the turbulent intensity of the mixture solution in the boiler at different particles concentration and the boiler temperatures. 205

6.19 Developing of the vapour of acetone in acetone/$ZnBr_2$ based on graphene nanoparticles at the symmetric view of the rectangular boiler up to 15 second. (Flow rate=3.66 ml/s, T_w=426 K and Φ=0.5 Vol %) at the VoF method. (present in colour) 207

6.20 Distribution of all phases (acetone liquid, vapour, acetone/$ZnBr_2$ and graphene cloud) at the symmetric view of the rectangular boiler up to 20 seconds. In specific conditions (Flow rate=3.66 ml/s, T_w=426 K and Φ=0.5 Vol %) for the mixture model. Last image is the cross section of the boiler in different points at the 20^{th} second. (present in colour). 209

6.21 Distribution of all phases (acetone liquid, vapour, acetone/$ZnBr_2$ and graphene cloud at different cross sections of boiler at 20 seconds. (Flow rate=3.66 ml/s, T_w=426 K and Φ=0.5 Vol %) for the mixture model. (present in colour). 211

List of Tables

2.1 Summary of working pairs for absorption system 17

2.2 Conventional solid-liquid suspensions compared to nanofluids . . 19

2.3 Summary of maximum enhancement in thermal conductivity for different nanofluid as found in the literatures. 36

3.1 Nanoparticles mass needed for each concentration. 62

3.2 Density of different concentrations of acetone / $ZnBr_2$ as found experimentally, from literature and if the volume of acetone not change when the $ZnBr_2$ added. 81

3.3 Empirical constants of the equation 3.8 89

3.4 Relation of the thermal conductivity with the concentration of the of $ZnBr_2$ in the acetone/ $ZnBr_2$ solution at 24 ^oC. 92

3.5 Thermal conductivity of the acetone/$ZnBr_2 - ZnO$ with increasing the concentration of nanoparticles. 93

3.6 Maximum enhancement in thermal conductivity for different nanofluid (based on ZnO) as found in the literatures. 94

3.7 Suggested numbers and distances between the graphene and ZnO nanoparticles with the different concentration 106

4.1 The values of the C_{sf} at different flow rate and wall temperature. 123

4.2 shows the measured values with the uncertainty for data measured and calculated for 5 trails for one case for pure acetone / $ZnBr_2$ solution and controlled temperature =180 ^oC. 130

5.1 Reynolds number at different mass fractions of acetone. 157

5.2 Mesh independence study of the fully developed region using acetone/50wt.% $ZnBr_2$ with Re=8000. 158

5.3 Skin friction ($\times 10^{-3}$) at different volume fractions at distance 0.2m from the inlet of the tube. 168

5.4 Numerical results of the heat transfer coefficient with different concentration of acetone and nanoparticles and different Re. . . 173

6.1 Comparisons of the results of the heat flux (HF), heat transfer coefficient (HTC) and the temperature at the outlet section of the boiler for different concentration of the liquid acetone (undergoing the evaporation) with the experimental results of these parameters. 182

6.2 properties of each phase used in the numerical analysis 189

6.3 Mesh independence study for the case 50 wt.% $ZnBr_2$, the hot surface temperature=426 K, inlet velocity = 3.66 ml/s, and the particles volume fraction = 0.1 vol. %. 190

6.4 The concentration of the Graphene and $ZnBr_2$ in the liquid phase at the exit section of the boiler in different cases of Acetone-$ZnBr_2/graphene$ boiling. 200

6.5 Concentrations of all phases (acetone liquid, Graphene cloud, acetone/$ZnBr_2$ and acetone vapour) at the symmetric view of the rectangular boiler at the same point indicated in Figure 6.20 at different time steps, for the case (flow rate=3.66 ml/s, T_w=426 K and Φ=0.5 Vol. %) at the mixture model. 208

A.1 Collected data of the acetone / $ZnBr_2$ density (kg/m^3) as mentioned in Chapter 3. ii

A.2 Collected data of the acetone / $ZnBr_2 - ZnO$ density (kg/m^3) as mentioned in Chapter 3. ii

A.3 Collected data of the acetone / $ZnBr_2 - G$ density (kg/m^3) as mentioned in Chapter 3. iii

A.4 Collected data of the acetone and acetone / $ZnBr_2$ viscosity ($mpa.s$) as mentioned in Chapter 3. iii

A.5 Collected data of the acetone and acetone / $ZnBr_2$ - ZnO viscosity ($mpa.s$) as mentioned in Chapter 3. iv

A.6 Collected data of the acetone / $ZnBr_2$ thermal conductivity ($W/K.m$) as mentioned in Chapter 3. iv

A.7 Collected data of the acetone / $ZnBr_2 - ZnO$ thermal conductivity ($W/K.m$) as mentioned in Chapter 3. v

A.8 Collected data of the acetone / $ZnBr_2 - G$ thermal conductivity ($W/K.m$) as mentioned in Chapter 3. v

A.9 Collected data of the acetone / $ZnBr_2$ heat capacity ($J/g.K$) as mentioned in Chapter 3. vi

A.10 Collected data of the acetone / $ZnBr_2 - G$ heat capacity ($J/g.K$) as mentioned in Chapter 3. vi

Nomenclature

List of Abbreviations

Ac. Acetone

CFD Computational fluid dynamic

CHF Critical Heat Flux

cl Centreline

CNT Carbon Nano-Tube

COP Coefficient of Performance

DLS Dynamic Light Scattering

DSC Differential scanning calorimetry

EG Ethylene Glycol

G Graphene

HP High Pressure

HT Heat Transfer

HTFs Heat transfer fluids

liq Liquid

LP Low pressure

NBF Nano-binary fluid

nf Nano fluid

NSF Nano-salt fluid

PVA Polyvinyl alcohol

PVP Polyvinyl pyrrolidone

QUICK Quadratic Upstream Interpolation for Convective Kinematics

RANS Reynolds Averaged Navier Stokes solver

RHX Refrigerant Heat Exchanger

RR Refrigerant reservoir

SDS Sodium dodecyl sulphate

SHX Solution Heat Exchanger

SIMPLE Semi-Implicit Method for Pressure Linked Equations

SSR Strong solution reservoir

STEM Scanning transmission Electron Microscope

TC Thermal Conductivity

TEM Transmission Electron Microscope

UDF User define function

vap Vapour

VARC Vapour Absorption Refrigeration Cycle

VARS Vapour Absorption Refrigeration System

VCRS Vapour Compression Refrigeration Systems

VOF Volume of fluid

Vol Volume

WSR Weak solution reservoir

wt Weight

ZnO Zinc Oxide

$ZnBr_2$ Zinc Bromide

Nomenclature

$\bar{A}$	Cross section area	m^2
β	accommodation coefficient	
$\triangle$	Uncertainty	
Δ	Difference between two quantities	
$\dot{v}$	Volumetric flow rate	m^3/s
ϵ	time relaxation factor	1/s
μ	Dynamic viscosity	mPa.s
ν	Velocity	m/s
ρ	Density	kg/m^3

v	Velocity	m/s
c_{p_s}	Specific heat	$\frac{kgm^2}{Ks^2}$
C_{sf}	Rohsenow constant	
D	Translational diffusion coefficient (velocity of Brownian motion)	m/s
d_b	bubble diameter	m
D_H	Hydrodynamic diameter	m
d_p	particle diameter diameter	m
E	Energy	J
g	Gravity	m/s^2
H_{fg}	Enthalpy	J/mole
h_{fg}	Latent heat	J/kg
I	Turbulence intensity	
k_b	Boltzmann constant (1.38×10^{-23})	J/K
K_t	Turbulence kinetic energy	J
M	Molar mass	kg/mol
m	Mass	kg
P	Pressure	kg/ms^2
q	Quantity of heat	J
R	Universal gas constant (8.314)	$J/molK$
S_d	Standard deviation	

S_E	Energy source	J/m^3s
S_M	Mass source	kg/m^3s
S_{er}	Standard error	
t	Time	s
V	Volume	m^3
V_{err}	Error volume	m^3
d	Diameter	m
h	Heat transfer coefficient	W/m^2K
N	Number of measurements	
Nu	Nusselt number	
Pr	Prantdl number	
Re	Reynolds number	
T	Temperature	K
x	Variable	

1 INTRODUCTION

1.1 Context

A Lot of waste heat and greenhouse gas are released from the factories to the environment. The waste heat can be used to generate cooling using absorption refrigeration systems. Utilizing energy that would otherwise be lost to the environment helps to decrease the global environmental problems which are related to CO_2 emission. Another benefit of using absorption refrigeration is that it can operate using low grade heat and can give more useful output from the low grade thermal energy than alternatives like power generation. Absorption refrigeration operates smoothly and relatively quietly because only the liquid pump has moving parts and there is no effect on the performance by reducing the load. On the other hand, there are some disadvantages from using absorption refrigeration which present to have a lower coefficient of performance relatively comparing with the compression refrigeration (even they use different grade energy); temperature limitation of the heat source (system cannot operate under this limit) and in some systems (systems working with $H_2O/LiBr$), crystallization is a significant problem which must be avoided at the design stage. The performance of absorption refrigeration depends on its type and the working fluid [1].

The particular heat transfer fluids (HTFs) such as water, oil and glycols has a great influence on the size of the system depending on its ability to transfer the heat. However, they have generally poor heat transfer efficiency because of the low thermal conductivity. Researcher efforts is applied to enhance the thermal properties of fluids. To improve the thermal properties of the fluid, powdered materials such as silver, copper, iron, alumina, CuO, SiC and carbon nano-tubes, which have much higher thermal conductivity can be added to the fluid. This idea was proposed by Maxwell in 1881 (Maxwell 1873) [2]. Early cases studied, solid particles of micrometre, and millimetre scale mixed with the base fluids to make suspensions. However, these particles cause problems, such as damaging of the surface, blocking the micro-channels, corroding the pipeline and increasing the pressure drop, which considerably limits the practical applications. The difficulty of producing smaller particles was a limiting reason for using the micro-suspension liquid.

Generally, nanofluids are a dispersion nanometre-scale particles (1-100 nm) into heat transfer fluids. The large surface area per unit volume, dimension and size-dependent physical properties like thermal conductivity and viscosity, and lower momentum kinetic energy due to the tiny size are beneficial properties of the nanoparticles. In addition, the large surface area gives the nanoparticles better and more stably dispersed in base fluids. A most attractive characteristic of nanofluids is improving the thermal conductivity even by adding only small amount of nanoparticles. The improvement of nanofluid's thermal properties will enhance the efficiency of heat exchanging especially in the boiler and the absorber of VARS, reduce the size of the systems by reducing the sizes of these components, save pumping power, and reduce operational cost. The properties of nanofluids mainly depend on the type of the nanoparticles and the basefluid as well as the stability of the nanofluid. The affect of

the nanoparticles is investigated on a low boiling temperature nanofluid in a high pressure part of the VARS, which includes the boiler. This was achieved by investigating the effect of different concentration of the nanoparticles on the improvement of heat transfer. According to Hamilton [3], VARS with acetone/$ZnBr_2$ operates at a low temperature (just above ambient) and this system is suitable for the solar PV cooling. but the outcome of this thesis (experimentally and numerically & with and without nanoparticles) showed, it is unlikely that the system can be used with solar PV, because no boiling can be generated at 80 ^oC. This study also shows how the boiling rate in the VARS improves using nanoparticles with acetone/$ZnBr_2$ by developing a novel model for the numerical boiling method.

The rapid development in computer power over the last few decades has motivated the use of computational fluid dynamics (CFD) in two-phase flow research. This is due to its relatively low cost compared to the costs of experiments. Many approaches have been developed to simulate the simultaneous flow of two-phases. These include Eulerian-Eulerian and Eulerian-Lagrangian methods.

Boiling process is more complicated and difficult to correlate in cases where the liquid flows through the heater due to a circulation effect. There are two effects, which cause heat and mass transfer in nucleate boiling, firstly, the bubble creation and motion near the hot surface and secondly, the direct sweeping of the heater surface by the liquid itself. Both of the flow and nucleate pool boiling contribute to the heat transfer mechanism. There is no general definitive method of correlating flow boiling data. A lot of studies treating different issues in the pool boiling numerically and experimentally were found, (described in 2.4.1). There are sufficient number of research works dealing with flow boiling experimentally. However, a very few numerical studies of

flow boiling have been done because there is no general correlation or model covering this area. The most acceptable correlation that could deal with this process experimentally is Rohsenow correlation (Chapter 4). Adding a salt to the liquid in flow boiling makes the process more complicated because of the variations of concentration. Adding nanoparticles to the fluid makes the flow boiling process more intricate. To make just one component evaporate in this blended solution with three components numerically is challenging. A new technique is developed in this research to deal with this problem (making just the acetone evaporates from the mixture). Therefore, in the domain (boiler) there are four different component (liquid acetone, dissolved salt, nanoparticles and vapour of the liquid). The numerical technique is explained in chapter 6.

1.2 Aims and Objectives

The aim of this project is to investigate the effects of the nanoparticles on the heat transfer enhancement and the performance, both experimentally and numerically on the VARS, a good knowledge of the nanofluid behaviour on the heat transfer as well as a knowledge on the CFD programming is required. There are a lot of studies related to boiling nanofluid (experimentally) and a very small number related to numerical studies dealing with dynamics of bubbles in pool boiling. All these studies involve a single base fluid such as water & ethylene glycol (EG). In addition, just a few studies were found related to flow boiling. There is no work related to flow boiling of **binary-fluid and nano-binary-fluid** (the base-fluid is binary-fluid) experimentally or numerically. Therefore, there is a need to carry out reliable experimental work using a nano-binary-fluid (acetone-$ZnBr_2$-nanoparticles) as a working fluid for the first time in the VARS and generate a new CFD method for flow boiling simulating an evaporation of one component (acetone) from this

mixture.

Hence, the **objectives** of the present study are:

1. *Investigate the effect of the nanoparticles (graphene & ZnO) on the properties of the working fluid (acetone-$ZnBr_2$)* by preparing the nanofluid and measuring the properties (density, viscosity, thermal conductivity and specific heat capacity) and compare them with the calculating methods which are found in the literature for there properties.
2. *Investigate the effect of the nanofluid on the performance of VARS* by running the nanofluid in the single effect VARS test rig, change the physical parameters (velocity, volume fraction and temperature) and checking the effect of each of these parameters by measuring the temperature of the solution in and out the boiler and the mass flow rate in the condenser and the evaporator.
3. *Generate a CFD model to compare the single and the two phase methods of the nanoparticles in the flow.* Then use the best approach in the boiling process.
4. *Generate a CFD model of the flow boiling process for the nanofluid in the boiler* by developing a new method of boiling the acetone from the mixture (acetone-$ZnBr_2$- nanoparticle) using the two phase approach for the nanoparticles and the volume of fluid (VOF) method and mixture method models for the multiphase simulation, then validate these models with the experimental data.

1.3 Structure of the thesis

The layout of this thesis is summarised as follows:

Chapter 1 – *Introduction*– This Chapter includes an introduction to the three main subjects related with this thesis (VARS, Nanofluid and CFD modelling). In addition this chapter defines the question of research, the aims and objectives of the study, methodology and the structure of the thesis.

Chapter 2 – *Literature review*– This chapter explores critically most studies related to this study, including different types of absorption refrigeration, properties of the nanofluid and the parameters affecting them and the numerical modelling of the single and two phase flow, boiling, evaporation and condensation processes.

Chapter 3 – *Preparation and properties of the nanofluid*– This Chapter shows how the nanofluid was prepared and clearly shows the effects of the nanoparticles on the properties of the solution as well as the effect of different concentrations of the salt. It also shows the images and the structures of the nanoparticles. At the end of this chapter there is an answer about the possibility of moving the nanoparticles remaining in the liquid when boiling the nanofluid rather than rising with the vapour.

Chapter 4 – *Experimental study of flow boiling in the VARS*– This chapter includes the rig description, experimental procedure, ways of calculating and measuring the parameters and the results which include the effects of the nanoparticles, the effects of the boiler temperature and the effects of the flow rate on the heat transfer, vapour rate generation and temperature of the solution.

Chapter 5 – *CFD assessment of the effects of nanoparticles on the heat transfer properties of acetone/$ZnBr_2$ solution for single and two phase flow*– Because the numerical modeling of the boiling nanofluid can be done under the

effects of the single or two phase flow, this chapter shows a comparison between these two techniques against the experiment results. A Computational Fluid Dynamics (CFD) model of the binary-fluid with zinc oxide nano-particles in a flat tube flow is simulated with validation against literature results.

Chapter 6 – *Numerical study of flow boiling of the nano-salt-fluid in the boiler*– This chapter describes the method for numerical modelling of the flow boiling of the nano-salt-fluid, defining the mathematical model and describing the geometry, computational, meshes and the boundary conditions. Then it demonstrates validation by comparing the results with the experimental results; this is followed by all the quantifying results for the mixture models and visualising results for both the mixture and VOF methods.

Chapter 7 – *Conclusions and Recommendations*– Describes the processes used for the investigations in this thesis and presents the main outcome, together with areas of further work that were identified during this research.

2

LITERATURE REVIEW

This chapter introduces literature related to this work, including: the fundamentals of absorption refrigeration as the intended final application to highlight the potential for improvements related to heat transfer enhancement; the concepts and developments of nanofluid technology, as a method for improving the heat transfer; and the state of numerical models applicable to heat transfer and nanofluid boiling as a facility to represent the physical processes of the heat transfer. This background gives the developments related to the field of research which is the intent of this thesis and presents the areas in which this thesis contributes new knowledge.

2.1 Development of Absorption Refrigeration

The absorption cycle was developed in the 18^{th} century and in 1810 water was converted into ice in a vessel which was connected to another vessel containing sulfuric acid; the acid absorbed water vapour which caused reduction in the temperature of the water as it evaporated and consequently a layer of ice appeared on the surface of the water [1]. In 1828, Windhausen used the same principle for the single stage vapour absorption refrigeration cycle (VARC) which worked with H_2O/H_2SO_4 as working fluids [4]. In 1845, Edmund Carre developed a water-sulphuric acid machine which was used for cooling drinking

water [5]. In 1859, Ferdinand Carre developed a new cycle using NH_3/H_2O as the working fluid and this machine was used to make ice, (as shown in Figure 2.1) [5, 6] and this machine was subsequently used as a commercial VAR in USA [7]. In 1922, at the Royal Institution of Technology, Stockholm, a three fluid (Water, Ammonia and Hydrogen) system was designed by two students. In which, the cycling of the weak and strong solution is done by heating based on a bubble pump and hydrogen is used to reduce the pressure of the Ammonia in the evaporator [8]. In 1950 $H_2O/LiBr$ was used as a working fluid and after several years the double effect cycle (cooling cycles improve the performance of absorption systems by using the input heat twice) was developed as an alternative type of absorption refrigeration cycle with improved performance [1].

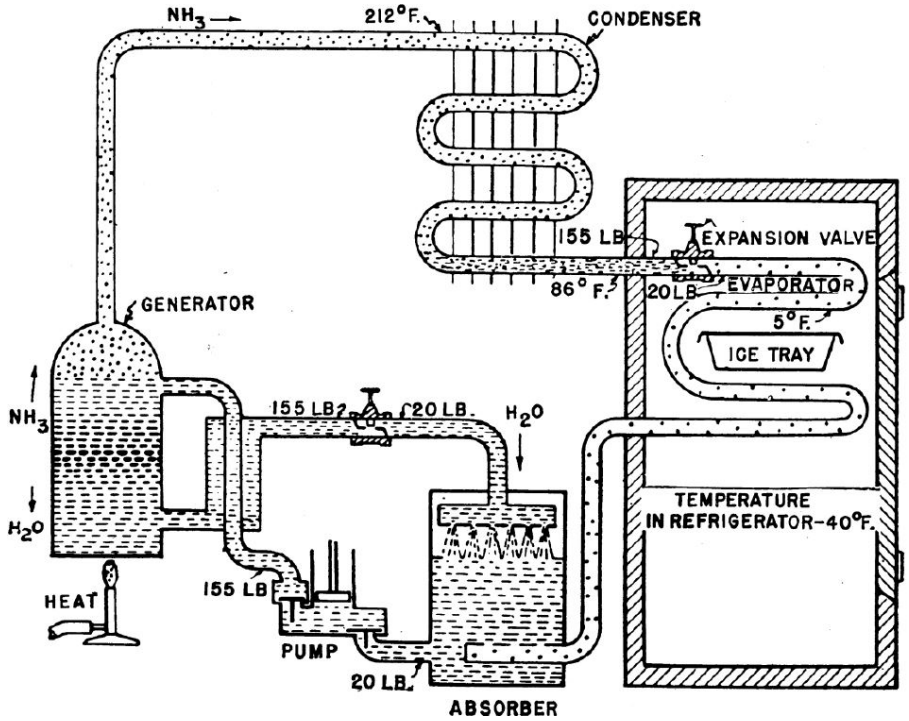


Figure 2.1: Absorption refrigeration machine sketch by Ferdinand Carre [6]

Absorption refrigeration suffered because of alternative technology in the form of vapour compression refrigeration systems (VCRS) which has better performance; but after the oil and economy crises of the 1970s and with rising

fuel and electricity prices, there was increased interest in VARS. Today, there is again renewed interest because of the drive to reduce energy demand by utilizing waste heat, and absorption refrigeration is one of the most efficient technologies for utilizing that heat [7]. After the Second World War, Japanese companies such as Kawasaki, Mitsubishi and Hitachi noticed the importance of this technology. In 1964 Kawasaki released the first production of the double effect cycle to the market. At the end of the last century, the interest in VARS increased as it became the subject of a possible and helpful solution for reducing global warming, protecting the ozone layer, using environmentally friendly fluids and taking advantage of solar or waste energy[5].

Nowadays, researchers trying to develop the performance of the absorption refrigeration. Some researchers tried to develop a specific part of the system to improve the performance and the most common part is the absorber [9, 10]. Others have developed new types of refrigeration devise depending on the source of energy and the output power, for example, the hybrid types developed by J.Jeong et al. at 2011 [11], the co-generation system done by Hua et al. at 2014 [12] and the tri-generation configuration developed by Mathkor et al. at 2015 [13]. The study of thermophysical properties of the working fluid is done by some researchers [14, 15]. to understand the general idea regarding the principle of the system operations, the basics of the single absorption cycle included as following.

2.1.1 The Basic principles of absorption cycle

The principle of working in VARS is similar to VCRS with two important differences: 1) the absorption cycle is driven mostly by heat transfer 2) a secondary fluid is used in addition to the refrigerant which is called the absorbent or sorption medium [5]. Generally, the mechanical compressor in VCRS is

replaced by a thermal compressor, which comprises a generator, absorber, mechanical pump and optional solution heat exchanger (SHX) as illustrated in Figure 2.2. VARS like VCRS works under two levels of pressure: high pressure in the refrigerant separating side which is represented by the condenser and generator; and low pressure in the evaporator and absorber. The high pressure is greater than the lower by approximately 4 times. The working principle of VARS can be described by the following steps [5, 16]: (the following numbers illustrated on figure 2.2 b in red colour)

1. The refrigerant is boiled out of the absorbent solution in the generator by input heat; this refrigerant is a vapour at high pressure and the absorbent remains liquid.
2. The refrigerant is condensed to liquid; the hot and high pressure vapour flows to the condenser where it's cooled through an external heat sink.
3. The refrigerant pressure is lowered as the liquid passes through an expansion valve and to the evaporator pressure level.
4. The refrigerant evaporates in the evaporator, an external heat source at low temperature makes the refrigerant boil to vapour again and this is the point at which the refrigerant effect is felt.
5. The saturated and low pressure refrigerant vapour passes into the absorber which contains the strong solution (absorbent) coming from the generator, and there the absorbent absorbs the vapour, producing a weak solution, with the consequent production of heat of solution which is exchanged to the surrounding.
6. The weak or diluted solution (rich in refrigerant) is pumped again to the generator and the process starts again in there.
7. If a solution heat exchanger (SHX) is used in the system, the diluted

solution may gain some heat from the strong solution (absorbent) which leaves the generator through (SHX); consequently, the diluted solution needs lower heat input at the generator to continue the cycle, and this process enhances the coefficient of performance (COP) which can be defined as equation 2.1 [1, 17].

$$COP = \frac{\text{cooling capacity obtained in evaporator}}{\text{Heat input to generator + work input to the pump}} \tag{2.1}$$

The pump input work is negligible compared with generator input heat, and this work can be neglected for the purpose of thermodynamic and mathematical analysis.

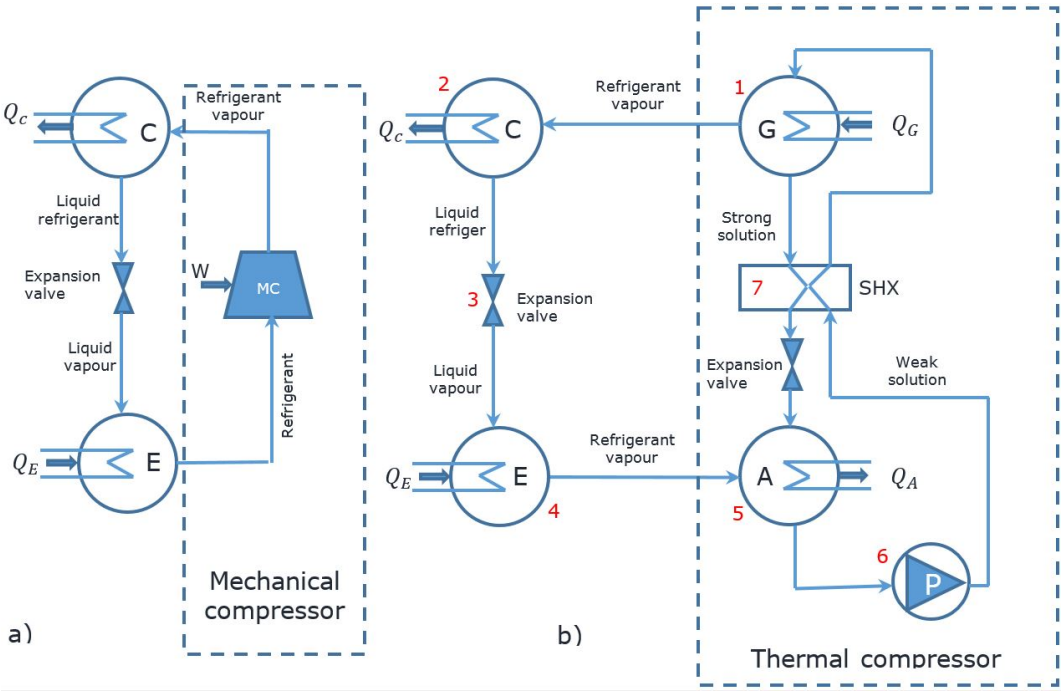


Figure 2.2: a) VCRS and b)VARS, where C: condenser; E:evaporater; G:generator; A: absorber; Q_c:condenser heat transfer; Q_E:evaporater heat transfer; Q_a:absorber heat transfer; Q_G: generator heat transfer; SHX: solution heat exchangeer and MC: compressor motor [5].

2.1.2 Types of absorption system

The single effect absorption refrigeration cycle (shown in Figure 2.3) is the simplest and most common type and the general principle of its operation is described in 2.1.1. Aphornratana [18] confirmed according to experimental study that the COP increases by 60% when the solution heat exchanger (SHX) between the absorber and the generator is used as shown in Figure 2.3). Karno and Ajib [19] experimentally and theoretically studied the single effect cycle with a new working fluid (Acetone/Zinc Bromide). They confirmed that use of both (SHX) and a refrigerant heat exchanger (RHX) which connects the condenser with the evaporator gives increased COP.

$$COP_{SHX+RHX} > COP_{SHX} > COP_{RHX} > COP_{withoutHX}$$

The most common working fluid in a single effect cycle is $H_2O/LiBr$ [1], but when volatile solution such as NH_3/H_2O is used, a rectifier should be connected to the cycle between the generator and the condenser and the job of this rectifier is separating the refrigerant vapour (Ammonia vapour) from some of the absorbent vapour (water vapour) which leaves the generator and allows only the refrigerant vapour to pass to the condenser [5]. Other fluids used in single effect absorption refrigeration cycles include: $H_2O/LiNO_3 + KNO_3 + NaNO_3$ [20], $NH_3/LiNO_3$, $CH_3OH/LiBr + ZnBr_2$, $H_2O/LiCl$ (cited in [1]), $H_2O/LiBr$ [21] and $(CH_3)_2CO/ZnBr_2$ [3, 19].

In order to achieve a high system performance of the absorption refrigeration, a double effect cycle was developed in 1956 [22]. There are three types of fluid circulations in a double cycle; series, parallel and reverse parallel (In the series flow type, the working solution flows from the absorber into the high pressure generator and intermediate pressure generator successively. In the parallel flow type, the solution flows from the absorber into the high pressure

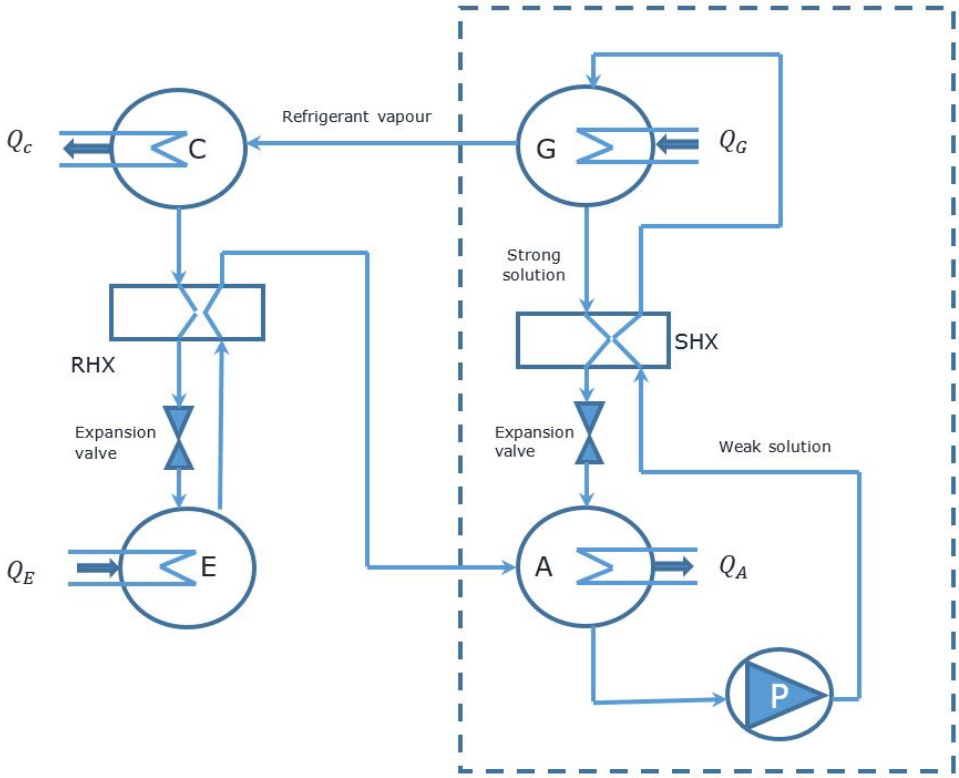


Figure 2.3: Single effect absorption cycle with two heat exchangers: refrigerant heat exchanger RHX and solution heat exchanger SHX [19]

generator and the intermediate pressure generator at the same time. In the reverse flow configuration, the solution from the absorber first flows into the intermediate pressure generator and then into the high pressure generator [23]). A comparison between these three types was studied by Frashi and Mahmoudi [24] using $H_2O/LiBr$ to investigate the COP in each type; they found that the parallel and reverse parallel have approximately the same COP which is higher than the series type. Xu et al. [25] studied the thermodynamic analysis and the effect of design parameters in a series double effect absorption system and they studied the parallel type in 1997 [26]. Arun et al. [27] evaluated the equilibrium temperature for the low pressure (LP) generator (second generator) in the double effect, series system working with $H_2O/LiBr$ and they found that the equilibrium temperature of the LP generator increased with increasing the temperature of the high pressure generator HP, condenser and

evaporator and decreased with increasing absorber temperature. In 2000, the same group made a comparison between double effect parallel and series flow with $H_2O/LiBr$ as working fluid [28]. In 2004 Liu and Wang [29] studied the efficiency prediction of a new designed solar gas driven double effect absorption system working with $H_2O/LiBr$ and this system used additional energy more effectively and less dependence on the solar radiation.

For applications which operate at a lower temperature, the half-effect absorption refrigeration cycle system was developed [22]. A review reveals several works done with this system. In 2002 Kim and Machielsen [30] studied several types of air-cooled solar absorption systems with regards to cost and performance. They found that the half effect requires 40% more heat exchange area and less than 60% more collector surface. Also, they confirmed that the $NH_3/LiNO_3$ is the best paired fluid mixture for this unit. Arivazhagan et al. [31] experimentally investigated the performance of a two stage half effect absorption cooling system using tetrafluoroethane/dimethylacetamide ($R134a/DMAC$). They found that the evaporation temperature is -7 ^oC when the generator temperatures vary between 55 to 75^oC and they found that the COP is 0.36 when the generation temperature is between 65 - 70 ^oC. Gebreslassie et al. [32] evaluated the effect of the heat source temperature on the coefficient of performance and analysed exergy of multi-effect $H_2O/LiBr$ absorption units in half, single, double and triple cycles. They found that the COP decreases from triple to half cycle and the maximum exergy efficiencies are lowest for the half effect followed by the single effect.

The most important part of these systems is the working fluids (as reviewed in the next section), as they affect the performance, and the size of the system depending on their thermal and transport properties as well as their ability to transfer heat.

2.1.3 Working fluid for absorption refrigeration systems

Chemical and the thermo-physical properties of the working fluid (absorbent and refrigerant) have a great influence on the performance and efficiency of the absorption cycles. There are some characteristics required for refrigerant and the absorbent ([1, 5]):

- Low freezing temperature for the refrigerant.
- Difference in boiling temperature between the refrigerant and the absorbent should be as large as possible.
- Both of them should have no chemical reaction together under any state of pressure and temperature.
- Both fluids should be stable to avoid any undesirable reactions.
- It is preferable that the fluid has a low toxicity and low cost.

The most familiar working fluids are $H_2O/LiBr$ and NH_3/H_2O [33]. $H_2O/LiBr$ is used in many literatures for various purposes described in the following [26, 27, 28, 29, 32, 34, 35]. Kim and Machielsen [30] evaluated the air cooled solar half effect absorption cooling system using NH_3/H_2O, $NH_3/NaSCN$ and $NH_3/LiNO_3$ and they found that the last solution showed the best results regarding COP. Sencan et al. [36] used artificial neural network to analyse the absorption system using $H_2O/LiCl$ and $H_2O/LiBr$ and they found that the $H_2O/LiBr$ has a greater COP than $H_2O/LiCl$. Grossman et al. [20] simulated the absorption system by computer modelling using different solutions such as $H_2O/LiBr$, NH_3/H_2O, $CH_3OH/LiBr - ZnBr_2$ and they wrote a code for the properties of each solution. Table 2.1 shows a summary of the possible working fluid pairs for the absorption system. In 2008 Ajib and Karno did two studies [14, 19] related with the properties of acetone / zinc bromide ($(CH_3)_2CO/ZnBr_2$) and analysis of an absorption refrigeration system, a fluid combination which works well with a low temperature and it is proposed that

it is used in the present research.

Karno and Ajib [14] experimentally found that the COP for the single effect absorption refrigeration with $acetone/ZnBr_2$ is 0.4 with a heat source under 60 ^oC. This pair were mentioned in the review of Sun et al, in 2012 [37] as a low temperature working fluid. The acetone has a melting point of -94.6 ^oC and it can provide sub 0 ^oC cooling temperature, however, the $ZnBr_2$ has a boiling temperature of 650 ^oC and it is not volatile [38]. In 2016, Hamilton [3] analysed a low temperature waste heat source (80 ^oC) for an absorption system working with $acetone/ZnBr_2$. He stated that the absorption refrigeration system has ability to provide adequate heat removal at the heat source and the ability to deliver cooling from this low level energy. One of the ideas to improve the heat transfer in the absorption system is by converting the basefluid (acetone / $ZnBr_2$ in our case) to a nanofluid. The following section describes the development and the properties of nanofluid.

Table 2.1: Summary of working pairs for absorption system

Refrigerant	Absorbent
H_2O	$NaCl$
	$LiBr$
	$LiClO_3$
	$CaCl_2$
	$ZnCl_2$
	$ZnBr$
	H_2SO_4
	$Alkali\ Nitrate$
	$Alkali\ Hydroxides$
NH_3	H_2O
	$LiNO_3$
	$LiNO_3 + H_2O$
	$Alkali\ thiocyanates$
SO_4	$Organic\ solvents$
$Acetone$	$ZnBr_2$

2.2 Nanofluids

Solid nanomaterials such as silver, copper, alumina, CuO, SiC and carbon nanotubes have much higher thermal conductivity than VARS base-fluids. These materials enhance thermal conductivity when mixed with the relatively low conductivity fluids as mentioned by Maxwell in 1881. Before discovering nanomaterials, solid particles in micrometre, and millimetre scale were mixed into base fluids to make micro-fluids and milli-fluids. However, these relatively large particles cause problems, such as clogging micro-channels, corrosion of pipes and increasing the pressure drop in the tube, which have a significant effect on practical applications. A nanofluid was described as suspension of different nanoparticle metals in various fluids in 1995 by Choi and Eastman as described by Han [39].

Nanomaterials have important properties, such as large surface area to volume ratio which makes nanoparticles more stably dispersed in base fluids compared with micro-fluids and milli-fluids. Nanofluids maintain the transport properties of the base fluid, and because of the homogeneous dispersion of nanoparticles in the fluid, nanofluid behave like a single phase [40]. The increase in thermal conductivity by adding even a little amount of nanoparticle to the fluid is a most attractive characteristic of nanofluids, for example Eastman et al. [41] reported that by adding only 0.3% volume fraction of Copper (Cu) nanoparticles with diameter 10 nm to Ethylene Glycol (EG), the thermal conductivity increased by 40 %. Generally, the benefits of nanofluids are [2]:

- Higher thermal conductivity: large surface area of nanoparticles improves the heat transfer and because the thermal conductivity of the nanoparticles is greater than the base-fluid, thermal conductivity of the nanofluid increases.
- Dispersability (Stability): because nanoparticles are very small and

they have small mass, so their likelihood of sedimentation is insignificant and this characteristic suggests the nanofluid are stable.

- Cooling without clogging in microchannels: High conducting fluid and large heat transfer area are provided by combination of nanofluid with microchannel and this cannot be attained with micro-particles which have larger size and may clog the microchannel.
- Decreasing the rate of erosion: because nanoparticles are very small, the momentum caused by these particles on pipe wall such as heat exchanger, pipelines and pumps is much smaller and erosion is reduced.

The fluid produced in practice is a solid-liquid suspension (not nanofluid) because the particles sediment after a specific time (days or months) depending on the type of the particles and the base fluid. A true nanofluid should be a completely new fluid with a new property not changing with time [40]; the differences between true nanofluid and solid-liquid suspensions are highlighted in Table 2.2.

Nanofluids are considered as a promising fluid for their unique features. Therefore, they are used in different areas specially for the heat transfer purpose. The next section presents a review of the application of nanofluid.

Table 2.2: Conventional solid-liquid suspensions compared to nanofluids

Criteria	Conventional (solid-liquid suspension)	Nanofluids
Stability	Settle	Stable
Surface/volume ratio	Low	High
Thermal Conductivity	Low	High
Clogging	High	Low
Pumping Power	Large	Small

2.2.1 Applications of nanofluids

Nanofluids are commonly used by different areas such as transportation, energy generation, microsystems and chemical technology and biotechnology. For example, it can be used to cool car engines, welding tools and high heat-flux instruments like high power microwave tubes and high-power laser diode arrays. It could be used in coolant flows through tiny passages in $MEMS$ to enhance the performance. Nanofluids can be a part of the nuclear application to improve the heat flux in a forced convection loop. Nowadays, many companies observe the potential of the nanotechnology for the manufacting applications. In transportation commerce, nanocars, GM and Ford, among others are concentrating on nanofluids research developments [42, 43, 44]. In the US, 320 billion kWh of electricity which corresponds to 5.5 million barrels of oil per year, could be saved, if the efficiency of the chillers enhanced by 1% with the nanofluids [45, 46].

Heat exchangers can be smaller with enhanced heat transfer in vehicle radiators and reducing the weight. Many methods are available to improve heat transfer. The amount of the heat transfer can be calculated using the equation bellow:

$$Q = hA\Delta T$$

Where Q is heat, h is heat transfer coefficient, A is heat transfer area, and ΔT is temperature difference. Heat transfer can be enhanced by increasing the temperature difference. However, ΔT is limited by the material composition and process restraints. For instance, in nuclear power the temperature should not reach a maximum to avoid accidents. Furthermore, using the minimum temperature to increase the temperature difference leads to reducing the rate of nuclear reaction which reduces the efficiency of the system [47]. The surface

area A can be increased, but, increasing the surface area is limited as well, especially in microprocessors and micro-electro-mechanical system ($MEMS$). Even in larger scales, the area is limited by the size and weight of the system [47]. Heat transfer coefficient (h) can be improved by enhancing the thermal properties of the heat transfer fluid. Adding ethylene glycol (EG) to water reduces its freezing point and increases its boiling point. The thermal conductivity of EG is relatively low compared to that of water and engine oils are even worse heat transfer fluids than EG in thermal flow performance. Adding solid particles of nano-scale to the coolant (creating a nanofluid) can enhance the thermal properties and has the ability to enhance the heat exchange rates and fuel efficiency. This development could either be used to reduce the size of cooling systems with the same heat transfer efficiency or remove more heat from the vehicle engine by keeping the same size of the cooling system [47, 48, 49, 50, 51].

Many researchers studied the performance of the nanofluid as the heat exchanger fluid [52, 53, 54, 55, 56]. Pantzali et al. [54] investigated the efficacy of nanofluids (water base 4 vol.% CuO) as coolants. They stated that when the heat exchanger operates under turbulence conditions, the use of nanofluids has a benefit, if the increase in the thermal conductivity is accompanied by a marginal increase in viscosity, which seems very difficult to be achieved. On the other hand, the researcher concludes that if the heat exchanger operates under laminar conditions the use of nanofluids looks worth, however, it is considered as a high price and difficult to produce a stable nanofluid. In 2009 Lee JH [55] evaluated the effect of $H_2O - Al_2O_3$ nanofluids as a new phase change fluid for the thermal energy storage for cooling systems. The outcomes suggested that the freezing rate of nanofluids was improved. They found that the total freezing time can be saved by 20.5% by only mixing 0.2 wt. % Al_2O_3

nanoparticles into water, Thus, the application of nanofluids in cooling industry can improve the efficiency and the operating time of refrigeration systems. Liu et al. [56] investigated the possible ways to enhance the performance of water chillers using 0.1 vol.% of $MWNT$. They found that the increase of thermal conductivity of the nanofluid relative to the base fluid is only 1.3% at room temperature. Also, they stated that one of the possible mechanisms for the significant rise of system performance is due to the dynamic dispersion of the nanoparticles in the working fluid.

Generally, nanofluids can be classified according to their function in different and specific areas as reported by Saidur et al.[57]. They classify nanofluids into heat-transfer nanofluids, tribological nanofluids, surfactant and coating nanofluids, chemical nanofluids, process/extraction nanofluids, environmental (pollution cleaning) nanofluids, bio- and pharmaceutical-nanofluids and medical nanofluids (drug delivery and functional tissue–cell interaction). The applications of the nanofluid can be summarized as: engine cooling, engine transmission oil, in diesel electric generator as jacket water coolant, boiler exhaust flue gas recovery, heating and cooling of buildings, cooling of electronics, cooling of welding, in transformer cooling oil, nuclear systems cooling, solar water heating, drilling, heat exchanger, chillers, defence, space, high-power lasers, microwave tubes, biomedical applications, lubrications, thermal storage and drag reductions [57].

The synthesis of the nanofluid has a significant impact on the stability, properties and the ability to transfer heat. In the next section, the method of the synthesis of the nanofluid is reviewed.

2.2.2 The synthesis and nature of Nanofluids

Nanofluids are prepared either by the one step or the two steps method. The one-step method, which is developed by Eastman et al. [41] involves preparing the nanoparticles and dispersing them to create a nanofluid simultaneously. This method avoids the processes of drying, storage, transportation, and dispersion of nanoparticles, so agglomeration rate of particles is reduced and the stability of the nanofluids is increased. On the other hand the one-step method physically cannot produce nanofluids in large scale, and it is costly [58]. Two-step preparation is done by mixing base-fluids with available nanomaterials obtained from different routes such as milling, grinding, and vapour phase methods and by precipitation; most experimental studies depend on this method [59, 60, 61, 62, 63, 64, 65] which is illustrated in the schematic Figure 2.4 .

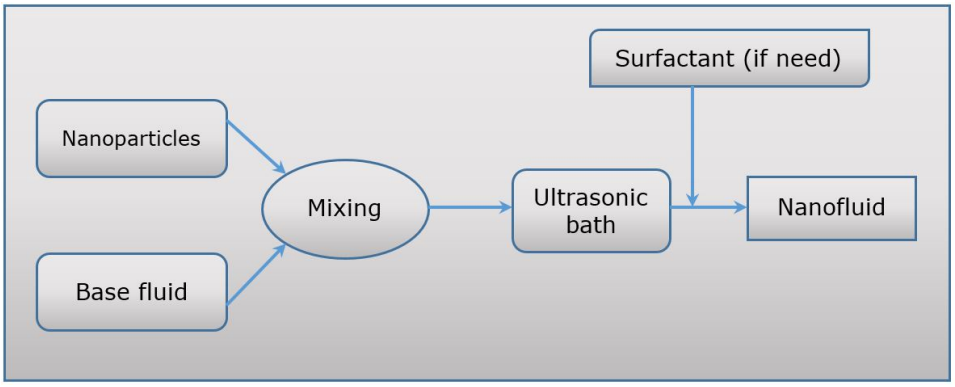


Figure 2.4: Two-step preparation method of nanofluids.

An ultrasonic bath vibrator or higher shear mixing device is usually used to mix nanoparticles with the base-fluid [66]. Some nano-powders have a tendency to aggregate because of the high surface area and surface energy (the excess energy at the surface of a material compared to the bulk); preventing this problem and improving the stability of nanofluid can be done by steric barrier (non-bonding interactions that influence the shape and reactivity of ions, particles and molecules) around the particles as a coating layer, for ex-

ample, when the particles are covered by polymeric surfactants, the particles can generate a barrier to prevent aggregation. Also, an ionic surfactant can be use, by which the particles are coated with specific charge coating (positive or negative) and the particles repel each other. The behaviour of surfactants under high temperature is also a significant concern because the temperature effects on the physical properties of the surfactants themselves [58].

The preparation of nanofluids by two step method is well reported in the literature. Wang et al. [67] and Li et al. [68] produced alumina nanofluids using the two-step method. Xuan and Li [69] prepared a nanofluid of water and transformer oil with commercially available copper nanoparticles using the same method. [41] assumed that the two-step preparation method is more appropriate to prepare nanofluids containing oxide nanomaterials than those including metallic nanomaterials. Murshed et al. [70] used the same method to prepare a $TiO_2 - H_2O$ nanofluid. Lee et al. [71] prepared nanofluids made with Nanotube (CNT) and Al_2O_3 based in NH_3/H_2O to create enhanced performance heat transfer solutions. Suganthi et al. [72] made preparations of ZnO-Ethylene Glycol (EG) and $ZnO - (EG)/H_2O$ nanofluids and evaluated their performance as coolant fluids. The time of the ultrasonication affects the stability but it depends on the nature of the materials used. For example Lee et al. [71] synthised the Al_2O_3 and Carbon nanotube (CNT) based in NH_3/H_2O by using the ultrasonic bath for 1 hour and leaving the solution for 72 hours to get a stable distribution. On the other hand Williams et al. [73] used ZnO and Al_2O_3 based in water for +12 hours in ultrasonic bath without getting a stable fluid. The main advantage for two step method is that it is economical for producing large quantities of nanofluid.

The potential for using nanofluids in the different applications appears to be promising. But the growth of the area is delayed by (i) conflict of agreement

on results found by different researchers; (ii) poor suspensions and stability; (iii) lack of theoretical understanding of the property changing mechanisms. Studies on nanofluids focus on specific different challenges such as stability, properties and the cost of nanofluids.

The stability of the nanofluid has a great influence on the properties and consequently on the heat transfer; and the most stable nanofluid does not necessarily have the most enhanced characteristics [74]. Eastman et al. [41] found that thermal conductivity of the nanofluid (EG + 0.3 vol.% Cu) reduces with time. They measured the thermal conductivity of nanofluids twice (2 days and 2 months) after the preparation. They found that the fresh nanofluid (after 2 days) has a higher thermal conductivity. They suggested that the dispersion of some particles over a long period of time reduces the stability. Lee and Mudawar [75] compared the stability of the nanofluid $H_2O + Al_2O_3$ visually over time. They found by keeping the nanofluids for 30 days some settling appeared. It showed long term degradation in thermal performance of nanofluids may occur. Particles settling must be investigated carefully, as it may cause clogging in the coolant pipes.

Some of the unstable nanofluids can by stabilized using a surfactant. But, Choi et al. [53] stated that the amount of surfactant can have a deleterious effect on viscosity, thermal properties and on physical and chemical stability, and therefore it is recommended to control the amount and the type of the surfactant carefully. They also found that the method of preparing the nanofluid has an effect on the stability. Fluid prepared with the single step method is more stable than that prepared with the two step method, but unfortunately, the single method is not used for manufacture over a wide range of combinations. According to Wu et al. [76] the stability of the nanofluid depends on the size of the nanoparticles. However, Hiemenz and Paul[77] state that the

viscosity and the density of the base-fluid and the density of the nanoparticles are the main effectors on the stability according to Stoke's law (equation 2.2).

$$\nu = \frac{2R^2}{9\mu}(\rho_p - \rho_l)g \tag{2.2}$$

where ν is settling velocity of the particles, R is the average radius of the particles, μ is the viscosity of the base-fluid and ρ_p and ρ_l are the density of the nanoparticles and the liquid respectively.

In two separate studies [78, 79] Takabi et. al numerically studied the effect of the hybrid nanofluid (two or more types of nanoparticle in the form of a mixture or composite suspension in a basefluid [80]) which presented Al_2O_3 – Cu / H_2O effects on the heat transfer in a uniform heated circular tube for turbulent and laminar regimes. They found that the heat transfer improved for the hybrid nanofluid more than the pure water or Al_2O_3 / H_2O. in the laminar case, which was studied in [79] the Nusselt number (Nu) which presents heat transfer enhanced by 7.2 % for the hybrid nanofluid compared with the base fluid. However, in [78] which involved turbulent flow, with the wide range of Re (10^4 – 10^5) and volume fraction of the nanoparticles (0 – 2 %) they confirm that the maximum improvement in the Nu reaches to 32 % in the hybrid nanofluid compared with the pure fluid.

The stability also depends on the type of base-fluid. Generally, the suspension of particles in water and EG are more stable than in other liquids. In the current study, the solution of liquid acetone-$ZnBr_2$ is used as a base-fluid. It was difficult to keep the stability with using a surfactant and a longer sonication time [81].

Because the performance of the heat transfer in the VARS is affected by the properties (such as density, viscosity, heat capacity and thermal conductivity) of the working fluid and the numerical investigation also needs to identify

these properties, the properties of the nanofluid are explored and reviewed in the following section.

2.2.3 Properties of the nanofluid (analytical expressions and experimental observation)

This section will focus on some thermodynamic and transport properties which are relevant to experimental studies and numerical models with nanofluids. Thermal conductivity is given special attention, as it has more influence on the results of heat transfer. The parameters having effect on the thermal conductivity such as type of nanoparticles and base fluid, shape and concentration of nanoparticles are also described. The most common experimental methods used for the estimation of thermal conductivity will also be discussed. Some relevant experimental results for nanofluid density, viscosity and specific heat are also reported.

2.2.3.1 Density

Most researchers, who deal with nanofluids, calculate the density analytically using the equation 2.3, depending on the physical properties of the particles and fluids.

$$\rho_{nf} = (\frac{m}{V})_{nf} = \frac{m_f + m_p}{V_f + V_p} = \frac{\rho_f V_f + \rho_p V_p}{V_f + V_p} = (\Phi_f)\rho_f + \Phi_p \rho_p$$

$$\rho_{nf} = (1 - \Phi_p)\rho_f + \Phi_p \rho_p \tag{2.3}$$

Where

$$\Phi_p = \frac{V_p}{V_f + V_p}$$

Where p and f refer to the particle and the base fluid respectively, m, ρ, V and Φ are the mass, density, volume and volume fraction, respectively. As can be seen, it is a straight forward mixture proportion relationship and there is increase in the density by increasing the volume fraction of the particles because the density of the particles is greater than the density of the fluid, and the relationship is purely a linear combination of each, suggesting no molecular level interactions and a straightforward suspension of the solid in the liquid. Ho et al. [82] experimentally studied the effects of the temperature and the volume fraction on the different properties of Al_2O_3/Water nanofluid and they found that the density increases with increasing volume fraction and slightly decreases with increasing temperature at the same rate as the base fluid as illustrated in Figure 2.5. They found good agreement between experimental and analytical results. Khanafer and Vafai [83] studied different experimental and analytical results for different studies. They derived a correlation of the density depending on the temperature for the results presented by [82] as shown in equation 2.4.

$$\rho_{nf} = 1001.064 + 2738.619\Phi_p - 0.2095T \tag{2.4}$$

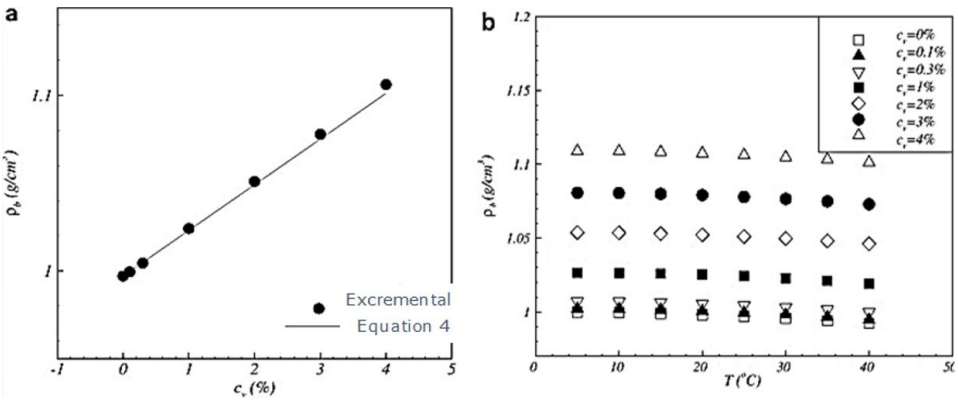


Figure 2.5: Effects of a) volume fraction and b) temperature on the density of the nanofluid. [82]

2.2.3.2 Viscosity

There are different models of viscosity developed in each theoretical and experimental field and most of these formulae are functions of volume fraction. Viscosity of liquid with spherical particles can be expressed by Einstein equation (2.5).

$$\mu_{nf} = \mu_f(1 + 2.5\Phi_p) \tag{2.5}$$

Where μ is viscosity and this equation is suitable for volume concentrations less than 3% because the interaction between the particles can be neglected [39]. By increasing the concentration, particles suffer hydrodynamic interaction and viscosity is no longer a function of volume fraction linearly but of higher order. For example Brinkman [84] used equation (2.6)

$$\mu_{nf} = \frac{\mu_f}{(1 - 2.5\Phi_p)^{2.5}} = (1 + 2.5\Phi_p + 4.375\Phi_p^2 + ...)\mu_f \tag{2.6}$$

Batchelor[85] studied the effect of the Brownian motion on the bulk stress in a suspension of spherical particles and derived an alternative, equation (2.7), they state that this equation is suitable for suspension with up to 10 vol.%

$$\mu_{nf} = (1 + 2.5\Phi_p + 6.2\Phi_p^2)\mu_f \tag{2.7}$$

Peyghambarzadeh [86] studied experimentally heat transfer in a radiator using water and ethylene glycol (EG) based nanofluid. They used equation (2.8) for water which was developed by [49].

$$\mu_{nf} = (1 + 3.7\Phi_p + 123\Phi_p^2)\mu_f \tag{2.8}$$

For the EG, they used equation (2.9) which developed by [87]

$$\frac{\mu_{nf}}{\mu_f} = 1 + \frac{\rho_p \upsilon_B d_b^2}{72C\delta} \tag{2.9}$$

Where υ_B (velocity of Brownian motion), δ (the average distance between the centres of two particles) and C (correction factor) all found by equations 2.10, 2.11 and 2.12.

$$\upsilon_B = \frac{1}{d_p}\left(\frac{18K_bT}{\pi\rho_p d_p}\right)^{(1/3)} \tag{2.10}$$

$$\delta = \left(\frac{\pi d_p}{6\Phi}\right)^{1/3} \tag{2.11}$$

$$C = \frac{a\Phi + b}{\mu_f} \tag{2.12}$$

Where K_b is Boltzmann constant (1.38 x 10^{-23} m^2kg/s^2K), a=-0.00004 and b=7.13 x 10^{-7}.

Equation 2.9 was evaluated by Delavari and Hashemabadi [88] and Masoumi et al. [87]. Masomi et al. found it to be valid only when $\Phi \leq -b/a$. In addition to theoretical equations there are experimental correlations. Khanafer and Vafai [83] correlated the data for viscosity from [89] for Al_2O_3 based on EG and the equation which they found is given by equation (2.13)

$$\mu_{nf} = (1 + 0.164\Phi_p + 302.34\Phi_p^2)\mu_f \tag{2.13}$$

Suganthi et al. [72] experimentally studied the performance on the heat transfer of $ZnO - EG$ nanofluid and they claim that the viscosity increases with increasing the volume fraction only when volume concentration is less than 0.25% and then it drops when the concentration of the particles is greater;

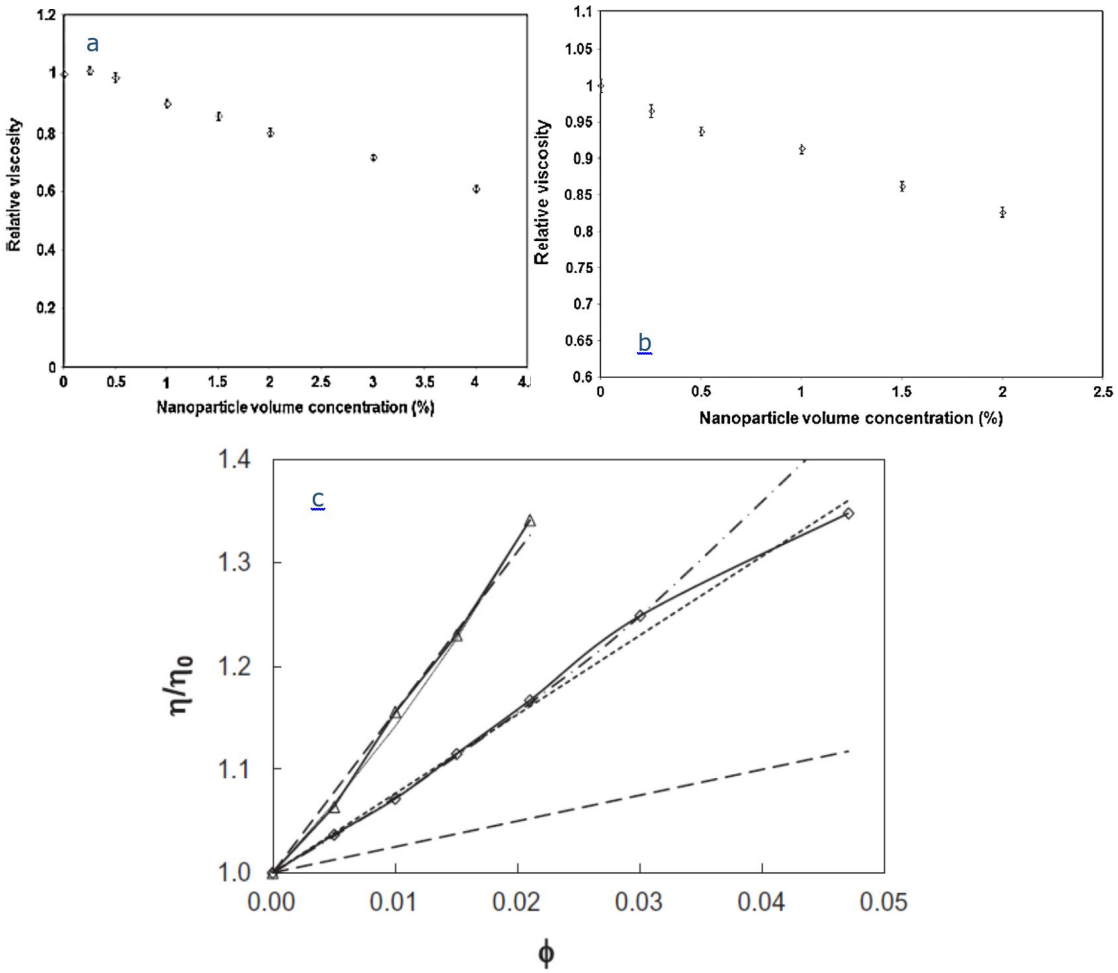


Figure 2.6: a) Influence of nanoparticle volume concentration on relative viscosity of ZnO–EG, nanofluids; viscosity increases with Φ, when $\Phi \leq 0.25\%$, and decreases when $\Phi \geq 0.25\%$. b) Influence of nanoparticle volume concentration on relative viscosity of ZnO–EG/water, nanofluids; viscosity decrease with increasing Φ for any range of concentration [72]. c) Influence of small concentration of ZnO nanoparticles in EG; viscosity ratio increase with increasing Φ [90]

but for $ZnO-EG$/water, viscosity decreases with increasing concentration for any range of volume fraction and this result shows conflicting behaviour with viscosity to those found in [90] who reported that the viscosity of $ZnO-EG$ increases with increasing nanoparticle loading as shown in Figure 2.6. Suganthi et al. [72] justified the reduction by disturbance of the hydrogen bonding network of ethylene glycol by ZnO nanoparticles and they developed an empirical equation to calculate viscosity as shown in equation (2.14).

$$\mu_{nf} = (1 + 0.164\Phi_p - 518.98\Phi_p T^{-0.9014})\mu_f \tag{2.14}$$

There still exists a controversy regarding to the experimental finding of the viscosity. Das et al. [91] found that the viscosity slightly changes with increasing the shear rate which exhibited a non Newtonian behaviour, when they measured it in water/Al_2O_3. However, Wang et al. [67] measured the viscosity of the same fluid and they observed a non-Newtonian behaviour. Wang et al. state that the viscosity increases by 90% over the base fluid when the volume fraction of the Al_2O_3 is 10%, however Pak and Cho [92] showed that the viscosity increases 200 time for the same concentration of nanoparticles, as well as showing that the nanofluid has a Newtonian behaviour.

2.2.3.3 Specific heat capacity

The specific heat c_p of the nanofluid has received little concern compared to the other properties, but, the specific heat is important to assess the thermal performance of the system working with nanofluid [93]. Some researchers showed that the specific heat is strongly affected by the volume fraction [92, 94, 95, 96, 97, 98] . However, in other studies, the influence of the nanoparticles on the c_p is not considerable [99, 100].

Thermal equilibrium between nanoparticles and the base fluid is assumed in order to calculate the heat capacity of the nanofluid through equation 2.15 which is used in many studies[86, 95].

$$(c_p)_{nf} = (\frac{q}{m\Delta T})_{nf} = \frac{q_f + q_p}{(m_f + m_p)\Delta T} = \frac{(mc_p)_f \Delta T + (mc_p)_p \Delta T}{(m_f + m_p)\Delta T}$$

$$(c_p)_{nf} = \frac{(\rho c_p)_f V_f + (\rho c_p)_p V_p}{\rho_f V_f + \rho_p V_p} = \frac{(1-\Phi)\rho_f (c_p)_f + \Phi_p \rho_p (c_p)_p}{\rho_{nf}} \tag{2.15}$$

This equation is again a straight forward linear combination based on mass.

Others used a simpler equation (equation 2.16) which is based on the mixing theory for ideal gas mixture [93] to evaluate the thermal performance of the nanofluid experimentally [75, 92, 94, 101], however some researchers used it for the theoretical simulations and calculations [102, 103].

$$(c_p)nf = (1-\Phi_p)(c_p)_f + \Phi_p (c_p)_p \tag{2.16}$$

By using the data of [93] for Al_2O_3/water, good agreement was found between the experimental results and equation 2.15, however, the results of equation 2.16 has a big difference with the experimental. The results are shown in Figure 2.7. The main outcome of this part of review is that equation 2.15 is more suitable to predict the actual results than the other model.

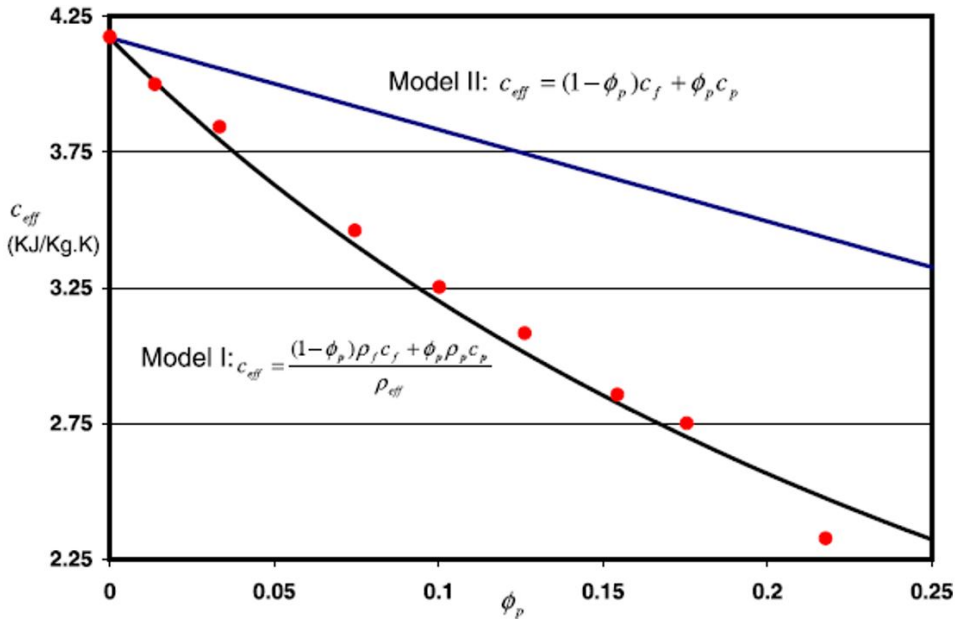


Figure 2.7: Comparison between experimental data of Zhou and Ni [93] (red points) and models (2.15 & 2.16) of thermal capacity.

2.2.3.4 Thermal conductivity

Analytical investigations

There are several theoretical models which are used by most studies to find thermal conductivity. The first theoretical model was Maxwell in (1873) and his model defined effective thermal conductivity of isotropic material with randomly distributed spherical inclusions and it depends on the volume fraction only as in equation 2.17 [2].

$$k_{nf} = \frac{k_p + 2k_f + 2(k_p - k_f)\Phi_p}{k_p + 2k_f - (k_p - k_f)\Phi_p} k_f \tag{2.17}$$

Where k is thermal conductivity. Hamilton-Crosser [104] modified the Maxwell model by adding the shape factor to the model to be more accurate in equation 2.18.

$$k_{nf} = \frac{k_p + (n-1)k_f + (n-1)(k_p - k_f)\Phi_p}{k_p + (n-1)k_f - (k_p - k_f)\Phi_p} k_f \tag{2.18}$$

Where n is the shape factor and when n=3 (for spherical particles) Hamilton-Crosser model is similar to that of Maxwell.

In (2004) Jang and Choi [105] modelled the thermal conductivity of the nanofluid depending on the fluid properties and motion and the concentrations of the nanoparticles shown in equation 2.19. In this model the energy transport is by: 1) conduction of nanoparticles. 2) conduction of base-fluid. 3) collision between the particles and 4) micro convection caused by motion of nanoparticles.

$$k_{nf} = k_f(1 - \Phi_p) + k_p\Phi_p + 3C_1\frac{d_f}{d_p}k_f Re_f^2 Pr_f \Phi_p \tag{2.19}$$

C_1 is a proportionality constant, d_f is the diameter of fluid molecules, d_p is the diameter of the nanoparticle and Pr_f is the Prandtl number of the base fluid.

Experimental investigations

Significant numbers of experimental and theoretical studies are done to investigate the enhancement of the thermal conductivity (TC) and heat transfer (HT) in nanofluids. All these studies confirm that the thermal conductivity increases by using nanofluid rather than the base-fluid alone, but there is disagreement about the mechanism and the range of this improvement, because there are contradictions in the results of the TC despite using the same particles, base-fluid and test conditions. In (2010) Lee et al. [71] found that the heat transfer increased by 29% by adding 0.02 vol.% of Al_2O_3 to NH_3/H_2O, and the heat transfer rate increased by 17% by adding 0.02 vol. % of CNT to the same base-fluid. On the other hand, Shima and Philip [106] experimentally studied the role of TC in EG based on Ag and Fe_3O_4 nanoparticles and they found that low particle loading (1.16 vol.%) does not affect the TC Also, they suggested that the low volume fraction of nanoparticles at a given TC give the same heat transfer coefficient. Wang et al.[67] studied the TC of nanofluid mixture using Al_2O_3 and CuO in (EG) and they found that the TC of the nanofluid increases with decreasing particle size and they stated that the enhancement of the TC depends on the dispersion technique and the microscopic motions of the particles. Also, they added that the increase in the TC is according to Maxwell's law 2.17 and this claim is conflicted by Suganthi et al. [72] who confirm that the thermal conductivity increases linearly with concentration according to the equation 2.20.

$$k_{nf} = k_f(1 + 7.926\Phi_p) \tag{2.20}$$

Suganthi et al.[72] compared their correlation with the Hamilton Crosser (2.18) model of thermal conductivity of dispersion of spherical particle, they found that their gradient is greater than Hamilton Crosser model by 2.64. Jang and Choi [105] observed that the largest increase in thermal conductivity is approximately 1.3% for 4nm diameter Au particles in Ethanol and they confirmed that they cannot observe significant enhancement with small volume fraction (less than 0.1%). They found that the maximum increase possible in nanofluid with volume fraction less than 1% for spherical particles is $3\Phi k_f$. Xuan and Li [69] studied the heat transfer in Cu/water nanofluid and they found that the nanofluid shows TC enhancement from 0.24 to 0.78 by increasing the volume fraction of Cu from 2.5% to 7.5%.

Table 2.3 summarises the enhancement in the thermal conductivity for different types of nanofluid depending on the different studies. Because the thermal conductivity is the most effective factor on the heat transfer and it is affected by many parameters like volume fraction, type of the nanoparticle, type of the base-fluid, particles size and shape and temperature, the effects of these parameters reviewed in details in the following section.

Table 2.3: Summary of maximum enhancement in thermal conductivity for different nanofluid as found in the literatures.

Base-fluid	Particles	Vol. fraction	Size of particles (nm)	Enhancement	Ref.
Hexadecane	Ag	0-0.5%	≈ 4	8%	[106]
	Fe_3O4	0-8%	≈ 7	23%	
EG	Al_2O_3	0-8%	28	$\approx 40\%$	[67]
Water	Al_2O_3	0-5.5%	28	$\approx 18\%$	
EO	Al_2O_3	0-7.5%	28	$\approx 30\%$	
EG	CuO	0-15%	23	55%	
$water$	CuO	0-10%	23	35%	
Ethanol	Au	085%	4	$1.3\% \pm 0.8\%$	[107]

Continued on next page

Table 2.3 – *Continued from previous page*

Base-fluid	Particles	Vol. fraction	Size of particles (nm)	Enhancement	Ref.
Oil	Cu	7.5%	≈100	43%	[69]
water	Cu	2.5-7.5%	≈100	78%	
EG	ZnO	4%	25-40	33%	[72]
EG-water	ZnO	2%	25-40	17.26%	
EG	ZnO	5%	10-20	26.5%	[108]
EG	ZnO	6%	≈4.6	33%	[90]
water	AL_2O_3	4%	38.4	8%	[105]
	CuO	3.5%	24.4	10%	
EG	CuO	4%	24.4	20%	
	Cu	0.5%	6	14%	
EG	Cu	0.55%	> 10	13%	[41]
	$Cu + acid$	0.25%	> 10	42%	
Water	AL_2O_3	4.5%	≈24.4	8%	[68]
	CuO	3.5%	≈18.6	12%	
EG	Al_2O_3	5%	≈24.4	17%	
	CuO	4%	≈18.6	22%	
Water	TiO_2 (rod)	5%	10*40(dia.*len.)	33%	[70]
	TiO_2 (Sphere)	5%	15	30%	
Water	Al_2O_3	4%	33	15%	[82]
Water	Al_2O_3	4%	38.4	24%	[94]
	CuO	4%	28.6	36%	
EG-Water	AL_2O_3	5%	60.4	29%	[109]
Po/glycerole	Al_2O_3	5%	60.4	27%	
Water	TiO_2	3%	21	7.4%	[110]
CTAB	$DWCNT$	1%	≈70*7000	7.6%	[111]
	$MWCNT$	0.6%	130*20000	34%	

2.2.3.5 Parameters influencing thermal conductivity

Volume fraction

Experimental studies show that thermal conductivity of nanofluids is affected by many factors such as nanoparticle concentration, particle type, size and shape, base fluid type and temperature. These factors can change the transport and thermal behavior of the nanofluid. Amount and types of additives and the acidity of the nanofluid were also shown to be effective in the thermal conductivity enhancement.

According the literature, particles volume fraction of the most parameters effects on the thermal conductivity. All these studies agreed that increase in volume fraction enhances the heat transfer but they differ with the amount and the cause of the increase. Some confirm that the increase in TC is linear with volume fraction [67, 68, 72]. Wang et. al [67] found that the enhancement of TC for Al_2O_3 and CuO dispersed in water, engine Oil (EO) and EG, experimentally is linear and higher than that predicted via Maxwell law as explained in Figure 2.8a. Suganthi et. al [72] who experimentally tested the heat transfer in $ZnO - EG$ and $ZnO - EG$-water found that $ZnO - EG$ with 4 vol.% nanoparticles and $ZnO - EG$-water with 2% nanoparticles increases linearly the thermal conductivity by approximately 33.4% and 17.26% respectively.

Others found the the relationship between the TC and the particles concentration is nonlinear [59, 108]. Yu et al. [108] studied the TC and viscosity for EG based nanofluid containing ZnO (10-20) nm diameter. They found that the enhanced value of 5 Vol.% $ZnO - EG$ nanofluid is 26.5% and this increase is nonlinear with the volume fraction but by calculating the TC by a theoretical model it appears as a linear relationship as shown in Figure 2.8b.

TC of the nanofluids is expected to be higher than the TC of the base fluid, because the thermal conductivities of most solid materials are higher

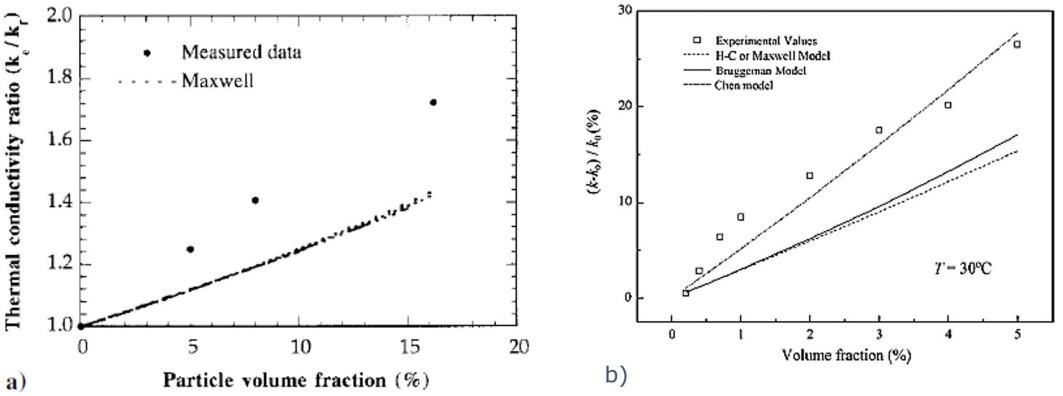


Figure 2.8: (a). Measured thermal conductivities of Al_2O_3–EG at different volume fraction (experimentally and theoretically) [67]. (b) Measured the TC of $ZnO-EG$ for different nanoparticles concentrations [108].

than those of liquids. Increasing in volume fraction has limitation to get very high percentage enhancement because of two reasons: firstly, density mismatch between base-fluid and the particles is very large for example density of water is 990 kg/m^3 but for Al_2O_3 the density is 3970 kg/m^3. Secondly, Cost considerations.

Type of material

The type of particle material also shows a significant influence in TC and heat transfer as shown in many studies [39, 94, 105, 111]. The effect of the temperature on the TC was studied by Putra et al. [94], they found that the TC increased by 36% and 24% by adding 4 vol% of CuO and Al_2O_3 respectively to water at 51^oC. Jang and Choi [105] studied the role of Brownian motion to enhance TC using different types of nanoparticles. By adding 4% of Al_2O_3 to water the enhancement in TC is 8% and by adding 4% of CuO to water a 12% increase was observed. In the same study the enhancement around 14% and 2% was found by adding Cu and CuO respectively to EG. This supports the statement of Han [39] who says that the metallic nanoparticles have higher thermal conductivity than oxides of those metals for the same volume fraction. From these studies it is clear that the enhancement in the TC by nanofluid

containing CuO is much better than the same fluid containing Al_2O_3, although the thermal conductivity of Al_2O_3 is greater than CuO. These phenomena confirm that the enhancement in the thermal conductivity is not dependent on the TC for the material only but on the other properties like temperature, density and size and shape of the particles.

Assael's group [111] studied the thermal conductivity for both carbon multi-walled nanotube ($C-MWNTs$) (130nm diameter $\times 20\mu$m length) and carbon double-walled nanotubes ($C-DWNTs$) (70nm diameter $\times 7\mu$m length) dispersed in hexadecyl trimethyl ammonium bromide ($CTAB$). They found the TC increased by 34% by adding just 0.6 Vol.% of ($C-MWNTs$) to ($CTAB$) and by only 7.5% by adding 1% of ($C-DWNTs$). From their results it is clear that the enhancement in TC increases with increasing aspect ratio (length to diameter ratio) in the nano-scale range.

Type of basefluid

According to Maxwell's Model 2.17, as thermal conductivity of the base-fluid increases, the enhancement of TC of the nanofluid decreases and most of the experimental results agree with this model. For example, Jang and Choi [105] found that water containing 4 Vol.% CuO has an enhancement in TC about 12% and this amount of improvement is lower than the enhancement in TC which is caused by $CuO-EG$ which was 20% for the same concentration, although the thermal conductivity of water (0.609 $W/m.K$)is greater than EG (0.258 $W/m.K$). Wang et al. [67] studied thermal conductivity for different base-fluids (water, EG, Pump oil (PO) and engine oil (EO)) containing CuO and Al_2O_3 nanoparticles. Their results show that the enhancement in TC for EG containing nanoparticles is higher than other fluids with same type and volume fraction of nanoparticles although, the TC of EG is lower than the other basfluids. Engine oil shows slightly lower enhancement than the EG and

water and pump oil have lower enhancement ($k_{EG} > k_{water} > k_{EO} > k_{PO}$). This phenomenon is contradicted by some researchers [69, 112]. Xuan and Li [69] studied the heat transfer of water (k=0.609 $W/m.K$) and transformer oil (k=0.136 $W/m.K$) containing Cu nanoparticles. They found that the enhancement in TC for Cu-water suspension was 75% for 7.5Vol%, while the enhancement in TC of Cu-transformer oil was 43% for the same volume fraction and under same condition.

Size of nanoparticles

The size of the particles has an effect on the thermal conductivity and there are conflicting results related to this parameter. Some researchers [105, 112, 113, 114] found that the TC of the nanofluid increase as the size of the nanoparticles decreases. Jang and Choi [105] explained this behavior by the increase of the Brownian driven velocity of the particles; for smaller particles, velocity increases and the heat transfer consequently improves as well as with the smaller particles there is larger surface area to volume ratio. Kim et al. [113] studied the effect of particle size on TC in ZnO-water and $ZnO - EG$ by using three different sizes of ZnO (10, 30 and 60)nm in diameter and they found that TC of water mixed with 1 vol.% of 10 nm and 60 nm ZnO are 6.37($W/m.K$) and 6.18($W/m.K$) respectively as explained in Figure 2.9a. Duan [114] experimentally studied the properties of the Al_2O_3-water and their results are partially compatible with [105]. They found that TC increases with decreasing particle diameter between 10-35 nm and this phenomenon reverses for diameter greater than 35 nm. On the other hand, there are disagreeing opinions from some researchers [115, 116] with these results. For example, Beck et al. [115] measured TC of nanofluids with seven different sizes of Al nanoparticles (8-282) nm and they found generally that heat transfer is reduced with decreasing particle size. They observed also that the amount of enhancement for particle size less than

50 nm in diameter is lower than those that have size greater than 50 nm and they explained this by the thermal conductivity for smaller nanoparticles is smaller itself than the larger nanoparticles. Their results are illustrated by the Figure 2.9b. This principle was confirmed by Xie et al. [116], when they used different sizes of Al_2O_3 in EG and they found better enhancement in TC using large particles.

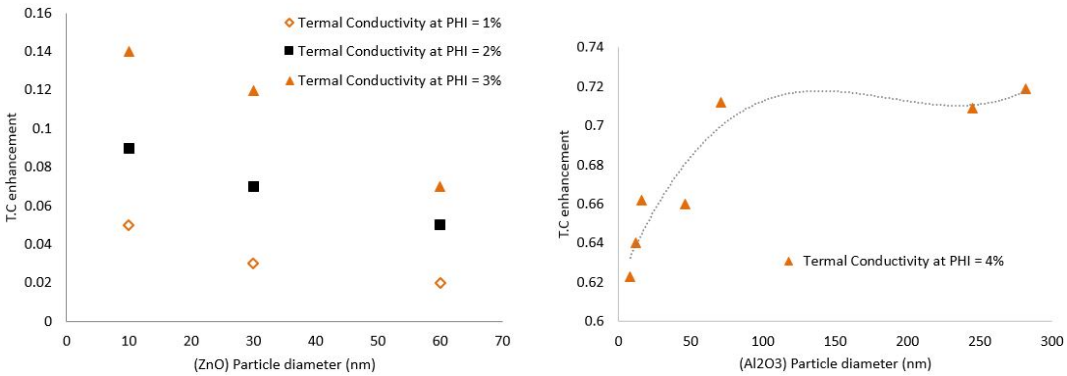


Figure 2.9: a) The effect of (ZnO) nanoparticle size on the TC of water (adapted from [113]). b) Effect of (Al_2O_3) nanoparticle size on the TC (adapted from [115])

.

Shape of particles

There is a wide variation in enhancement of the heat transfer which is effected by the shapes of the nanoparticles [70, 104, 111, 117, 118, 119]. Hamilton and Crosser [104] were the first researchers who modified the Maxwell equation (2.17) by including the shape factor and they found that the enhancement for the fluid containing cylindrical particles is higher than those with spherical. In 2005 Murshed et al. [70] investigated the enhancement in TC of water containing TiO_2 nanoparticles, with spherical (15 nm in diameter) and rod shape (10 $\times$ 40) nm (diameter $\times$ length) and they found that for 5 vol.% TC an enhancement approximately 33% for the fluid containing the rod shape and 30% for the fluid containing the spherical shape. Timofeeva et al. [118] studied the thermal properties of Alumina-EG/H_2O nanofluid under the effect of shape factor. They found that the enhancement in thermal conductivity

and viscosity for nanofluid with cylindrical nanoparticles was greater than the other shapes shown in Figure 2.10, but according to the Hamilton and Crosser equation different results for TC can be obtained.

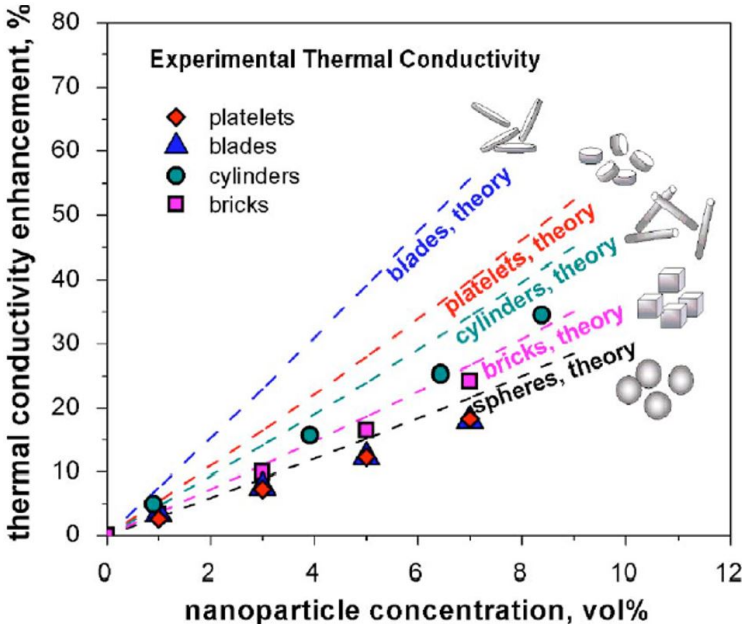


Figure 2.10: The shape factor of (Al) effects on the thermal conductivity [118]

.

Xie et al. [117] studied the thermal properties of SiC/water as well as SiC/EG nanofluids using spherical shape (26 nm diameter) and cylindrical shape (600 nm diameter). For both types of base-fluids they found that the nanofluid with cylindrical nanoparticles enhances the TC greater than the other fluid with spherical particles. For example, it was found that the 4.2 Vol.% spherical particles water enhances the TC by 15.8%, whereas 4 vol.% of the water with the cylindrical particles in water enhances TC by 22.9%. In (2005) Assael et al. [111] investigated TC in multi wall nanotube ($MWNT$) and double wall nanotube ($DWNT$) and they confirm that heat transfer and TC increase by increasing the aspect ratio (length to diameter) of the particles. According to Ozerinc et al. [119] CNT has general enhancement in thermal conductivity of nanofluid greater than spherical shape and the reason for this phenomenon is the heat transfer through a relatively long distance in the

nanotube itself which has length in millimeters.

Temperature

Temperature has an influence on the TC and viscosity of the nanofluid, depending on both of the particles and fluid temperatures. Jang and Choi [105] modeled TC according to equation 2.19 which, depends on several parameters including temperature. They found that the amount of enhancement in the TC increases with increasing temperature. Murshed et al. [120] investigated the TC of water, EG and engine oil (EO) mixed with Al_2O_3 and Al nanoparticles. They also found that the enhancement increased with increasing temperature as shown in Figure 2.11. The amount of improvement in TC for Al/EO increased from 22% to 38% by increasing the temperature from 20 to 60^oC and their result shows a good agreement when compared with Putra et al. [94] who studied a temperature dependence of the TC enhancement of nanofluid. An experimental study of natural convection heat transfer of Al-water has been done by Ho et al.[82], they found TC enhancement increases with increasing temperature and their results show good agreement with [94]. In (2009) Turgut et al. [110] measured TC of TiO_2 (21 nm diameter)/water which is synthesized by the two step method. The measurement was made with varying temperature (13, 23, 40 & 55 ^oC) and they found that there is no dependence of TC related to temperature but the temperature effect on the viscosity, which decreases as temperature increased. There are conflicting results reported by Masuda and others in (1993) who studied the thermal properties of Al_2O_3 nanofluids. They confirmed that the enhancement of the TC for 4.25 vol.% particles loading in water decreases with increasing temperature, for example the enhancement decrease from 34% to around 27% by decreasing the temperature from 32 to 67 ^oC [121].

After reviewing the effects of each parameter on the nanofluid properties,

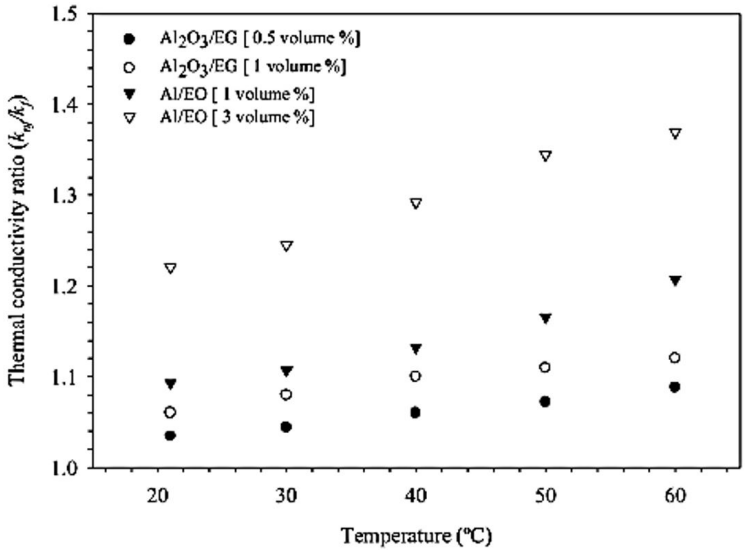


Figure 2.11: Thermal conductivity enhancement with Temp. for Al_2O_3 (80 nm)/EG and Al (80 nm)/EO base nanofluid [120]

.

the relation between these parameters and nanofluid properties are summarized in Figure 2.12 which explains how each parameter affects a single property.

By presenting the fundamentals, synthesis and properties of the nanofluid, a better understanding about the behavior and the effects of the nanofluid on the heat transfer application is obtained. One aim of this research is investigating whether the nanofluid is suitable for the binary VARS. This can be checked using the fluid directly to the VARS experimentally, and via numerical method of the processes involved in this work with validation, as will opened up in following section.

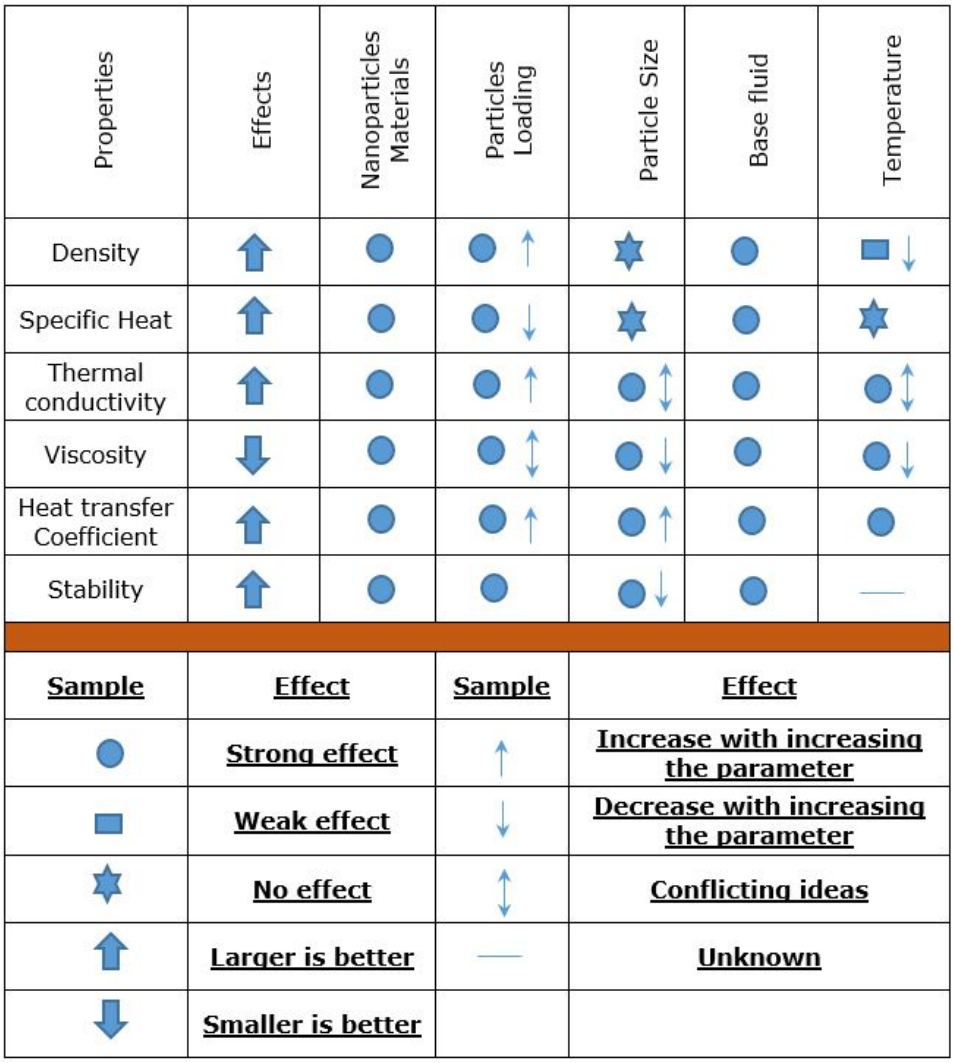


Figure 2.12: Effect of parameters on the properties of nanofluid.

.

2.3 Modelling Review

There are two kinds of models: empirical and mathematical. The empirical model presents the data-set from a physical system or process which represents the model while the mathematical describes the database from a system based on physical laws. A model can be used to improve the process based on analysing simulation data [122].

Both types of modelling are done by various researchers in application to VARS. Gordon and Ng [123] studied the thermodynamic model for the absorption chiller using both theoretical and experimental methods and the principles

which controlled the performance of the absorption chiller are fitted to the experimental data using the regression method. Joudi and Lafta [34] studied a computer simulation model to find the performance of absorption refrigeration using $LiBr - H_2O$ as a working fluid. The model was based on the energy and mass balance on each part (generator, absorber, condenser and refrigerator) individually. A theoretical steady state model of NH_3/H_2O absorption system was presented by Selverio and Figueiredo [124] and their theoretical model confirmed that the efficiency of the absorber improves by increasing the absorber heat transfer area, for example, the increase of approximately 40% in the absorber heat transfer area enhances the COP by approximately 15%. Kaynakli and Kilic [125] theoretically studied the performance of an absorption refrigeration system working with $H_2O/LiBr$, using a thermal equilibrium method in each part; they found that the Solution Heat Exchanger (SHX) has more effect on the performance than Refrigerant Heat Exchanger (RHX) and they found that the COP increased by 44% using SHX while only 2.8% enhancement was found due using RHX. They found that the COP value increases with decreasing the generator thermal load and the generator and the absorber thermal load decrease by increasing the temperature of the generator and the evaporator. Micallef and Micallef [16] presented a simple linear model for an absorption refrigeration unit using both of $H_2O/LiBr$ and NH_3/H_2O; they obtained results for both fluids without using the SHX and they set the evaporator temperature constant and other temperatures were variable.

In 1987, Grossman et al. [20] developed a computer code in fixable and modular form for simulating absorption system with different configuration cycles and using various working fluids. The code is based on system units which contain the governing equation for each component in the system and the equations are solved simultaneously. There are two lines of calculations:

1) temperature, pressure, volume fraction, vapour fraction, and mass flow rate at each point of the system, 2) the heat transfer at each unit which is restricted the COP. They found that the program successfully simulated the single and the double cycle and dual-loop heat pump with the following working fluids: $(H_2O/LiBr)$, (NH_3/H_2O), $(NH_3/LiBr - H_2O)$, $(CH_3OH/LiBr - ZnBr_2)$. Sozen and Akcayol [126] used ANN method to study and model the performance analysis of a solar-driven ejector-absorption refrigeration system ($EARS$) with ammonia/water as a working fluid. Artificial neural network (ANN) method is applied with 6-6-9-1 (6 input layers - 6 Hidden layers - 9 Hidden layers and 1 output layer) configuration used to solve the model of the double effect series flow absorption chiller by [127]. The model predicted the chiller performance depending on the temperature of the inlet and outlet chilled water. They show that the result predicted with ANN, can be used to predict the performance of the absorption chiller exactly. The ANN predicted COP is $\pm 1.2\%$ error.

Generally, there are several types of model which are normally applied at design stage of the absorption refrigeration, and these models are:

- Thermodynamic model (TD).
- Adapted Gordon-Ng model (GNA).
- Adapted characteristic equation method $\Delta\Delta$t'.
- Artificial Neural network (ANN).

2.4 Numerical Modelling

There are no previous CFD models for vapour absorption refrigeration working with nanofluids to our knowledge. CFD models have been done for the boiling process as presenting the physical process in the generator in VARS and the single and multiphase flow for the nano-binary-fluid. Therefore, it is important

to review the literature related to these processes.

2.4.1 Boiling

Boiling is the phase change process happening when the solid surface temperature is higher than the saturated temperature of the liquid. Boiling may take place under quiescent liquid environments, which is described as pool boiling, or under forced flow circumstances, which is described as forced convective boiling or flow boiling which happen in the boiler of VARS. In the pool boiling the process begins with natural convection boiling at the low temperature difference ΔT between the surface and the bulk; this state gives a low heat flux. Increasing the ΔT, the nucleate boiling regime appears and the heat flux increases till it reaches to maximum or critical heat flux (CHF). Then, increasing the ΔT generates a transition boiling or unstable film boiling regime and it drops the heat flux because the contact area with the surface decreases, then the boiling film generate and the heat flux increases even through there is no contact area of the fluid with the surface; this is because the radiation heat transfer across the film plays a significantly greater role as the excess temperature increases (the pool boiling explained in Figure 2.13). In nucleate flow boiling, the heat transfers due to a combination of two effects: (1) the bubble formations and motions close the surface and (2) the direct sweeping of the heater surface by the solution itself. The heat transfer mechanism is a combination of the nucleate pool boiling and a forced convection phenomenon [128]. The local heat transfer coefficient of the liquid under flow boiling depends on the vapour concentration, phase velocities, heat flux, flow bath geometry and direction, multiphase flow pattern, and fluid properties.

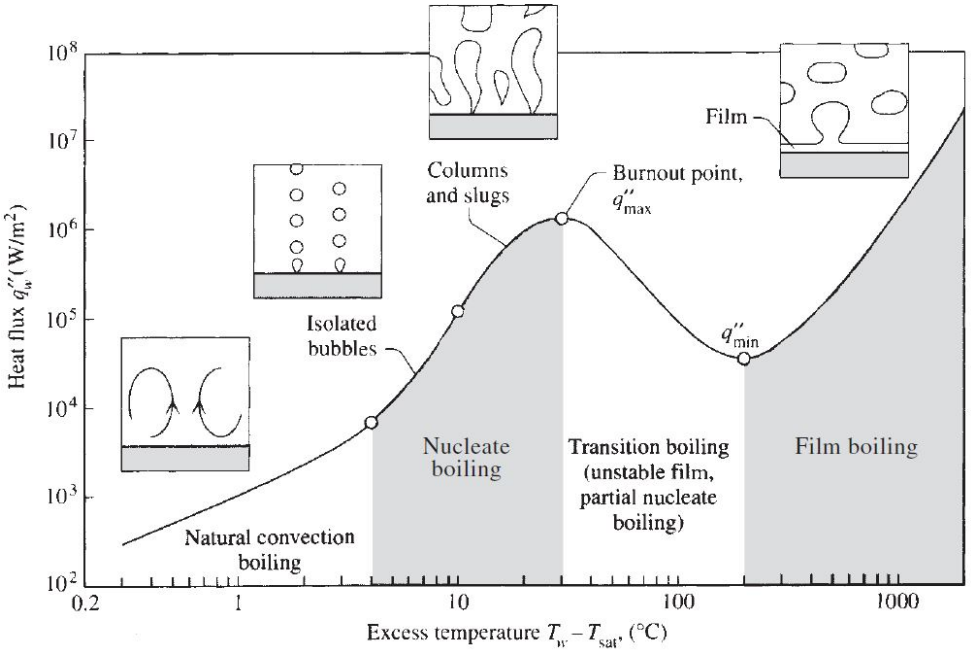


Figure 2.13: Regimes of pool boiling in water at atmospheric pressure [128]

.

Boiling of nanofluid in experimental studies

Flow boiling heat transfer occurs in vapour absorption refrigeration systems as well as in various industrial areas, such as refrigeration systems in many applications, power generation, chemical engineering, high-power electronics component cooling, and nuclear reactor cooling [129]. To improve the heat transfer of the fluid, the behaviour and the properties of the fluid itself must be enhanced. Nanofluids are an alternative to normal working fluids for thermal and industrial applications, due to their modified thermo-physical properties which can enhance the efficiency of processes such as boiling [130]. Improvements in flow boiling heat transfer systems can improve energy efficiency and offer a route to reduce global energy consumption. In the United States, air conditioners consume 6% from the electricity produced, which costs annually $29 billion and consequently around 117 million metric tons of CO_2 is released in to the environment [131].

The number of studies of nanofluid boiling has increased significantly over the last decade with emphasis mainly on pool boiling rather than flow boiling,

even though flow boiling has more applications (such as steam generation in helically coil and the steam generation inside the nuclear reactor core) rather than pool boiling [132]. There are several recent experimental studies on flow boiling effects of nanofluids with significant consequences for enhancing boiling heat transfer. Kim et. al [133] studied the enhancement of the flow boiling CHF, the maximum heat flux for nucleate boiling, for alumina nanoparticle based nanofluid in water at low pressure. They found that the CHF can improve up to 30% with 0.01Vol.% of alumina nanoparticles. Henderson et al. [134] studied the flow-boiling heat transfer of R-134a-based nanofluids in a horizontal tube, and found that the nanofluid has an insignificant influence on the flow pressure drop compared to the base fluid and that the heat transfer coefficient increases to double over the base-fluid. Kim et al. [135] studied subcooled flow boiling (boiling adjacent to a surface hotter than the saturated temperature T_s, whilst the bulk temperature of the local fluid is below T_s) using different types of nanofluid. They found that the heat transfer coefficient and mass flux of the nanofluid increases during boiling and that the flow boiling CHF (maximum heat flux is at the point of changing between the transition and film boiling) was enhanced using nanoparticles. Boiling heat transfer and pressure drop through a rectangular channel of nanofluid is experimentally studied by Boudouh et al.[136]. Here, the local heat flux, vapour volume fraction and heat transfer coefficient increase with increasing nanoparticle concentration and varying axial location. CHF improvement during forced convection of flow boiling of a nanofluid on a short heated surface is experimentally studied by Ahn et al. [137]. They found that the nanofluid flow boiling heat transfer is enhanced under forced convection and they suggest that this enhancement is mostly caused by nanoparticles depositing on the heater surface during boiling.

Not all studies confirm the enhancement of boiling heat transfer as the nanoparticles concentration increases. For example, Abedini et al. [138] investigated experimentally a comparison of nanofluid flow boiling in vertical and horizontal tubes. They found that the subcooled flow boiling decreases with increasing the concentration of TiO_2 nanoparticles. They found that the bulk temperature decreases at the end of the channel in the nanofluid compared to water, implying that the vapour volume fraction increases in the nanofluid. Witharana [139] in 2003 confirmed experimentally that the boiling heat transfer coefficient behaviour of the nanofluid depends on the type of the nanoparticles, where Au-water nanofluid showed a clear enhancement in the heat transfer coefficient but SiO_2-water and SiO_2-ethylene glycol (EG) showed weakening of the heat transfer coefficient. These results imply that careful consideration of nanoparticle to base fluid is necessary to enhance heat transfer.

Pool boiling characteristics are addressed by many researchers, with the heat transfer behaviour varying significantly between studies. Several researchers found the heat transfer coefficient is insensitive to nanoparticle concentration [140, 141] or even negatively correlated [91, 142]. However, others have found an increase in the heat transfer coefficient with increasing concentration of the nanoparticles [143] and some studies confirm a significant increase in the CHF even with low concentrations of nanoparticles [63, 140, 141, 144].

Kim et al. [144] found that the water based nanofluid significantly improves the CHF compared with a pure fluid and enhancement of the CHF of the water due to nanoparticle coating of the heater (prepared by deposition of suspended nanoparticles during pool boiling of nanofluids, immersed in pure water) increases as the concentration of the nanoparticles increases. They

conclude that the reason for this improvement of CHF is the change of surface microstructure and topography of the heater because of the nanoparticle surface coating during pool boiling of nanofluids.

Boiling of nanofluid in numerical studies

There are several numerical studies dealing with boiling heat transfer effects in nanofluids using CFD. Hasheminia et al. [145] numerically studied the effect of different parameters of forced boiling of nanofluids. They found that the CHF in Al_2O_3 /water and SiO_2/water nanofluids decreases with increasing nanoparticle volume fraction. They justified this behaviour by stating that the contact angle increases with increase in concentration because each single particle may contact with other particles at more locations. They found that the vapour volume fraction increases with increasing heat flux as a direct result of the nanoparticle addition to the base fluid. Abedini et al. [146] numerically investigated the subcooled flow boiling of nanofluids, finding that the heat transfer coefficient increases with increasing nanoparticle concentration. They also found that in subcooled flow boiling, decreasing the inlet mass flow rate can cause the heat transfer coefficient to rise or fall depending on the effect of forced convection and latent heat transport on the overall heat transfer coefficient. Experimental and numerical investigation of the dynamics of bubbles in the nanofluid pool boiling was studied by Shoghl et al. [147]. They found that both CHF and boiling heat transfer coefficient were enhanced by hydrophilic surfaces and worsened by hydrophobic surfaces and they found that by addition of surfactant (SDS), the number of the bubbles with smaller size increases because of the reduction of surface tension.

According to [132], Al_2O_3 and CuO are the most commonly investigated nanoparticles materials used in flow boiling which present 42,2% and 20% of the overall types used in boiling heat transfer respectively as shown in Figure

2.14. Figure 2.15 shows that water is the main liquid used in flow boiling (77.8%) followed by different refrigerants (17.8%).

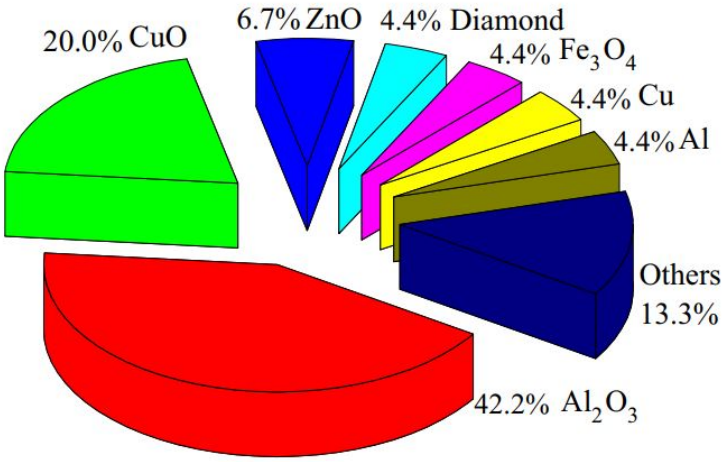


Figure 2.14: Nanoparticle materials used in the experimental investigations of nanofluid flow boiling. [132]

.

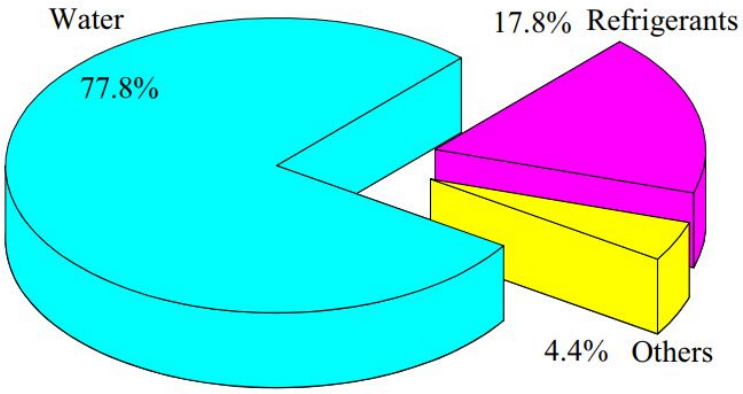


Figure 2.15: Working fluid used in the experimental investigations of nanofluid flow boiling. [132]

.

From reviewing the boiling process, there are no works done related to flow boiling of **binary-fluid and nano-binary-fluid** experimentally or numerically. Thus, there is a necessity to perform reliable experimental work using a nano-binary-fluid (acetone-$ZnBr_2$-nanoparticles) as a novel working fluid in the VARS and create a new CFD method for flow boiling simulating boiling of one component (acetone) from this mixture.

Heat transfer including boiling process of the multiphase fluid, could be

modeled numerically via a single phase (consider the primary fluid is single fluid by finding the fluid properties) or multiphase (use the properties of each phase separately in the equations) flow. The following section investigates how these two methods used by the other researchers.

2.4.2 Single and two phase models for nanoparticles simulations

The single and the two phase model can be presented in the boiler for the VARS working with a binary nanofluid. Heat transfer in nanofluids can be modelled using classical correlations (based on Maxwell) for single-phase fluids with adjustment for properties with the nano-particles, such as those models reported by some researchers [118, 148, 149]. Others have stated that the heat transfer behaviour obeys a two phase model with variation due to concentration of nano-particles varying in the flow. There is a debate in the literature about which analysis provides a better prediction [81, 88].

Pantzali et al. [150] investigated a nanofluid of 4 Vol.% CuO in H_2O numerically and experimentally using a laminar flow on a plate heat exchanger. By using the single phase model, they found that the flow rate of the nanofluid required for a particular heat transfer rate was lower than the base fluid.

Utomo et al. [151] investigated using CFD the heat transfer coefficient arising from alumina, titania and CNT nanofluids. They found that the addition of nanoparticles to liquids enhances the heat transfer coefficients by no more than 10% at a constant turbulent velocity. They state nanofluids behaved as homogeneous mixtures with experimental Nusselt numbers following classical relations developed for the single-phase approach, modified for the mean nanoparticle concentration, being accurate to within $\pm 10\%$. This uncertainty is explained by movement of nanoparticles due to Brownian motion and viscosity gradient due to concentration, with non-uniform shear rate having

insignificant effect on heat transfer. Similar uncertainty was found previously for metal oxide nanofluids [152] and for CNT nano-fluids [153].

A two dimensional single phase CFD model was numerically studied by Demir et al [154] using Al_2O_3 and TiO_2 in water nanofluid in a horizontal pipe heat exchanger. They found that the heat transfer increased with the concentration of nanoparticles. Goktepe et al. [155] studied the single and the two phase models for nanofluid inside a uniformly heated tube. They found that the convective heat transfer coefficient is more correctly predicted with a two phase model than the single phase.

Amoura et al. [156] studied the heat transfer for three different types of nanofluid (H_2O/CuO, H_2O/Al_2O_3 and H_2O/TiO_2) in horizontal tubes in 2D with different Reynolds number up to 600 and different volume fraction of nanoparticles (0, 0.01, 0.02, 0.03 and 0.1) using a single phase technique. They found that the Nusselt number of nanofluids is larger than that of the base fluid and that the pressure loss coefficient reduces by increasing Reynolds number for all types of nanofluids. Moraveji et al. [157] modelled fully developed flow in a circular tube with laminar flow, assuming constant heat flux on the tube wall, and using a single phase approach. With nanofluid (upto 6 wt.% Al_2O_3 + water), they recorded higher heat transfer than base fluid. Akbari et al. [158] showed, theoretically, the heat transfer improvement with increasing Reynolds number (Re) and concentration of nano-particles in the nanofluid solution (H_2O/Al_2O_3). The two phase model was applied in three different CFD based multi-phase approaches, i.e. volume of fluid (VOF), mixture and Eulerian. The predictions by the multi-phase models are essentially the same. Therefore, the less expensive model (VOF) is to be preferred for this problem.

For general multi-phase modeling there are two approaches for simulating. Lagrangian-Eulerian is suitable for the low concentration of particles and as-

sumes the Eulerian method for the base-fluid and Laqrangian for the solid particles. Conversely, Eulerian-Eulerian approach is suitable for high volume fractions because the calculation of many trajectories for the large dispersion of particles makes the Lagrangian method impractical and non-representative without a large number of particle injections [88, 158].

Apparently contradicting results in the literature can be related to the method of comparison used. For example some experiments are based on either constant Reynolds number (Re) or constant velocity. Pak and Cho [92] states that the heat transfer is enhanced for turbulent flow of Al_2O_3-water compared with the basefluid when Re is maintained constant between tests. However, by considering the same value of the velocity for the same case, the heat transfer of the nanofluid reduces. This is because, by adding the nanoparticles to the basefluid the viscosity of the fluid increases, which means the fluid needs more velocity to reach the value of the constant Re, with related heat transfer enhancement by increased turbulence. Yu et al. [159] studied analytically the effects of constant Re, constant velocity and constant power pumping on the heat transfer coefficient improvement, by assuming that the nanofluid obeys a 'classical', single phase, relation of the thermophysical properties. They conclude that the constant pumping power comparison is the most unambiguous; the constant flow velocity comparison can give quite good results under certain conditions but the constant Reynolds number comparison distorts the physical situation, because of changing properties (density and viscosity) of the fluid, and therefore, should not be used.

2.5 Summary

This review describes a brief history of refrigeration systems by reviewing a principle and background of different type of vapour absorption refrigeration. It concludes that the performance of each cycle depends on the design of system and the working fluid and each cycle cannot be operated at temperature lower than its limit. The working fluid including nanofluid which improves the heat transfer of the system was studied by different researchers and their outcomes can be summarized as properties of the nanofluid and type of base-fluid considerably affect heat transfer, and these properties are affected by several parameters: material; geometry of nanoparticle; volume fraction; temperature. The viscosity of the nanofluid can either increase or decrease depending on the base fluid. Different types of modelling are done for absorption systems: thermodynamic model; adapted characteristic equation method; artificial neural network (ANN). Although CFD models of nanofluid boiling exist, no numerical modelling or experimental results of the flow boiling for nano-salt-fluid is found in the literature. This project aims to model the boiler of the absorption refrigeration system numerically. As a start to the work, numerical modelling of some previously published work to investigate the capability to model the flow of the nanofluids with both single and two phase nanoparticle modelling approach. It concludes that the two phase model has better predicted heat transfer coefficient and Nu for experimental data than the single phase. as confirmed in literature for other fluid. This project finds a suitable way to assess vapour absorption systems working at low temperatures with acetone-zinc bromide solution, with nanoparticles to enhance the process. The work focuses on the modelling of the boiling process and produces novel CFD models validated against a test campaign at laboratory scale.

3

PREPARATION AND PROPERTIES OF NANOFLUID

3.1 Introduction

This Chapter explored a novel VAR solution consisting of dissolved salt in refrigerant mixed with nanoparticles and we refer to it as a nano-binary fluid (NBF) or nano-salt-fluid (NSF). The importance of this chapter are to use the properties measured into the experimental work and the numerical modeling also this part of work is giving a better understanding of the behavior of nano-salt-fluid and how the properties affected by chanching the concentrations of the salt and the nanoparticles. The study covers the properties of the acetone/$ZnBr_2$ as a binary (base) fluid and nanofluid by adding zinc oxide (ZnO) and graphene (G), separately. The properties of acetone/$ZnBr_2$ are studied by Ajib and Karno [14]. To have criteria for the improvement of the properties of nanofluid, some of the properties that were measured and published by Ajib and Karno [14] are repeated. We have prepared the solution with different concentrations of $ZnBr_2$ and nanoparticles. In the following we are going to illustrate the preparation method including the stability behavior and the thermo-physical properties of this working solution (acetone/$ZnBr_2$) as a basefluid and nanofluid.

3.2 Sources of the materials

The materials were purchased from different companies depending on the quality and the price. Sigma-Aldrich company Ltd. provided the acetone (Product code: 270725-1L), $ZnBr_2$ extra pure (product code: 02128-1kg) and ZnO nanoparticles ($\leqslant 50nm$) (product code: 677450-5g). However, the Graphene nanoplatelets (6-8 nm thick $\times$ 5 microns wide) (catalog Number: $06-0210/25g$) were purchased from Strem chemical, Ltd. company.

3.3 Preparation

Two methods have been developed in creating nanofluids. The first is a single (one)-step method and the second is a two-step method. The one-step process can prepare uniformly dispersed nanoparticles, and the particles can be stably suspended in the base fluid. The two-step method consists of adding dry nanoparticles to the base fluid as described in Figure 2.4. A dry nanoparticles powder is prepared by inert gas condensation, chemical vapour deposition, mechanical alloying or other suitable techniques, and the nano-sized particles are then dispersed into a fluid in a second stage to synthesize a nanofluid. Agglomeration of nanoparticles in the two step is higher than the one step, especially in the process of drying, storage, and transportation of nanoparticles. Agglomeration in a nanofluid will decrease the thermal conductivity. To minimize the nanoparticle aggregations and improve the dispersion behaviour, techniques such as ultrasonic agitation or the addition of surfactants to the fluids are often used [73].

To prepare the binary nanofluid (acetone/$ZnBr_2-(ZnO)$ or (G)), a base-fluid (acetone/$ZnBr_2$) is prepared with various mass concentrations (40 wt.% - 65 wt. % with increasing step 5%) of $ZnBr_2$. During mixing the refrigerant (acetone) and the absorbent ($ZnBr_2$), heat is released from the mixture,

depending (proportional) on the amount of the $ZnBr_2$ mixed and the temperature of the solution may reach to 65 ^oC when 65 wt. % of $ZnBr_2$ is added to the acetone. This heat is generated as a result of dissolving the absorbent in the refrigerant and breaking the bonds between the absorbent molecules and atoms. Upon successful prepration of the solution, stability (both solutions with ZnO & G) and Transmission Electron Microscope (TEM) analysis of the samples provided as well as the properties of density, heat capacity, thermal conductivity and viscosity of the solutions were measured and compared with those data in Ajib and Karno [14].

3.3.1 Zinc Oxide (ZnO)(Suspension stability study)

The first experiment produced an $acetone - ZnBr_2/ZnO$ nanofluid with 50 wt. % of $ZnBr_2$ and different volume concentration of ZnO, prepared with the following steps:

1. 150 ml of the base fluid (acetone - $ZnBr_2$) with 50 wt. % $ZnBr_2$ was prepared. The density of the base fluid is 1360 kg/m_3 as measured.

$$Density(\rho) = \frac{Mass(m)}{Volume(V)} \tag{3.1}$$

$m = 1360kg/m^3 \times 150ml \times 0.001l/ml \times 0.001m^3/l \times 1000g/kg$

$m = 204g$

So, 102 g of both of acetone and $ZnBr_2$ was mixed to give 150 ml of the solution, then the 150 ml sample was divided into six test samples (25 ml) each.

2. Six different concentrations (0.005, 0.1, 0.3, 0.5, 1, 1.2 vol. %) of

suspension of solid-liquid were made by adding ZnO nanoparticles($\leqslant 50nm$).

To calculate the mass of ZnO, needed for 0.1 vol. %:

Volume of the solution: 0.025 l

Density of ZnO : $5610kg/m^3$

For 0.1 % Volume fraction of nanoparticals in 25 ml solution= $25ml \times 0.001l/ml \times 0.001m^3/l \times 0.001 = 25 \times 10^{-9}m^3$

Mass of nanomaterial = $2.5 \times 10^{-8} \times 5610$ = 0.00014025 kg

= 0.14025 g

By applying the same procedure for the other concentrations the mass of nanomaterials in each concentration are shown in a Table 3.1:

Table 3.1: Nanoparticles mass needed for each concentration.

Vol. concentration %	0.1	0.3	0.5	1	1.2
Mass (g)	0.14025	0.42075	0.70125	1.4025	1.683

The safety measures used in these processes are:

a) Fume cupboard.

b) Lab. coat, lab. Shoes and gloves.

c) Face mask.

d) Safety specs.

e) Spread a piece of foil in the working area surface to capture any dropped material.

The solution samples are put into the sonication bath (38 KHz) model SW1H produced by NICKEL-ELECTRO LTD., shown in Figure 3.1, for 2

hours. During the sonication, some sedimentation appears with concentrations 1 and 1.2 vol. %, which was not dispersed by sonication.



Figure 3.1: The sonication bath used to prepare the nanofluid Ac-$ZnBr_2 - ZnO$.

Figure 3.2 shows nanofluid suspensions with different concentrations of ZnO and different sonication options. For the 0.3 vol. % concentration (bottle number 1), the solution converts to a brown colour because it was left in the ultrasonic bath for 24 hrs (to check the effect of the long sonication period on the stability of nanofluid). The heat generated through the sonication process converts the solution colour from white to brown (the heat and (or) light convert the zinc bromide-acetone solution to brown within, 24 hrs at $\approx 55^oC$ in brightly of laboratory; and 15 days with light at the lab temp. $\approx 20^oC$ is also enough to change the colour). Bottle number 2 was prepared without sonication. The other samples were left in the ultrasonic bath for 2 hrs. It is obvious from Figure 3.2 that the sonication process time, has no significant influence on the time of the suspension (during this period, the progress went with different concentrations and times of sonication. Unfortunately, there was no time to revisit and study the effect of the sonication process time with a single concentration of nanoparticles, which is more convincing). By comparing the top part of the bottle 4 with the top part of the bottle 3 in Figure 3.2d, it can be seen that the top part of the bottle 4 is clearer than the same region of bottle 3, this is because, bottle 4 contains more concentrated nanoparticles and

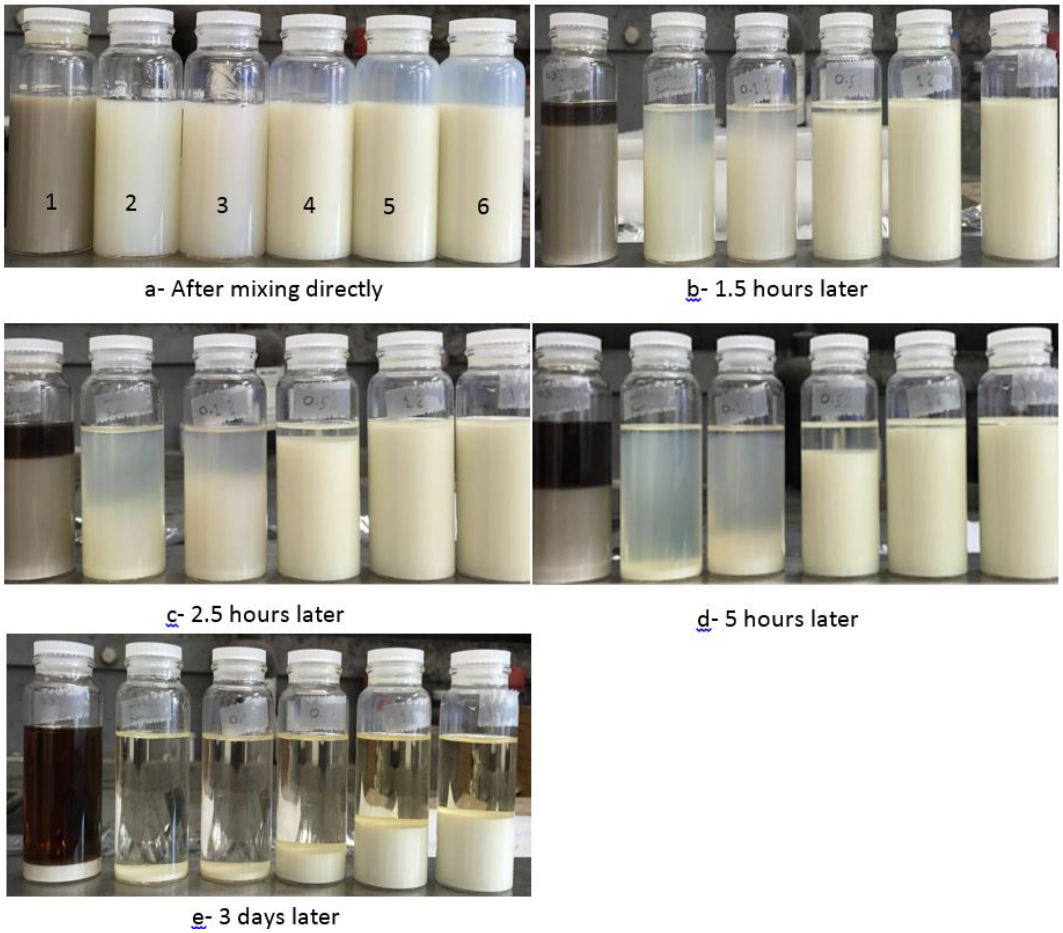


Figure 3.2: Sedimentation of different concentration of ZnO nanoparticles in acetone - $ZnBr_2$. 1- 0.3 vol. % 24 hrs Sonication. 2- 0.5 vol. %(without sonication). 3- 0.1 vol. % (2 hrs Sonication). 4- 0.5 vol. % (2 Hrs Sonication). 5- 1 Vol. % (2 Hrs Sonication). 6- 1.2 Vol. % (2 hrs Sonication).

the particles are close to each other and because of the high surface area of the nanoparticles, they gather and agglomerate to produce bigger agglomerations of particles and consequently faster sedimentation, but in bottle number 3 the particles are separated by relatively large distance between them and they need a time to reach each other and agglomerate. From this behaviour it is concluded that the higher concentration of nanofluids sediment totally faster than the dilute nanofluid.

To check the effect of surfactants, three samples were prepared with the same concentration of the nanoparticles (0.5 vol.%) and by adding 1 wt. % of the surfactants (Poly vinyl pyrrolidone (PVP), Sodium dodecyl sulphate

(SDS) and Polyvinyl alcohol (PVA)) as shown in Figure (3.3). By comparison with the settling time in Figure 3.2, it can be recognized that these types of surfactants are initially effective on the sedimentation time of nanoparticles. But after 1 hour, the surfactants gather on the top surface of the samples and the particles start to settle. Also, the PVA can't dissolve in the acetone / $ZnBr_2$ solution.

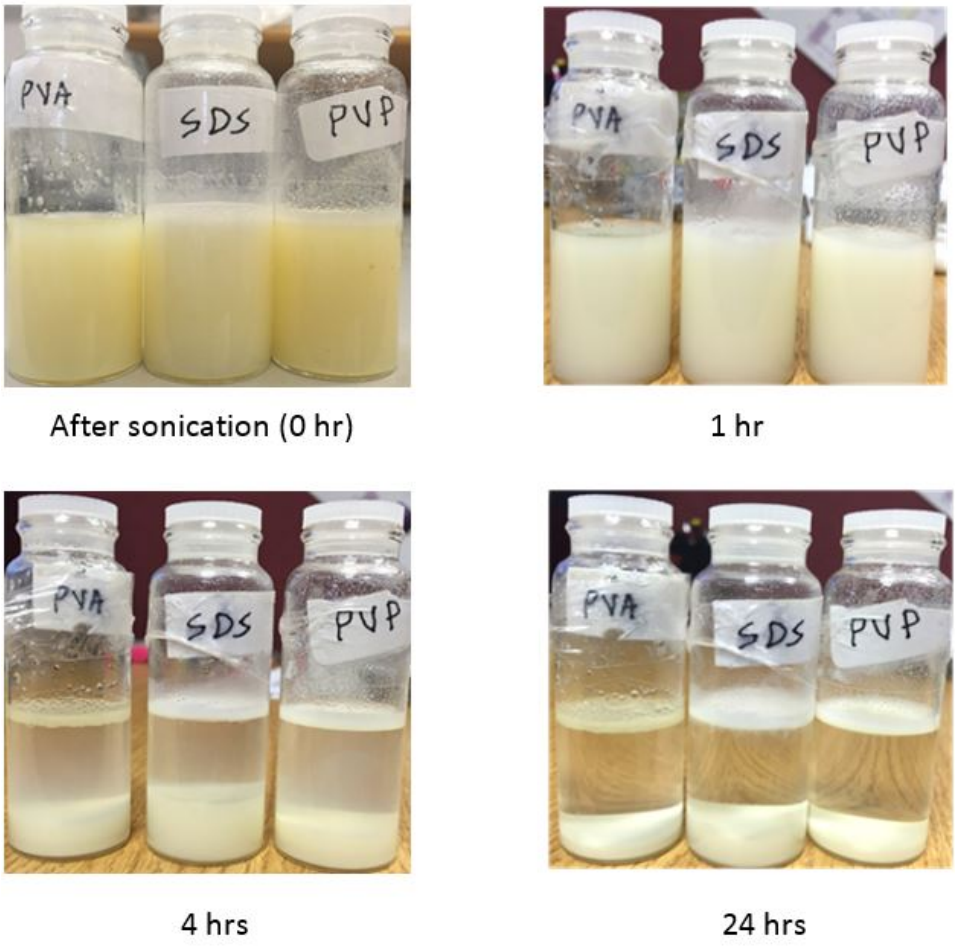


Figure 3.3: Settling of nanoparticles ZnO in the base fluid (Acetone / $ZnBr_2$) nanofluid for different times, using different surfactants.

3.3.2 Graphene (G)(Suspension stability study)

A sample of a nanofluid (acetone/$ZnBr_2$-Graphene) was prepared with 50 wt. % $ZnBr_2$ and 0.1 vol. % Graphene nanoplatelets (6-8 nm thick × 5 microns wide) provided by Strem company with catalogue number: 06-0201.

The sample is sonicated with a probe sonication for two hours using 45% of maximum amplitude. The probe sonication was carried out using Cole-Parmer 750-Watt and 20 kHz Ultrasonic Homogenizer with Temperature Controller, 115 VAC, provided by Cole-Parmer fluid handling and analysis company as shown in Figure 3.4.

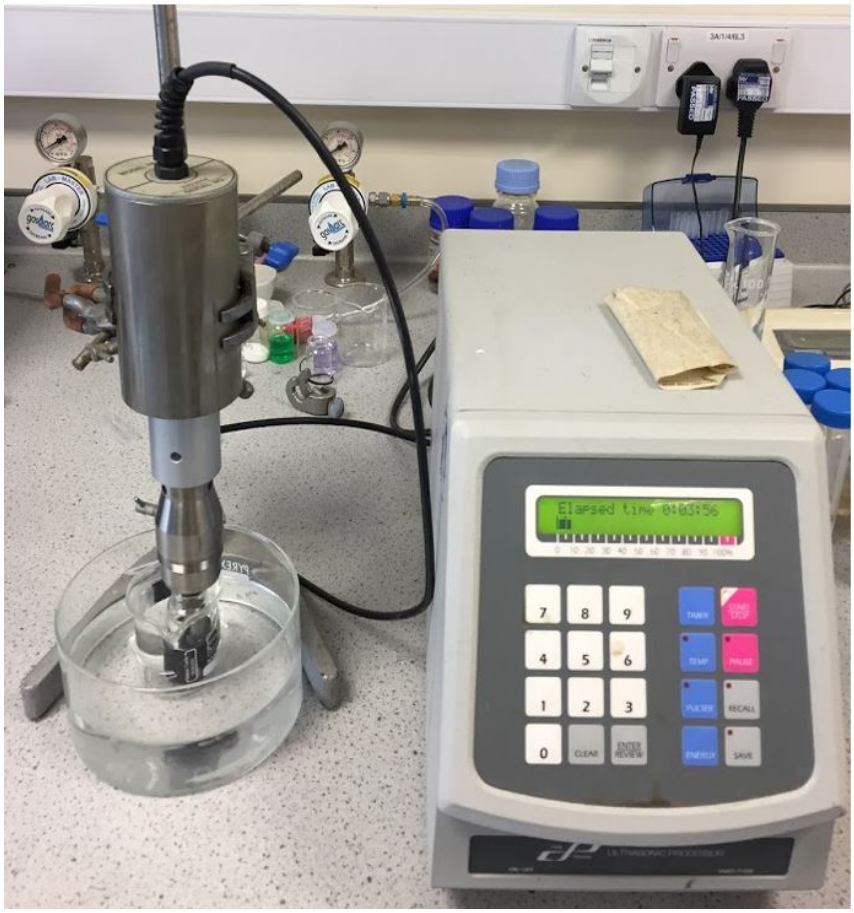


Figure 3.4: Cole-Parmer 750-Watt Ultrasonic Homogenizer with Temp Controller; 115V. Item number: EW-04711-40.

The sample was kept in a stationary place after the sonication (Figure 3.5). It can be seen that the sample looks stable for 36 hours. After 72 hours (last image on right) the particles settled partially. Some particles stick on the bottle wall as shown in Figure 3.5. The temperature of the sample increased with sonicating duration, because energy transfers from the probe to the molecules and particles which increases their kinetic energy and velocity, consequently more collision and friction is produced, which increases the

temperature. Increasing the temperature leads to evaporation of some of the acetone, consequently, the $ZnBr_2$ concentration in the solution increases and makes the solution more dense and viscous.

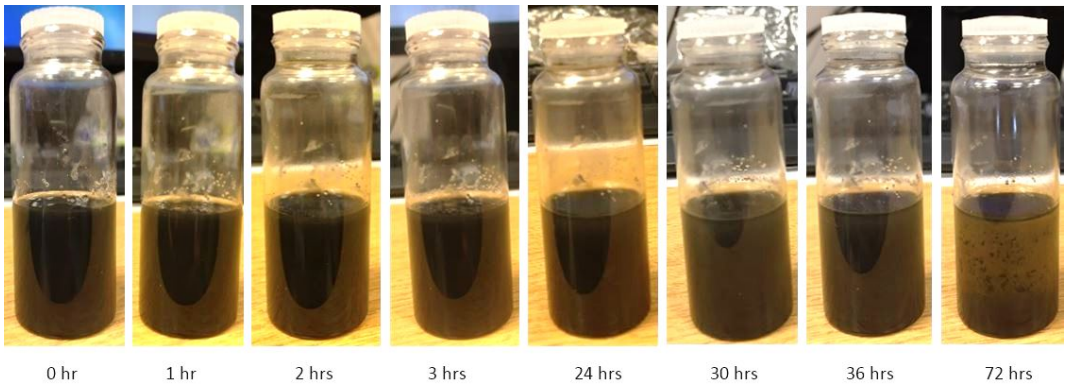


Figure 3.5: A sample of a nanofluid acetone/$ZnBr_2$-Graphene ($ZnBr_2$=50 wt. % and Graphene=0.05 vol. %), sonication time= 2 hrs and amplitude= 45%.

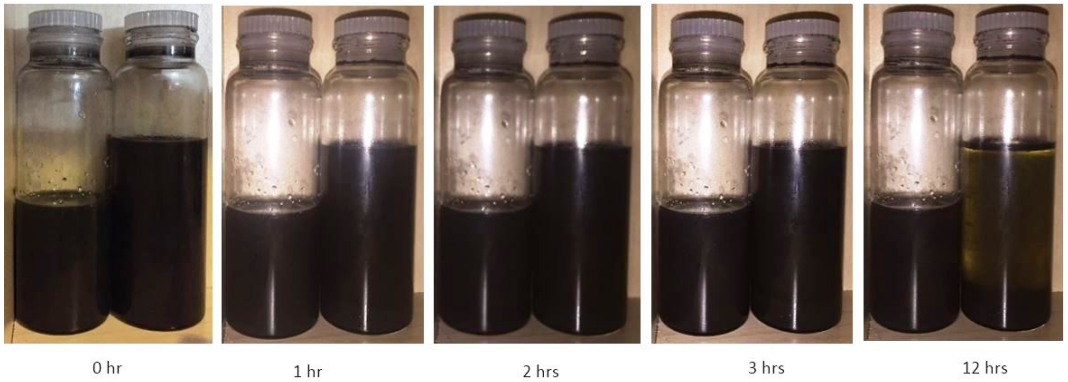


Figure 3.6: Samples of a nanofluid acetone/$ZnBr_2$-Graphene ($ZnBr_2$=50 wt. % and Graphene =0.05 vol. %), Right sample had sonication time= 4 hrs and amplitude= 65%. and acetone added to compensate the evaporated acetone. Left sample had sonication time= 2 hrs with amplitude= 45%.

To improve the stability of the solution another sample was prepared with the same concentration of the first sample and sonicated for 4 hours with amplitude 65% in order to break the smaller agglomerations. An amount of acetone was added to the sample to compensate for loss of acetone due to evaporation. The particles settled within 12 hours as shown in Figure 3.6 (right sample). The left sample is the old sample which is shown in Figure 3.5, shaken and used to compare between the samples in terms of the settling time.

A further two samples were prepared with 50 wt. % $ZnBr_2$, with different concentrations of graphene (0.05 and 0.2 vol. %) with 2 hrs sonication and 45% amplitude of the probe. During the sonication an amount of acetone was added to the solution to compensate for loss of acetone by evaporation, the amount of the additional acetone being calculated by measuring the weight of sample before and after sonication:

Mass of added acetone = Mass before sonicating – Mass after sonicating.

As shown in Figure 3.7, the two samples on the right show reduction in stability gradually. After 16 hrs, the particles have completely settled because by adding acetone the density of the solution decreases which help the particles to settle faster. The left sample is the same sample as used in Figure 3.5 in different container.

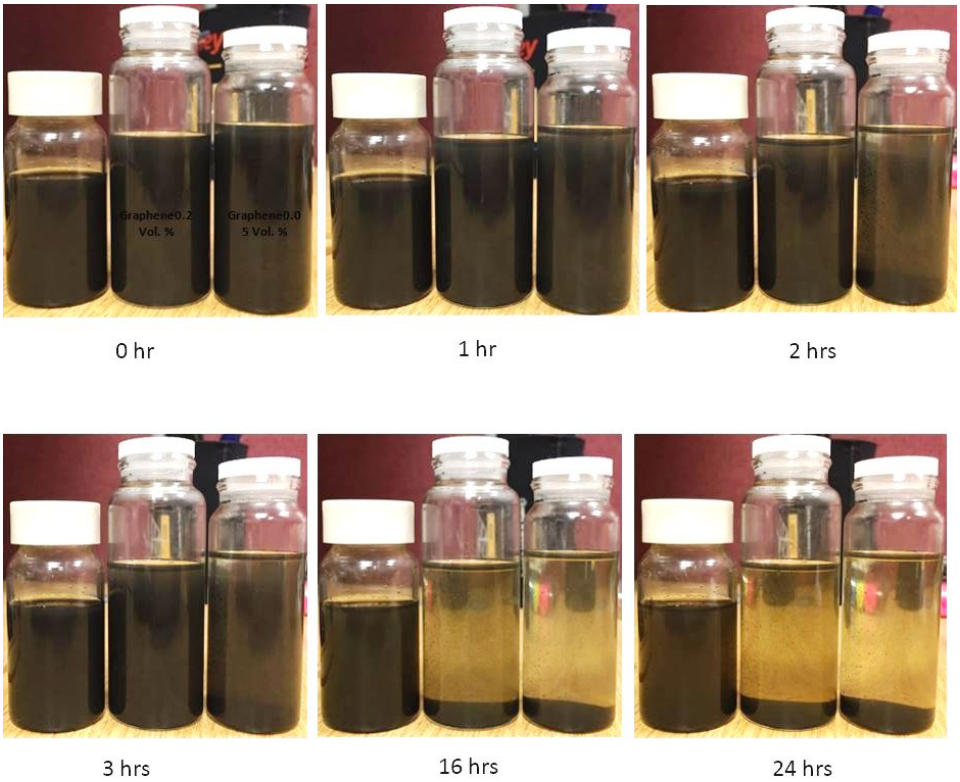


Figure 3.7: Samples of a nanofluid acetone/$ZnBr_2$-Graphene ($ZnBr_2$=50 wt. %), the two samples on right had concentrations=0.05 and 0.2 vol. % with sonication time= 2 hrs, amplitude= 45%. and acetone added to compensate the evaporated acetone. Left sample had sonication time= 2 hrs, amplitude= 45%. Without adding acetone.

Figure 3.8 shows the nanofluid acetone / $ZnBr_2$ – Graphene with two concentrations of $ZnBr_2$ and constant concentration of graphene (0.05 vol. %) under different effects. The first four samples at the left hand side have the same concentration of $ZnBr_2$ (50 wt. %). Sample (a) was prepared without sonication, sample (b) sonicated for 1 hour, sample (c) sonicated for 2 hours and sample (d) sonicated with 2 hours then centrifuged for 30 minutes with speed 500 rpm. However, sample (e) has a concentration 60 wt. % of $ZnBr_2$ and 0.05 vol. % of Graphene and is sonicated for 30 minutes; all of these samples are sonicated with 45% of the sonication power. Sample (f) has a concentration of 50 wt. % with 0.05 vol. % sonicated for 2 hours with 70% power of the sonication and centrifuged for 30 minutes. Because of the high power sonication in that particular case, the temperature of the solution increased

and a part of the acetone evaporated, therefore raising the concentration of the nanoparticles and the $ZnBr_2$.

For sample (a), the particles start to settle between 2 and 4 hrs and completely sediment by 24 hrs. Samples (b), (c) and (d) show that there are no differences in stability between them while they have a better stability than sample (a); this indicates that the sonication with 1 hour is enough to break the agglomeration that can be achieved with that sonication power; keeping the sample sonicated for longer time has no advantage; also centrifuging the sample, which can remove the big agglomerations that are not separated by sonication results in no improvement. Sample (e) shows a better stability than the others, because with increasing concentration of $ZnBr_2$ the density and viscosity of the nanofluid solution increases, which helps the particles to settle slowly according to Stokes Law (which calculates the velocity of the particles ie. the free fall velocity in the stationary solution) Equation 3.2. As noticed, after 5 days there are still some particles suspended.

$$\upsilon = \frac{(D_H)^2}{18\mu}(\rho_p - \rho_l) \cdot g \tag{3.2}$$

υ is the terminal velocity of the particles, ρ_p is the density of the particles, ρ_l is the density of the base-fluid, g is the gravity and μ is the viscosity of the base fluid.

To investigate how the concentration of the $ZnBr_2$ affects the suspension time of the nanoparticles, six samples were prepared (Figure 3.9) with different concentrations of $ZnBr_2$ (40 wt. % (far right) – 65 wt. % (far left)) with 5 % increase steps. The concentration of graphene nanoplates is constant (0.05 vol.%) and all the samples are sonicated for 1 hour with 45 % of the available power of the probe sonicator. As seen the effect of density and viscosity is

strongly reflected by the stability of the nanofluid. The lowest density and viscosity solution (low concentration of $ZnBr_2$) equal to 1.291 g/cm^3 and 1.291 mPa.s [14], respectively, this solution can't carry the particles for a long time, the majority of the particles settle within 10 hours. According to the theoretical equation 3.2 the particles will settle within 8 hours considering the hydraulic diameter 2.514 μm, corresponding to the average of the nanoplate diameter (5 μm) and the hydraulic diameter of the cross section of the thickness of the plate (5 $\times$ 0.007 μm^2). However, in the highest concentration of $ZnBr_2$, the particles start to settle after 2 – 5 days. The solution has density and viscosity of 2.292 g/cm^3 and 72 $mpa.s$ [14] respectively. The Stokes equation can not apply in this case because the density of the particles (1800 kg/m^3) is lower than the solution itself, so, according to this equation all the particles should gather at the surface of the solution, which is not observed in reality. But according to our measurement, the density is 1662 kg/m^3 which is lower than 1800 kg/m^3 which makes the equations reflect the fact of the suspension.

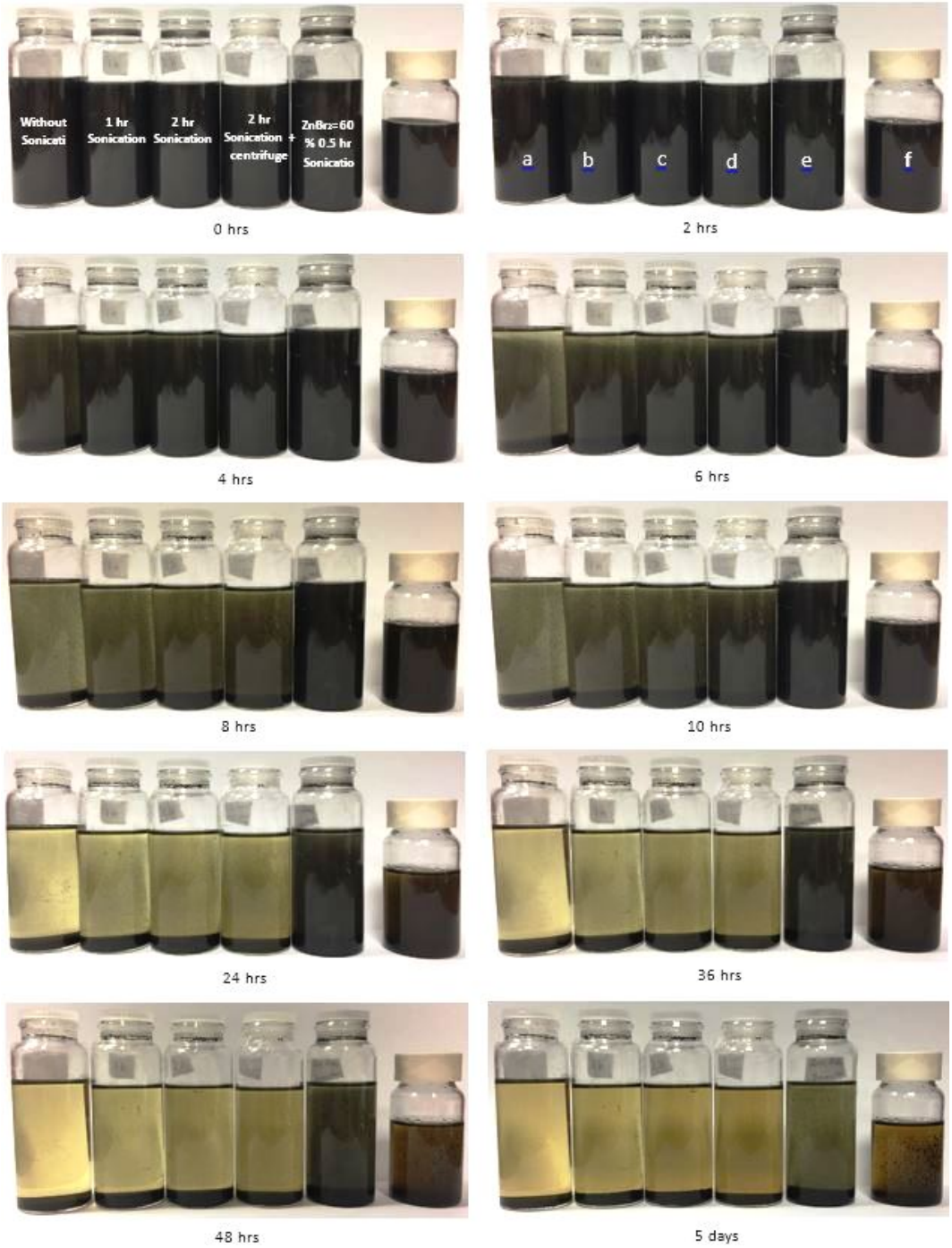


Figure 3.8: Samples of a nanofluid acetone/$ZnBr_2$-Graphene ($ZnBr_2$=50 wt. %, graphene=0.05 vol. %), a) prepared without sonication, b) sonicated with amplitude= 45% probe sonication for 1 hr, c) sonicated for 2 hrs, d) sonicated for 2 hr and centrifuged, e) has a concentration of $ZnBr_2$ =60 wt. %. and f) sonicated for 2 hours with 70% power of the sonication and centrifuged for 30 minutes



Figure 3.9: Samples of a nanofluid acetone/$ZnBr_2$-Graphene. With different concentration of $ZnBr_2$ (40 wt. % (far left) – 65 wt. % (far right)) with 5 % increase steps. The sonication time is 1 hour with 45 % of the probe total power. The graphene concentration=0.05 vol. %).

3.3.3 Transmission Electron Microscope (TEM) analyzer:

TEM is the primary technique to verify single particle dimensions and to identify agglomerations of particles. The electron beam can be used to see features on the nanometer level. A major drawback to the use of TEM is that samples must be dried out of solution in order to be attached to the carbon matrix (grid). Therefore the particles are not exactly in nanofluid state and agglomeration might occur during drying.

TEM was performed using a JEOL 2100F transmission electron microscope (field emission electron gun source, information limit 0.19 nm). TEM samples were prepared by casting several drops of the sample solution onto copper-mesh holey-carbon film TEM grids (Holey Carbon support films (HC range) provide a carbon support film with a range of relatively small hole sizes, particularly suited for suspensions of nano and virus like particles as shown in Figure 3.10 [160]) and dried under ambient conditions. A scanning transmission electron microscope (STEM) images were acquired using the JEOL digital STEM system. Statistical analysis was performed using Image J software.

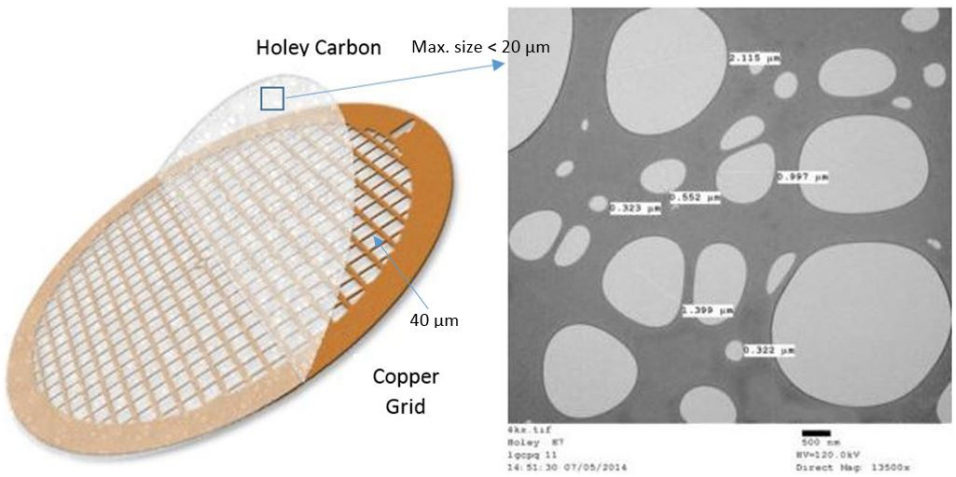


Figure 3.10: a- Copper mesh holey Carbon film. b- Holes in the carbon film. [160]

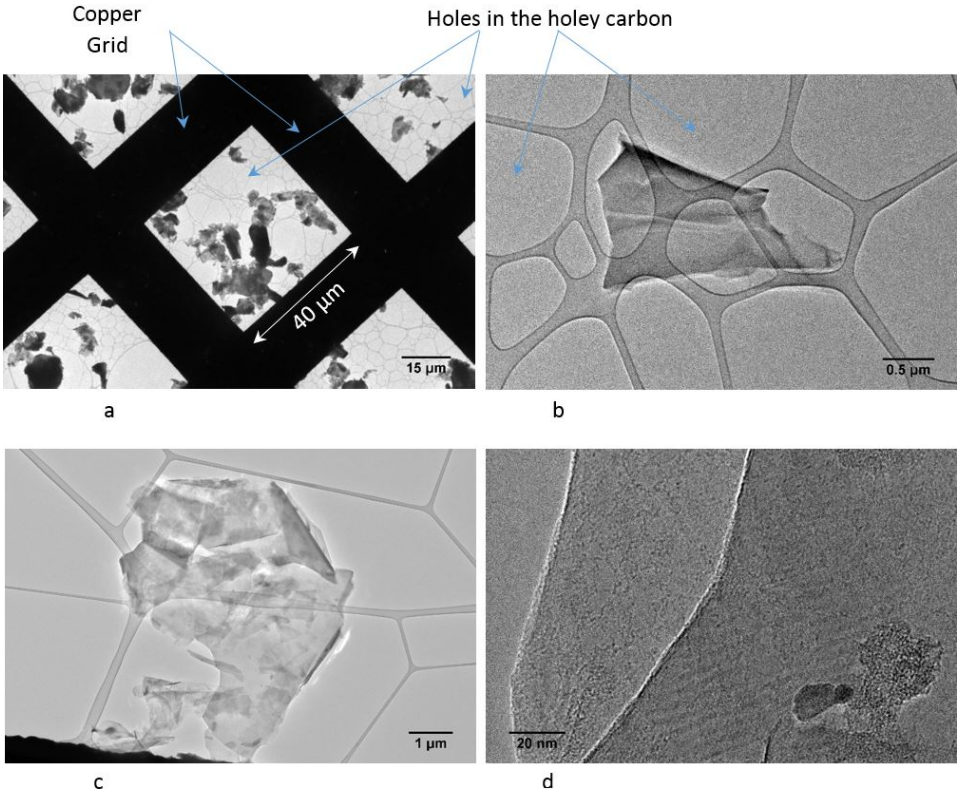


Figure 3.11: Different TEM images of graphene from suspension in the pure acetone on the Copper mesh holey Carbon film, a) shows a distribution of graphene from acetone/graphene sample on the Carbon film, b) shows a particle stuck on the film, c) show particles stuck on the film and d) shows the surface of the nanoplate view.

The nanoparticles dried from three samples were imaged with this technique, acetone based on 0.5 vol. % graphene; acetone/$ZnBr_2$ based on both 0.5 vol. % graphene; 0.1 vol. % ZnO. The samples were dried without dilution to keep the concentration of the $ZnBr_2$ at high level to see how they separate out of the solution. Figure 3.11 shows the distribution of graphene from the acetone/graphene sample on the carbon film. From Figure 3.11 the grid size of the copper is 40 μm. However, the size of the carbon film's holes are different between 0.5μm & 20 μm. The Figure shows the suspension of the graphene particles on both film and grid. The suspensions appear in different colour levels between grey and black because of the thickness of the particles, which is caused by the agglomeration. Whereas the thick part of the body makes a black trace because the thick part prevents the electrons stream to

pass through it and most of these electrons are scattered in the high angles. While, the grey colour means a thin part of the body, which allows most of the electrons to pass. Figure 3.11 (b) and (c) show particles stuck on the carbon film. While Figure 3.11 (d) illustrates the surface of the nanoplate view. The figure also show that there are different regions between light and dark, which clarify how the layers of graphene overlaps on each other.

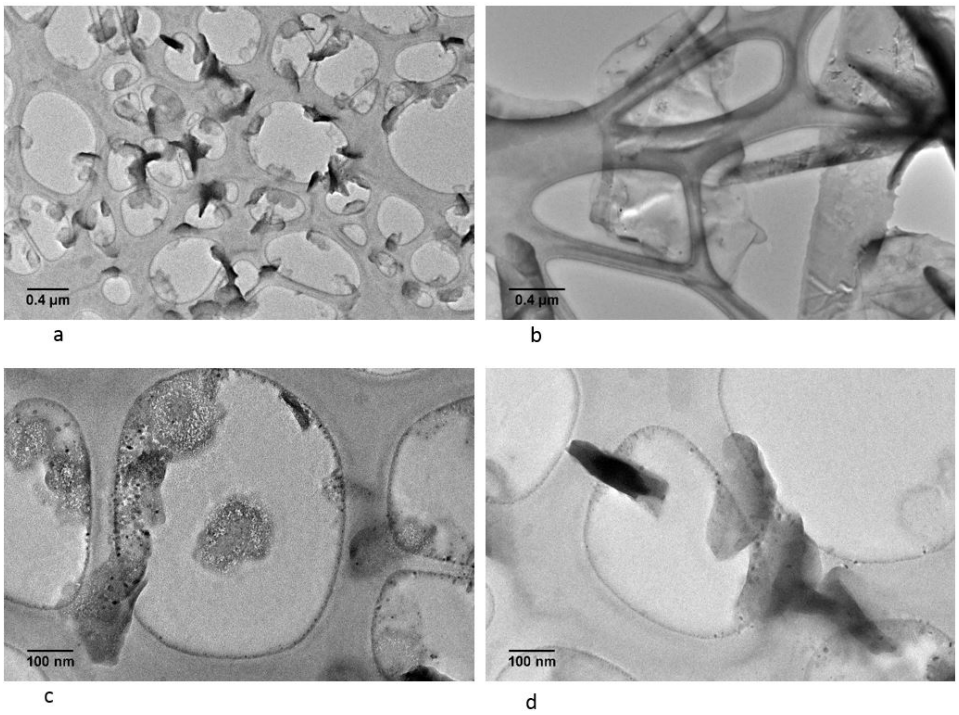


Figure 3.12: Different TEM images of graphene suspend in the acetone / $ZnBr_2$ on the Copper mesh holey Carbon film, a) nanoparticles distribute on the film between the holes, b) single particle on the film and crystallization of the $ZnBr_2$ (appears as a black part), c) shows grains of the non crystallized $ZnBr_2$, and d) shows some particles on the film in different scale.

Figure 3.12 shows the graphene from the acetone-$ZnBr_2$ sample on the carbon film. From Figure 3.12 (a), the nanoparticles, which have a grey colour distribute on the film between the holes. However the black colour is either dried $ZnBr_2$ or it is a several layers of graphene. The image shows also that all the bodies have a dimension less than 300nm. From Figure 3.12 (b), a small amount of the crystallization of $ZnBr_2$ appears in a black colour at the lab. light. From Figure 3.12 (c) and (d) it can be recognized that there are

some grains of the non-crystallized $ZnBr_2$, which have very small size (around 1 nm).

Figure 3.13 shows different images, illustrating the ZnO nanoparticles with $ZnBr_2$ behaviour on the copper grid and the carbon film for the sample Acetone/$ZnBr_2$ based on ZnO. Figure 3.13 (a) and (b) show random star shapes inside the holes of the carbon film; this is caused by the crystallization of the $ZnBr_2$ with ZnO particles. Figure 3.13 (c) and (d) show very small grains appear between the holes of the carbon film, which seem to be $ZnBr_2$ crystals, because these grains just appear when the acetone / $ZnBr_2$ is used as a base fluid and they don't appear when the acetone only is used as a base fluid.

Figure 3.14 shows that there are spots on the carbon film between the holes. These spots seem to be ZnO particles for three reasons, Firstly, they don't appear in the other samples; Secondly, the atomic number of Oxygen (O) is 8, still lighter than the Bromide (Br) which has an atomic number equal to 35. Therefore, the oxygen allows more electrons to pass through it, thirdly, they appear to be of the right size ($\leqslant 50nm$).

Figure 3.15, shows the same image of 3.13 (a) but with different technique, called Scanning Transmission electron Microscope (STEM), which offers unique imaging mode and enhanced microanalysis capability. Transmitted electrons collected on axis in the STEM give the bright field or phase signal. These electrons have either not been scattered at all or have been inelastically scattered through angles of milli-radians or less.

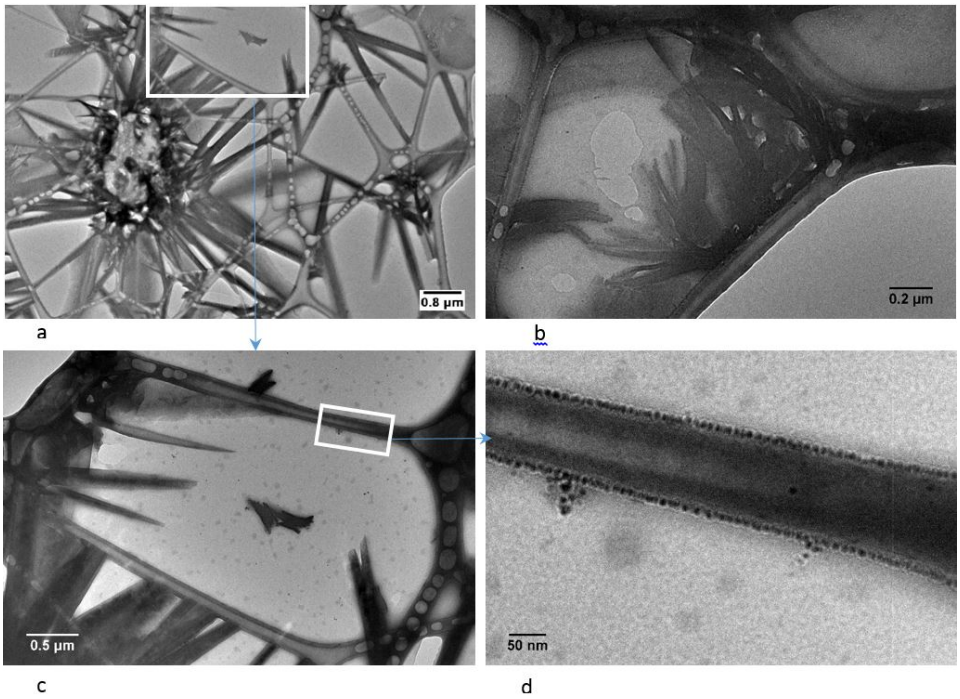


Figure 3.13: Different TEM images of ZnO suspension in the acetone / $ZnBr_2$ on the Copper mesh holey Carbon film, a & b) show a random star shape of the $ZnBr_2$ crystallization and c & d) show grains appear between the hole of the carbone film.

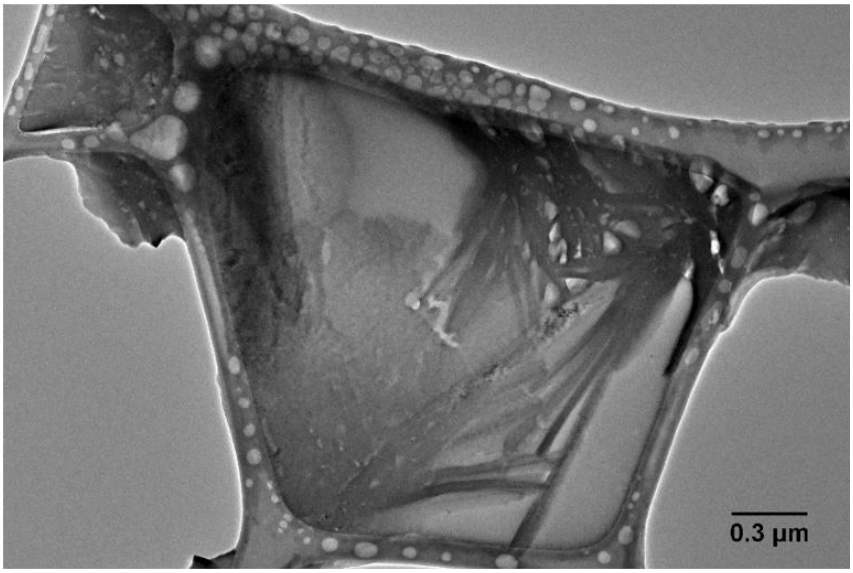


Figure 3.14: TEM images of ZnO suspension in the acetone/$ZnBr_2$ on the Copper mesh holey Carbon film.

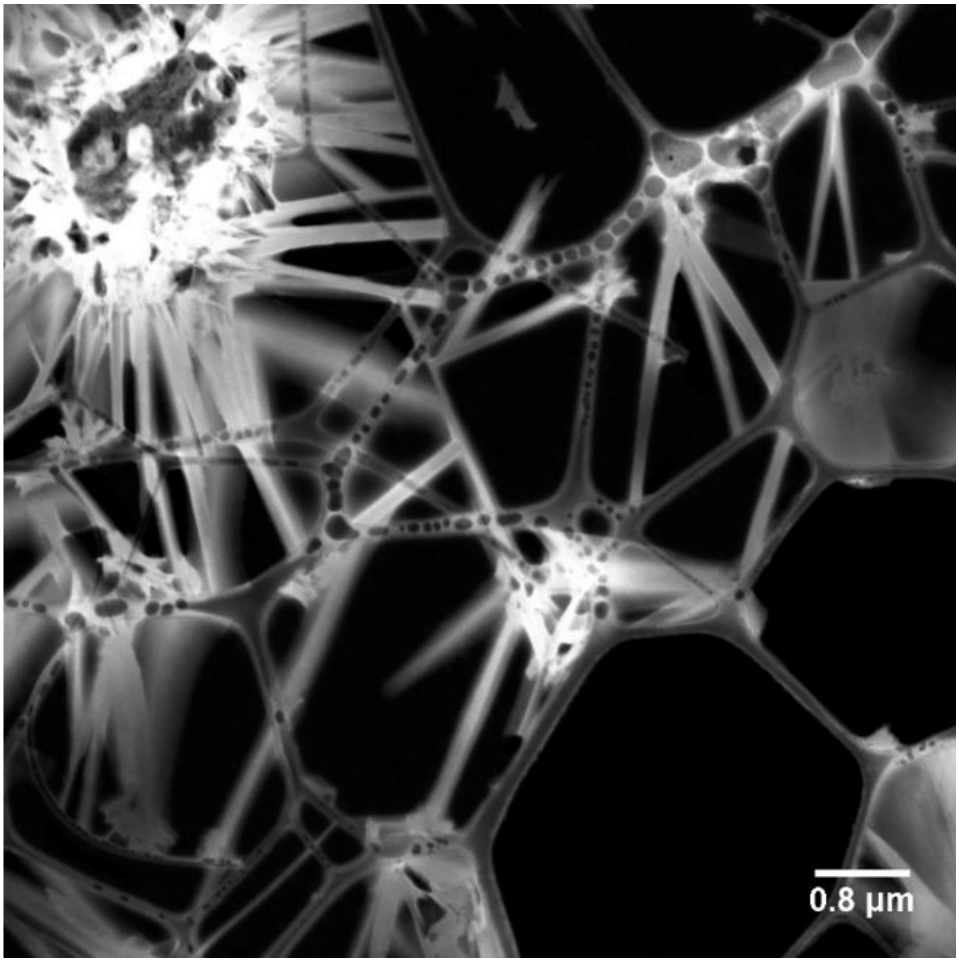


Figure 3.15: STEM image of ZnO nanoparticles suspension in acetone/$ZnBr_2$.

3.4 Properties Investigations

3.4.1 Density

The density of $acetone/ZnBr_2$ was measured for different concentrations of $ZnBr_2$ (40 - 65 wt. %) at 20 ^oC, the results found from this test show a significant difference to the results measured for this particular fluid in the only available published literature [14], as shown in Figure 3.16. An explanation for this difference, it appears that [14] may have a methodology error to calculate the density. The current method is:

1. Weigh a clean, empty and dry volumetric flask.
2. Pour solution which prepared with different concentration of $ZnBr_2$ till the mark of scale (10 ml).
3. Weigh the sample.

From the weight and volume of the sample, the density is calculated. For example the mass of the solution ($acetone/ZnBr_2$) with 50 wt. % $ZnBr_2$ is 13.602 g for 10 ml. That makes the density equal to 1360 kg/m^3. While, in the literature [14] it is calculated as 1581 kg/m^3. The possible explanation for this difference is the literature may assume that when the salt ($ZnBr_2$) is added and dissolved in the acetone, the volume of the total solution is the same as the initial acetone volume. For example:

The mass of 10 ml acetone with density 790.5 kg/m^3 is:

$m = 790.5kg/m^3 \times 10ml \times 10^{-6}m^3/ml = 790.5 \times 10^{-5}kg(7.905g)$.

Add same quantity (7.905 g) of $ZnBr_2$

$m_{sol} = m_{Ac} + m_{ZnBr_2}$

$m_{sol} = 7.905 + 7.905 = 15.81g$

If the original volume of 10 ml is assumed:

The density of acetone / $ZnBr_2(50wt.\%ZnBr_2) = (15.81 \times 10^{-3})/(10 \times 10^{-6}) = 1581kg/m^3$

Which is the value found in the literature, strongly indicating that the previously published results contain an inherent error.

Table 3.2: Density of different concentrations of acetone / $ZnBr_2$ as found experimentally, from literature and if the volume of acetone not change when the $ZnBr_2$ added.

	Density as reported in [14] (kg/m^3)	Density as found by assuming no change in volume (kg/m^3)	Experimental density (kg/m^3)
40 %	1293	1317.5	1164
45 %	1420	1437.2	1228
50 %	1581	1581	1360
55 %	1778	1756.6	1426
60 %	2013	1976.2	1550
65 %	2292	2258.59	1662

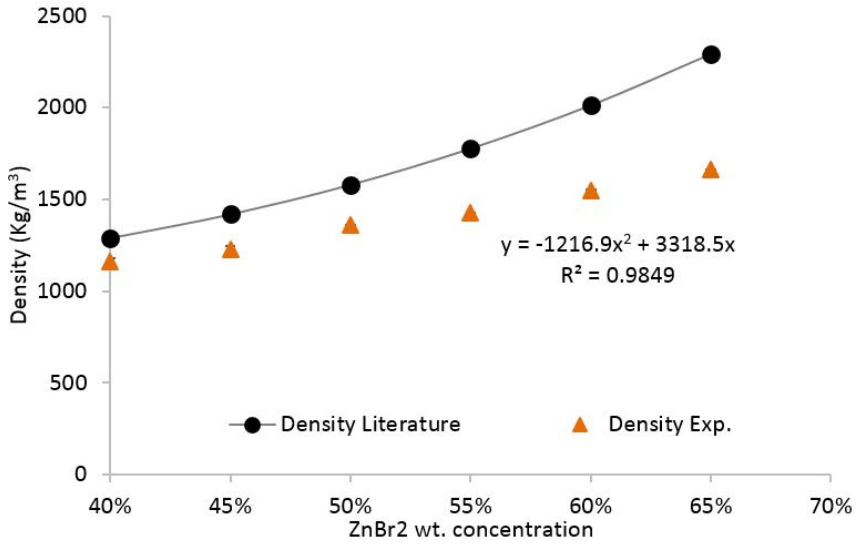


Figure 3.16: Density of acetone / $ZnBr_2$ with different concentration of $ZnBr_2$ as measured experimentally at 20 ^oC and those based on the data from literature [14].

Table 3.2 shows the difference between the densities of different concentrations of acetone / $ZnBr_2$ as found experimentally, from literature and if the volume of acetone not change when the $ZnBr_2$ added. The volumetric flask had a narrow neck, which reduces the error. The fluid level on the flask's mark

may have an error of ±0.5 mm and the diameter of the neck of flask is 10 mm, which make the error volume:

$V_{err} = \frac{\Pi}{4}(0.01)^2 * 0.5 * 10^{-3} = 0.3926 * 10^{-7} m^3 = 0.0392 ml$

Volume of solution = 10 ml

$Error = \pm\frac{0.0392}{10}100\% = \pm 0.4\%$

Regarding the nanofluid, the density of the nanofluid is well represented by a simple mixture combination method as explained in section 2.2.3.1. This method is used by researcher dealing with a nanofluid via the CFD volume of fluid (VOF) approach.

The density of the nanofluid increases with increasing concentration of ZnO nanoparticles, for example, the density increases from 1368 to 1417 kg/m^3 by increasing the volume fraction from 0.001 to 0.012. From the Figure 3.17 it can be seen that the experimental results are approximately the same as the theoretical density found by equation 2.3. The same behaviour applied for the Graphene nanoparticles, whereas, the density of the solution with 60 wt. % $ZnBr_2$ increases from 1550.025 to 1551.25 kg/m^3 by increasing the concentration of Graphene from 0.01 to 0.5 vol. % as shown in Figure 3.18.

To get a better idea of the actual data of the density and characterize the uncertainty of these values, the measurement for each case was repeated five times in different sized containers. After collecting all the data (as shown in the Tables A.1, A.2 and A.3 in the appendix), the following characteristics have been calculated [161]:

Average (x_{av}): the average of all the values of the variable x which is density in this case

$$x_{av} = \frac{\sum_{i=1}^{N} x_i}{N} \tag{3.3}$$

where x is the measurement of the variable, and N is the number of measurements.

Standard deviation (S_d): explains how the values of the measurement differ from the mean value,

$$S_d = \sqrt{\frac{\sum_{i=1}^{N}(x_i - x_{av})^2}{N}} \tag{3.4}$$

Standard error (S_{er}): estimates the standard deviation based on the population.

$$S_{er} = \frac{S_d}{\sqrt{N}} \tag{3.5}$$

Uncertainty of the measurement ($\triangle x$): it is the uncertainty in the single measurement of x. Therefore, we know that x is somewhere between x_{max} and x_{min}

$$\triangle x = \frac{x_{max} - x_{min}}{2} \tag{3.6}$$

Uncertainty mean ($\triangle x_{av}$): the uncertainty of the mean value of x. Therefore the real value of x is in the point around x_{av}

$$\triangle x_{av} = \frac{\triangle x}{\sqrt{N}} \tag{3.7}$$

On Figures 3.16, 3.17 and 3.18 the uncertainty of each measurement appears as the error bars (in the Figure 3.16 the error bars are very small). It is clear that the uncertainty value of each case is very low compared to the real value. The maximum values of the uncertainty, were 1229 ± 20, 1403 ± 6 and 1550 ± 3 for cases acetone/45 vol.%$ZnBr_2$, acetone/50 vol.%$ZnBr_2$ with

0.01 volume fraction of ZnO and acetone/60 vol.%$ZnBr_2$ with 0.005 volume fraction of graphene, respectively.

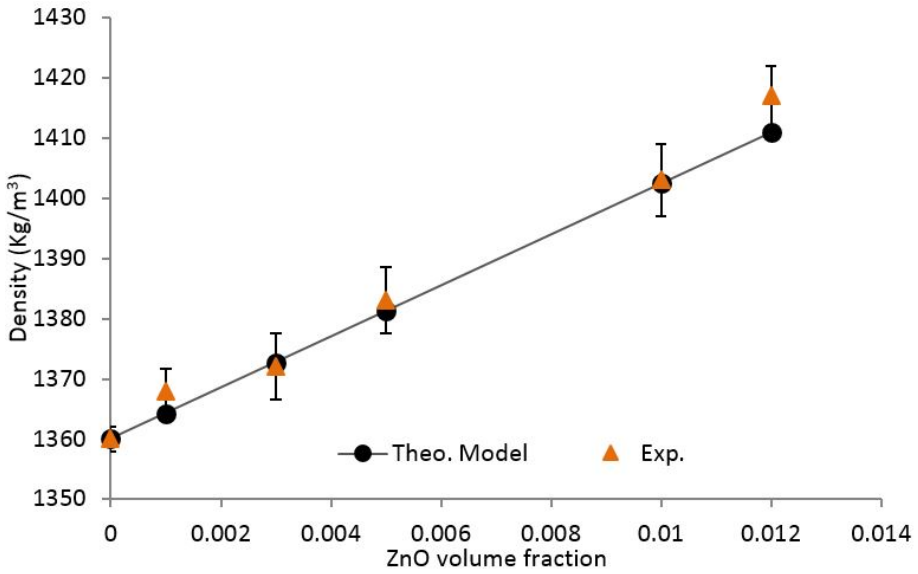


Figure 3.17: Effect of the ZnO nanoparticle volume fraction on the density of nanofluid experimentally at 20 ^oC and theortically based on equation 2.3.

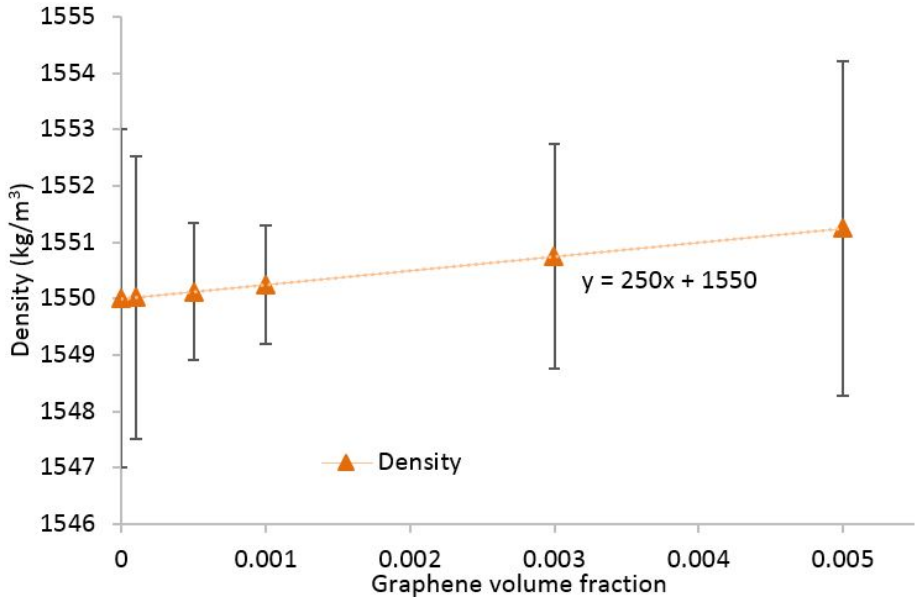


Figure 3.18: Effect of the graphene nanoparticle volume fraction on the density of nanofluid at 20 ^oC.

It is worth mentioning here that the true density of particles are more than 30 - 40 times the apparent density. Hence the volume of the solid was determined by calculating the equivalent weight of the solid using the true density,

neglecting the weight of air trapped inside the sample. The density of graphene is 1800 kg/m^3. The measured weight for graphene nanoplate (without compression) is 0.000503 kg for a 10 ml sample, which makes the apparent density equal to 50.3 kg/m^3 (true density = 35.78 × apparent density).

3.4.2 Viscosity

The viscosity of the acetone- $ZnBr_2/ZnO$ nanofluid was measured for different concentrations of nanoparticles and different temperature (25, 30, 35, 40 and 45^oC) using hts-VROC Viscometer Rheometer On a Chip produced by RheoSense simply precise, shown in Figure 3.19. The measuring cell or "chip" contains a rectangular slit flow channel constructed of borosilicate glass, with a uniform cross-sectional area as shown in Figure 3.20. The sample is injected at a constant flow rate though the flow channel where multiple pressure sensors mounted within the base monitor the pressure drop from the inlet to the outlet. The pressure drop is correlated with the shear-stress at the boundary wall. The shear rate and shear stress are directly related to the geometry of the rectangular slit and the flow rate which allow for viscosity measurements.

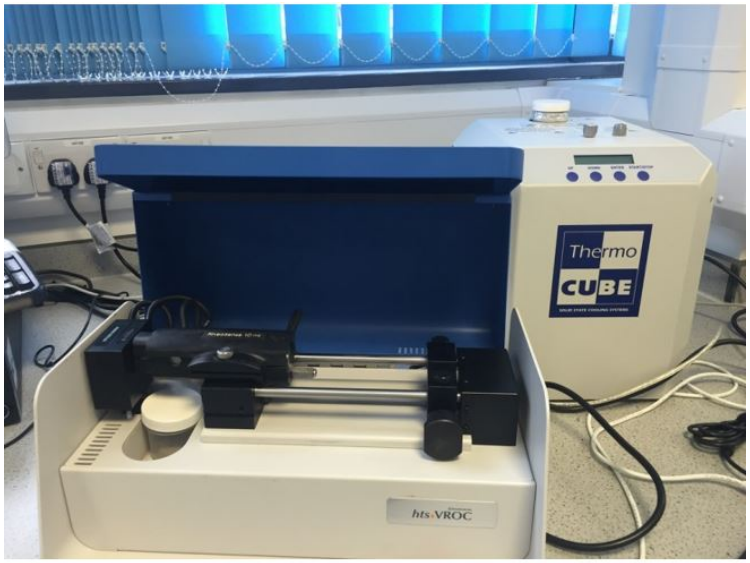


Figure 3.19: hts-VROC Viscometer Rheometer On a Chip.

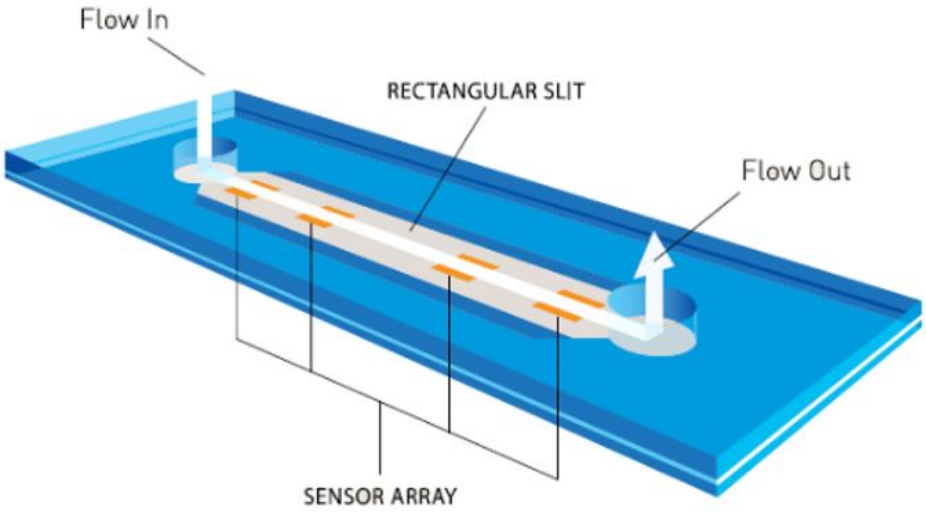


Figure 3.20: Cell or "chip" which contains a rectangular slit flow channel constructed of borosilicate glass, with a uniform cross-sectional area and multiple pressure sensors.

The viscosity of the acetone/ $ZnBr_2$ nanofluid with different concentrations of ZnO at 25 ^oC is measured. The viscosity increased from 3.228 to 4.79 m Pa.s with increasing concentration of nanoparticles from 0 to 1.2 vol. % as shown in Figure 3.21. The measurement was repeated by the viscometer ten times for each sample. The viscosity of the acetone alone was found to be 0.308 $\pm$ 0.007 m Pa.s depending on the equation of uncertainty of measurement, the maximum uncertainty was 0.4 mPa.s for the acetone / 50 vol.% $ZnBr_2$ with 1.2 vol.% ZnO as shown in Figure 3.21. All data is presented in Tables A.4 and A.5 in the appendix.

Figure 3.22 shows the shear stress versus shear rate for 0.5, 1.0 and 1.2 wt.% nanofluids at 25 ^oC. The results for other concentrations samples are similar. The linear relationship between shear rate and shear stress indicates the Newtonian (i.e like a single phase liquid) behaviour of the acetone/$ZnBr_2$ based ZnO nanofluids at a shear rate higher than 0.05 s^{-1} for all volume fractions and temperatures investigated. This is more clearly shown in Figure 3.23, where the viscosity is plotted against the shear rate for the 0.5, 1.0 and 1.2 wt.% nanofluids at 25 ^oC and it shows that the viscosity is not changed

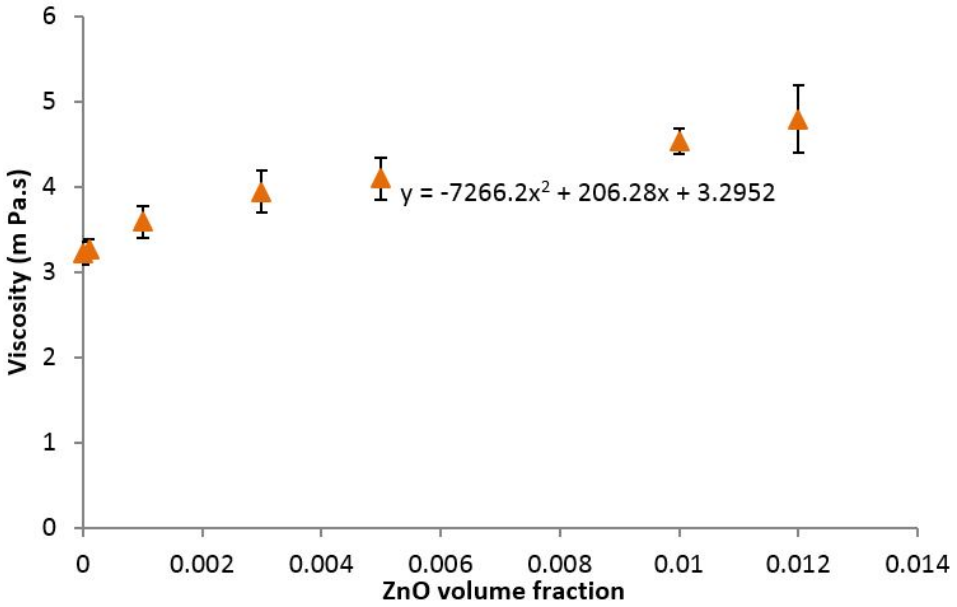


Figure 3.21: Relation of the viscosity with the volume fraction of ZnO nanoparticles in acetone / 50% $ZnBr_2$ at 20 ^oC.

with changing shear rate. The Newtonian behaviour has also been observed by Wang et al [67] and Das et al [91] for water–Al_2O_3 nanofluids, Wang et al [67] for EG–Al_2O_3 nanofluids, Xuan and Li [69] for water–Cu nanofluids and Chen et al. [162] for EG based on TiO_2. This test covers a wide range of shear rate (0.05 –60000 s^{-1}) and the observed Newtonian behaviour for the nano-salt-fluid for a first time.

Figure 3.24 shows the measured viscosity at different temperatures (25, 30, 35, 40 and 45 ^oC) for 0.0, 0.01, 0.1, 0.3, 0.5, 1 and 1.2 wt. % of ZnO suspended in acetone/$ZnBr_2$. the viscosity of the nanofluids is strongly affected by the temperature, since, the viscosity decreases with increasing temperature. By increasing the temperature the energies of both particles and molecules increase and this leads to more activity and motion of the fluid and consequently the viscosity drops. Effort was therefore made to find a relation between the nanofluids viscosity and the temperature at each volume fraction of nanoparticles as shown in equation 3.8. Table 3.3 shows the values of these constants (A and B) for all the nanofluids samples. The Table also includes the R^2

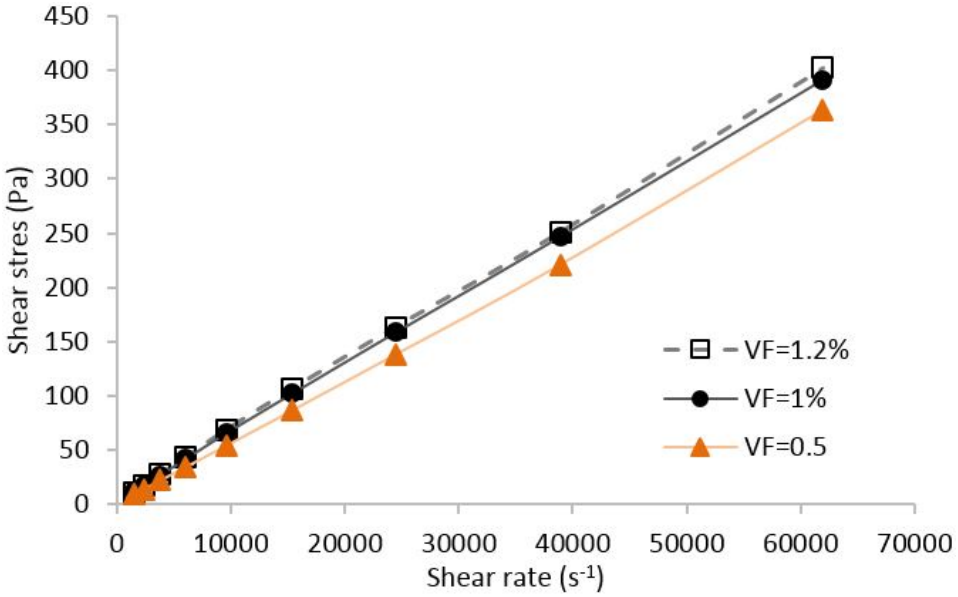


Figure 3.22: Relation between the shear stress and the shear rate of the acetone / 50% $ZnBr_2$ based on different concentration of ZnO at 20 ^oC.

which is a statistical measure of how close the data are to the fitted regression line; the experimental data almost fit perfectly with the correlation line. Also, the relation between viscosity, temperature and particles volume fraction are correlated in one equation as shown in equation 3.9 using minitab software. Figure 3.25 shows the same contents of Figure 3.24 but in a 3 dimensional graph.

$$\mu = Ae^{B}T \tag{3.8}$$

$$\mu = Exp(6.32 - 0.0171T(K) + 29.7\Phi) \tag{3.9}$$

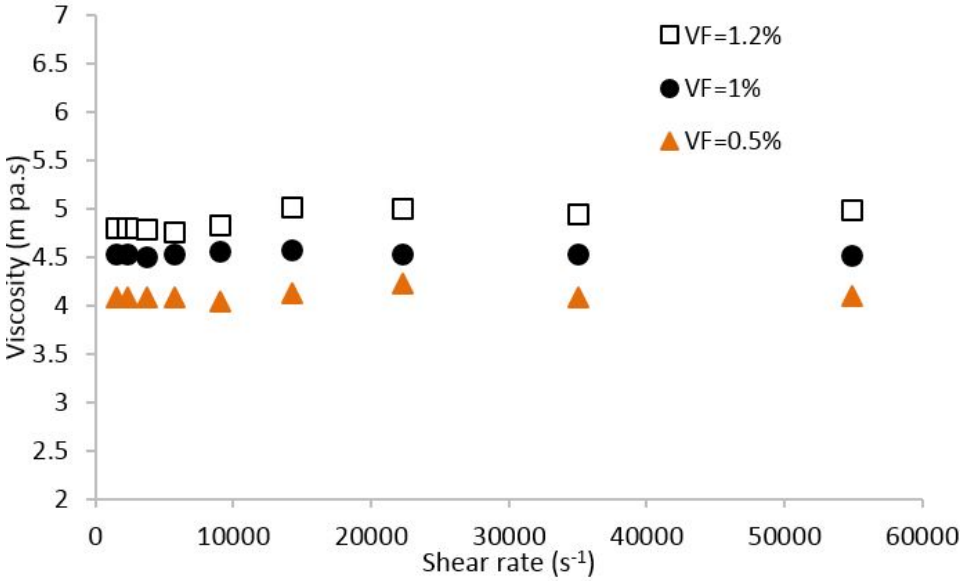


Figure 3.23: Relation between the viscosity and the shear rate of the acetone / 50% $ZnBr_2$ based on different concentration of ZnO at 20 ^oC.

Table 3.3: Empirical constants of the equation 3.8

Vol. Fraction	A	B	R^2
0	677.6	-0.017	0.999
0.01	704.16	-0.017	0.998
0.1	852	-0.018	0.997
0.3	914.64	-0.018	0.9959
0.5	773	-0.018	0.9974
1	378	-0.016	0.998
1.2	419.35	-0.016	0.999

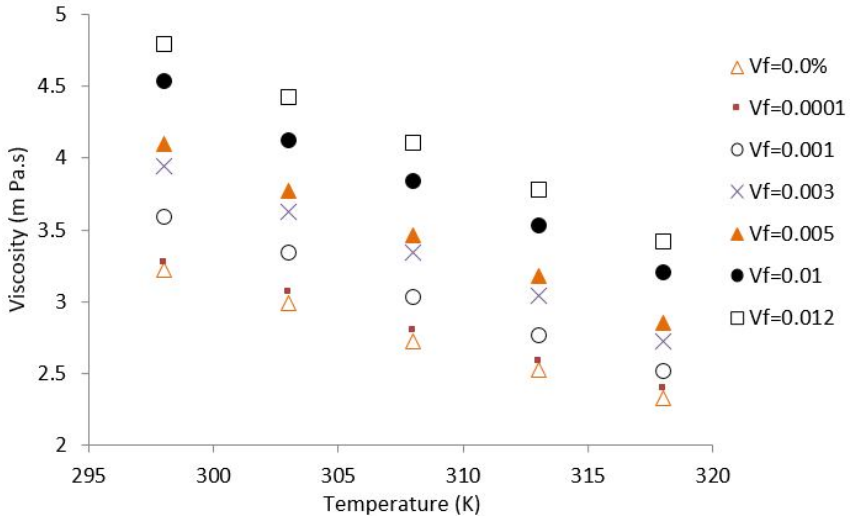


Figure 3.24: Relation between the viscosity of the nanofluid and the temperature for the different volume fraction of the ZnO nanoparticles.

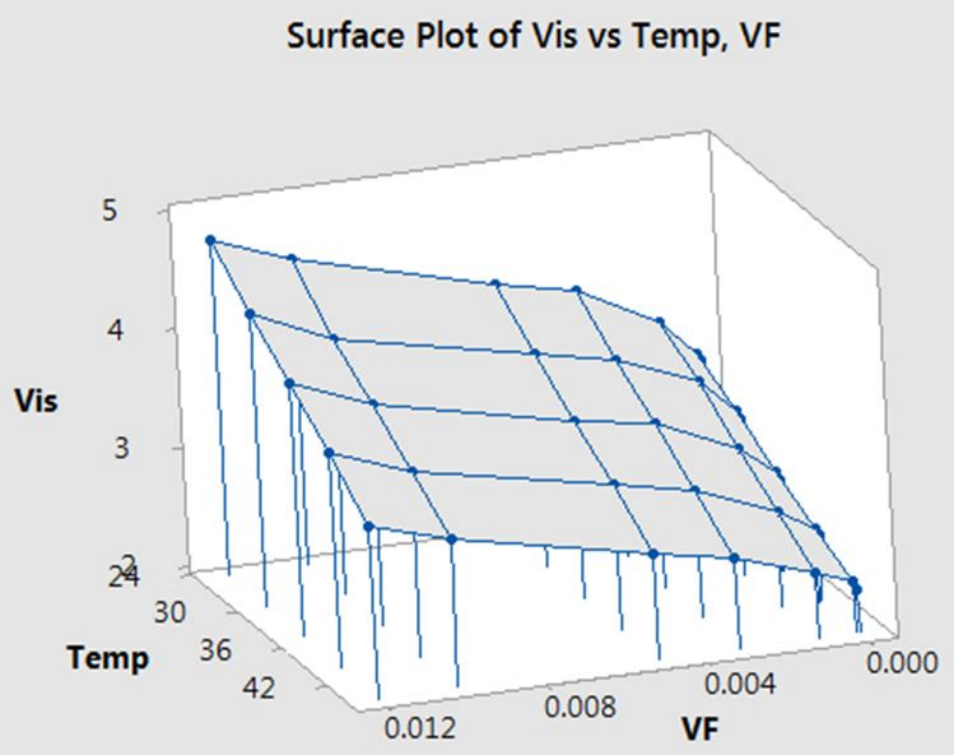


Figure 3.25: Three dimensional surface explain the relation between the viscosity (in m.Pa s), temperature (in Celsius) and the volume fraction.

3.4.3 Thermal Conductivity

There are several theoretical models and correlations which are commonly used to find thermal conductivity, as explained in section 2.2.3.4.

Thermal conductivity of the acetone-$ZnBr_2$ for different concentrations of $ZnBr_2$ in the solution (40 – 65 wt. %) was measured using the thermal conductivity analyser C-THERM TCI produced by C-THERM TECHNOLOGIES as shown in Figure 3.26. In this instrument, an amount of heat transfer is provided by applying a known current to the sensor (Modified transient plane source (MTPS)) heating element. A guard ring surrounds the sensor coil to guarantee the one dimensional heat transfer to the sample as shown in Figure 3.27 [163]. The temperature in the interface region between the sample and the sensor rises due to the current which causes a change in the voltage drop of the sensor element. The thermal properties of the sample are determined by the rate of increase in the sensor voltage. The thermal conductivity is inversely proportional to the temperature increasing at the region of contact between the sensor and the sample [163].



Figure 3.26: Modified transient plane source (MTPS) sensor a)taken from C-therm company website [163] and b) lab instrument.

It was found that the thermal conductivity of the solution decreases from 0.159 to 0.149 W/m.K with increasing concentration of $ZnBr_2$ from 40 – 65

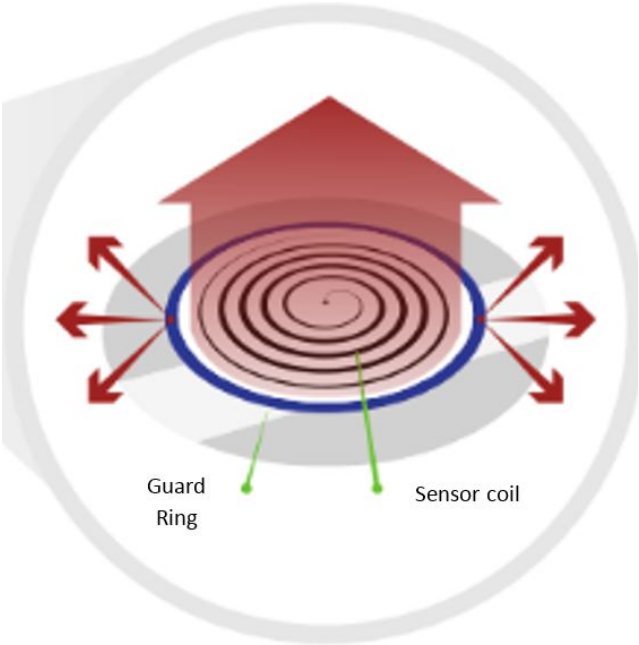


Figure 3.27: Illustration of how C-therm operation [163].

wt. % as shown in Table 3.4 and Figure 3.28. The thermal conductivity of the pure acetone and solid $ZnBr_2$ (salt) were measured separately by the same method and found 0.164 and 0.1 W/m.K respectively. The Table shows how the thermal conductivity of the salt solution decrease with increasing the concentration of the salt.

Table 3.4: Relation of the thermal conductivity with the concentration of the of $ZnBr_2$ in the acetone/ $ZnBr_2$ solution at 24 ^oC.

Concentration of $ZnBr_2$ wt.%	40	45	50	55	60	65
Thermal conductivity (W/m.K)	0.15927	0.15425	0.15242	0.15146	0.15053	0.14981

The solution of acetone /$ZnBr_2$ with 50 wt. % $ZnBr_2$ was converted to nanofluid with five different concentrations (0.1, 0.3, 0.5, 1, 1.2 vol. %). The thermal conductivity was measured after keeping these samples for 2 hours in the sonication bath. The thermal conductivity increases from 0.152 to 0.168 W/m.K when the concentration of the Zinc Oxide nanoparticles increased from 0 to 1.2 vol. %, this means that the thermal conductivity increased by 10.53%

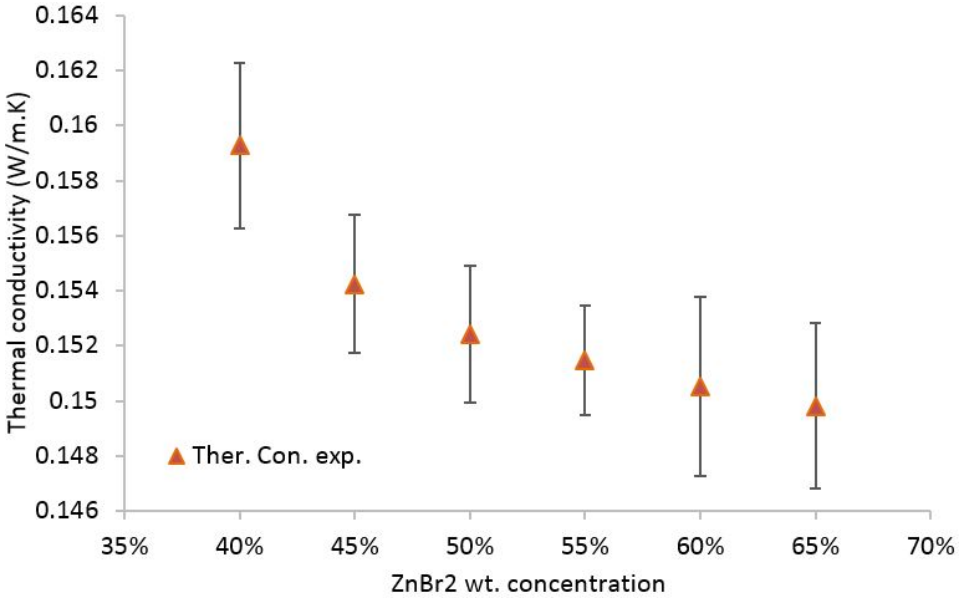


Figure 3.28: Relation between the thermal conductivity and the concentration of the $ZnBr_2$ in the acetone / $ZnBr_2$ solution at 20 ^oC.

as shown in Table 3.5. The enhancement in the thermal conductivity for the specific nanoparticles is mainly dependant on several parameters such as type of basefluid and the size of the particles. Table 3.6 shows how the improvement in the thermal conductivity differs in the nanofluid (based on ZnO) when the size and the volume fraction of the nanoparticles change.

Table 3.5: Thermal conductivity of the acetone/$ZnBr_2 - ZnO$ with increasing the concentration of nanoparticles.

ZnO nanoparticles (Vol. %)	Thermal conductivity (W/K.m)	Enhancement %
0	0.152	-
0.1	0.153	0.96
0.3	0.157	2.97
0.5	0.159	4.79
1	0.164	8.12
1.2	0.168	10.53

Table 3.6: Maximum enhancement in thermal conductivity for different nanofluid (based on ZnO) as found in the literatures.

Base fluid	Vol. fraction %	Size of particles (nm)	Enhancement	Ref.
EG	4	25 - 40	33.4%	[72]
EG - water	2	25 - 40	17.26%	[72]
EG	6	∼4.6	33%	[90]
EG	5	10 - 20	26.5%	[108]

Figures 3.29 and 3.30 present the relation between thermal conductivity and volume fraction of the nanoparticles for acetone/ 50 wt. % $ZnBr_2$ based on ZnO and acetone/ 60 wt. % $ZnBr_2$ based on graphene (because the graphene is more stable in higher $ZnBr_2$ concentration), respectively. They show also how the experimental results differ with the theoretical which are based on Maxwell 2.17 and Suganthi's models 2.20. Figure 3.29 shows that the thermal conductivity is proportional to the concentration of nanoparticles. The uncertainty for each case with and without nanoparticles are calculated depending on the uncertainty of measurement equation (half difference between maximum and minimum values). The maximum values of the uncertainty are 0.005 and 0.004 for the cases concentration of ZnO 0.1 vol.% and volume concentration of Graphene 0.1%, respectively (data shown in the Appendix Tables A.6, A.7 and A.8).

The experimental relationships compare well with the Suganthi model. The Maxwell model does not fit well. Figure 3.30 shows the behaviour of the thermal conductivity of the nanofluid based on graphene as a function of graphene concentrations. The trend lines of these relations show a polynomial relation which can expressed as:

ZnO

$$k = 9432.7\Phi^3 - 172.7\Phi^2 + 2.0573\Phi + 0.1518 \tag{3.10}$$

Graphene

$$k = -10^7\Phi^4 + 257649\Phi^3 - 1429.6\Phi^2 + 3.9131\Phi + 0.1506 \tag{3.11}$$

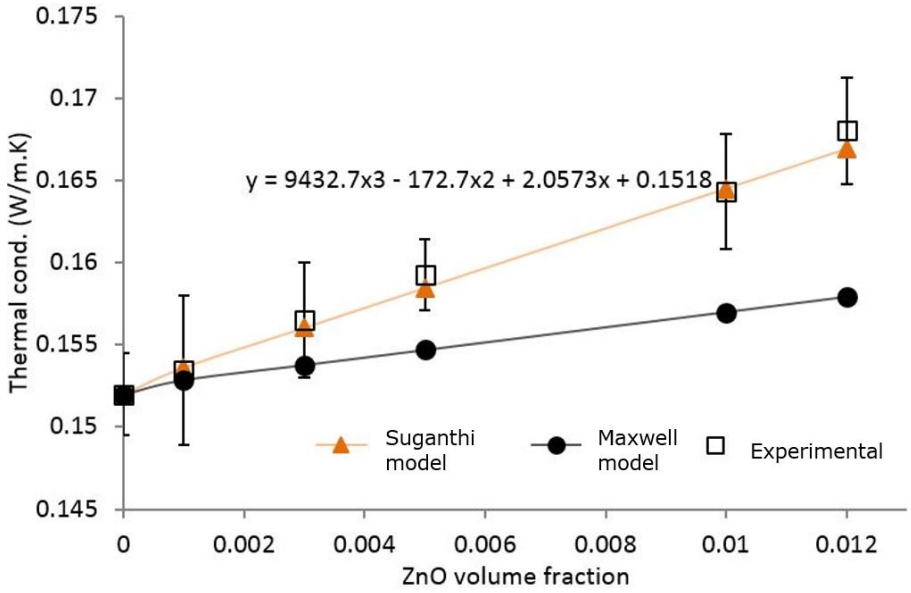


Figure 3.29: Experimental and theoretical (based on Suganthi [72] and Maxwell's [2] Models) relation between thermal conductivity of the acetone / 50% $ZnBr_2$ with different concentrations of ZnO nanoparticles at 20 ^oC.

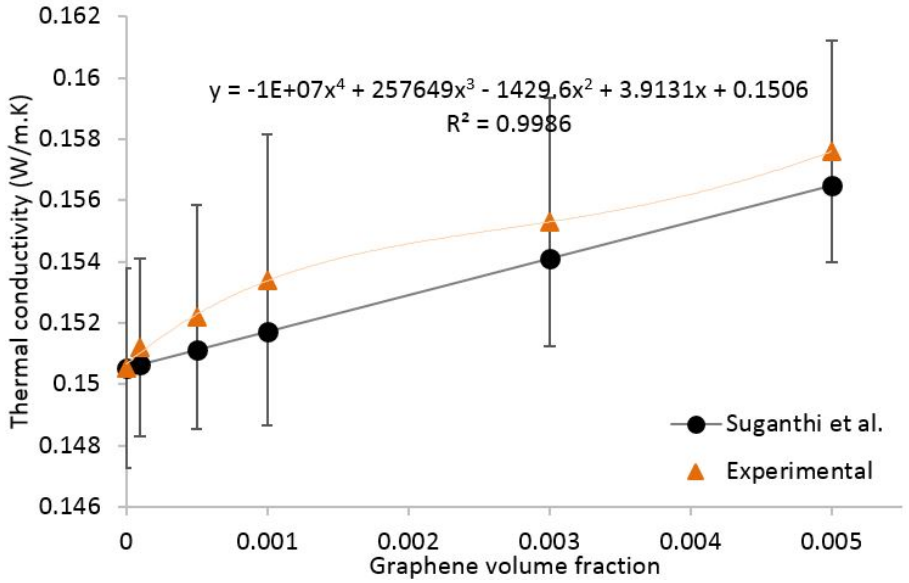


Figure 3.30: Experimental and theoretical (based on Suganthi model [72]) relation between thermal conductivity of the acetone / 50% $ZnBr_2$ with different concentrations of Graphene nanoparticles at 20 ^oC.

3.4.4 Specific heat capacity

Specific heat capacity is measured for acetone/$ZnBr_2$ with different mass concentrations of $ZnBr_2$ (40, 45, 50, 55, 60 and 65 wt. %) as a basefluid. It is also measured for this solution as a nanofluid, based on ZnO nanoparticles with different concentrations (0.1, 0.3, 0.5, 1 and 1.2 wt. %) and Graphene nanoplates with concentrations 0.01, 0.05, 0.1, 0.3 and 0.5 vol. %. A TA instrument Q10 Differential Scanning Calorimetry (DSC) was used which is a thermo-analytical technique in which the amount of heat needed to rise the temperature of a sample and a reference sample is measured as a function of temperature as shown in Figure 3.31. The measurement was done by heating up three pans shown in Figure 3.32 (crucibles (Al) (bottom) and DSC-lid (Al) (top)). The first pan is empty, the second one has a reference material in this case sapphire (α–Al_2O_3) used with known specific heat at different temperatures. The third pan contains the sample of the nanofluid. The specific heat of the samples was calculated through equation 3.12 which is found in the ASTM

international standard test method for determining specific heat capacity by DSC [164].

$$c_{p_s} = c_{p_{st}} \frac{l_s m_{st}}{l_{st} m_s} \tag{3.12}$$

Where c_{p_s} is specific heat of the sample, $c_{p_{st}}$ is specific heat of the standard sample, m_s is the mass of the sample, m_{st} is the mass of the standard sample (sapphire), l_s the difference of heat flow between the empty pan and the sample and l_{st} is the difference of heat flow between the empty pan and the standard sample. The difference of the heat flow can be found through Figure 3.33 which presents the relation between the heat flow and the temperature for the tested and standard samples.

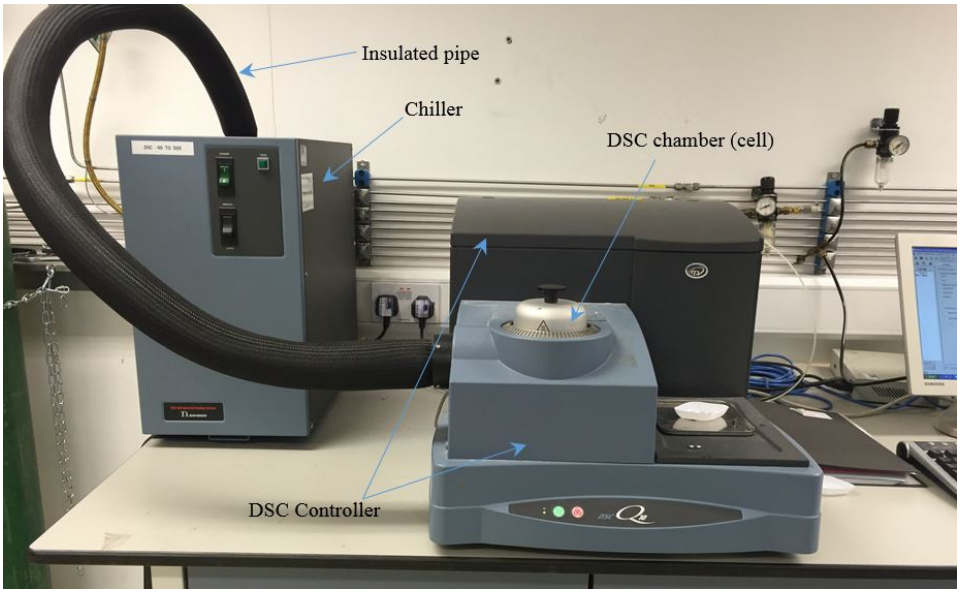


Figure 3.31: Differential Scanning Calorimetry DSC, which used to find a Cp for the acetone/$ZnBr_2$ based ZnO nanofluid.

Figure 3.34 illustrates an inverse relation between the heat capacity and the mass concentration of $ZnBr_2$. The Figure also shows that there are differences with results from literature [14], although, both results are found using the same technique (DSC). However, different models of DSC instrument may



Figure 3.32: Crucibles (Al) (bottom) and DSC-lid (Al) (top).

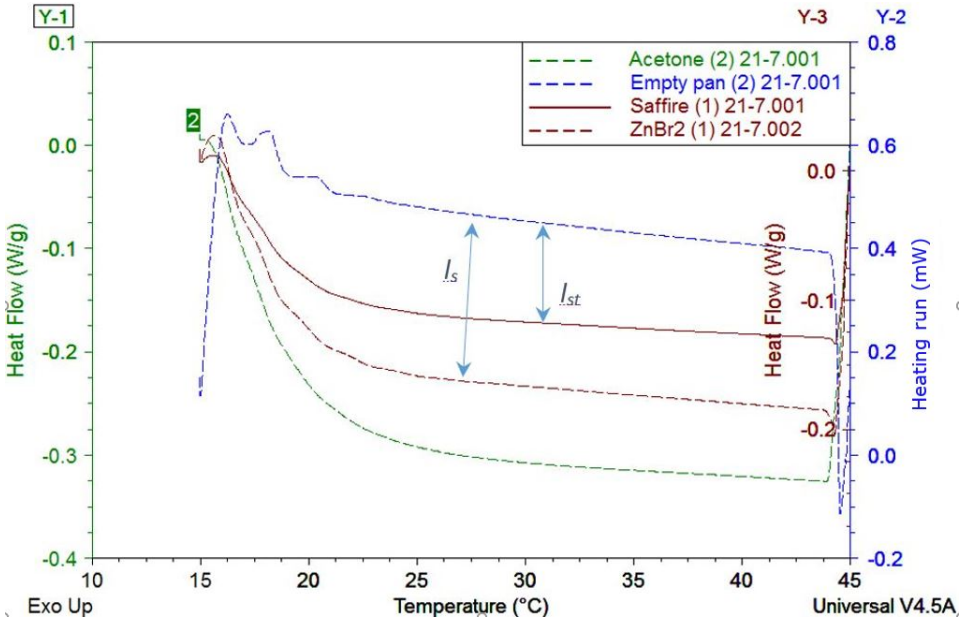


Figure 3.33: The DSC output graph of the relation of heat transfer and the temperature for the empty pan, standard sample sapphire and the test sample ($ZnBr_2$). This Figure should be printed in colour.

create this difference. Whereas, Ajib and Karno ([14]) used a DSC 7, however, a DSC Q10 is used in the current tests. Figure 3.35 shows that the specific heat capacity is inversely proportional with particles (ZnO) concentration because the specific heat of these particles is low (0.487 J/g.K) compared with the specific heat of the base fluid (1.14 J/g.K). Figure 3.35 also shows that the difference between the theoretical results found using equation 3.13 and the experimental results increase for a higher volume fraction. Equation 3.13 is a simple mixture method used for thermal analysis of the nanofluid [86, 93].

$$(c_p)_{nf} = (\frac{q}{m\Delta T})_{nf} = \frac{q_f+q_p}{(m_f+m_p)\Delta T} = \frac{(mc_p)_f\Delta T+(mc_p)_p\Delta T}{(m_f+m_p)\Delta T}$$

$$(c_p)_{nf} = \frac{(\rho c_p)_f V_f + (\rho c_p)_p V_p}{\rho_f V_f + \rho_p V_p} = \frac{(1-\Phi)\rho_f c_{p_f} + \Phi_p \rho_p c_{p_p}}{\rho_{nf}} \tag{3.13}$$

Also, the specific heat is measured for the acetone and solid $ZnBr_2$ and they were 2.12 and 0.329 J/g.K respectively, and which are 2.16 J/g.K and 76.21 J/mole.K (0.3384 J/g.K) in the literature [14, 165] respectively.

To convert 1 mole of $ZnBr_2$ to gram:

The molar mass for Zn = 65.38 g/mole and for Br = 79.904 g/mol.

Molar mass for $ZnBr_2$ = 65.38 + (2 × 79.904) = 225.188 g/mol.

c_p = 76.21 (J/K.mol) × 1/225.188 (mol/g) = 0.3384 J/g.K.

To check the validity of the specific heat measurement the sample with 1 wt. % ZnO was repeated 10 times. The average value of the specific heat was found to be 1.02 J/g.K with standard deviation 0.0895 and standard error equal to 0.0283. Furthermore, as for the other properties, the uncertainty is calculated using the uncertainty of the single measurement equation, the maximum uncertainty is 0.135 when the concentration of $ZnBr_2$ is 50 wt.% without nanoparticles and 0.065 when the concentration of Graphene is 0.01 vol.% (see the data in Tables A.9 and A.10).

The relation between heat capacity of the nanofluid and the volume concentrations of nanoparticles (Graphene) has been illustrated in Figure 3.36. It shows the same behaviour of the last nanofluid (acetone / $ZnBr_2$ – ZnO). The inverse relation appears between the heat capacity and the concentration of graphene as well as a difference between experimental results which show a polynomial relation (3.14) and those found by equation 3.13.

$$(c_p)_{nf} = 7 \times 10^7 \Phi^4 - 817492\Phi^3 + 3108.7\Phi^2 - 5.6325\Phi + 1.0198 \qquad (3.14)$$

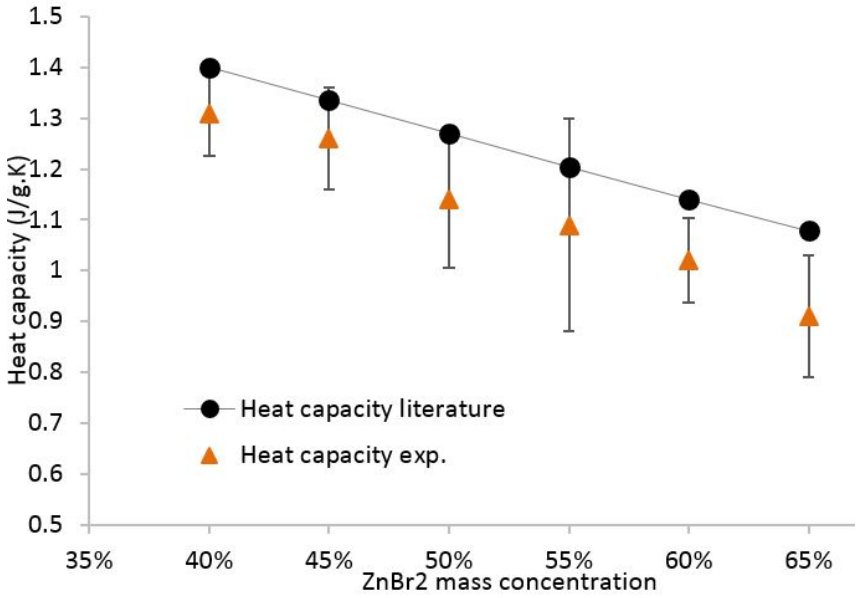


Figure 3.34: Relation between the specific heat capacity of acetone / $ZnBr_2$ with different concentrations of $ZnBr_2$ experimentally and compare with results from literature [14].

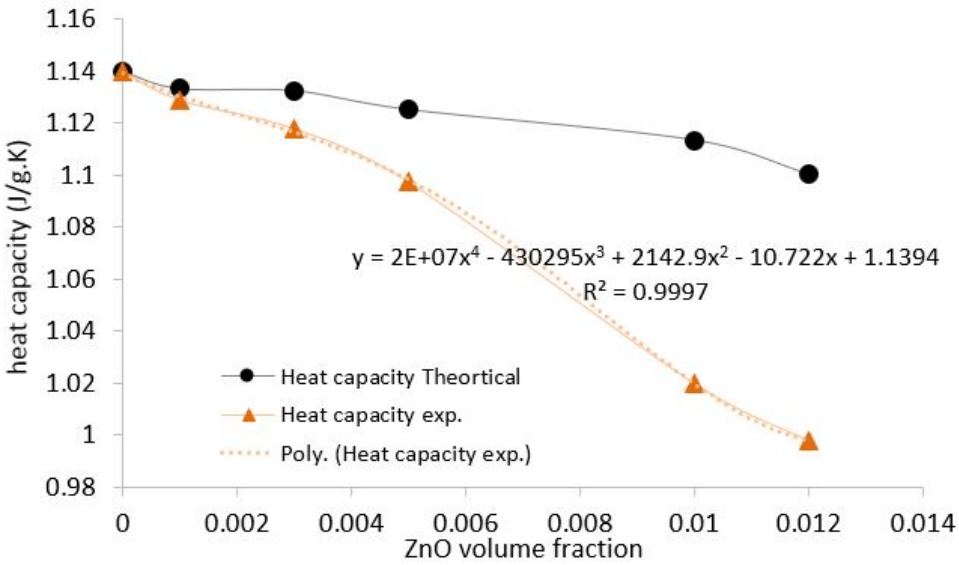


Figure 3.35: Relation between the specific heat capacity and nanoparticles concentration experimentally and theoretically (using equation 3.13) for the solution acetone/ 50% $ZnBr_2$ based ZnO.

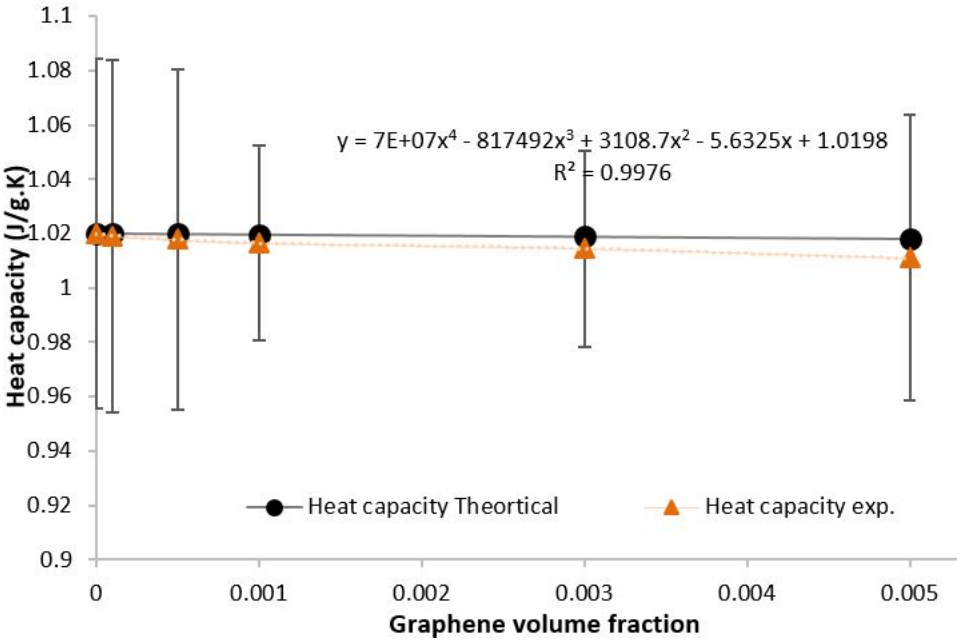


Figure 3.36: Relation between the specific heat capacity and nanoparticles concentration experimentally and theoretically (using equation 3.13) for the solution acetone/ 50% $ZnBr_2$ based Graphene.

3.4.5 The size of the nanoparticles

The size of the nanoparticle was measured using Dynamic Light Scattering (DLS) manufactured by Malvern Instruments. DLS is a technique used to measure the size (hydrodynamic diameter) of the particle in sub-micron scale, dispersed in a liquid. The measurement of the particle size is done through the Brownian motion which can be defined as a random motion of particles due to the effectiveness by the solvent molecules that surround them. The smaller particles are affected further by the surrounding liquid molecules and move faster than the larger particles. During the measurement, the temperature should be fixed because the viscosity of the liquid is related to the temperature. The size of the particle is calculated from translation diffusion coefficient using Stokes-Einstein equation [166]:

$$D_H = \frac{k_b T}{3\Pi\mu D} \tag{3.15}$$

Where

D_H is hydrodynamic diameter, D is translational diffusion coefficient (velocity of Brownian motion), k is Boltzmann Constant, T is temperature, and μ is dynamic viscosity of the liquid.

The diameter that is measured in a DLS technique is the diameter of a sphere particle that has the same transitional diffusion coefficient (velocity of Brownian) as the particle in the solution. The particle transitional diffusion coefficient depends on the size of the particle, surface structure which affects the diffusion speed, as well as the concentration and the type of electrical charge in the medium.

In DLS, the particle diffusion velocity caused by the Brownian motion is measured by determining how the intensity of the scattered light fluctuates

when detected using a suitable optical arrangement. The mechanism of the DLS is by illuminating a particle by a laser and the sample cell is viewed by using forced glass screen. A speckle pattern would be seen as shown in Figure 3.37. This pattern will be fixed both in particle size and location because the whole system is stationary. The dark patches appear when the phase additions of the scattered light are mutually destructive and cancel each other (Figure 3.38A). The bright patches of light in the particle pattern appears when the light scattered from the particles arrives with the same phase and interfere constructively to form a bright patch (Figure 3.38B) [166].

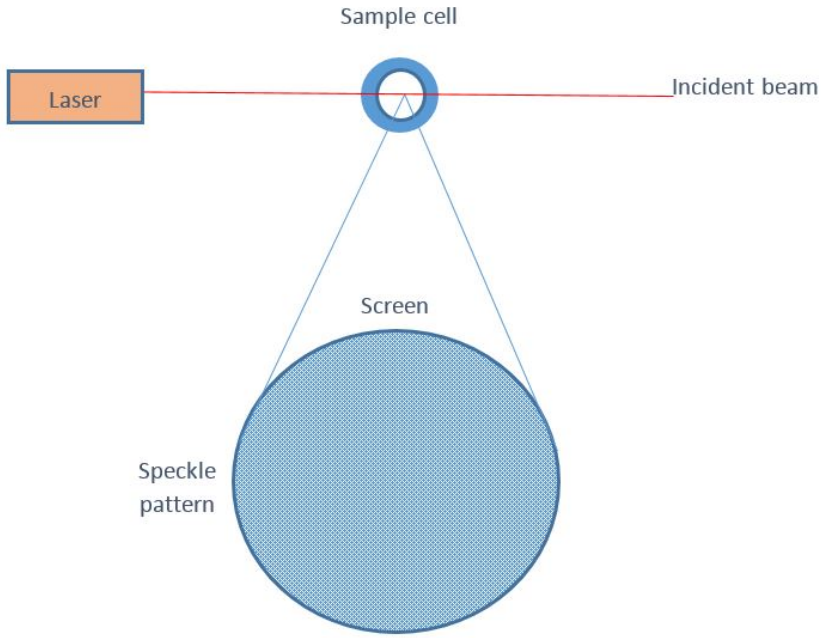


Figure 3.37: Schematic representation of the speckle pattern [166].

For the particles undergoing Brownian motion, a speckle pattern is detected and the speckles are in constant motion. This is because the new patterns are created due to the phase addition from the moving particles. The intensity of these patterns depends on the speed, and size of the particles.

Figure 3.39 schematically illustrates typical intensity fluctuations developed from a dispersion of large and small particles. The larger particles cause the intensity to fluctuate slower than the smaller particles. It could be mea-

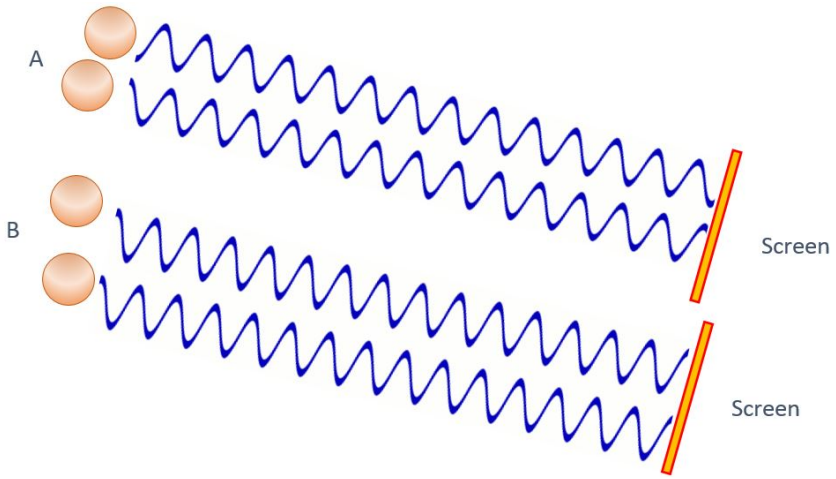


Figure 3.38: The observed signal bases on the phase pattern of the scattered light falling. A) two beams with opposite phase makes the outcome zero intensity detector. B) two beams with the same phase and enhance each other resulting in the sum of the intensity detector [166].

sured from the spectrum of frequencies contained in the intensity fluctuations developing from the Brownian motion of particles, but it is inefficient to do that. The best way is to use a digital auto correlator instroment [166].

The particle size was measured using Dynamic Light Scattering DLS at 25 ^oC for two samples of acetone/$ZnBr_2$ based on 0.1 vol. % and 1.2 vol. % ZnO respectively and two samples of acetone/$ZnBr_2$ based on 0.1 vol. % and 0.5 vol. % graphene. For all the samples, the scattered angle of the laser line is 173^o (forward incident). It was found that the size of the particle in dilute concentration (0.1 wt. % ZnO) solution is 8450 nm (8.45 μm) and it is 22800 nm (22.8 μm)for the high concentration (1.2 wt. % ZnO), however, for graphene was 23.54 μm and 35.41 μm for the diluted and the high concentration, respectively. All sizes are caused by particle agglomeration and they are very large compared with the nanoscale particles size. The differences between these sizes is caused by the distance between the particles in the solution. In the high concentration solution, the particles are close to each other and they have a higher chance of gathering and creating large particles. However in the dilute solution the distance between the particles is relatively bigger, and the

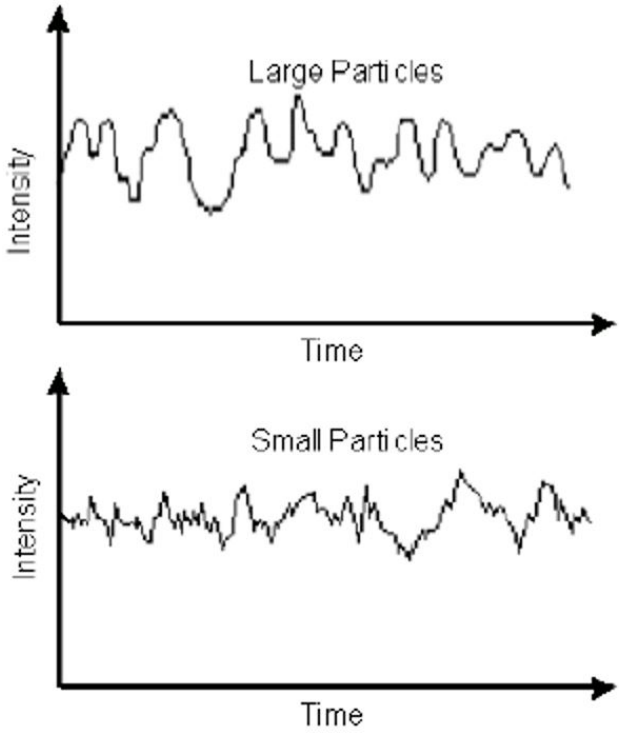


Figure 3.39: Typical intensity fluctuations for the large and small particles [164].

particles have a low opportunity for gathering. These results show that the agglomerating rate for the ZnO is higher than the graphene, which explains that the shapes of the particles also has an impact on the agglomeration.

The velocity of the particles (free fall velocity) in the stationary solution can be calculated by Stokes law (equation 3.16):

$$\nu = \frac{{D_H}^2}{18\mu}(\rho_p - \rho_l)g \tag{3.16}$$

Where ν is the terminal velocity of the particles, ρ_p is the density of the particles, ρ_l is the density of the base-fluid, g is gravitational constant and μ is the viscosity of the base fluid. Using equation 3.16 to calculate the velocity of the particles in the solution, the velocity will be 5.11×10^{-8} m/s for dilute concentration and 3.726×10^{-7} m/s for a higher concentration solution thus particles will need 11.3 and 1.55 days respectively, to totally settle in the bottom of the 5 cm long bottle.

The distance between the nanoparticles in the base-fluid depends on the stability of the nanofluid and the size and concentration of the nanoparticles. By assuming stability state of the nanofluid, the distance is calculated by calculating the empty spherical space around each nanoparticle. By introducing the volume of the single nanoparticle and the concentration, the volume of the nanoparticles and the number of the nanoparticles in the 1 litre sample can be calculated. The spherical space around each nanoparticle has been calculated depending on the number of the nanoparticles and the sample size. The distance between two particles is found to be equal to double the spherical space radius. Table 3.7 below shows the number of the nanoparticles and the distance between them in one litre basefluid.

Table 3.7: Suggested numbers and distances between the graphene and ZnO nanoparticles with the different concentration

	Graphene (6-8 nm x 5 μm)		ZnO (D=50nm)	
Concentration	Number of nanoparticles $\times 10^{16}$	Distance (nm)	Number of nanoparticles $\times 10^{16}$	Distance (nm)
1%	1820	47.2	1.91	464
0.5%	910	59.4	0.955	584
0.3%	546	70.5	0.573	693
0.1%	182	102	0.191	1000
0.05%	91	128	0.0955	1260
0.01%	18.2	219	0.0191	2154

3.4.6 Do the nanoparticles transfer with the vapour during the boiling?

Because of the tiny size of the nanoparticles and the low density of the graphene, there is a question raised: do the nanoparticles transfer with the vapour during the boiling? To answer this question, an experiment was done. The idea of this experiment was: vigorous boiling of a nanofluid with a high temperature, condense the generated vapour by a condenser then collect the condensed sam-

ple in another flask and check for any graphene transfers. The equipment used in this experiment are:

- Flask 100 ml with two necks (to boil the nanofluid solution).
- Flask 50 ml (to collect the condensed acetone).
- Glass Liebig condenser.
- Heater (EMA Heating and Stirring Electromantles (EMA0250/CEB 250ml – $T_{max} = 450^oC$)).
- Digital thermometer.
- Two stands to hold the flasks on.

The description of the rig is as follow:

The big flask is held in a stand and put on a heater (without contacting the hot metal grid of the heater). One neck of the big flask is connected to a side of the glass condenser by a connector adapted for the purpose to bend downwards into the flask; the other side of the condenser is connected to the collection flask which is supported by the other stand through a standard connection. The condenser is cooled by tap water through a plastic pipe. The thermometer sensor is passed through a rubber bung in the other neck of the big flask into the solution as shown in Figure 3.40.

Two types of nanofluids are tested acetone – Graphene and acetone/$ZnBr_2$ – Graphene. When the heater is turned on the temperature of the solution increases gradually and starts to boil at 56 ^oC, while the acetone/$ZnBr_2$ – graphene boiled at 58 ^oC. The temperature increased till 100 ^oC to generate a strong boiling, implying a vapour pressure of about 3 bar gauge. The generated vapour condensed in the condenser due to the temperature difference between the wall and the vapour. Because of the inclined position of the condenser, the condensed acetone moved to the collection flask. The collected acetone was

left for two hours (enough time to settle the graphene, just in case there are a very small amount of the particles transferred) and it was quite clear, showing acetone without particles as shown in Figure 3.41.

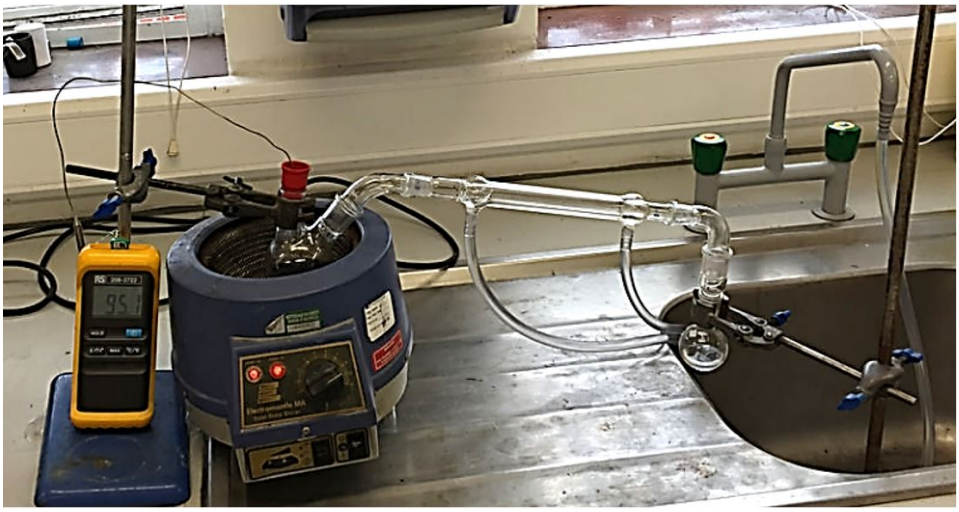


Figure 3.40: Rig of evaporation and condensation of nanofluid, used to check the possibility of transferring a nanoparticles with a vapour during the boiling.

.

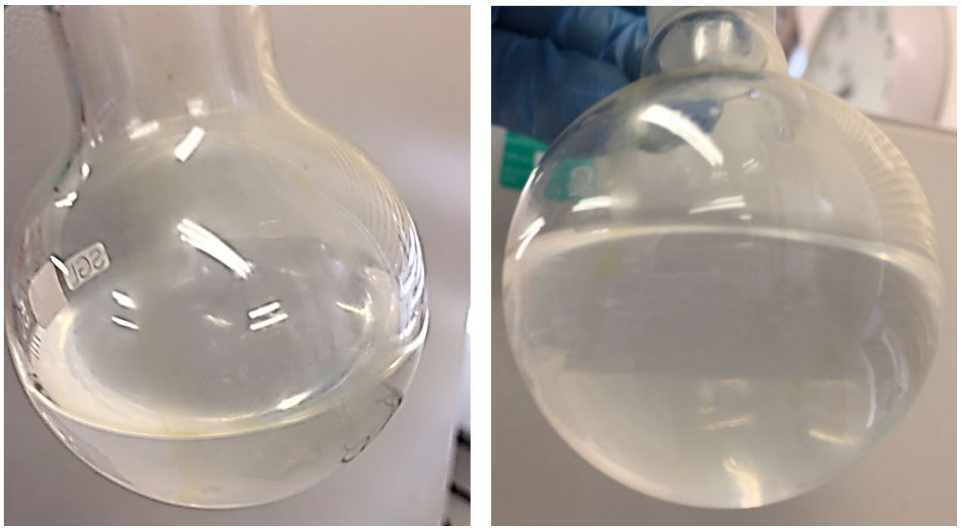


Figure 3.41: A clear acetone collected from the condensation of acetone vapour, which confirm that there are no nanoparticles transfer with a vapour during the evaporation or boiling processes of nanofluid.

3.4.7 Summary

In this Chapter, different aspects of a novel solution consisting of dissolved salt in refrigerant, mixed with nanoparticles which is described as nano-binary fluid or nano-salt-fluid were studied, including preparation and different properties. The solution which was acetone $/ZnBr_2$ based on different concentrations of ZnO and graphene nanoparticles was prepared with the two steps technique. This solution is recommended as a promising liquid for the absorption refrigeration system, and this study aims to investigate the potential for improvement in thermal properties of the nanofluid. The main findings from this part of work can be summarized by the following points:

1. $Acetone/ZnBr_2$ changes colour to brown under effects of light and heat.
2. The high concentrated nanofluid sedimens faster than the dilute nanofluid.
3. The surfactants (PVA, PVP and SDS) have insignificant impacts on improving the nano-binary-fluid.
4. The probe sonication have better effects than the sonication bath for enhancing the stability.
5. The density of the basefluid has a significant effect on the stability of the nanofluid. With a concentration of 65 % $ZnBr_2$ which makes the solution dense (1550 kg/m^3), the liquid stays stable for 48 hrs.
6. The density of the solution increases as the concentrations of the salt or nanoparticles increase.
7. A considerable difference is found between the experimental density and those in the literature due to the error in the methodology used in the literature.
8. Viscosity of the solution increases with increasing the concentration

of the salt or the nanoparticles.

9. A reverse relationship was observed between the temperature and the viscosity.
10. The nano-salt-fluid prepared shows a Newtonian behaviour depending on a wide range of shear rate.
11. The thermal conductivity of the pure solution drops from 0.159 to 0.149 W/m.K with increasing the salt concentration from 40-65 wt.%.
12. The thermal conductivity of the nanofluid increases by 10.5% and 4.6%with increasing the concentration of the ZnO from 0 to 1.2% and graphene from 0-0.5%, respectively.
13. The heat capacity decreases with increasing the salt or the nanoparticles concentrations.
14. The agglomeration size caused by ZnO is bigger than those caused by graphene, whereas, the agglomeration size affected by the concentration and the type of the nanoparticles. the particle size become $8.48\mu m$, $22.8\mu m$, $23.5\mu m$ and $35.4\mu m$ when the volume fractions are 0.1% ZnO, 1.2% ZnO, 0.1% graphene and 0.5% graphene.
15. The nanoparticles stay with the liquid phase and not transfer with the vapour even during strong boiling.

4

EXPERIMENTAL STUDY OF FLOW BOILING IN THE VARS

4.1 Introduction

This chapter describes the high pressure part of the VAR system test rig and investigates the performance of the working fluid. The rig evaluates the heat transfer improvement in the boiler side of VARS by use of nanofluid instead of the normal binary fluid, which is acetone/$ZnBr_2$ in this case. Flow rate, temperature and the concentration of the nanoparticles are varied to observe the heat transfer and the fluid flow characteristics. The tests validate the results of new numerical method for modelling part of this work, which simulates the boiling of the salt-nanofluids, in order to justify the use of the CFD as a design tool for VARS. In this chapter:

- The rig description section presents the combination of the test rig together with the aid of a diagram and plots describing the process of the experiment and test rig. It includes also the combination of the working solutions of the VARS.
- Results section to present the outcomes of the test campaign and offer explanation for the observations in the experiment.
- Conclusions section to present the main outcomes of this experimental work.

4.2 Rig description

The test rig, is described in Figures 4.1 - 4.5. Figure 4.1 and 4.2 illustrate overall layout, Figure 4.3 and 4.4 show the micropump and the controller and Figure 4.5 shows the boiler. The rig comprises of the following components as illustrated in Figure 4.1:

1. 1 litre loading (weak solution) reservoir (WSR).
2. A R400BL conical revolution micropump (made by TCS Micropumps Company), which is controlled by a pulse width modulation flow rate controller which, transports the weak soloution (WS) from the WSR to the boiler via an EPDM rubber tube (made by fisher scientific) which is chemically compatible with the acetone/$ZnBr_2$ solution.
3. Boiler consists of a 250 W strip heater (15 cm length) fixed to the flat plate heat exchanger on the lower face of the rectangular boiler channel; K-type thermocouples equally spaced by 3 cm are inserted from the top surface of the channel position at 5 locations and extend to the midway in the height of the boiler channel as shown in Figure 4.5.
4. The temperature of the boiler is controlled via a PID controller type Omega (CSi8D series).
5. After the boiler, the strong solution (SS) with the acetone vapour (refrigerant) passes to the SS reservoir (SSR) with Dreschel head on top to separate the refrigerant from the SS.
6. The refrigerant passes to the condenser (Liebig condenser) which is cooled by tap water (flow rate =26 g/s).
7. The condensed refrigerant is collected in the refrigerant reservoir (RR).

8. Both the refrigerant and the strong solution reservoirs are ended by valves at their bases. The ends of the last two reservoirs are connected with the WSR using a three way connector.

Thermocouples are connected to the rig as described below:

- 5 thermocouples measure the temperature of the flow solution in the boiler (T1-T5).
- 1 thermocouple measures the temperature of the boiler wall from bottom for the heater control through the PID (T6).
- 1 thermocouple measures the temperature of the solution at the exit of the boiler (T7).
- 1 thermocouple measures the temperature of the solution at the entrance to the condenser (T8).
- 1 thermocouple measures the temperature of the tab water (T9).
- 1 thermocouple measures the temperature of the pump surface (just for cases of nanofluid) to check the pump temperature during the process (T10).
- 1 thermocouple measures the temperature of the refrigerant at the exit of the condenser (T11).
- 1 themocouple measures the temperature of the strong solution at the exit of SSR (T12).

The thermocouples are sealed with graphite ferrules into Swagelok unions. A GE unik 5000 pressure sensor (0-3 bar absolute) measures vapour pressure between the S.S reservoir and condenser via Swagelok unions. The Swagelok unions are connected to the glass fittings using EPDM rubber tube and o-clips. All thermocouples are connected to the National Instrument (N.I) type TC (NI 9213) and the pressure sensor connected to TC (NI 9219). The N.I interface is connected to the P.C. The flow rate of the micropump is controlled through

the on-board potentiometer on the controller provided by TCS Micropumps Company as shown in Figure 4.4.

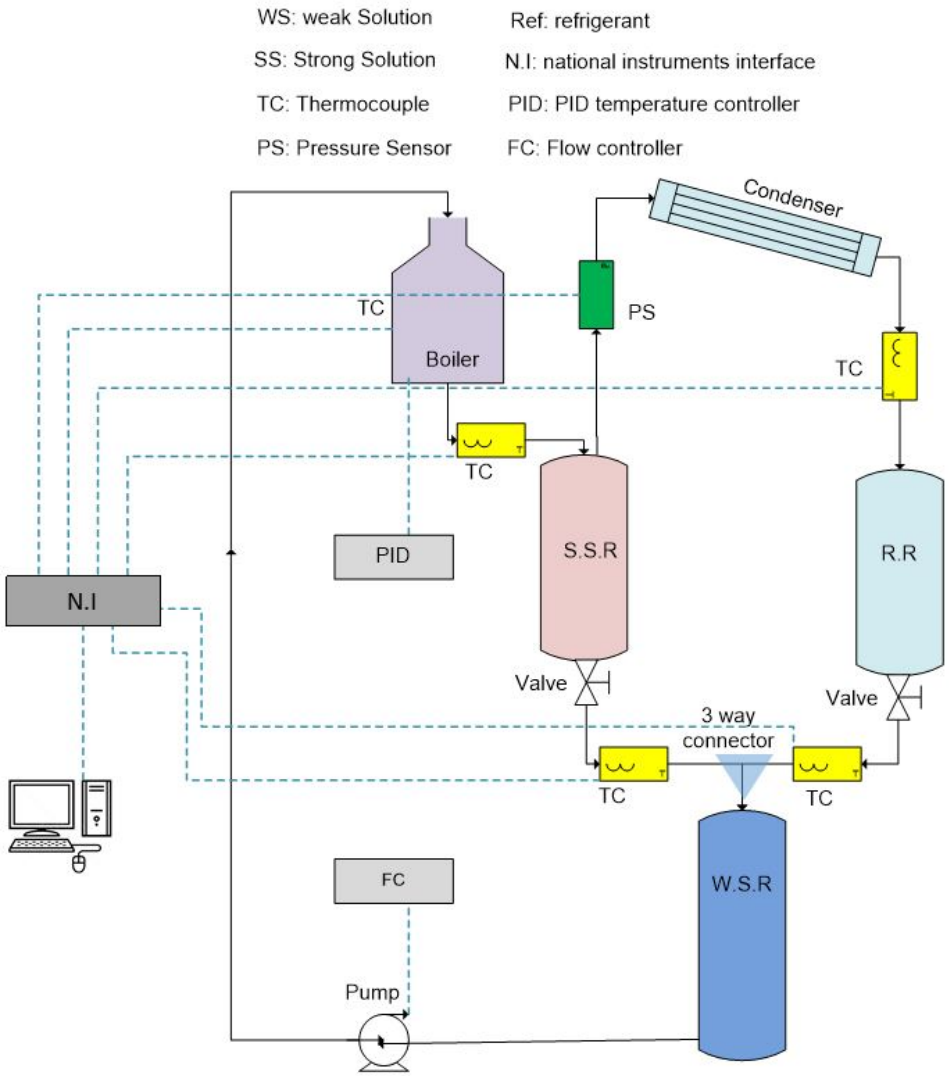


Figure 4.1: Equipment schematic of the high pressure side of the VARS.

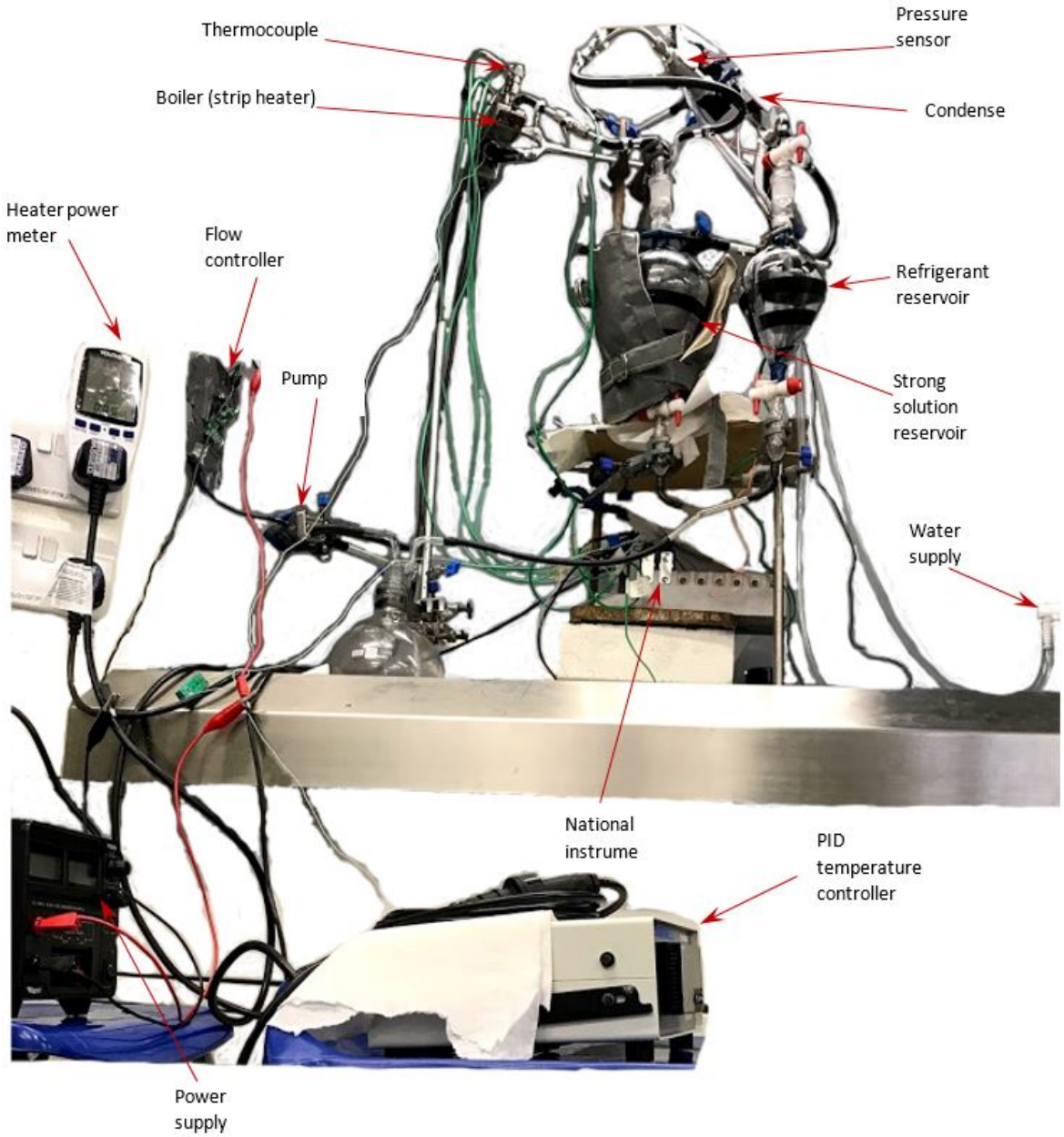


Figure 4.2: Photo of the high pressure part of the vapour absorption refrigeration system experimental test rig.

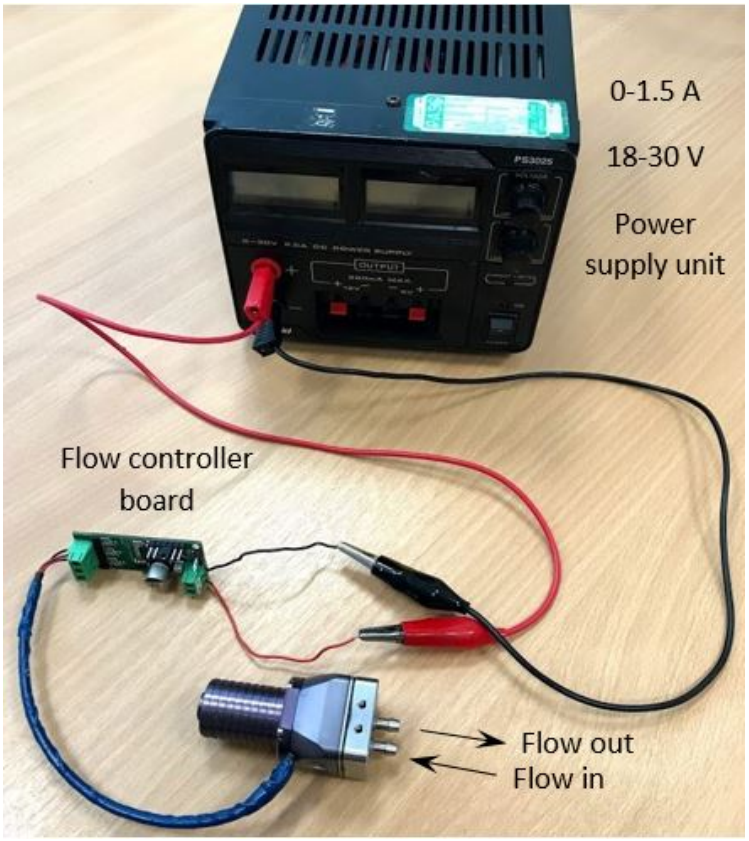


Figure 4.3: The feeding system of the absorption refrigerator experimental test rig, shows the power supply, the Micropump (R400BL) and the flow controller.

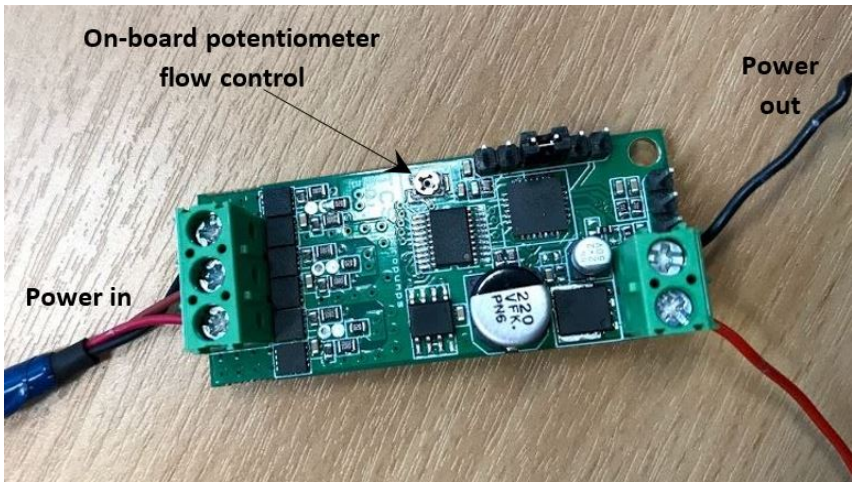


Figure 4.4: The flow controller provided by TCS Micropumps Company. Input Voltage 12-30 V(dc), Flow can be controlled via an on-board Potentiometer. Or a 0-5 V signal and Operating Temperature 0 - 80 ^oC.

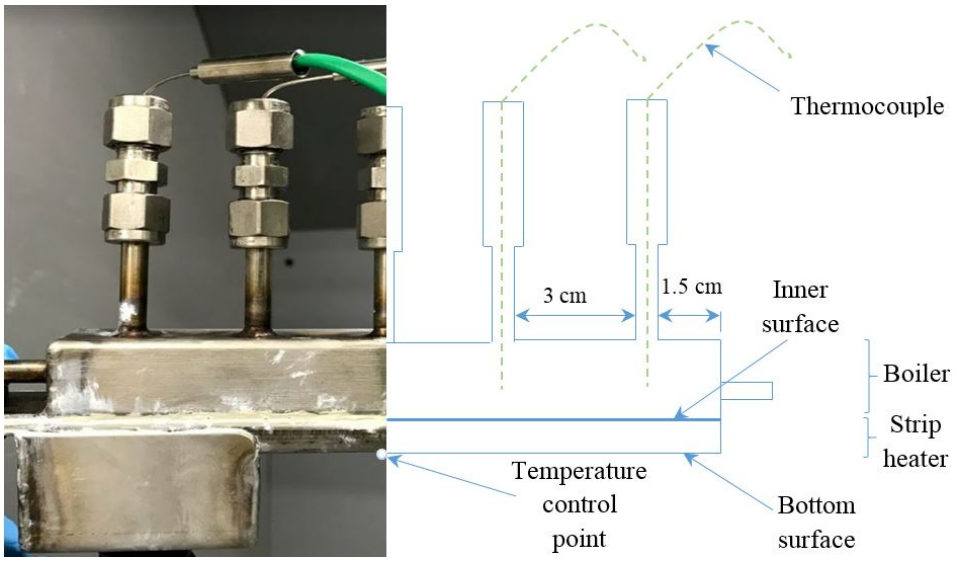


Figure 4.5: Strip heater and boiler used in this experiment. Type Caloritech, 250 W.

4.3 Experimental procedure

Acetone / $ZnBr_2$ with 50 wt.% $ZnBr_2$ is prepared by dissolving 500 g of $ZnBr_2$ into 500 g of acetone which make 0.734 litres depending on the measured density of 1362 kg/m^3. Tests on effects of boiler temperature and flow rate were conducted and after each test, the rig was flushed with acetone. The density of the solution is checked in case of acetone evaporates through the joints or some salt crystallises in the joints. In the cases that density differed from the original density prior to test, less than 5 ml in each case of acetone was added to the solution. After base fluid tests, a new sample of acetone / $ZnBr_2$ with the same volume (0.734 L) is prepared to make up a nano-salt-fluid sample with the identical formulation of base fluid.

According to the density of graphene (1800 kg/m^3) and the volume fraction of the nanoparticles loading required, a quantity of the nanoparticles were mixed with the basefluid. For example in case of 0.1 vol. %.

$$0.734 \times 10^{-3} m^3 \times 0.001 \times 1800(\frac{kg}{m^3}) = 0.00132kg(1.32g)$$

Adding this amount of nanoparticles to the solution has insignificant influence on the total density. It is not possible after each test to find if there is loss of nanoparticles from the solution which may adhere the joints or on the pipe's walls or settle somewhere in the reservoirs. The solution is sonicated before each test with a probe sonication for 30 minutes to break the agglomerations and after each test acetone was used to flush the rig to remove any residual salts and nanoparticles.

After preparing the working fluid (acetone / $ZnBr_2$ with different concentration of nanoparticles), the solution is loaded to the weak solution reservoir (WSR) and all connections checked. The pump is operated without the boiler being heated to measure the flow rate of the system by collecting the solution in the SSR for several volume levels (the SSR is marked for different levels showing different volumes). The flow rate is controlled through the potentiometer on the controller to get each specific flow. The temperature of the bottom plate of the heater is controlled also by the PID controller.

The solution is passed through the pump from WSR to the boiler, where it starts to boil. Acetone vapour (refrigerant) is generated, then both the solution and the refrigerant pass into the SSR. The refrigerant filling all the empty space in the SSR as it expands and pushes the air (in the rig before operating) to the condenser and the refrigerant reservoir (RR). By increasing the vapour in the rig, the pressure increases. Because of accumulation of the cold air (non condensable gas) in the system, the refrigerant can not condense in the condenser. To extract the air, the join between the condenser and the RR is opened and closed quickly when the pressure reaches around 1.3 bar. When the join opened the pressure decreases, and after closing the join, more vapour is generated which increases the pressure again to 1.3 bar. The join is opened and closed again to extract more air. At the third time, all the air

is expelled out and just a warm refrigerant is still in that part of the rig as vapour. The condenser then starts to condense the refrigerant effectively see Figure 4.6. The temperature of the flow in the condenser is rapidly increase to the saturation temperature. After that the pressure of the system stabilizes when the condensation and the boiling rate equalize. The condensing rate is calculated by measuring the flow rate of the refrigerant which collects in the RR in the same way that the flow rate into the boiler is calculated depending on collecting the SS. Both the SS and the refrigerant mix again in the 3 way connector to produce a WS which is collected in the WSR then the process is continued.

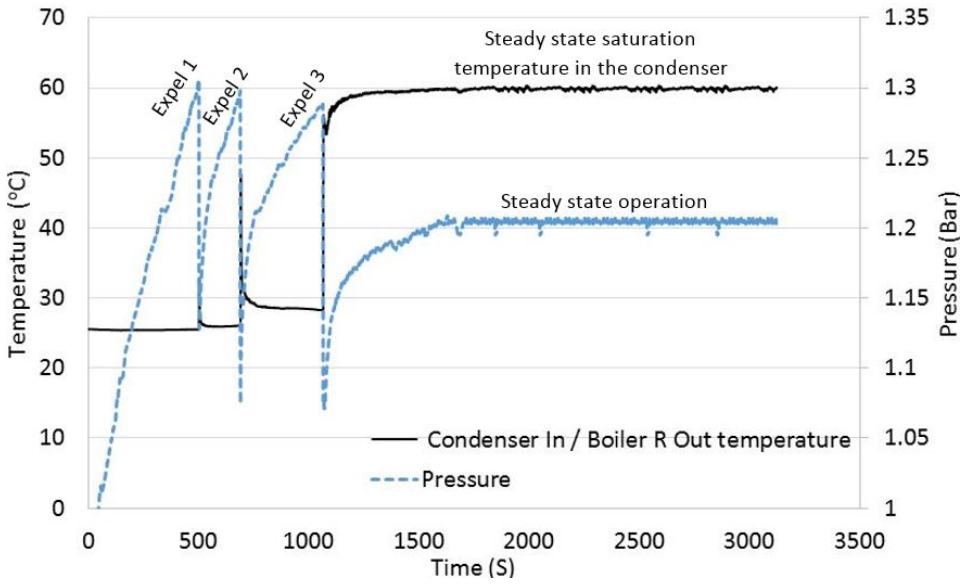


Figure 4.6: The temperature of the condenser and the pressure of the system as a function of time. In case (flow rate 3.6 ml/s, 180 ^oC and 0 concentration of nanoparticles).

4.3.1 Controlling the boiler temperature

The temperature of the boiler is controlled by the PID temperature controller, which has a thermocouple connected to the bottom surface plate of the heater as shown in Figure 4.5. The PID controls the temperature of the point that connects to within 6-8 ^oC. For example when set on 180 ^oC, the power turns on when the temperature reaches 178 ^oC and cuts off when it reaches 182 ^oC, but because of the thermal capacity of the boiler, its temperature reaches to 186 ^oC before starting to cool down. So, the bottom surface temperature of the boiler varies between 178 and 186 ^oC. The outer bottom surface is different to the inner surface of the boiler that is in contact with the flow as shown in Figure 4.5. To measure the difference between them, a separate test checked the temperature of the bottom surface and measured the temperature of the inner surface, by extending one of the thermocouples to touch the inner surface and record the data. In each case both temperatures are measured with time and the difference in average recorded temperature at the stable situation is calculated by $(T_{lower-sur} - T_{inner})$, it was found that the difference varies depending on the lower surface temperature. But it settles after 180 ^oC on 27 ^oC difference as shown in Figure 4.7. Each case was repeated 5 times to get better accuracy. The error bars calculated for each case as a half difference between the maximum and minimum values representing uncertainty in the measurement. For example, in the 180 ^oC case, the minimume and the maximum temperature difference between the bottom surface and inner surface were 29.1 ^oC & 26.1 ^oC. Figure 4.8 shows how the temperature difference varied with time between the two surfaces.

The saturation temperature of the pure acetone or even salted acetone is below 72 ^oC, however, the solution needs to heat up till 180 ^oC to give a good results presented by a sufficient generation rate of acetone vapour, which be

enough to keep the rig work sustainability.

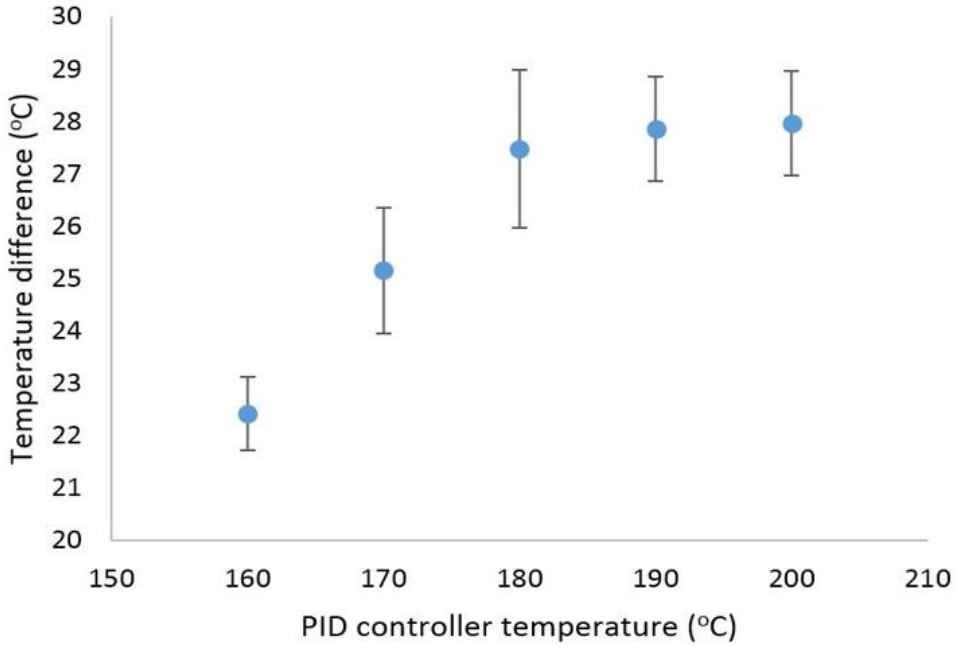


Figure 4.7: Temperature difference between the bottom and the inner surface of the boiler.

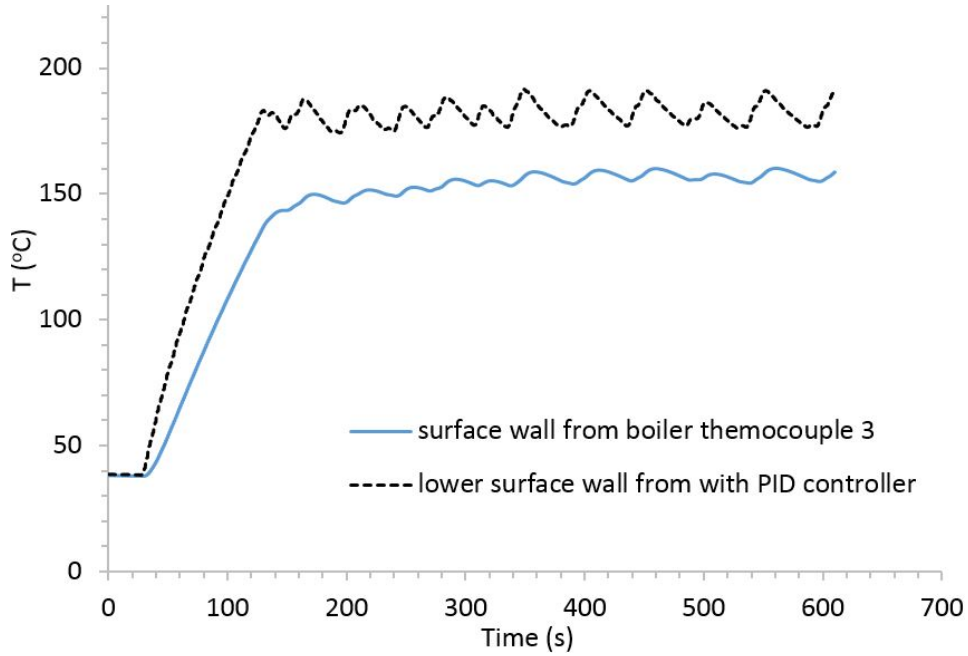


Figure 4.8: Difference between the temperatures of the controlled surface in the boiler inner surface (adjacent with the solution) in the specific time (PID set on 180 ^oC).

4.3.2 Calculation and measurement of the flow rate and heat transfer parameters

The outcome from the experiment, was assessed by heat flux, heat transfer coefficient, Rohsenow correlation constant, viscosity of the nanoparticles cloud, electrical power to heater and the concentration of the salt and the nanoparticles in the solution.

Flow boiling heat transfer is complicated and difficult to correlate as it depends on two effects, the bubble creation within the flow near the heated surface and the convection of liquid over the surface. There are no general correlations for flow boiling. The heat transfer rate combines two sources, nucleate boiling and forced convection as shown in equation 4.1 [128]:

$$q^{"} = q^{"}_{w} + q^{"}_{c} \tag{4.1}$$

Where $q^{"}$ is over all boiling heat transfer, $q^{"}_{w}$ is the nucleate boiling heat transfer and $q^{"}_{c}$ is single phase convection boiling heat transfer.

The nucleate regime boiling is calculated using the most successful correlation used by many researchers such as [167] and [168]. This correlation was developed by Rohsenow (equation 4.2) and it applies on clean smooth surfaces and depends mainly on the properties of the fluid as well as a constant C_{sf} referred to as the Rohsenow constant which depends on the particular fluid interaction with the surface.

$$q^{"}_{w} = \mu_l h_{fg} [\frac{g(\rho_l - \rho_v)}{\sigma}]^{0.5} [\frac{c_{p,l}(T_w - T_{sat})}{Pr_l C_{sf} H_{fg}}]^3 \tag{4.2}$$

μ is the viscosity, h_{fg} is latent heat, σ is surface tension, C_{sf} Rohsenow constant (dimensionless) and H_{fg} is enthalpy.

The C_{sf} of acetone / $ZnBr_2$ on stainless steel (boiler metal) is unknown.

C_{sf} found depending on the equation 4.2 using the electrical power input for all the cases (different flow rate and different wall temperature) and the average C_{sf} was calculated which equals to 0.217. Table 4.1 shows all values of the C_{sf} as found based on experiments.

Table 4.1: The values of the C_{sf} at different flow rate and wall temperature.

Flow rate (ml/s)	C_{sf}	Temperature (^oC)	C_{sf}
2.31	0.21	160	0.177
3.35	0.217	170	0.198
3.66	0.2155	180	0.217
4.27	0.22	190	0.239
7.1	0.222	200	0.255
Average	0.217	Average	0.217
Total average		0.217	

The single phase heat flux $q_c^{"}$ was found by ([128])

$$q_c^{"} = h_c(T_w - T_m) \tag{4.3}$$

$$h_c = \frac{Nuk}{d} \tag{4.4}$$

$$Nu = 0.019Re^{4/5}Pr^{0.4} \tag{4.5}$$

$$Re = \frac{\rho ud}{\mu} \tag{4.6}$$

where Nu is Nusselt number, Re is Reynold number, u is the mean velocity of the flow and D is the hydraulic diameter of the channel. The 1D velocity of the flow can be found as

$$\upsilon = \dot{v}(\frac{ml}{s}) \times \frac{1}{10^{-6}}(\frac{m^3}{ml})(\frac{1}{\bar{A}}) \tag{4.7}$$

υ is velocity, $\dot{v}$ is volumetric flow rate and $\bar{A}$ is the cross section area of the boiler.

In this way, the volume rate of the solution through the boiler was set before each test by knowing the flow rate in the system.

The overall heat transfer coefficient in the boiler calculated using equation 4.8

$$U = \frac{q_c^{"}}{(T_w - T_m)} \tag{4.8}$$

The average power consumed by the heater is calculated depending on the time (on and off) as the boiler connects to the PID controller. When the power is on, the boiler warms up till a specific temperature (set up via the PID) and the heater gets 244 Watt from the source during that time. When it turns off the boiler cools down till 2 ^oC under the set up temperature then it works again. For all the cases, the heater takes 30 seconds to warm up 4 ^oC, and 120 seconds to cool down by 4 ^oC .

Average power from the boiler = power $\times$ average time on = $244 \times \frac{30}{150} = 48.8W$.

The mass flow through the boiler is calculated by volume flow (measured before the test) and the density of the solution (measured in separate test).

$$\dot{m}_{liq.in-boiler} = \dot{v}_{liq.in-boiler} \times \rho_{Ac/ZnBr_2} \tag{4.9}$$

Because the weight concentration of the $ZnBr_2$ in the boiler is 50% then the mass of both the acetone and the $ZnBr_2$ are the same (liquid mass flow/2).

Acetone flow rate to the SSR is the difference of the acetone flow between the boiler and condenser. The concentration of acetone and $ZnBr_2$ in the SSR is calculated from acetone flow rate in the SSR as described below.

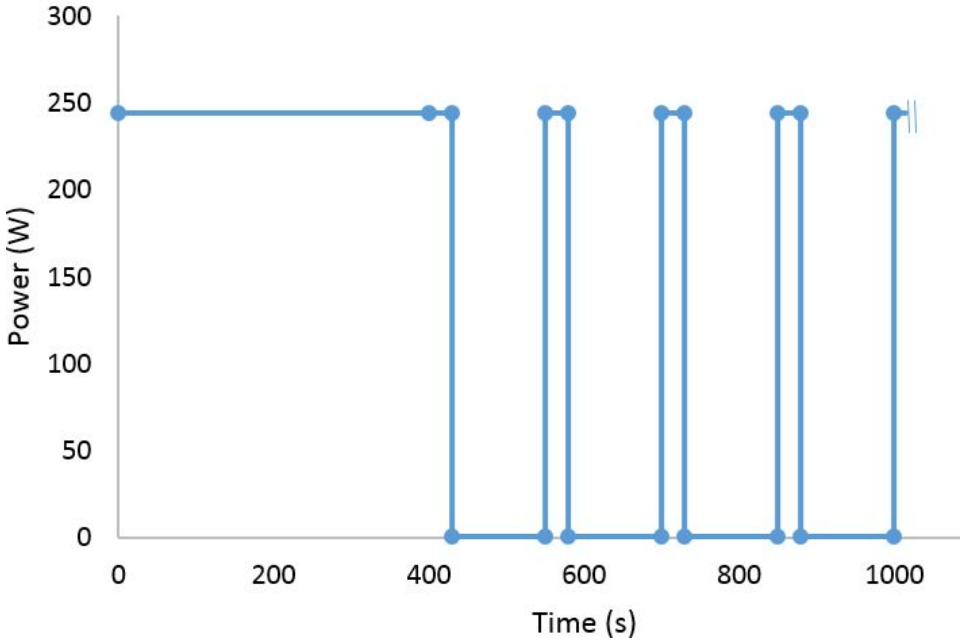


Figure 4.9: Consumption the electric power by the heater controlled by the PID controller.

$$\dot{m}_{Ac.in-SSR} = \dot{m}_{Ac.in-boiler} - \dot{m}_{Ac.in-condenser} \tag{4.10}$$

$$\Phi_{Ac.in-SSR} = \dot{m}_{Ac.in-SSR}/(\dot{m}_{liq.in-boiler} - \dot{m}_{liq.in-condenser}) \tag{4.11}$$

Concentration of the salt is:

$$\Phi_{Saltin-SSR} = 1 - \Phi_{Ac.in-SSR} \tag{4.12}$$

Acetone vapour volume flow rate in the condenser is calculated from the acetone liquid in the RR and the density of the acetone vapour.

$$\dot{v}_{vap.in-condenser} = \frac{\dot{m}_{Ac.in-RR}}{\rho_{Ac.vap.}} \tag{4.13}$$

General liquid mass flow in the SSR is the difference of the solution mass flow on the boiler and acetone flow in the condenser.

The solution volume in the SSR is calculated by the weight and density of the solution.

$$\dot{v}_{liq.in-SSR} = \frac{\dot{m}_{liq.in-SSR}}{\rho_{Ac/ZnBr_2}} \tag{4.14}$$

Then, the total volume of the SSR is the summation of liquid volume in the SSR and the vapour volume in the condenser.

$$\dot{v}_{total-in-SSR} = \dot{v}_{liq.in-SSR} + \dot{v}_{vap.in-condenser} \tag{4.15}$$

The vapour and the liquid volume fraction out of the boiler is calculated from the outcome of previous calculations.

$$\Phi_{vap} = \frac{V_{vap.-in-condenser}}{V_{total-of-SSR}} \tag{4.16}$$

$$\Phi_{liq.} = \frac{V_{liq.in-SSR}}{V_{total-of-SSR}} \tag{4.17}$$

4.4 Error Analysis:

The aim of the experimental measurements were to make a validation with the numerical results as well as studying the effect of different parameters (heater temperature, flow rate and the concentration of nanoparticles) on the saturation temperature, pressure and condensed acetone in the condenser and the heat transfer in the boiler. These measurements are subject to inaccuracy due to uncertainty of these measurements. Always, there are errors built in all measurements. Error is defined as the difference between the measured and true values. However, the actual value of a quantity is not often known and therefore, the error is not known. The uncertainty which is a method

of approximating the limits of error with some confidence and describing the quality of experimental data.

Instrument limitation, random error and systematic error are the only types of error which accompany any experiment. Any measuring instrument can only be used to measure with a certain level of accuracy. Random errors are produced by random variations in a measurement system (caused by a small change in the experiment environment). However, random uncertainty estimates the limits of random errors. Systematic error is the difference between averaged measured value and the true value. It's caused by calibration errors, scale reading errors, and data acquisition errors (error which does not change). Systematic uncertainty estimates the limits of systematic errors. And when a parameter is not directly measured, but calculated from two or more directly measured parameters (like the heat flux and the heat transfer coefficient in the current experiment), the uncertainty in the calculated parameter must be calculated from those in the measured parameters from which it is determined. This is the idea of propagation of uncertainty.

In the current experiment, all the previous types of the error exist, and these errors affect the final results of the calculated parameters. The measuring instruments used in this experiment have a tolerance, for example, for the thermocouples is $\pm 2.5\ ^oC$ and for the pressure transducers is $\pm 0.04\%$ of the scale (makes the maximum error in the pressure 3 bar $\times$ 0.0004 = $\pm$0.0012 bar) [169]. The tolerance in the thermocouples affect directly on the calculations of the heat flux then the heat transfer coefficient. Also, the heater temperature could not be controlled perfectly through the PID controller. For example, when the controller is set on 180 ^oC, the temperature of the heater fluctuated between 178 ^oC to 186 ^oC or so as shown in Figure 4.8, and this has an effect on the heat transfer to the solution and the amount of the generated vapour.

There are differences between the temperature of the hot surface which is adjacent to the solution (inner surface of the boiler) and the controlled surface and this difference changes from one case to another. For example at 160, 170 and 180 ^oC the differences are 22.4, 25.1 and 27.4 ^oC and stable approximately at the last value for the other controlled temperature (190 and 200) ^oC as shown in Figure 4.7. In this experiment, it was dependent on the average value of the differences of 180, 190 and 200 ^oC. Furthermore, the water supply to the condenser could not be controlled, the tap was fully opened which will affect the acetone condensing rate. The last point of error regarding the rig is losing heat in many sections in the rig i.e. losses from the wall of the heater, walls of WSR, walls of SSR and the tubes.

On the other hand there are errors caused by the solution during the preparation (weighing and checking their volume) the nanofluid. This will have effects on the properties of the running solution. Another source of error is measuring the properties of the solution itself (mentioned with details in chapter 3). A tiny error in the properties will effects directly on the calculation of the heat transfer, which calculated by Rohsenow equation 4.2. Also, there are some random errors which cannot be controlled such as:

- Changing the properties of the solution by changing the laboratory temperature during the test. The temperature of the first day of the test was 23 ^oC and it was fluctuated between 20 and 26 ^oC and this will affect the properties of the solution and heat loss rate to the environment.
- Some salts and nanoparticles stuck in the rig (in the joins and the tubes) which has an effect on the concentration of the $ZnBr_2$ and nanoparticles in the solution and consequently, effect on the measured and calculated results.

- Some acetone vapour may escape from the rig during the ventilation (opening the joint between the condenser and the RR to extract the cold air from the rig), also, this with affect on the concentration.
- Amount of acetone vapour condensed on the wall of the SSR. So, not all the vapour generated in the boiler condenses in the condenser. And this happen even before the condenser starts condensing acetone.

The flow rate also has an influence on the outcome, specially, at the case of studying the effect of the temperature and the effect of the nanofluid while the flow rate is maintained constant. One case for the pure basefluid with temperature (180 ^oC) repeated 5 times and in each case the volumetric flow rate measured showed a small difference, then the uncertainty of the other parameter was calculated using the uncertainty of the mean value for each parameter using equation below:

$$Uncertainty(\triangle) = \frac{Xmax - Xmin}{2\sqrt{Average}} \tag{4.18}$$

The measured values and the uncertainties calculated are in acceptable range which was 3.685 $\pm$ 0.040 ml/s for the flow rate and 8703.89 $\pm$ 85.14 W/m^2 for heat flux, the data are shown in Table 4.2. This range of error can be applied on all other cases because of the similarity between them.

4.5 Effects of the nanoparticles volume fraction with constant boiler temperature and flow rate:

Flow boiling in channels has more applications in thermal engineering systems than pool boiling, and it has the potential to improve the heat transfer, CHF, and energy efficiency of thermal systems. Many parameters affect the process of flow boiling such as the solution type, roughness of the heated surface, mass

Table 4.2: shows the measured values with the uncertainty for data measured and calculated for 5 trails for one case for pure acetone / $ZnBr_2$ solution and controlled temperature =180 ^oC.

Parameter	1^{st} trial	2^{nd} trial	3^{rd} trial	4^{th} trial	5^{th} trial	Average	Measured value
Flow rate (ml/s)	3.57	3.61	3.66	3.7	3.75	3.658	3.685±0.040
q (W/m^2)	8558	8618	8653	8745	8939	8703	8704±85
h $(W/m^2.K)$	103.1	103.6	103.9	104.1	105.2	104	104±0.5
T_{mean} (K)	343	342.8	342.7	342	341	342.3	342.3±0.4
T_{sat} (K)	335.3	335.1	335	334.7	334	334.8	334.8±0.3
Cond. Flow (ml/s)	0.075	0.076	0.0772	0.0785	0.08	0.0773	0.0773±0.0011

flux, vapour quality, flow regime, flow direction, channel size, and subcooling. The process is also affected by the properties of the solution and the physical properties and the concentration of the nanoparticles in the case that a nanofluid is used.

In this part of the work, we studied the effect of increasing nanoparticles in the base fluid on the pressure, heat transfer, heat transfer coefficient, saturation temperature of the system, average boiler temperature and the condenser flow rate. The nanoparticles concentration used in this study were (0.1, 0.2, 0.3, 0.4 and 0.5 vol. %) with a constant flow rate and temperature of the lower surface of the boiler of 3.63 ml/s and 180 ^oC, respectively. The pump used in this experiment broke twice at a concentration of 0.5 vol. % as the temperature of the pump significantly increases with nanoparticles concentration. The increase in the temperature is caused by three factors, (1) increasing the viscosity of the nanofluid with increasing the concentration, (2) increasing the concentration enhances the heat transfer (will discuss later in this section), consequently, the fluid becomes hotter and this raises the temperature of the pump, (3) increasing the nanoparticles increases the thermal conductivity of the fluid and by making a collision and friction with the pump wall more en-

ergy transfers to the pump. Figure 4.10 shows the temperature of the pump with different concentration of the nanoparticles in the base fluid. From the Figure it's clear that the pump temperature increase with the concentration, and at 0.5 vol. % the pump collapsed because of the high temperature.

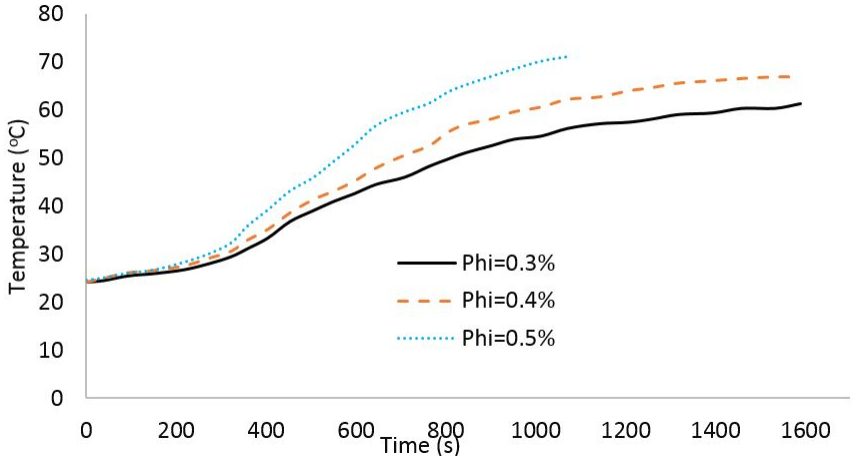


Figure 4.10: Temperature of the pump at different concentration of nanoparticles.

The concentration of the nanoparticles has an effect on the pressure of the system. There are many studies related to the pressure drop across the heating section (between the inlet and the outlet due to frictional losses) but no study is found related to the overall pressure of a boiling system. Generally, it was reported that the pressure loss in nanofluids is always greater than those of the base fluid and it increases as the nanoparticle loading increases because of the friction losses and higher viscosity of the nanofluid compared with the base fluid [75, 136, 170]. Yu et. al [171] carried out an experimental investigation of subcooled flow boiling of Al_2O_3/water nanofluids with two nanoparticle loadings of 0.01 and 0.1 vol. % in a circular stainless steel tube with 1.09 mm ID. They found that the pure water has much larger pressure drop oscillations than the Al_2O_3/water nanofluids, and that the oscillations decreased with increasing the nanoparticle volume fraction, and they thought that this effect is due to nanoparticle deposition on the channel surface as well as the thinning of thermal boundary layer due to shear-induced nanoparticle redistribution.

Also, there are some studies which claim that there is an insignificant effect of the nanoparticles on the pressure loss [134, 172, 173].

Our study investigated the pressure behaviour in the high pressure part of VAR system, related to the vapour pressure rather than pipe losses. It was found that that the pressure increases (in the region of stable operation) as the concentration of the nanoparticles increases as shown in Figure 4.11. The pressure increased from 1.17 bar to 1.2 bar when the concentration increases from 0.1 % to 0.4 %. The reason for this is the nanoparticles enhance the heat transfer and the fluid takes more heat from the hot surface, then the temperature of the solution increases which generates more acetone vapour, consequently, increases the pressure of the system due to intensification of the boiling. The line of the highest concentration was cut at 2500 (s) because the pump broke down at that time. Because the pressure is affected by concentration, the saturation temperature at the condenser side for pure acetone is also affected as shown in Figure 4.12.

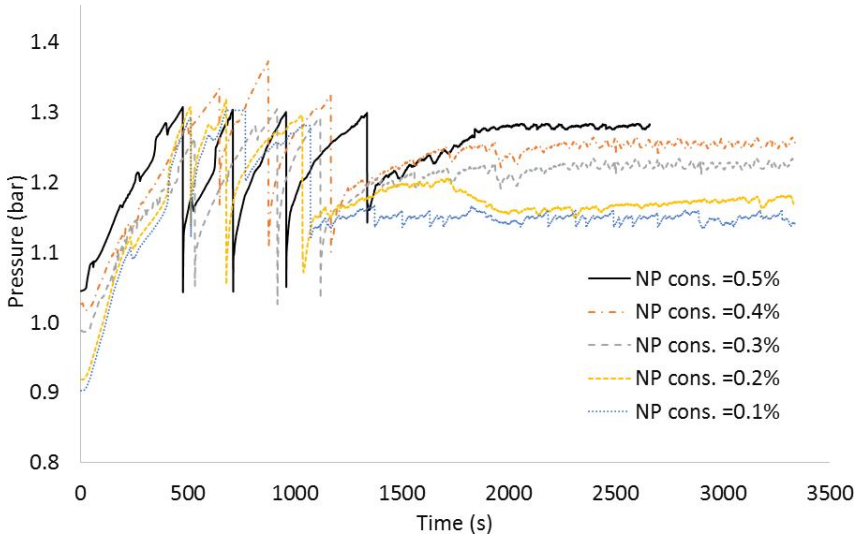


Figure 4.11: Developing the pressure of the system at different nanoparticles concentrations.

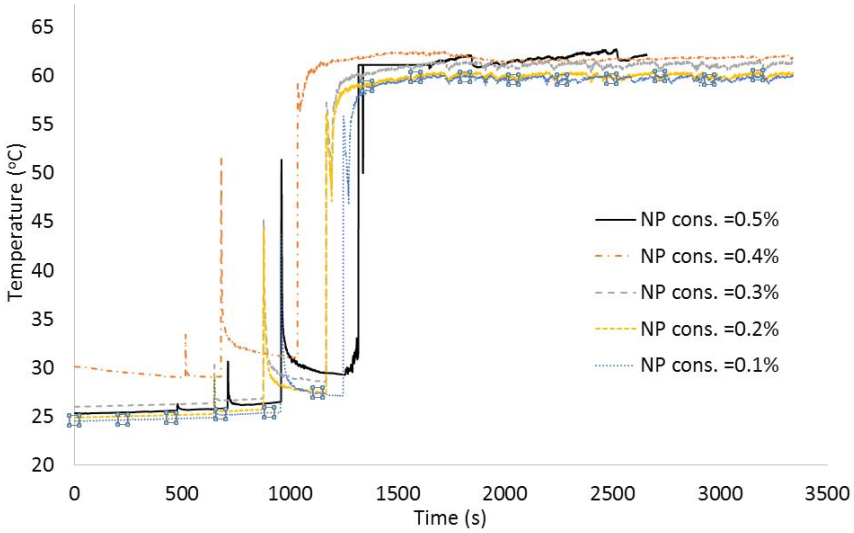


Figure 4.12: Developing the saturation temperature (at the entrance of the condenser) of the system at different concentration of nanoparticles.

Figure 4.13 shows that the heat transfer coefficient and the heat flux of the heater increases (in a parabolic shape) as the concentration of the nanoparticles increases. The reasons for this increase is increasing the loading of the nanoparticles which enhances the thermal properties of the nanofluid and Brownian motion of the nanoparticles which generates more collisions between themselves, with the molecules of the fluid and with the surface of the heater; therefore, as acetone evaporates on the surface, the particles take the heat from the surface away into the liquid. These effects have more impact than increasing the vapour near the wall which decreases the heat transfer. The heat transfer coefficient and the heat flux are increasing from 104 $W/m^2.K$ and 8.65 kW/m^2 to 167 $W/m^2.K$ and 13.16 kW/m^2, respectively, when the particles loading increases from 0 vol. % to 0.5 vol. %.

The condensing rate of acetone vapour is highest at the maximum concentration of nanoparticles (0.35 ml/s) and the lowest at pure acetone / $ZnBr_2$ (0.077 ml/s). This means that the condensation rate increases around 3.6 times with increasing the loading from 0 to 0.5 vol. % as shown in Figure 4.14. Because of that, the salt concentration in the SSR increases also as more

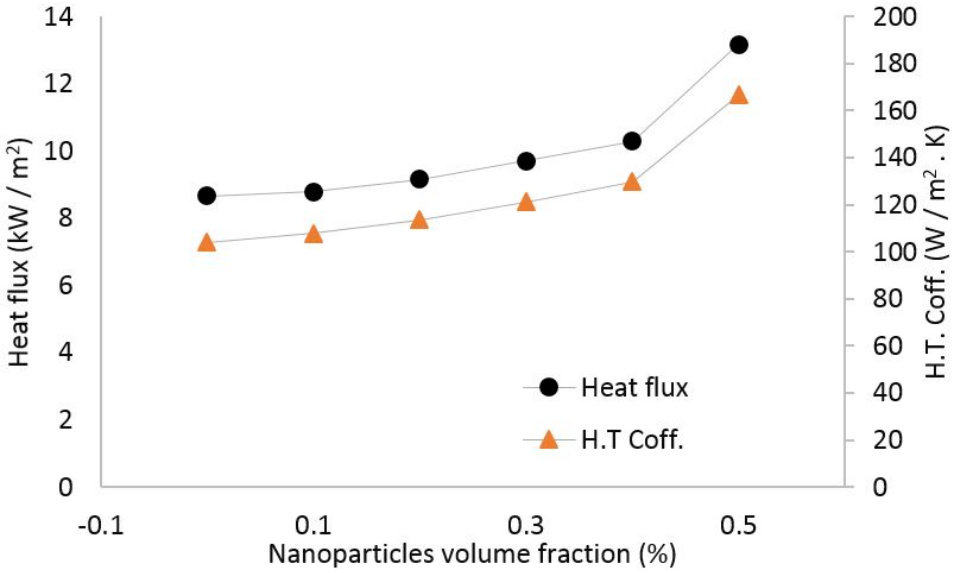


Figure 4.13: Relationship between the heat flux and the heat transfer cofficient in the boiler with the different concentration of nanoparticles.

acetone leaves the solution which is shown in the same Figure (orange points). For the same reason the concentration of the nanoparticles increases in the SSR.

Increasing the concentration of the nanoparticles, enhances the average temperature of the liquid in the boiler which, starts at 342.7 K at 0 % and ends at 347 K at 0.5 vol. %, because the high thermal conductivity of the nanoparticles, increases the heat transfer with increasing nanoparticles loading. With increasing pressure of the system, the saturation temperature of the pure acetone in the condenser increases, consequently, the temperature difference of the saturation and the wall temperature increases which has an effect on the condensation process in the condenser. The saturation temperature of the acetone increases from 332.7 K to 335 K when the concentration increases from 0 to 0.5 vol. % as shown in Figure 4.15.

The temperature at the outlet (thermocouple 5) from the boiler can be taken together with the strong solution reservoir concentration and the pressure in the high pressure side of the system to extrapolate the point on the graph shown in Figure 4.16. The temperature indicated shows that the ther-

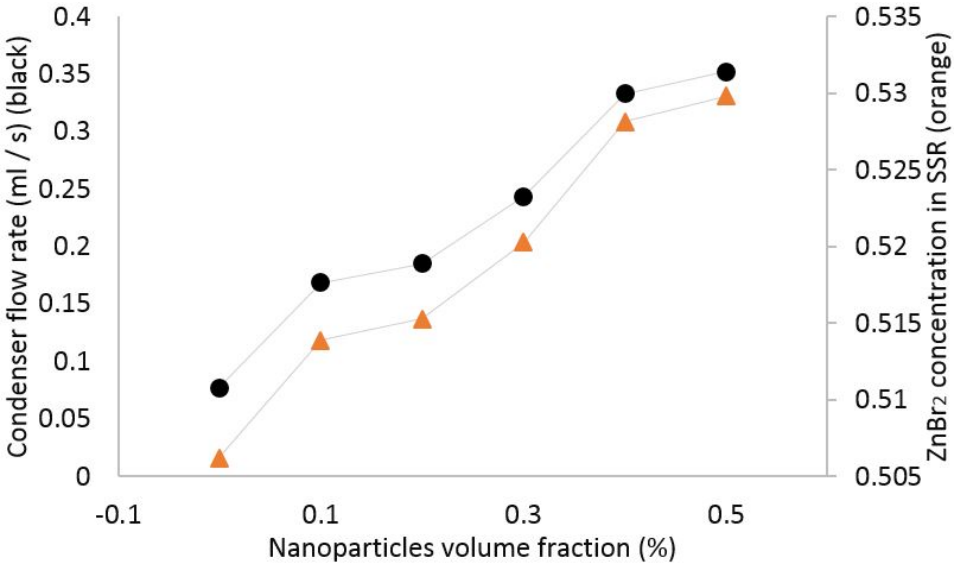


Figure 4.14: Relationship between the $ZnBr_2$ concentration in SSR and the condensed acetone flow rate in the condenser with the different concentration of nanoparticles.

mocouple represents the combination of the liquid boiling in touch with a vapour which when released is superheated above the saturation temperature corresponding to the boiler ambient pressure.

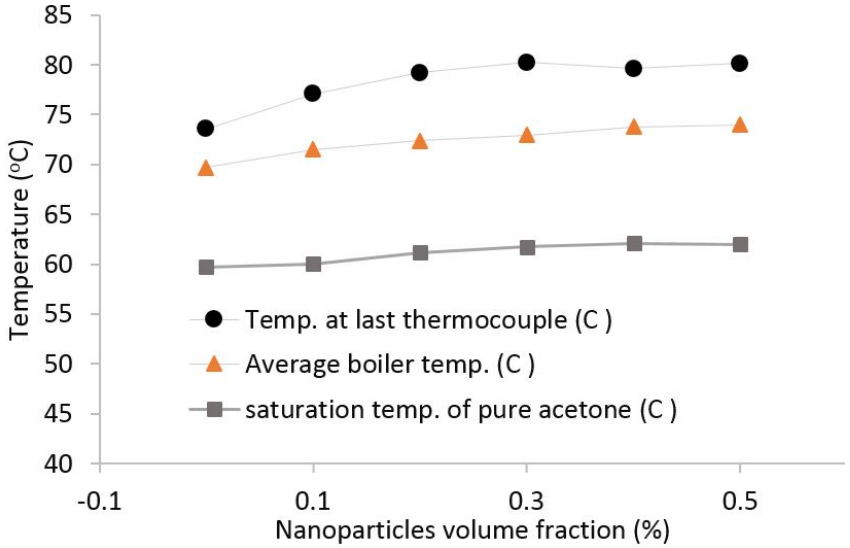


Figure 4.15: Relationship between the saturation temperature of acetone in the condenser, the average boiler temperature and the temperature recorded at thermocouple 5 (closest to the outlet section) with the different concentration of nanoparticles.

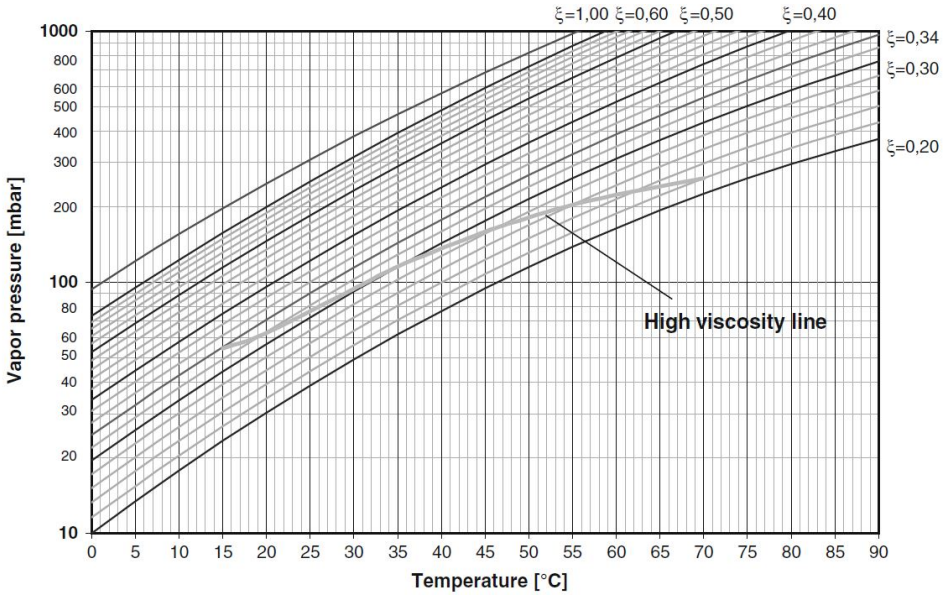


Figure 4.16: The P-T chart of the acetone in the salt solution acetone / $ZnBr_2$ [14]

4.6 Effects of the boiler temperature at constant flow rate on base-fluid:

In this study the effect of the wall temperature is investigated for the base fluid (acetone / 50wt.% $ZnBr_2$). The reason of using just the basefluid is to reduce the amount of costly nanoparticles used as well as determining similarity of the behaviour between the basefluid and nanofluid. 5 different surface temperatures (160, 170, 180, 190 & 200 ^oC) were included to study the effect on boiling of the salt solution at the constant flow rate (3.35 ml/s). The heat flux increases as ΔT_{sat} increases to reach the CHF then it decreases with increasing ΔT_{sat} to create transient boiling and film boiling regions as shown in Figure 4.17 [174]. As mentioned, the bottom surface was controlled at the control point (shown in Figure 4.6) and this surface is different from the inner surface which is in contact with the fluid (explained in 4.3.1).

The surface temperature has an influence on the pressure generated in the system as shown in Figure 4.18 which explains that the pressure increases with increasing surface temperature, e.g. at 160 ^oC it is 1.16 bar and at 200 ^oC the pressure stabilized at 1.39 bar. Also, increasing the wall temperature, leads to reducing the time needed for stabilization (in steady operation the condenser flow should be balanced with the boiler flow, to make condensing rate equal to the boiling rate to keep the pressure in the system stable. This also means that the system could not stabilize until the condenser starts to work). At 160 ^oC, the pressure stabilized after 40 minutes, however, it is stabilized in 25 minutes for the 200 ^oC case. At higher temperature more vapour is generated which produces higher pressure due to increased concentration of SS and yield of vapour at higher temperature. The saturation temperature of the pure acetone is different from that mixed in the salt solution depending on the chart shown in Figure 4.16 by [14]. The high pressure affects the saturation

temperature as shown in Figure 4.19. The saturation temperature of the pure acetone, measured at the entrance of the condenser, increases with increasing temperature of the boiler. The green points on each curves in Figure 4.19 mean that the acetone starts to condense, and these points also show that the acetone condenses faster at a higher boiler temperature. The condensing process starts before stabilising the pressure for example in case of 411 K the condensing starts at 1680 seconds, however, at 446 K it starts at 600 seconds.

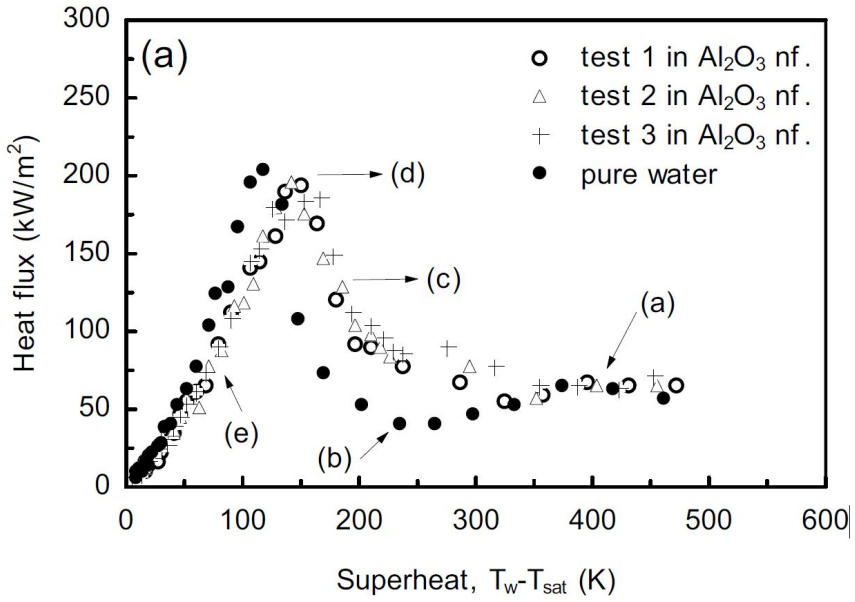


Figure 4.17: The characteristic boiling curves of water / Al_2O_3 nanofluid, (a) the film boiling, (b) the minimum heat flux (MHF) point, (c) the transient boiling, (d) the maximum heat flux point or critical heat flux (CHF), and (e) the nucleate boiling [174].

The average temperature of the vapour/liquid mixture leaving the boiler depends on the boiler temperature and it is just a few degrees above the saturation temperature between 343 K and 349 K. This is because the vapour phase is the majority at the boiler exit, and the vapour temperature in the boiler is either at the saturation temperature of the acetone in the salt solution or few degrees above (superheated stage), however, the temperature of the liquid phase (not measured in this work) could be higher than the saturation temperature of the acetone in the salt solution.

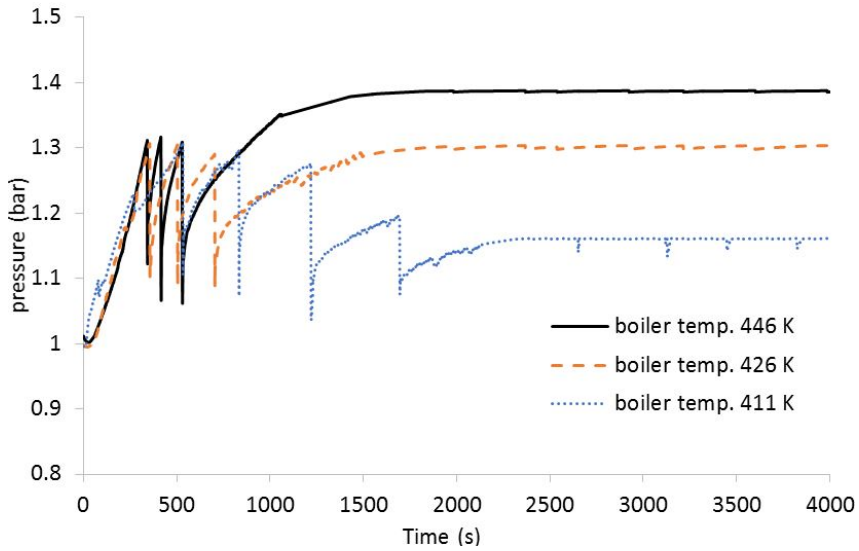


Figure 4.18: Developing the pressure of the system at different boiler temperature at 3.35 ml/s.

From the tests identifying different boiler temperatures, we found that the average temperature in the boiler measured by the 5 thermocouples increases with increasing boiler temperature (expected behaviour) and the average boiler temperature varies between 69.1 ^oC at 160 ^oC to 76.3 ^oC at 200 ^oC. The increasing in saturation temperature of the pure acetone as the boiler temperature increases is shown in Figure 4.20. It can be said that the average temperature shown in this Figure is approximately equal (or greater with small difference) to the saturated temperature of the acetone in the salt solution. It can be observed also that the temperature difference between the average boiler temperature and the temperature recorded by thermocouple 5 in case of 180 ^oC is lower than the difference between these two temperature in the case with presence the nanoparticles (shown in Figure 4.15). The reason for that is with nanoparticles, more heat transfer to the liquid due to the high conductivity of the nanoparticles consequently the liquid be warmer.

Many studies such as [91, 175, 140, 176, 143] show that the relationship between the heat flux and the temperature difference between the wall and the saturation ($\Delta T_{sat.}$) is linear. However, [137] found a linear relationship but

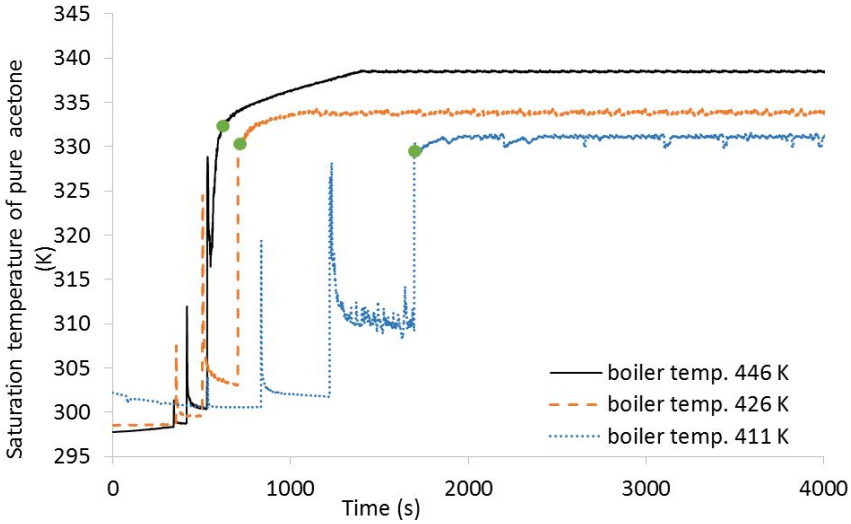


Figure 4.19: Developing the saturation temperature (at the entrance of the condenser) of the system at different boiler temperature.

with two gradients; a slight initial slope, then the gradient increases. Another study ([177]) found an exponential relationship between the heat flux and $\Delta T_{sat.}$. This relation appears because, by increasing $\Delta T_{sat.}$, transient and film boiling take place, which decreases the rate of heat flux. In our study the $\Delta T_{sat.}$ was between 102 ^oC and 135 ^oC and the overall heat transfer coefficient (U) (calculated in equation 4.8) increased approximately linearly but the heat flux ($q_w^{"}$) reflects a quadratic relationship increasing with increasing $\Delta T_{sat.}$ (as shown in Figure 4.21), suggesting that the process is in the nucleate boiling range. By increasing the $\Delta T_{sat.}$ in our cases, the relation becomes quadratic according to the left side of the typical positive skew curve seen in heat flux versus $\Delta T_{sat.}$ for flow boiling heat transfer indicating a condition well within the nucleate boiling regime.

Because of boiling, the acetone evaporates, and the concentration of the salt rises in the SSR, the concentration increases more as the boiler temperature increases, but even at the highest temperature (200 ^oC), the mass fraction increases only from 0.5 to 0.512 as shown in Figure 4.22. The Figure also shows how the condensed acetone flow rate in the condenser increases with increasing boiler temperature, since the condensing rate equals the evaporating

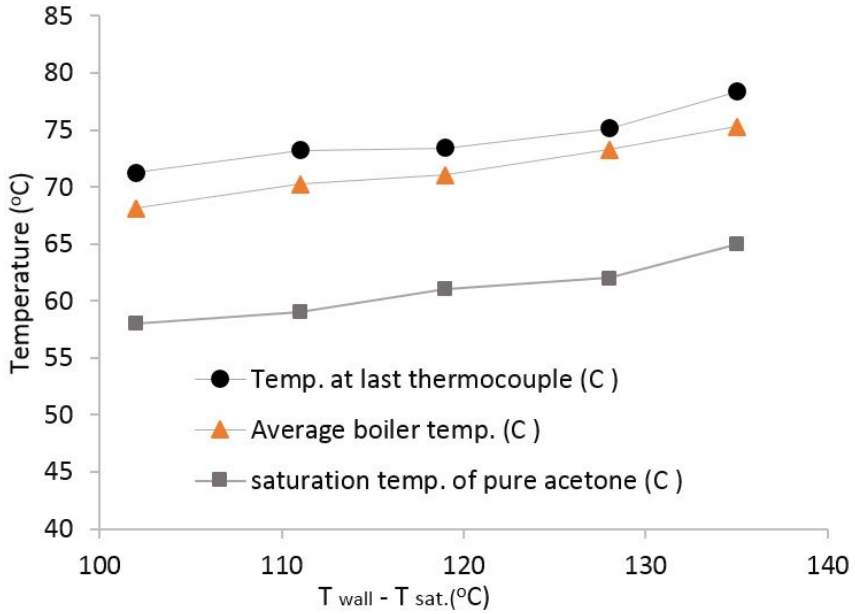


Figure 4.20: Relationship between the saturation temperature of acetone in the condenser, the average boiler temperature and the temperature recorded at thermocouple 5 (closest to the outlet section) with the different controlled temperature of the boiler.

rate in the boiler. Increasing the rate of condensing acetone means more liquid acetone flow into the evaporator (not investigated in this study), which may help to improve the performance of the evaporator in the VARS in case of applying a good heat exchanging with the load (evaporator heat source).

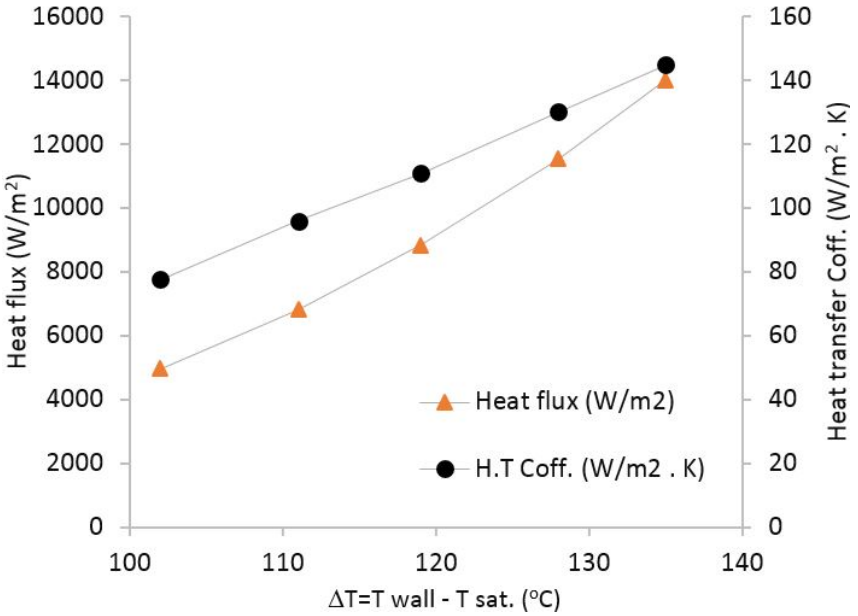


Figure 4.21: Relationship between the heat flux and the heat transfer coefficient in the boiler with the different controlled temperature of the boiler.

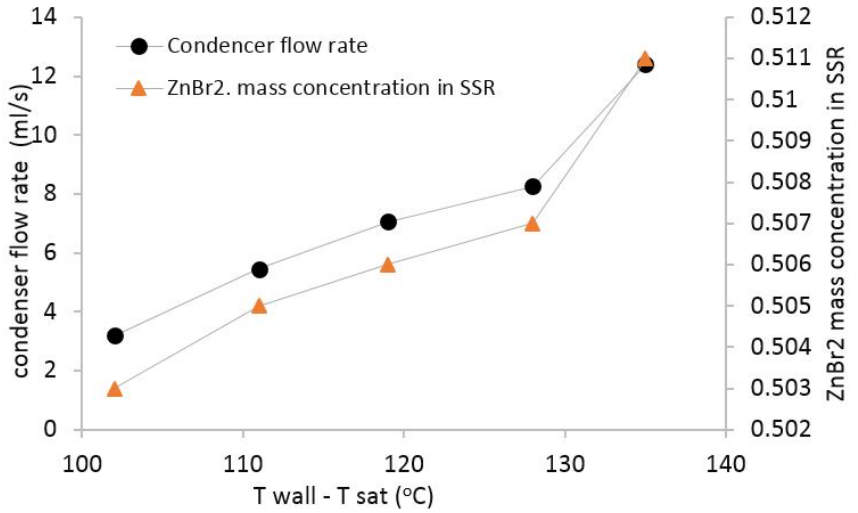


Figure 4.22: Relationship between the $ZnBr_2$ concentration in SSR and the condensed acetone flow rate in the condenser with the different controlled temperature of the boiler.

4.7 Effect of the flow rate at constant boiler temperature on basefluid:

Four different flow rates of basefluid without nanoparticles (2.31, 3.66, 4.27 and 7.1 ml/s) are used to investigate the influence of the flow on the heat transfer, temperature at the outlet, vapour generation in the boiler and the pressure of the system which controls the saturation temperature and the condensation rate of the condenser. The controlled temperature of the boiler was 180 ^oC. Thermocouples and sensors measure the temperature at different points and the pressure of the system. At the slowest flow rate (2.31 ml/s), the pressure starts from the atmospheric and rises gradually to 1.2 bar. At this pressure, the saturation temperature of the pure acetone is 60 ^oC and for salty acetone (50wt. %) is 74 ^oC [14]. The pressure and the temperature at the condenser inlet behave as shown in Figure 4.6. The pressure changes when the valves of the SSR and RR are opened and closed. The pressure in the system increases to a constant value with closing both of the valves. The flow control valve at outflow from the SSR and the RR are manually operated ball valves. For each experiment the precise position of the valve was adjusted until a steady level was observed in both the SSR and RR during steady operation.

The acetone in the condenser is pure acetone, however, it is salty liquid in the boiler which makes the saturation temperature of the acetone in the condenser lower than the superheated acetone vapour in the boiler. The saturation temperature in the condenser was measured but in the boiler it could not be measured because the thermocouples of the boiler measured the temperature of the mixture phases (liquid and generated vapour). In addition, the saturation temperature of the acetone in the salty solution varied with different evaporation rate of acetone because the concentrations of the $ZnBr_2$ differed (as shown in Figure 4.16).

The fluid in the boiler, suffers temperature increase as it flows over the heated plate. The temperature is measured by five thermocouples which extend to the middle of the section as shown the Figure 4.5. Also the vapour volume fraction increases during the flow, and at the outlet of the boiler, the vapour volume fraction is more than 90% depending on the case. Evaporating the acetone in the boiler makes the concentration of the salt ($ZnBr_2$) increase in the SSR.

From Figure 4.23 it is clear that the pressure at the stable region increases with decreasing the flow rate of the fluid, this is because with increasing the flow rate, less vapour is generated and then less pressure is produced as the boiling flow changes. This affects directly the saturation temperature at the condenser as shown in Figure 4.24. The Figure shows that the saturation temperature decreases with increasing velocity in the boiler for the same reason mentioned previously.

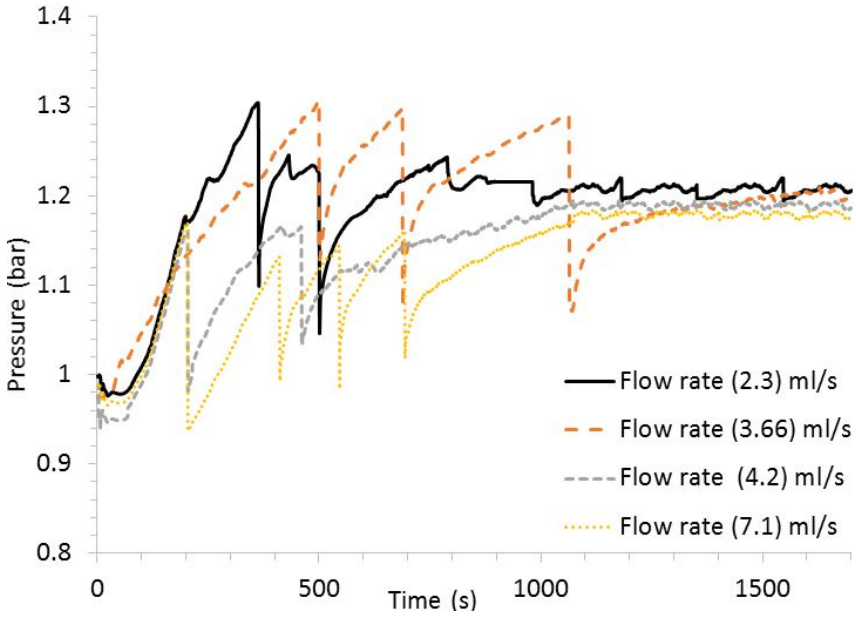


Figure 4.23: Developing the pressure of the system at different flow rate at the boiler temperature 180 ^oC.

The average temperature of the boiler increases with increasing flow rate. For example the boiler flow temperature increased from 67 ^oC to 73 ^oC when

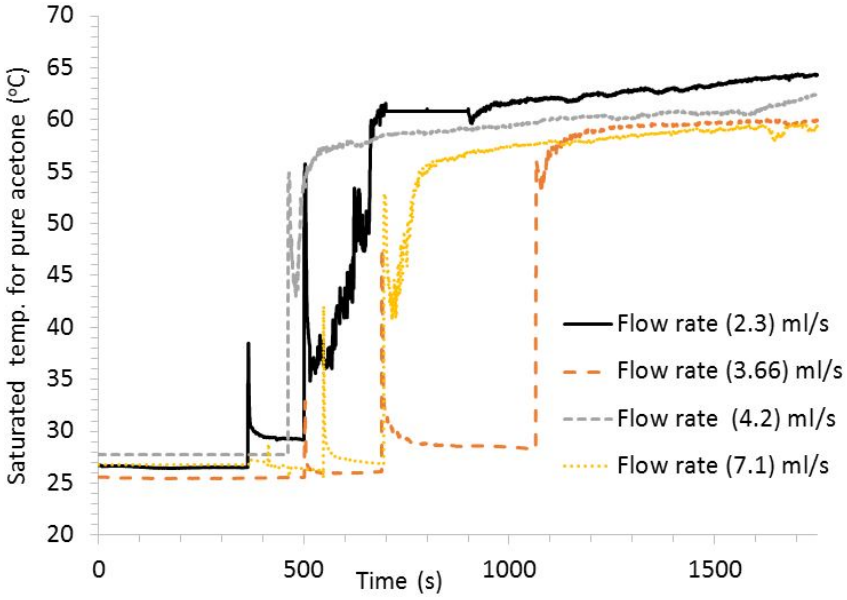


Figure 4.24: Developing the saturation temperature (at the entrance of the condenser) of the system at different flow rate.

the flow rate increased from 2.31 to 7.1 ml/s as shown in Figure 4.25. This behaviour happens because, with higher velocity, less vapour is generated so more liquid exists in the boiler, and with lower flow, more vapour is generated which generally cannot be warmer than the saturation temperature. Because the heat capacity of the liquid is higher than the vapour, then the liquid gains more heat and becomes warmer. Furthermore, with higher velocity, the fluid makes more circulations and gains more heat from the boiler. This is true for a certain (limited) range of values of the flow rate, after that the average temperature of the solution should decrease with increasing the velocity, as described by the general form of the boiling heat transfer.

Figure 4.25 also shows the temperature of the acetone in the condenser decreases with increasing flow rate, as explained previously. It decreases from 64 to 59 ^oC when the flow rate increases from 2.31 to 7.1 ml/s. This is because with increasing the velocity, less vapour is generated which decreases the pressure of the system and consequently the saturation temperature. The concentration of the $ZnBr_2$ in the SSR becomes more than 50wt. % with

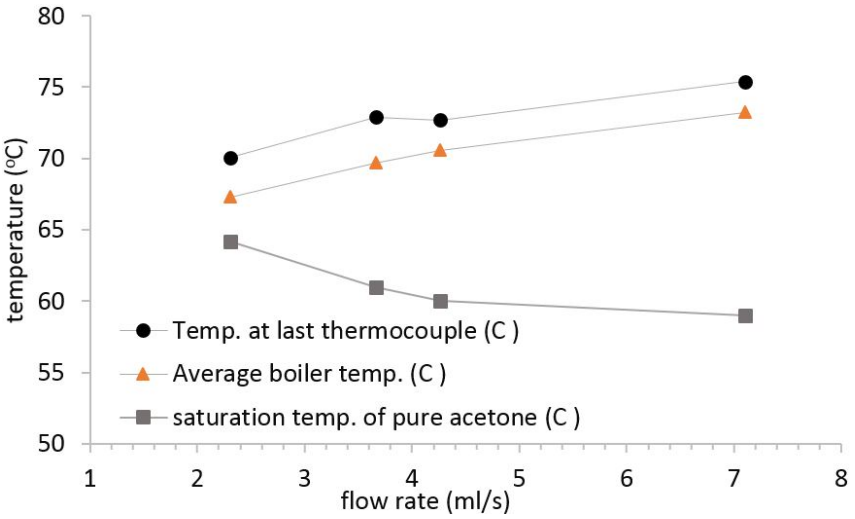


Figure 4.25: Relationship between the saturation temperature of acetone in the condenser, the average boiler temperature (average temperatures which measured from the thermocouples (1-5) of the boiler) and the temperature recorded at thermocouple 5 (closest to the outlet section) with the magnitude of the boiler flow rate.

increasing the flow rate depending on the velocity. The concentration of the $ZnBr_2$ increases due to evaporating more acetone which means with lower velocity, more $ZnBr_2$ concentration in the SSR as shown in Figure 4.26. Figure 4.26 shows how the condensed acetone flow decreases with increasing boiler flow rate as the system producing balance between the evaporation and condensation rates. The condensed acetone flow rate decreased from 0.104 ml/s to 0.0712 ml/s by increasing the flow rate in the boiler from 2.31 to 7.1 ml/s.

Figure 4.27 shows that the heat flux and the heat transfer coefficient of the heated surface increase as the flow rate increases. The heat flux and the heat transfer coefficient increase from 7878 W/m^2 and 92.9931 $W/m^2.K$ to 9931 W/m^2 and 124.5 $W/m^2.K$ respectively, as the flow increases from 2.31 to 7.1 ml/s. Heat transfer coefficient is the ratio of the heat flux against the temperature difference between the solid surface and boundary layer, and the heat transfer depends on the thermal conductivity of the boundary layer and its thickness. Changing the velocity influences the surface temperature and the measured bulk fluid flow temperature. The velocity might change (e.g., decrease) and the thickness of this laminar sub-layer where heat transfer is

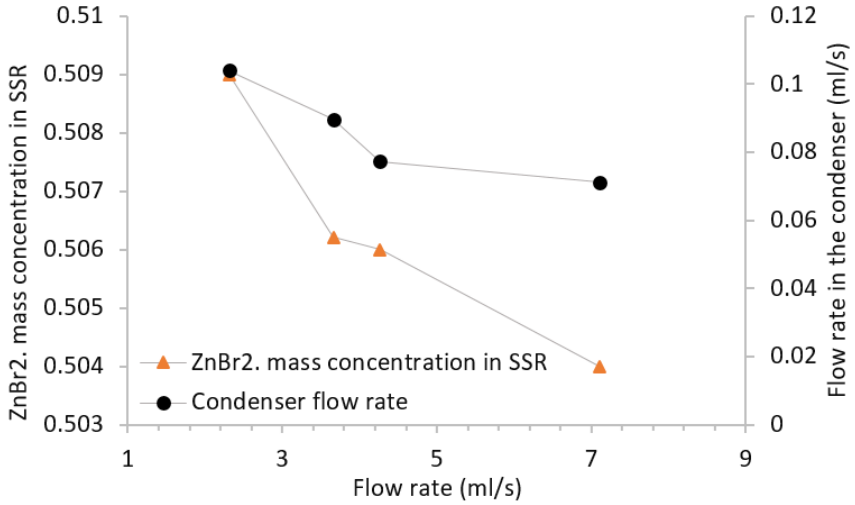


Figure 4.26: Relationship between the $ZnBr_2$ concentration in SSR and the condensed acetone flow rate in the condenser with the magnitude of the boiler flow rate.

conductive will be affected. As a result the heat transfer coefficient increases in case of decreasing velocity. There is also increase in the heat transfer due to connective effect on the temperature of the medium (sink) just behind the boundary layer which is induced by the motion.

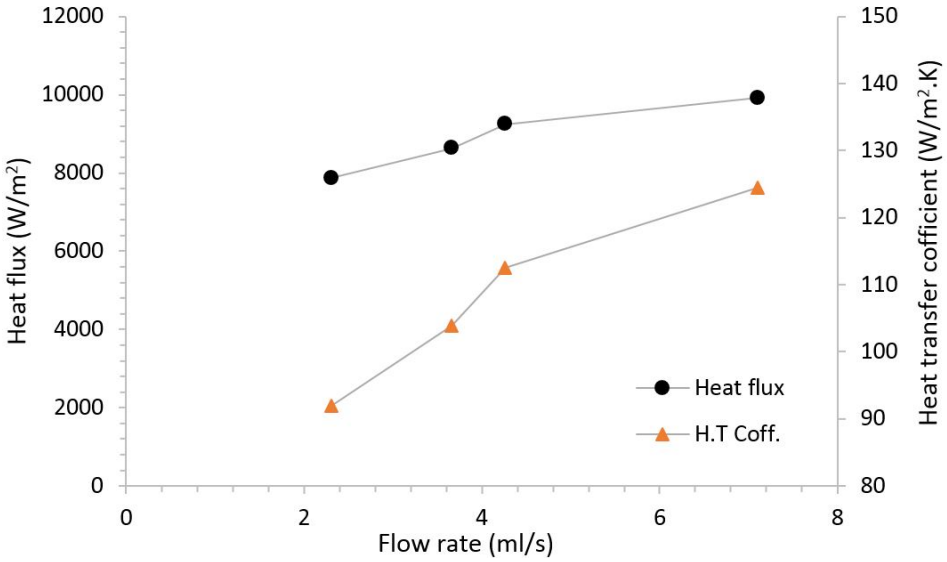


Figure 4.27: Relationship between the heat flux and the heat transfer coefficient in the boiler with the magnitude of the flow rate.

4.8 Summary

This study used a new nanofluid (nano-salt-fluid) acetone $/ZnBr_2$ based on graphene nanoparticles as the working fluid in the higher pressure part of a vapour absorption refrigeration system to look at how the different concentration of the nanoparticles (0 – 0.5 vol.%), boiler temperature (411, 418, 426, 436 and 446 K) and flow rate (2.31 - 7.1 ml/s) affect the behaviour of flow boiling. Also, the preparation and the properties of the new solution has been investigated. The results obtained can be summarized as:

- The Rohsenow constant of acetone / $ZnBr_2$ based Graphene on the stainless steel found as 0.217 depending on the Rohsenow nucleate boiling correlation and the power input.
- The stabilized pressure of the system will decrease with decrease in the concentration of the nanoparticles due to less vapour generation consequently, the saturation temperature decreases also.
- An exponentially increasing relationship appears for increasing the heat flux and the heat transfer coefficient with increasing the particles loading.
- Increasing the concentration of the nanoparticles, increases the vapour generation. When the system reaches balance state, the condensation rate increases too, consequently, the salt concentration in SSR increases.
- With increasing the boiler temperature the vapour generation increases which increases the pressure and the saturation temperature.
- The heat flux and the heat transfer coefficient also rises with increasing T_{wall}–T_{sat}.
- The average boiler temperature increases with increasing the flow rate. Because with higher flow rate, less vapour is generated, means

more liquid exist in the boiler then the fluid can gain more heat to become warmer. This also, make the saturation temperature in the condenser decrease.

- The heat transfer coefficient and the heat flux proportional with the flow rate in the system.

5

EVALUATION OF SINGLE AND TWO PHASE MODELS FOR THE NANOFLUID HEAT TRANSFER

5.1 Introduction

In this chapter a CFD model is presented to compare and evaluate both of the single and multiphase schemes using nano-salt-fluid (acetone / zinc bromide with zinc oxide suspension) in a flat tube. This assessment demonstrates the best model for heat transfer in a nanofluid, which can predict the experimental results of the boiling process and which model represents the zinc oxide nanoparticles as a distinct fluid phase. The cases of laminar and turbulent flow are explored numerically for acetone / $ZnBr_2$ with various nanoparticle concentrations. The velocity is varied between 1.5 and 6 $m.s^{-1}$, representing typical heat exchanger conditions. Reynolds number depends significantly on the salt and nanoparticles concentration.

A flat tube model, simulating part of an automotive heat exchanger provides a good base model for the test. There are several studies dealing with nanofluid flow in a flat tube [86, 88, 178, 179, 180, 181, 182]. Peyghambarzadeh et. al [86] experimentally studied heat transfer in a car radiator using H_2O/EG mixed with different amounts of aluminium oxide Al_2O_3 nanoparticles. They

found that the nanofluid enhanced the heat transfer 40% more than the base fluid. Delavari and Hashemabadi [88] presented a CFD model of the heat transfer of the Al_2O_3/H_2O and Al_2O_3/EG nanofluids in the same situation, testing the validity of the single phase and two phase models against experimental results of Peyghambarzadeh et. al [86] concluding that only the two phase model gives good representation of the physical system. They found also the Nusselt number increased by a factor of two by adding 1% Al_2O_3 to water.

In order to provide validation for the numerical simulations, the case of the experimental work of Peyghambarzadeh et. al [86] and the numerical work of Delavari and Hashemabadi [88] are numerically repeated with both models (single and two phase) to prove that the method works in our context. We then apply the same method with our alternative nano-fluid to evaluate its potential for use as the heat transfer fluid in a vapour absorption cycle. This chapter includes:

- Geometry and assumptions to present the computational method of the shape of the geometry.
- Description of the single and the two phase model with the main equations governing each model.
- Boundary conditions for the novel refrigerant simulation.
- Results and discussion:
  - Justification of mesh structure, where four mesh sizes were selected in order to achieve a minimum number of cells with accurate results.
  - Validation of this work, which includes a comparison with the results of the previous works dependant on the single and the two phase models.

  - Effects on the centreline velocity.
  - Effects on the turbulence intensity.
  - Effects on the wall shear stress and skin friction.
  - Effect on the heat transfer coefficient.
- Conclusions to present the main findings of this assessment.

5.2 Geometry and assumptions

The geometry is repeated from the work of Peyghambarzadeh et al. ([86]) and Delvari and Hashemabadi ([88]) in order to validate the method. The geometrical arrangement in Figure 5.1, is a flat tube with 31 cm length and 0.53 cm hydraulic diameter. The system is closed, the nanofluid is in-compressible, it is at steady state and under Newtonian flow and it is identical to that in [88]; evaporation of the acetone is neglected; density of the solution is constant under different pressures; the temperature and inlet velocity are constant; thermal equilibrium is assumed between the base fluid and the nanoparticles; the entering velocities of the fluid and the particles are the same. According to the length of the channel (0.31 m) and the average velocities of the solution (1.5 – 6 m/s), the average time for the solution to pass through end to end is between 0.05 – 0.2 s. The properties of all the materials (nanoparticles and the nanofluid) with different concentrations of the salt and nanoparticles are measured as explained in chapter 3 and used directly in these models.

5.3 Single phase model

This model deals with the nanofluid as a homogeneous fluid which mainly depends on the properties of the nanofluid. Most researchers suggest that this model is very suitable for low concentrations of nanoparticles [183] but according to the results of [88, 158] this model still under predicted heat transfer even

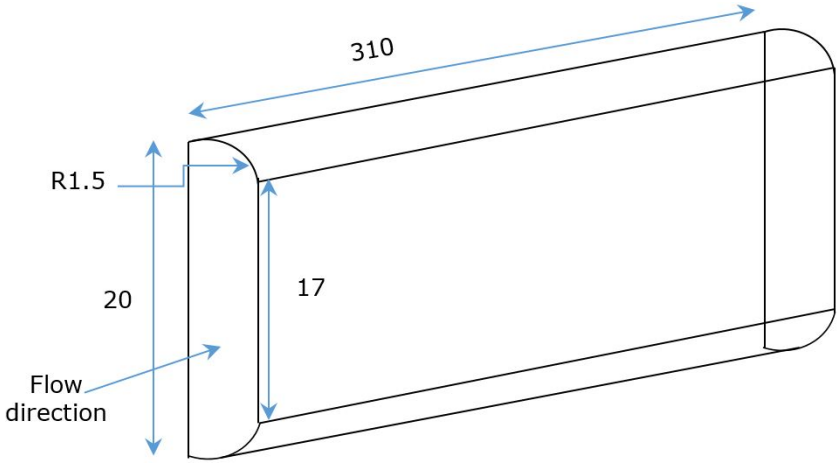


Figure 5.1: Dimensions of the symmetric flat tube in this study in mm (Not to scale).

for these small concentrations. The important step in this model (in the current study) is to use the laboratory measurement of the properties (as found in chapter 3) or use the most reliable correlations to find the properties of the nanofluid even though there are no universal correlations that can predict the properties of the nanofluid exactly and the properties of particular nanofluids are not available in many cases. All the properties used in this modelling are those measured in chapter 3. In this model the continuity (5.1), momentum (5.2) and energy (5.4) equations are:

$$\nabla.\nu = 0 \tag{5.1}$$

$$\rho_{nf}(\nabla.\nu)\nu = -\nabla P + (\mu_{nf} + \mu_t)\nabla^2\nu \tag{5.2}$$

Where

$$\mu_t = C_\mu \frac{K_t^2}{\varepsilon} \tag{5.3}$$

Where μ_t is turbulence viscosity, C_μ is empirical constant equals 0.09, K_t is turbulence kinetic energy and ε is rate of dissipation.

$$\rho_{nf} c_{pnf} (\nabla . \nu) T = k_{nf} \nabla^2 T \tag{5.4}$$

The Nusselt number in each simulated case can be calculated from the flow solution field by extracting the heat transfer coefficient at the wall (h_{nf-CFD}) and:

$$Nu_{CFD} = \frac{h_{nf(CFD)}.D_H}{k_{nf}} \tag{5.5}$$

5.4 Two phase CFD methodology

For the two phase model, there are two approaches for simulation: Lagrangian-Eulerian which is suitable for low volumetric concentration and assumes the Eulerian for the continuous fluid (base-fluid) and Lagrangian for the solid particles which are tracked as discrete particles. Eulerian-Eulerian is more suitable for high volume fraction of the particles because the model uses a reference coordinate for each particle in the Lagrangian approach but in the Eulerian, the model uses just one reference coordinate for all particles (simulate the particles as a continuous phase). The calculation of many trajectories for the large dispersion of particles makes the Lagrangian method impractical and non-representative without a large number of particle injections and Lagrangian fails to give a representation of the volume taken by the discrete phase in the continuous phase. This is demonstrated by Delavari and Hashemabadi [88], therefore, the Eulerian-Eulerian approach is used. The viscous model used in this method is standard k-epsilon model, with enhanced wall treatment, which is a near-wall modelling method that combines a two-layer model with, so-called enhanced wall functions. If the near-wall mesh is fine enough to be able to resolve the viscous sub-layer, then the enhanced wall treatment will be identical to the traditional two-layer zonal model. However, the restriction

that the near-wall mesh must be sufficiently fine everywhere might impose too large a computational requirement. The multiphase model is the mixture method and the SIMPLE scheme is used for the pressure-velocity coupling; the first order upwind method is used for all of momentum, volume fraction and the turbulent kinetic energy and PRESTO method is used for pressure velocity coupling [184]. The governing equations of the continuity, momentum and energy equations [88, 184] are:

Continuity

$$\nabla.(\rho_m \vec{\nu}_m) = 0 \tag{5.6}$$

Momentum

$$(\rho_m \vec{\nu}_m).\nabla \vec{\nu}_m = -\nabla P_m + \nabla.(\mu_m \nabla \vec{\nu}_m) + \rho_m g + \nabla.\sum_{k=1}^{n} \Phi_k \rho_k \vec{\nu}_{dr,k} \vec{\nu}_{dr,k} \tag{5.7}$$

where

$$\vec{\nu_m} = \frac{\sum_{k=1}^{n} \Phi_k \rho_k \vec{\nu_k}}{\rho_m} \tag{5.8}$$

$$\rho_m = \sum_{k=1}^{n} \Phi_k \rho_k \tag{5.9}$$

$$\mu_m = \sum_{k=1}^{n} \Phi_k \mu_k \tag{5.10}$$

$$\vec{\nu_{dr,k}} = \vec{\nu}_k - \vec{\nu}_m \tag{5.11}$$

Energy

$$\nabla . \sum_{k=1}^{n} \Phi_k \vec{\nu}_k (\rho_k E_k + P) = \nabla . (k_{ef} \nabla T) + S_E \tag{5.12}$$

where

$$E_k = h_k - \frac{P}{\rho_k} + \frac{\nu_K^2}{2} \tag{5.13}$$

Masoumi et al. ([87]) developed a formula to calculate the viscosity of the particle cloud for the second phase, with respect to the Brownian motion of particles:

$$\frac{\mu_{nf}}{\mu_f} = 1 + \frac{\rho_p \nu_B d_p^2}{72 C \delta} \tag{5.14}$$

Where ν_B is velocity of Brownian motion, δ is the mean distance between the centres of two particles and C is a correction factor found by equations 5.15 - 5.17.

$$\nu_B = \frac{1}{d_p} \times (\frac{18 k_b T}{\Pi \rho_p d_p})^{1/3} \tag{5.15}$$

$$\delta = (\frac{\Pi d_p}{6\Phi})^{1/3} \tag{5.16}$$

$$C = \frac{a\Phi + b}{\mu_f} \tag{5.17}$$

Where k_b is Boltzmann constant ($1.38 \times 10^{-23} m^2 kg/s^2 K$ or J/K), $a = -4 \times 10^{-5}$ and $b = 7.13 \times 106^{-7}$ and it is found to be valid only when $\Phi <$ -b/a ($\Phi < 2\%$). For the two phase model, the software calculates the properties of the nanofluid implicitly for varying concentration of nano-particles according to equations 5.10.

This technique which is finding the viscosity of the cloud of nanoparticles in the fluid is used by [87], however [86, 88] used a different strategy to find the viscosity of the nanoparticles using trial and error; the viscosity of the nanoparticles was varied until the pressure drop and Nusselt number of the very dilute nanofluid, pure ethylene glycol at Re=2440, and pure water at Re=9350, were equal. We confirm that the methods are equivalent in effect.

5.5 Boundary condition for the novel refrigerant simulation

Initially a validation exercise was conducted, repeating the simulation of Delavari and Hashemabadi to prove correct application of the method. Following this validation, the numerical calculation was done with laminar and turbulent flow conditions for the proposed nanofluid depending on the mass concentration of acetone. To keep the velocity of the fluid comparable to that used in the literature ([86, 88]), Reynolds number was taken in four ranges as shown in Table 5.1.

Table 5.1: Reynolds number at different mass fractions of acetone.

Acetone mass fraction	30%	40%	50%	60%	70%
Re	150-300	1500-3000	5000-10000	15000-25000	15000-25000

The temperature of the inlet flowing nanofluid is 323 K, the turbulence intensity is in the order of 10%, and the hydraulic diameter is 0.53 cm. A convection boundary condition was assumed for the wall from outside with the heat transfer coefficient at the wall specified as 150 W/m^2K and the external air temperature as 303 K as set in [86, 88].

5.6 Results and discussion

5.6.1 Justification of mesh structure

The commercial code Ansys® Fluent is used to simulate this flow situation using the Eulerian-Eulerian method (mixture model). Four mesh sizes were selected in order to achieve a minimum number of cells with accurate results. The meshes were compared by the heat transfer coefficient on the wall using 50 wt. % $ZnBr_2$ in the solution with a turbulent flow (Re=8000). The results shown in Table 5.2 were very similar especially for meshes (2, 3 & 4) but because meshes 3 & 4 have more nodes, and therefore lengthier simulation, the best mesh regarding accuracy and time was mesh 2 as shown in Figure 5.2. The computer used has processer 3.7 GHz (Intel® Xeon® CPU E5—1620 v2 @ 3.7GHz) with the memory (RAM) 32 GB.

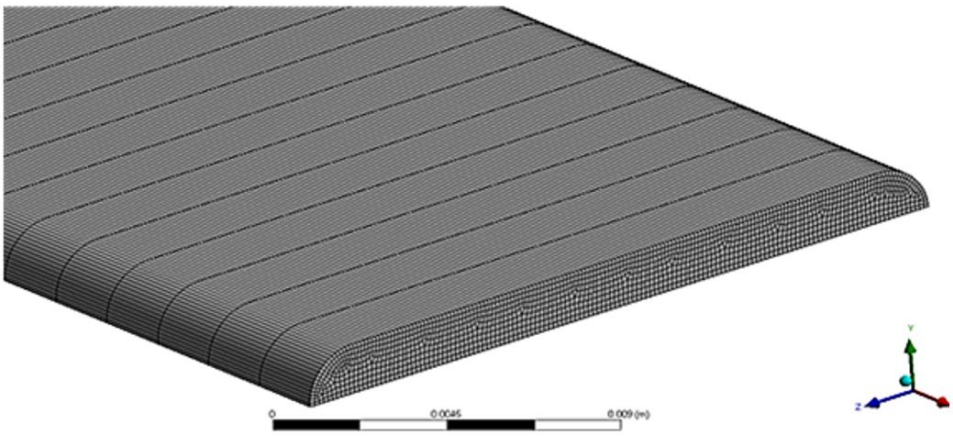


Figure 5.2: Mesh #2 used in this study.

Table 5.2: Mesh independence study of the fully developed region using acetone/50wt.% $ZnBr_2$ with Re=8000.

	Mesh (x × y × z)	h ($W/m^2.K$)	clock time for simulation (min)
1	130 × 130 × 15	3150.01	12
2	140 × 140 × 20	3151.916	14
3	150 × 150 × 20	3151.927	18
4	180 × 160 × 22	3151.933	25

5.6.2 Validation of the CFD Modelling

To validate the accuracy of this model, the experimental data of the heat transfer improvement using water based nanofluid (Al_2O_3 / H_2O) as a coolant in a car radiator which was presented by Peyghambarzadeh et al. [86] was compared to the corresponding current numerical results. Peyghambarzadeh et al. conducted uncertainty analysis for their experiments depending on the single sample uncertainty zeroth order (defined as fixed and random errors presented by the instrumentation, with no contribution from the process) analysis method for each measurement, which is described by Moffat [185]. They stated that the uncertainty of the Nu (18% 24<Nu<120) is caused by the error in Re (5.5% 1200<Re<23000) and the measured temperature. Furthermore, they compared their experimental Nu with the correlation of Xuan and Li [40] and they found a good agreement presented by 7% (vertical bar) error for the nanofluid Al_2O_3 / H_2O as shown in Figure 5.3. The Figure also shows how the 18% error of the measured Nu appears on the graph as the horizontal bar.

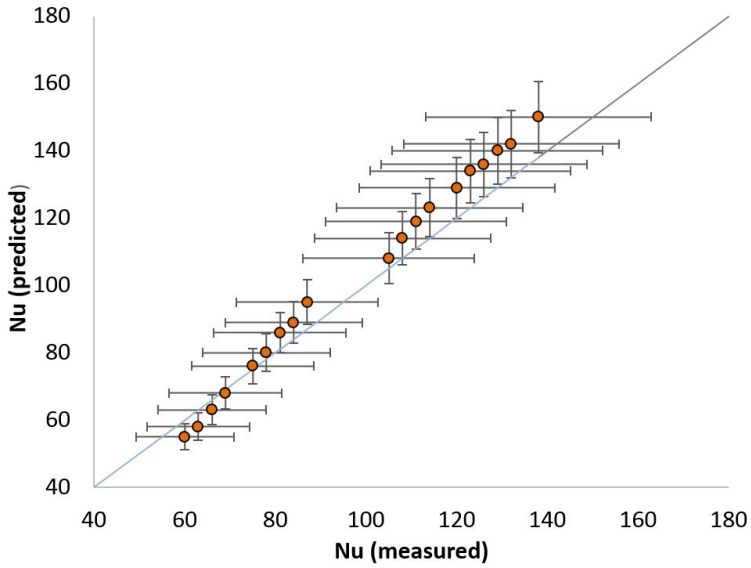


Figure 5.3: Comparison between the experimental Nu from [86] and the predicted Nu from [40]. Horizontal error bars are experimental uncertainty (18%) [86]; vertical error bars are error of analytical prediction (7%) [40]. This Figure is reproduced by permission from [86].

The validation of the simulation work with an experimental work has been done previously in many studies, such as the validations in [88, 186]. In our work, the same geometry of Peyghambarzadeh et al [86] is built in Ansys® Fluent and the same boundary conditions and properties of the nanofluid are applied in the numerical model (using the method described previously) as in the physical experiment. The results of the enhancement of Nusselt number as a function of the nanoparticles volume fraction, and of Nusselt number as a function of the flow rate show an acceptable agreement with the previous experimental work as shown in Figure 5.4 and Figure 5.5 respectively. Figure 5.4 shows the relation of enhancement of Nu with nanoparticle concentration at Re of 13800 and 23000 and inlet temperature of 308 K. It shows at most a 4 % discrepancy between the experimental and the two phase model numerical work, however this rate increased in case of the single phase to 16 %. Figure 5.5 shows Nu as a function of flow rate at the nanoparticle volume fraction of 1 % in both experimental (previous work) and CFD (current work), with maximum difference between the experiment and two phase numerical results of 9 % but with the single phase model it reaches to 43 %. The two phase model shows a better prediction than the single phase. The difference of the two phase technique could be caused by some factors such as particle size, which affects the viscosity, and temperature dependent properties and the Brownian motion of the particles which affects the thermal conductivity [69, 186, 187].

The accuracy of these techniques (single and two phase) is also investigated through comparison with another numerical work [88]. The same materials with the same volume fraction of nanoparticles is used with the same Re range. The results of the Nusselt number as a function of volume fraction of each value of Reynolds number shows a good agreement as illustrated in Figure 5.6. Since the model works well with water/ EG based Al_2O_3, then it is now applied to

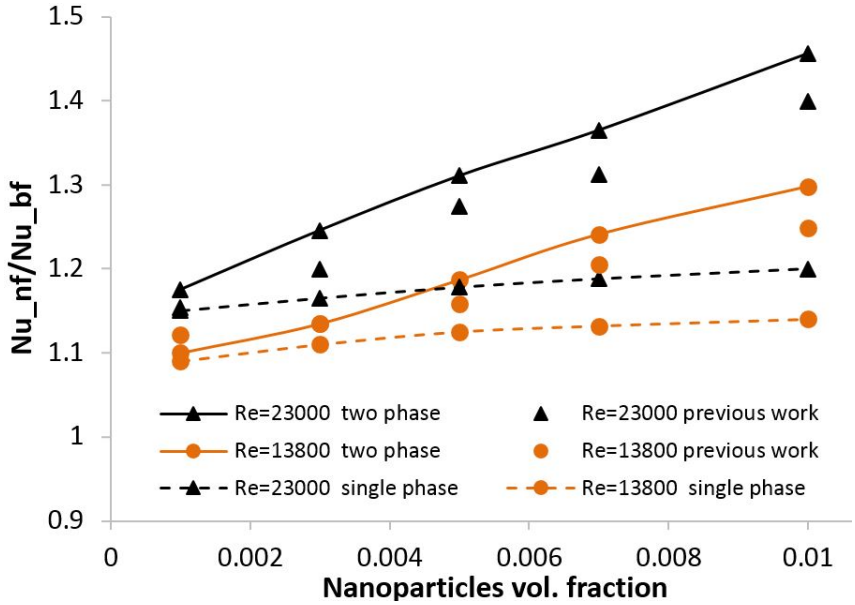


Figure 5.4: Comparison between the enhancement in the Nusselt number as a function of a nanoparticle volume fraction in water at 308 K for different Re in the cases of two phase, single phase of the current study and the previous experiment results of [86].

.

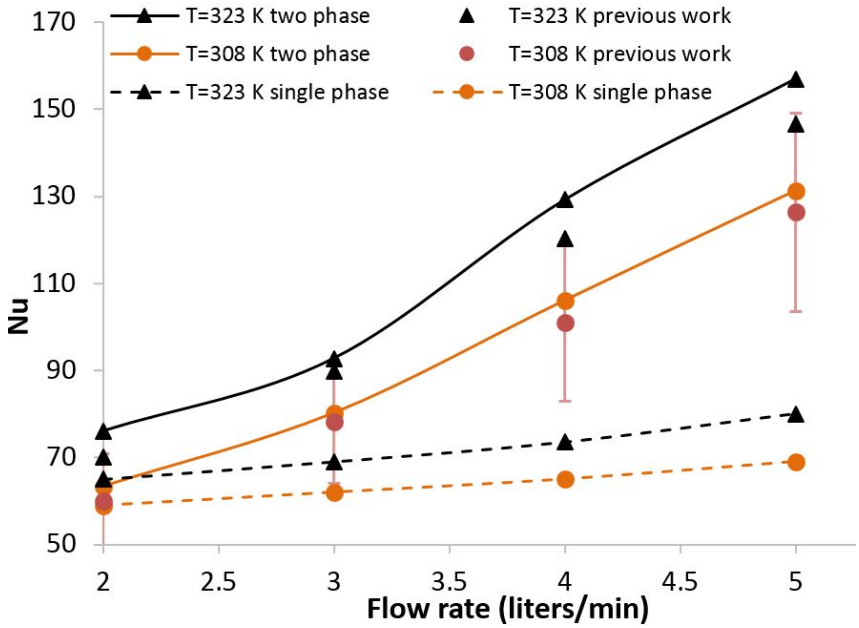


Figure 5.5: Comparison between Nusselt number as a function of a flow rate at the nanoparticles volume concentration of 1 % for different Re in the cases of two phase, single phase of the current study and the previous experiment results of [86].

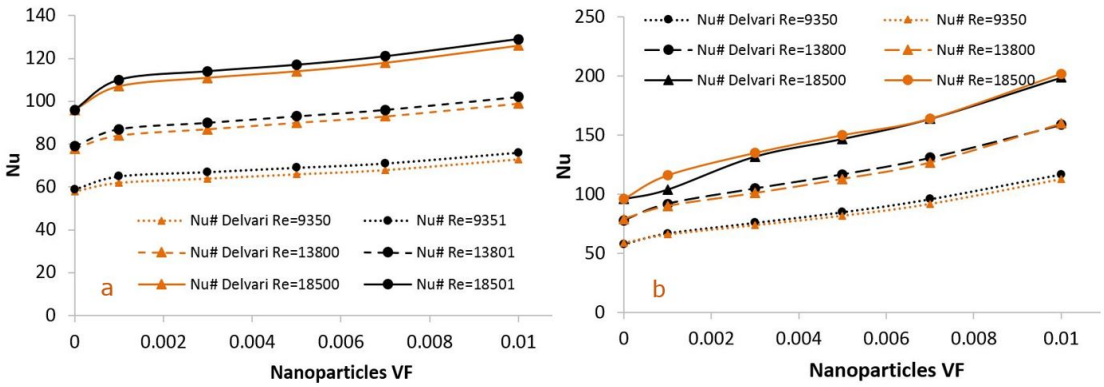


Figure 5.6: Comparison between Nu as function of volume fraction in present study and the numerical study of [88] for a- single phase and b- two models using water mixed with ZnO nanoparticles.

the salt-solution (acetone / $ZnBr_2$ based ZnO nanoparticles) to check the performance of the heat transfer prior to modeling the more complex case of the fluid in flow boiling. The following sections show the effects of different variations (salt and nanoparticles concentrations and Re) for both single and tow phase flow on different parameters such as flow velocity, turbulence and heat transfer.

5.6.3 Effects on the centreline velocity for the novel nanofluid

To understand the behaviour of the velocity development along the tube and how the various parameters affected it, the centreline velocity is analysed under the effects of the variation of the concentrations of both acetone (60 wt.% and 70 wt.%) and nanoparticles (0, 0.1%, 0.5%, 1%, and 1.5%) at Re equals 25000. This provides a reasonable representation of the variation of flow dynamics between the various cases. Centreline velocity is usually the maximum velocity in the pipe and it is greater than the average velocity. For example, for a laminar circular pipe flow, the maximum (centreline) velocity is equal to double the mean velocity and in the rectangular duct the maximum velocity is 1.5 of the average velocity [188].

The centreline velocity has a development length and settles to a final constant value (Figure 5.7). The centreline velocity decreases slightly by increasing the concentration of the nanoparticles as shown in Figure 5.8 due to increasing density and the viscosity of the nanofluid. Increasing acetone decreases the density, but the viscosity drops significantly, for example, it drops from 1.29 mPa.s to 0.63 mPa.s [14], when the mass fraction of acetone increases from 60wt. % to 70wt. %, the shape of the centreline velocity profile is correspondingly more uniform along the length (Figure 5.7). Thus although decreasing density implies increasing velocity, the viscosity increase flattens the velocity profile. According to the data collected from different cases in the present work, the maximum velocities in the laminar and turbulent flow for all cases with all concentrations are:

for laminar

$$v_{cl} = 1.4 v_{av} \tag{5.18}$$

for turbulent

$$v_{cl} = 1.15 v_{av} \tag{5.19}$$

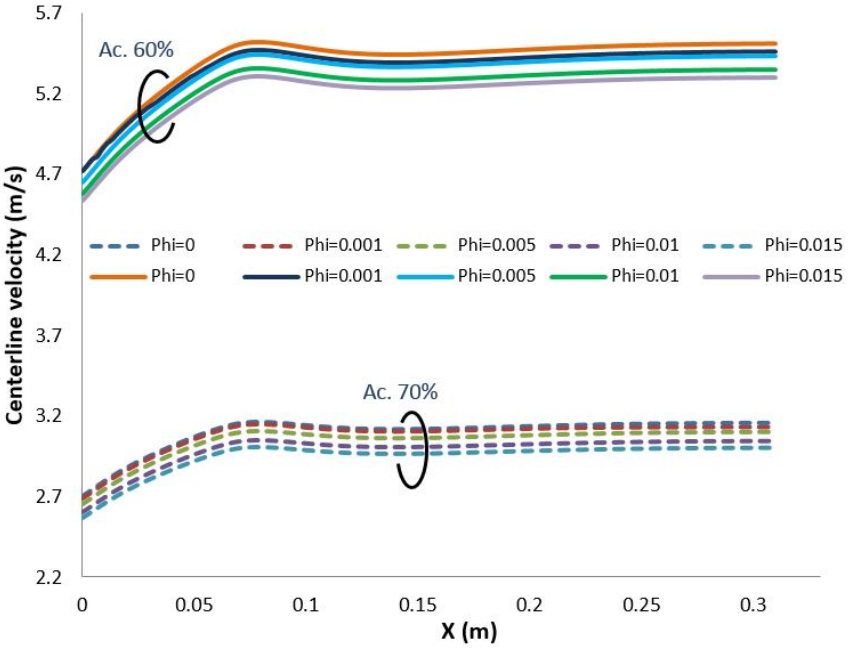


Figure 5.7: Centreline velocity along the tube with different concentration of ZnO nanoparticles and 60 wt.% & 70 wt.% of acetone at Re of 25000.(Present in colour).

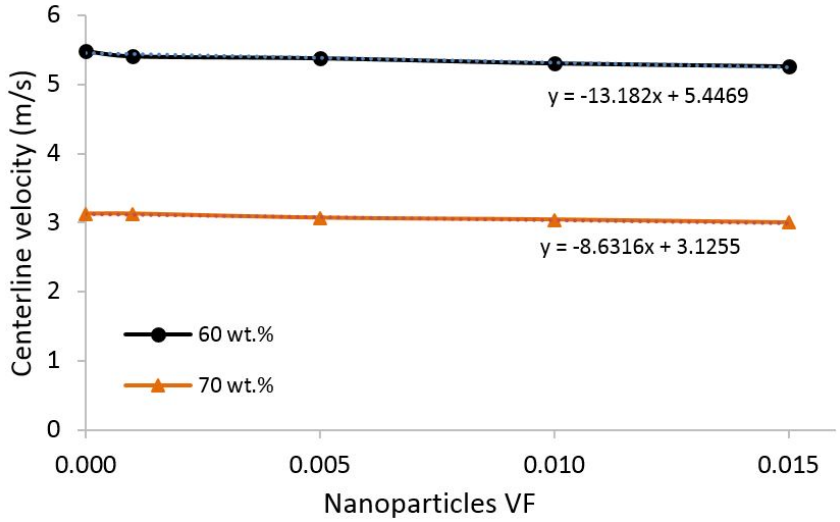


Figure 5.8: Centreline velocities as function of nanoparticles volume fraction at distance 0.15m from the inlet of the tube, for the both cases the acetone concentrations 60wt.% and 70wt.%.

5.6.4 Effects on the turbulence intensity

Turbulence intensity is the ratio between the root mean square of the turbulent velocity to the average velocity in the same location. Figure 5.9 shows that the turbulence intensity slightly decreases by increasing the concentration of nanoparticles along the tube (starts from 0.1 m to show the steady state region only) because by increasing the volume fraction of nanoparticles the density of the solution increases, consequently the velocity drops. The mass fraction of the acetone in the solution has an influence on the turbulence as shown in Figure 5.9 which illustrates that decreasing the acetone fraction leads to an increase in turbulence intensity.

Turbulence intensity has a higher value at the entrance of the pipe, it decreases for the first 5 cm from the entrance and increases to stability after 10 cm. Figure 5.10 illustrates that the turbulence intensity increases with increasing Reynolds number because of the increase in the turbulence velocity.

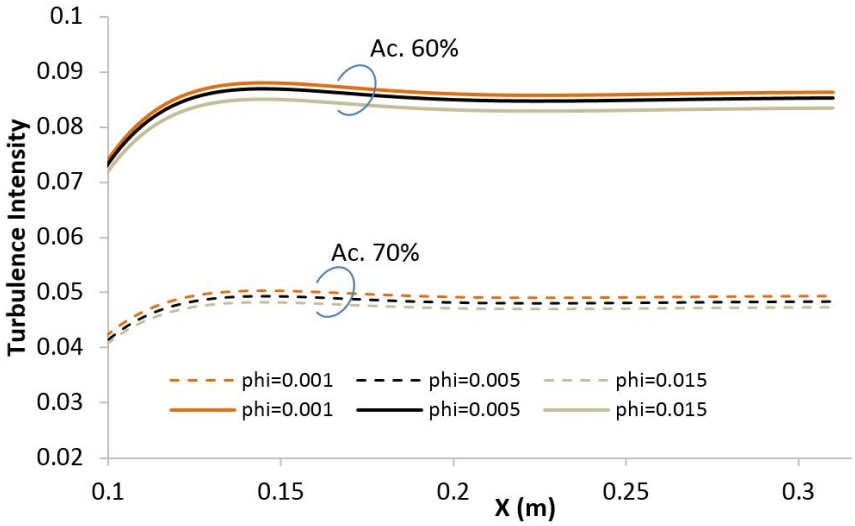


Figure 5.9: Turbulence intensity along the tube with different concentration of ZnO nanoparticles and 60% & 70% of acetone at Re of 30000.

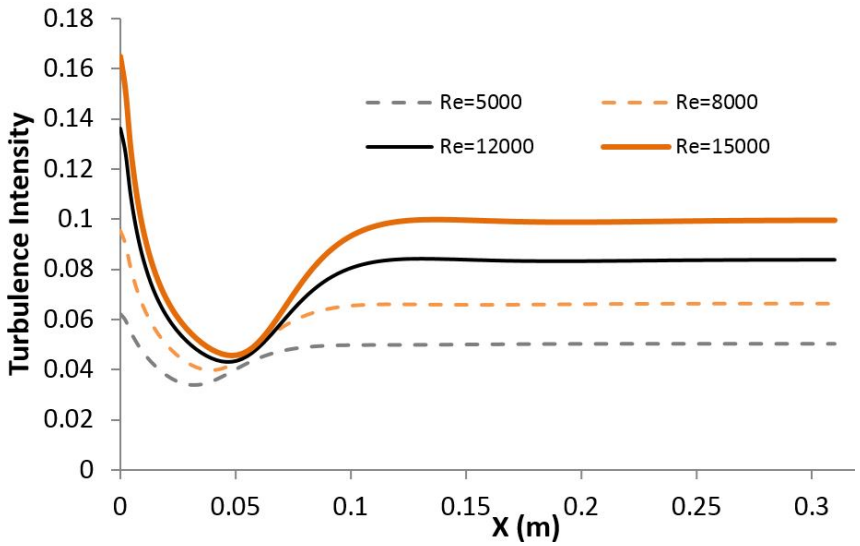


Figure 5.10: Turbulence intensity along the tube with different Re at mass concentration of acetone 50% and concentration of ZnO nanoparticles 0.015.

5.6.5 Effects on the wall shear stress and skin friction

Since each turbulence model simulates the boundary condition, the value of y^+ is an important parameter to predict the effects of the boundary layer. The average y^+ at the tube wall (for the case Re=8000, acetone concentration =50 wt. % nanoparticles concentration= 0.5 vol. %) was calculated. Enhanced wall treatment was implemented in the turbulent flow simulation, which should produce a y^+ value equal to one. The average y^+ at the tube wall is 8.1 for the curved edge of the wall (semi-circular wall) and 0.98 for the flat wall. The good agreement with the existing results, shows that the application of the method in our case is reliably repeated and the curved wall segment has negligible effect due to the y^+.

The magnitude of the wall shear stress, $\tau_w = \mu\frac{du}{dy}$ and the skin friction coefficient $C_f = \frac{\tau_w}{0.5\rho v^2}$ describe the heat transfer by virtue of the Reynolds analogy, $h = \frac{C_f}{2}$.

The effect of the acetone mass fraction on the wall shear stress is illustrated in Figure 5.11. The shear stress decreases sharply when the acetone concentration increases from 30 wt.% to 40 wt.%, the change becomes smoother between

40 wt.% and 55 wt.% and above that the stress becomes stable. The increase in the flow velocity and Re lead to increase in the wall shear stress has expected. The effect of the nanoparticles concentration is negligibly small on the wall shear stress as shown in Figure 5.12.

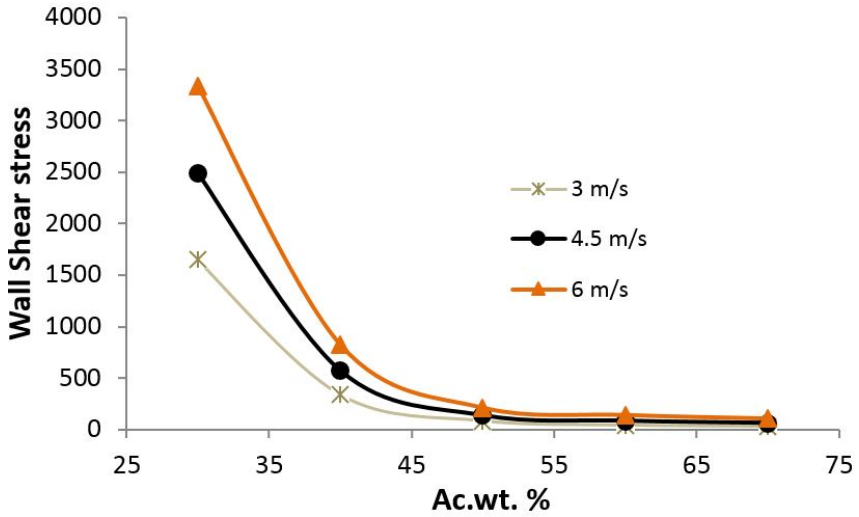


Figure 5.11: Relation between wall shear stress and the acetone concentration at different velocity and 0.01 volume fractions of nanoparticles.

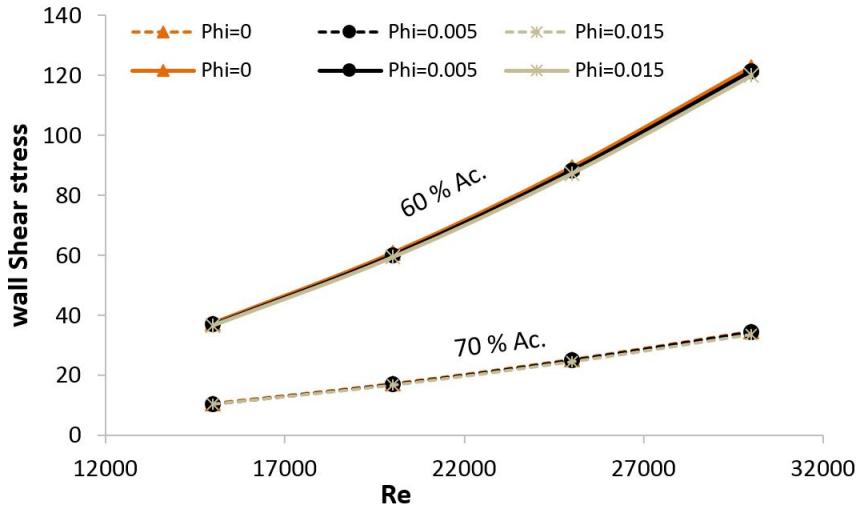


Figure 5.12: Relation between wall shear stress and Re different concentration of ZnO nanoparticles and 60 wt.% & 70 wt.% of acetone.

Figure 5.13 shows that the skin friction decreases with increasing acetone mass fraction as expected from the lowering of viscosity. It also illustrates that the skin friction decreases slightly with increasing the volume fraction of nanoparticles at 60% acetone. This is observed to a lower extent at 70%

acetone. Reducing the acetone concentration and the Reynolds number to less than 60% and 15000 respectively, causes the skin friction to increase with increasing volume fraction of ZnO (Figure 5.14). This result partially contradicts the result of Delavari and Hashemabadi [88] who stated that the skin friction only increases as the nanoparticles volume fraction increases in EG/water. For a high Re (low viscosity, e.g. 60-70 wt. % acetone) particles cause a reduction in skin friction; this may be explained by decreased interaction of particles, which are carried by the convective stream of fluid, in the steep velocity gradient boundary layer. However, for the low Re (i.e. low acetone or high viscosity) similar to the case of Delavari and Hashemabadi study [88] and for the 40 - 50 wt. % acetone case in the current work, the behaviour of the particles near to the surface may be different due to the less steep velocity gradient giving more time for particle interaction.

Table 5.3 details the skin friction variation with volume fraction of nanoparticles with high acetone content (i.e. 60 wt. % & 70 wt. %) at 0.2m from the entrance (the developed region). It shows clearly that the skin friction increases with increasing the nanoparticles concentration and decreases with increasing both of Re and the concentration of acetone.

Table 5.3: Skin friction ($\times 10^{-3}$) at different volume fractions at distance 0.2m from the inlet of the tube.

Nanoparticles VF	Skin friction (acetone 50wt.% Re=2500)	Skin friction (acetone 50wt.% Re=12000)	Skin friction (acetone 60wt.% Re=20000)	Skin friction (acetone 70wt.% Re=20000)
0	60.76	14.20	6.02	1.7
0.001	60.81	14.21	6	1.69
0.005	60.9	14.22	5.95	1.67
0.01	61.04	14.24	5.89	1.65
0.015	61.58	14.34	5.88	1.64

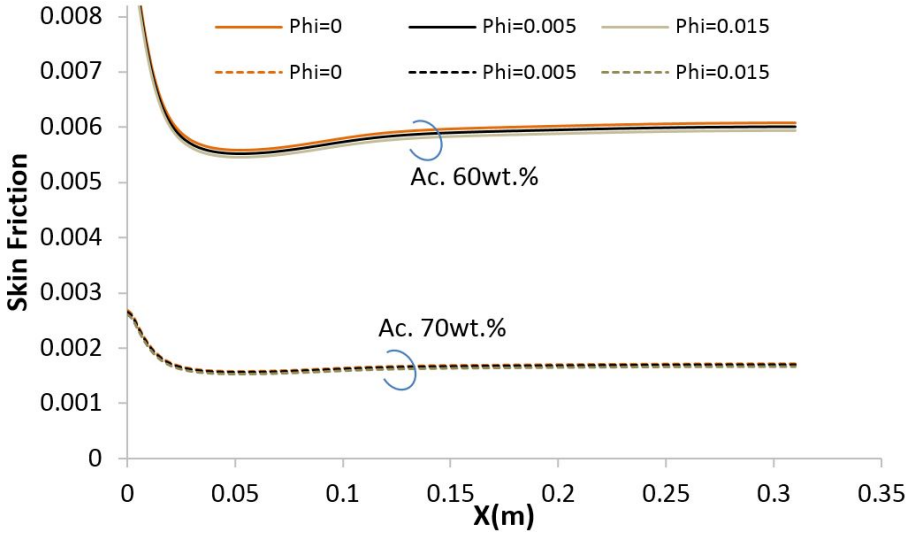


Figure 5.13: Skin friction along the tube with different concentration of a nanoparticles at Re=20000 and for acetone 60wt.% and 70wt.%.

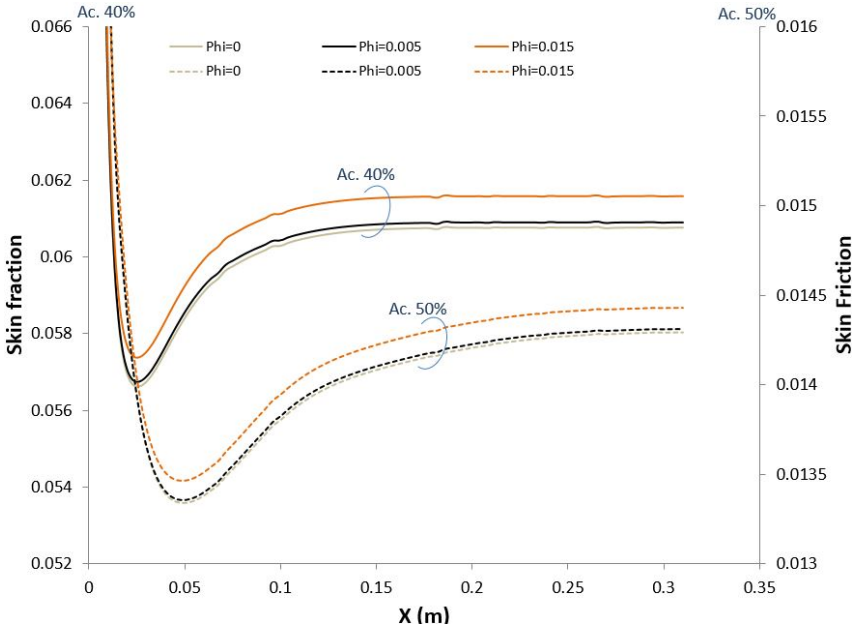


Figure 5.14: Skin friction along the tube with different concentration of a nanoparticles for acetone 40wt.% with Re=2500 and 50wt.% with Re of 12000.

5.6.6 Effect on the heat transfer coefficient

Heat transfer coefficient (h) along the tube was investigated in both the single and two phase model simulation cases under the same conditions. With single phase, acetone 40wt.% and the volume fraction of nanoparticles 1.5%, heat transfer coefficient is 1800 $W/m^2.K$ at the entrance of the tube and slightly decreases as the Reynolds number decreases as shown in Figure 5.15.

In the two phase model, the heat transfer coefficient starts at a higher value, decreases sharply for the first several centimetres and then decreases linearly to the end of the tube. In addition, Figure 5.15 shows that the heat transfer increases with increasing Reynolds number, and this is likely to be because the velocity of the fluid increases which leads to an increase in turbulent motion of the particles and molecules which consequently leads to more heat transfer.

Figure 5.16 shows the enhancement of the local heat transfer related to the concentration of nanoparticles; for the two phase model with acetone mass fraction 50% the enhancement reaches 180%, but in the single phase model a very poor enhancement is noticed and this behaviour is confirmed by many previous studies [14, 158, 189].

The difference between the single and the two phase models in calculating heat transfer coefficient happens because in the single phase model the heat transfers through the collisions between the molecules of the liquid and the molecules transport heat; but in the two phase model the heat transfer, in addition, is enhanced by collision between molecules and particles (Brownian motion), collision between the nanoparticles and these particles also transport heat within the material.

As shown in Figure 5.17 the heat transfer coefficient increases with increasing acetone mass fraction and the velocity of the fluid at 1% of nanoparticles concentration; this behaviour happened because with a low concentration of

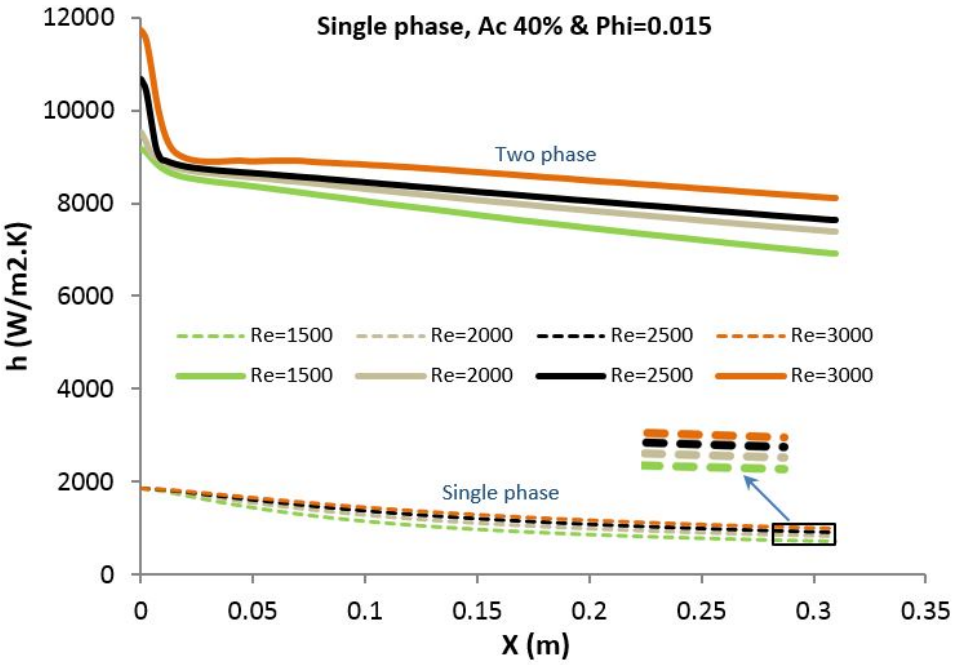


Figure 5.15: Variation of the heat transfer coefficient along the tube wall in both of single and two phase approaches for the same values of Re.(Presents in colour)

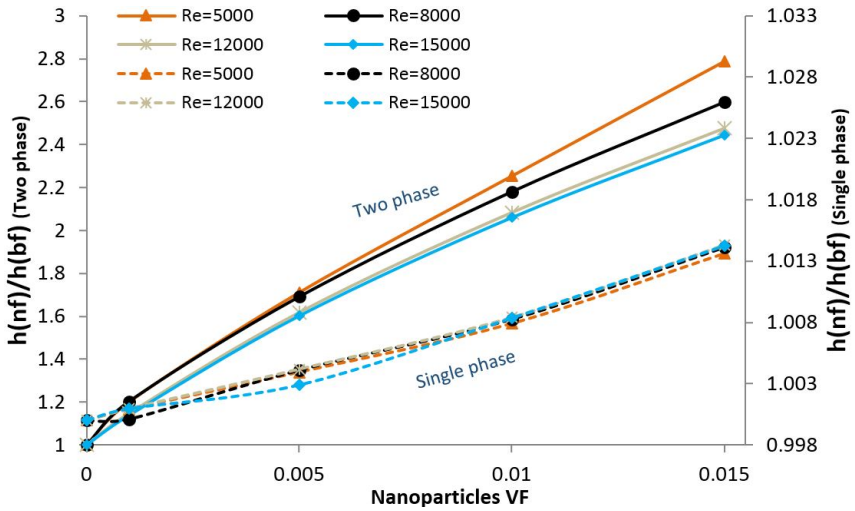


Figure 5.16: Variations of the numerical results of $h_{nf}/h_{bf}$with different concentration of nanoparticles in single and two phase approach (at acetone concentration of 50%).(Presents in colour)

acetone (for example 30 wt. %) the density and the viscosity of the fluid are very high 2617 kg/m^3 and 0.2633 Pa.s [14] respectively, thus, the particles and the molecules cannot move with high random motion and consequently the heat transfer has the lowest value especially with a low temperature. The Nusselt number increases with volume fraction increase of nanoparticles. The Nusselt of the acetone/$ZnBr_2$ (acetone 50 wt. %, 60 wt. % and 70 wt. %) is greater than the Nusselt of H_2O/Al_2O_3 which was used by [88] for the same volume fraction and Re as shown in Figure 5.18, this seems to be because the rate of the convection to conduction for the acetone/$ZnBr_2$ higher than the H_2O/Al_2O_3.

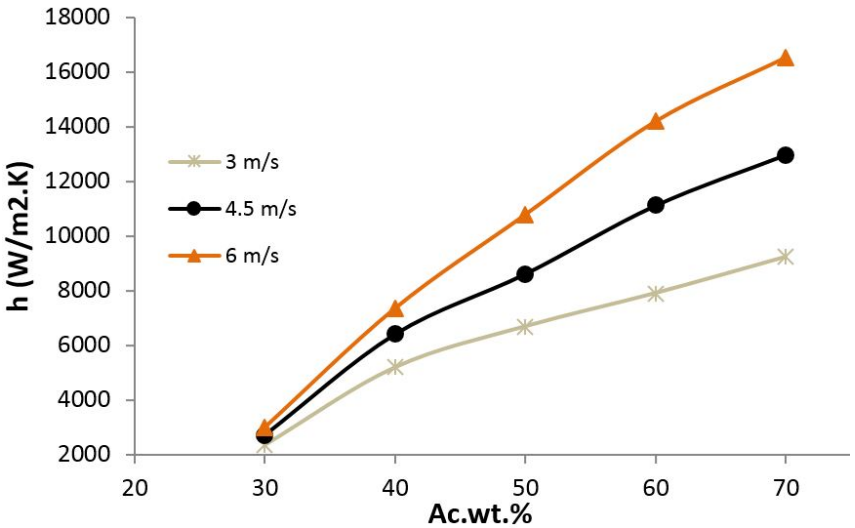


Figure 5.17: Relation between heat transfer coefficient and acetone mass fraction with different velocity of fluid and volume fraction of nanoparticles of 0.01.

Table 5.4 shows numerical results for the two phase approach of the heat transfer coefficient with different concentrations of acetone, different concentrations of nanoparticles and different Reynolds numbers. From the equations which calculate the properties of the nanofluid, the density, viscosity and thermal conductivity increase and the specific heat decreases with increasing the concentration of nanoparticles. Concentration of the nanoparticles has a significant effect on heat transfer coefficient; concentration of acetone also has

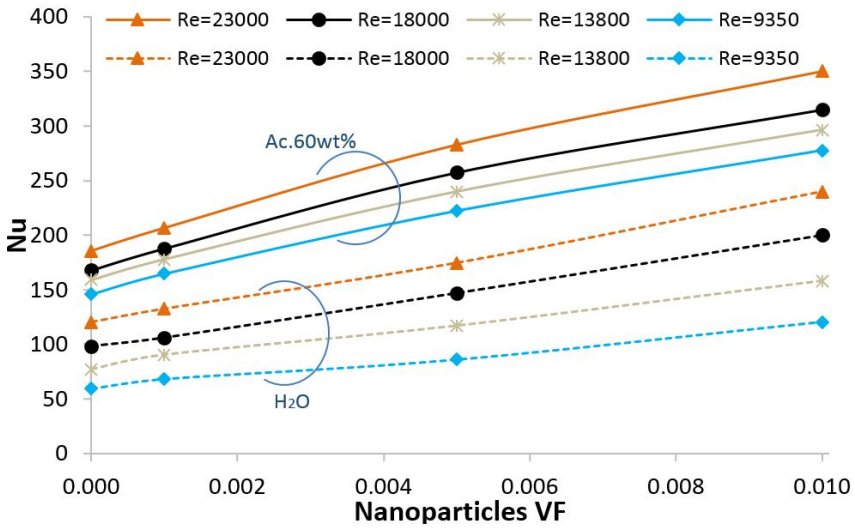


Figure 5.18: Nusselt number as function of the volume fraction for different Re and for the H_2O/Al_2O_3 case [88] and acetone $/ZnBr_2$ (acetone 60%)/ ZnO for a two phase model flow.

Table 5.4: Numerical results of the heat transfer coefficient with different concentration of acetone and nanoparticles and different Re.

Acetone mass fraction	Re	0%	0.1%	0.5%	1%	1.5%
		h$(W/m^2.K)$				
30%	200	1158	1360	1942	2559	3106
	250	1231	1463	2095	2763	3357
	300	1289	1550	2227	2942	3576
40%	2000	2641	3009	4356	6243	8013
	2500	3017	3415	4860	6483	8281
	3000	3384	3823	5372	7090	8657
50%	8000	3336	3792	5330	6874	8192
	12000	4290	4877	6875	8856	10526
	15000	5150	5856	8239	10599	12580
60%	20000	4786	5420	7458	9343	10841
	25000	5799	6575	9016	11286	13074
	30000	6788	7672	10536	13163	15229
70%	20000	3636	4106	5554	6809	7754
	25000	4400	4967	6702	8196	9318
	30000	5145	5804	7817	9545	10835

a significant effect on the variation of Re, which consequently significant effects on the heat transfer. The Brownian motion effect of the nanoparticles in the fluid has a significant impact on increasing the heat transfer for the nanofluid. The boundary layer thickness decreases because of the random motion of nanoparticles in the fluid and this leads to increasing the heat transfer between the wall and the bulk fluid [178].

5.7 Summary

Laminar and turbulent mixed convection of acetone/$ZnBr_2 - ZnO$ nanofluid inside a flat tube were studied numerically using a single phase and a two phase mixture approach. The validation of this work was confirmed by repeating a case for a nanofluid ($Al_2O_3 - H_2O$) which was used by the experimental work of Peyghambarzadeh [86] and numerical work of Delavari and Hashemabadi [88]. From the validation process it was verified that the two phase model gives a much better prediction than the single phase model as described in the literature. A good agreement was found from the validation, demonstrating reliable implementation of the method. The main part of the study goes on to show that for the acetone/zinc bromide solution with ZnO nanoparticles, the heat transfer increases with Re and concentration of both nanoparticles and acetone, as expected from the theory. The two phase method shows a strong effect of the nanoparticles on improving the heat transfer, which given the reliability of the method in the previous case of [88], provides reasonable confidence in a positive outcome in the event of using the fluid in a heat transfer situation like the absorption refrigeration cycle.

Wall shear stress increases with increasing Re and decreases with increasing acetone concentration because the viscosity of the fluid decreases; it is not altered noticeably by changing the concentration of nanoparticles. Increasing

the wall shear stress indicates improving heat transfer to the wall, therefore there is not a direct heat transfer benefit due to nanoparticles by the wall shear stress. The behaviour of the skin friction depends on the concentration of acetone as well as Re as reflected in the wall stress. The effect of increasing concentration of nanoparticles on the skin friction is significantly affected by acetone concentration and Re: the skin friction decreases with increasing concentration of nanoparticles at 70wt. % of acetone and Re of 20000, but it increases with increasing volume fraction of the nanoparticles at 60wt. % of acetone and Re of 15000. We suggest that this may be due to particles interaction increasing in the low Re velocity gradient, where there is increased interaction time as suggested in the formulation of nanoparticle cloud viscosity used. The overall performance of the solution with the nanoparticles shows a promising enhancement for the heat transfer challenge of the vapour absorption refrigeration system, since an enhancement of up to 180% of basefluid can be achieved with only 1.5% volume fraction of particles. The concentration of the salt solution base fluid has a significant effect on the heat transfer enhancement together with the nanoparticles.

6

NUMERICAL STUDY OF FLOW BOILING OF THE NANO-SALT-FLUID IN THE BOILER

6.1 Introduction

A new technique of a numerical solution characterizing the boiling process of nano-salt-fluid using four phase flow is described in this chapter. This technique evaluates the enhancement of the heat transfer in the boiling process of the novel fluid and investigates the behavior of the fluid in the boiler under the effect of different variations such as nanoparticles concentration, boiler temperature and the flow rate. In this Chapter:

- Summarizing the literature of the boiling process.
- Describing a novel method of the boiling process used in this study.
- Describing the mathematical modeling of this method.
- Describing the geometry, the mesh and the boundary condition with the validation of the method.
- Quantifying the mixture model by showing the effects of each variation on the behavior of heat transfer and fluid flow.
- Visualizing the flow with the VoF and mixture models.

6.2 Summary of related literature and justification for research

Enhancement of heat transfer properties of fluids can reduce the size of heat transfer systems and operational cost [146]. Flow boiling heat transfer occurs in vapour absorption refrigeration systems as well as in various industrial areas, such as refrigeration systems, power generation, chemical engineering, high-power electronics component cooling, and nuclear reactor cooling [129]. Improvements in flow boiling heat transfer systems can improve energy efficiency and offer a route to reduce global energy consumption. To improve the heat transfer of the fluid, the behaviour and the properties of the fluid itself should be enhanced. Nanofluids (i.e. homogeneous base fluids interlaced with nano-scale particles that are modified with chemical/physical processes such as sonication and adding surfactants) are an alternative to Newtonian fluids for thermal and industrial applications due to their modified thermo-physical properties which can enhance the efficiency of boiling process [130].

A considerable amount of research has been devoted to the investigation of heat transfer in the nanofluids numerically. This subject has received much attention from research workers:[81, 88, 102, 154, 180, 182, 183, 187, 189, 190, 191, 192]. A critical review of the heat transfer in the nanofluid is given by [129, 130]. Many researchers studied the boiling process of the nanofluid experimentally [63, 112, 134, 137, 138, 144, 174, 193, 194, 195]. Just a few works dealing with a numerical analysis of the nanofluid boiling were found [145, 146, 147, 196]. However, there remains much to be investigated and understood about the nanofluid boiling behaviour, and in particular the effects of the concentration of the nanoparticles in the solution. Moreover, reports on the mechanism of the flow boiling numerically are limited and there is no study found related to modelling and analysing nano-salt-fluid flow numerically. The validation of CFD models requires experimental data that charac-

terise the important flow parameters and over a wide range of values. In this chapter, a description of the CFD model and the results obtained will be presented and discussed. From the literature, forced convection for the nanofluid including experimental and numerical studies of flow and pool boiling for different types of nanoparticles in different basefluids has been reviewed. The current work adds a new line in this area, by studying and developing a novel CFD application technique simulating a four phases flow situation of boiling of nano-binary-fluid (for acetone / $ZnBr_2$ based on Graphene nanoparticles). The aim of this part of the work is to provide a better mechanism for understanding the heat and mass transfer behaviour of acetone boiling in the $ZnBr_2$ nano-salt-fluid under the effect of different variables in a rectangular symmetric boiler (part of a proposed VARS system). A user defined function (UDF) code was identified from the available literature ([197]) and used for the mass transfer and the phase change. This study uses both the mixture and VoF (volume of fluid) models with various boiler temperatures, inflow velocities and nanoparticles concentrations to find out what each model can offer in terms of characterizing the flow.

Different flow conditions (e.g. heat flux, heat transfer coefficient, flow rate in the condenser, pressure of the system) and nanofluid characteristics (e.g. boiling point temperature and the saturation temperature of the pure acetone in the condenser) are found using the results of experiment cases. In order to achieve an beneficial simulation, the results should present a real motion of the fluid. Therefore, the simulation was run under similar conditions to those used in the experimental investigation of this thesis so that a proper comparison with the experiments can be performed. The agreement is found to be both qualitatively and quantitatively satisfactory. CFD modelling cannot be a total exchange for experimental works, but it offers scope for investigation which

would be impossible to provide with physical experiments. Simulate different flow conditions and environments without the effort and expenses needed for real experiments is possible with CFD. Once a CFD model of a particular case setup has been validated as being of reasonable accuracy (by validating with real experimental results), the parameters governing the fluid flow can then be varied to suit different flow conditions using CFD simulations.

6.3 Method

There are two methods of simulating heat and mass transfer and flow of a nanofluid in Reynolds-averaged Navier–Stokes equations (RANS) CFD: the first method is a single phase approach with effective physical properties such as thermal conductivity, heat capacity, density and viscosity of a single composite fluid representing the characteristics of the nanofluid in bulk ([58]). The second method is a two (or multi-) phase approach, which defines the first phase as a fluid and the second phase as a fluid cloud of nanoparticles (solid properties represented in a dispersed medium) as described in last chapter. The two phase model is found in literature to provide improved predictions over the single phase model for the prediction of heat transfer in liquid flow situations ([88, 158]) and to provide useful indications of the behaviour of proposed novel nanofluids ([81]); such as the two phase method with Eulerian-Eulerian approach applied in this work. Further to the nanofluid component simulation, a part of the acetone in the binary fluid (acetone / $ZnBr_2$) will evaporate due to heating.

To make just the acetone evaporate from the solution (acetone / $ZnBr_2$), the salt solution is proposed as a two component fluid, the first fluid is acetone and the second fluid is acetone / $ZnBr_2$ and just the first fluid (acetone) undergoes evaporation. For example, when the concentration of the acetone

is 50wt. % in the solution (acetone / $ZnBr_2$), it is proposed that the pure acetone is 25wt. % which is undergoing the evaporation and the other 25 wt. % is the concentration of acetone in the solution (acetone / $ZnBr_2$). The reason for this technique is that the CFD method cannot separate and evaporate a specific component of the homogeneous solution. Therefore, four phases are represented in this work: 1- the solid phase as a cloud of nanoparticles, 2- the first liquid phase (pure acetone), 3- the second liquid phase (acetone / $ZnBr_2$) and 4- the vapour phase (acetone vapour). During and after the evaporation, the nanoparticles stay mixed with the liquid phase, consequently, the concentration of the nanoparticles in the solution at the outlet of the boiler is higher than the inlet section because a part of the liquid (pure acetone) will evaporate, and the liquid volume flux will be correspondingly less.

The mixture method is used to solve the boiling case but it does not show the bubble formation. Therefore, the VoF model is applied separately. It can model two or more immiscible fluids, and can show how the vapour phase behaves. Unlike the mixture method, fluids having different densities do not interpenetrate, and separation occurs.

In our VoF method, the densities of the nanoparticles and the liquid phases are artificially made to be the same (using equation 6.1) to overcome the buoyant separation and keep the solution well mixed using the equation below, but the density of the vapour is physically correct. However, in the mixture model the real densities of the phases were used.

$$\rho = \sum_{k=1}^{n} \rho_k \Phi_k \tag{6.1}$$

Generally, both methods offer different observations: the mixture method shows interpretation and stratification of the continuum and describes the phases behaviour. The VoF method is particularly useful for observing the

general behavior of the vapour bubble. Both methods use the two-phase approach for the nanoparticles.

The concentration of acetone liquid (25 %) undergoing evaporation was chosen after comparing the results of the heat flux (HF), heat transfer coefficient (HTC) and the temperature at the outlet section of the boiler for different amounts of acetone liquid (20 %, 23 %, 25 %, 27 % and 29 %) against the experimental results at 153 K boiler temperature and 3.66 ml/s flow rate and two different nanoparticles concentration 0 vol% and 0.3 vol%. For both cases, HF and HTC are more predicted the experimental results at the high concentration of liquid acetone, however, the outlet temperature predicts the experimental results at the low concentration. The 25 % concentration of liquid acetone was chosen as the standard concentration for running the models because it is collecting a sensible results of all parameters as shown in Table 6.1. The 29 % of the liquid acetone means that there is 21 % of acetone mixed with 50 % $ZnBr_2$, which makes the concentration of $ZnBr_2$ in the working solution 70 %. This is the maximum concentration of salt ($ZnBr_2$) that can dissolve in 30 % of acetone. The properties of the salt solution which used in the numerical modelling were also found till this level of concentration.

The instigation of bubble nucleation in the numerical model does not directly consider surface nucleation sites. It assumes that where the thermodynamic criteria for bubble generation are satisfied, that a bubble will form. This relies on the assumption that there are appropriate surface imperfections in the heated surface, which we consider to be a reasonable approximation given the surface roughness of a typical heated surface in the order of micrometres.

Table 6.1: Comparisons of the results of the heat flux (HF), heat transfer coefficient (HTC) and the temperature at the outlet section of the boiler for different concentration of the liquid acetone (undergoing the evaporation) with the experimental results of these parameters.

	VF=0.003, T=153 ^oC & $\dot{v} = 3.66ml/s$			VF=0, T=153 ^oC & $\dot{v} = 3.66ml/s$		
Liq. acetone concentration	HF (kW/m^2)	HTC (W/m^2K)	T_{out} (K)	HF (kW/m^2)	HTC (W/m^2K)	T_{out} (K)
20 % $(Ac/ZnBr_2 = 80\%)$	10.5	139	355	13	133	355.3
23 % $(Ac/ZnBr_2 = 77\%)$	10.2	133	353	13.4	134.4	355
25 % $(Ac/ZnBr_2 = 75\%)$	9.8	124	352.7	13.8	136.6	353.7
27 % $(Ac/ZnBr_2 = 73\%)$	9.7	123	351	13.8	139	352.5
29 % $(Ac/ZnBr_2 = 71\%)$	9.75	122	350.3	13.9	142	351.7
Experimental	9.7	123	354	13.8	144	357

6.4 Mathematical model

The liquid acetone, acetone/$ZnBr_2$ and nanoparticles cloud are miscible and well mixed phases. Therefore, it is best solved and presented via the mixture model. A mixture model can be used for homogeneous multiphase flows with very strong coupling and phases moving at the same velocity. The mixture is assumed to be incompressible fluid. Alternatively, VoF represents interaction of immiscible fluids. The governing equations used for the transient evaporation process are applied using models provided by Ansys Fluent® ([184]) and a UDF code for a mass and energy source terms.

In the mixture method, the following equations apply:

Momentum:

$$\frac{\partial}{\partial t}(\rho\vec{\nu}) + \nabla.(\rho\vec{\nu}\vec{\nu}) = -\nabla P + \nabla.(\mu\nabla\vec{\nu}) + \rho g + \vec{F} + \nabla.\sum_{k=1}^{n}\Phi_k\rho_k\vec{\nu}_{dr,k}\vec{\nu}_{dr,k} \quad (6.2)$$

Energy:

$$\frac{\partial}{\partial t}\sum_{k=1}^{n}\Phi_k\rho_k E_k + \nabla.\sum_{k=1}^{n}\Phi_k\vec{\nu}_k(\rho_k E_k + P) = \nabla.(k_{eff}\nabla T) + S_E \quad (6.3)$$

where P is pressure in $kg/m.s^2$, and

$$E_k = h_k - \frac{P}{\rho_k} + \frac{\nu_k^2}{2} \quad (6.4)$$

And S_E is a source term of energy in $(J/m^3.s)$.

The standard k-ε, turbulence model is used, ([184]) for turbulence kinetic energy (k) and dissipation rate (ε). The standard k-ε model is valid only for fully turbulent flows, appropriate for a boiling fluid.

In order to calculate the phase volume share, the volume fraction expression is used as follows

$$\frac{\partial}{\partial t}(\Phi_v\rho_v) + \nabla.(\Phi_v\rho_v\vec{\nu}_m) = -\nabla.(\Phi_v\rho_v\vec{\nu}_{dr,k}\vec{\nu}) + S_M \quad (6.5)$$

A user defined function (UDF) for the mass and energy source terms (the UDF code provided in appendix B) due to evaporation is included. The UDF for mass source S_M in $(kg/m^3.s)$ for each phase was developed depending on the mass and energy source terms (equations 6.6 - 6.7), previously defined by Lee in 1980 ([198]). These formulae have been validated and used successfully by several different authors, see for example ([196, 197, 199, 200]).

$$\mathcal{S}_{\mathcal{M}} = \begin{cases} 0 & T_l < T_{sat} \\ \epsilon \Phi_l \rho_l \frac{|T_l - T_{sat}|}{T_{sat}} & T_l \geq T_{sat} \end{cases} \tag{6.6}$$

$$S_E = \epsilon \Phi_l \rho_l \frac{|T_l - T_{sat}|}{T_{sat}} \Delta H_{fg} \tag{6.7}$$

Where H_{fg} is the enthalpy of the evaporation, T_{sat} is saturation temperature and ϵ is a time relaxation factor with unit 1/s, which can be calculated via equation 6.8.

$$\epsilon = \frac{6}{d_b} \beta \sqrt{\frac{M}{2\Pi R T_{sat}}} L \left(\frac{\Phi_v \rho_v}{\rho_l - \rho_v}\right) \tag{6.8}$$

Where d_b is bubble diameter which we assumed an average is 2mm (calculated as an average of different diameters measured for different single bubbles of the vapour volume fraction contour during the simulation of VoF model), β is accommodation coefficient, M is molar mass of acetone (0.058 $kg/mole$), R is universal gas constant (8.314 $J/mol.K$), L is latent heat for acetone (518000 J/kg), Φ_v is vapour volume fraction.

The accommodation coefficient (fraction of number of molecules entering the liquid phase to number of molecular collisions with the surface) is treated commonly as a two-step process: 1- the vapour molecules strike the surface then they are adsorbed, 2- the vapour can enter into the bulk of surrounding liquid. Consequently, if β is equal to unity, each molecule striking the surface enters into the liquid and is not adsorbed.

The viscosity of the nanoparticles cloud is calculated by equations 5.14 - 5.17 together with the viscosity of the combination of the base fluid alone and of the cloud of nanoparticles as expressed in equation 5.10 (explained in the last chapter).

The VoF method was also applied to illustrate the behaviour of the vapour

distinct from the liquid. The continuity equation for volume fraction performs the tracking of interfaces between the phases. The previously defined energy and mass source terms apply here as well as the viscosity term for the nano-particles.

$$\frac{1}{\rho_k}[\frac{\partial}{\partial t}(\rho_k \Phi_k) + \nabla.(\rho_k \vec{\nu}_k \Phi_k) = S_M + \dot{m}_{lv} \tag{6.9}$$

Where Φ_k is volume fraction of the phase k, l refers to liquid, v refers to vapour, i.e. $\dot{m}_{lv}$ is the mass transfer from the liquid to the vapour phase.

The volume fraction equation is solved by explicit time discretization. In the explicit method for the transient simulation, ANSYS Fluent's standard finite-difference interpolation structures are applied to the volume fraction values that were calculated at the previous time step.

$$\frac{\alpha_k^{n+1}\rho_k^{n+1} - \alpha_k^n \rho_k^n}{\Delta t} V + \sum_f (\rho_k U_f^n \alpha_{k,f}^n) = [S_E + \dot{m}_{lv}]V \tag{6.10}$$

$n+1$ and n are indices for current and previous time step respectively. α is face value of the q^{th} volume fraction, V is volume of cell and U_f is volume flux through the face, based on normal velocity.

The momentum and Energy equations are:

$$\frac{\partial}{\partial t}(\rho\vec{\nu}) + \nabla.(\rho\vec{\nu}\vec{\nu}) = -\nabla P + \nabla.(\mu\nabla\vec{\nu}) + \rho g + \vec{F} \tag{6.11}$$

$$\frac{\partial}{\partial t}(\rho E) + \nabla.(\vec{\nu}(\rho E + p) = \nabla.(k_{eff}\nabla T) + S_E \tag{6.12}$$

Where E is the energy which can be calculated through the following relation:

$$E = \frac{\sum_{k=1}^{q} \Phi_k \rho_k E_k}{\sum_{k=1}^{q} \Phi_k \rho_k} \tag{6.13}$$

Where E_k for each phase is dependent on the specific heat of that phase and the temperature. The properties ρ and k_{eff} (effective thermal conductivity) are common between liquid phases (as explained in 6.3). The source term, S_E contains the radiation and any other volumetric heat sources. To get more understanding of the fluid behaviour in the boiler, turbulence intensity (ratio of the root mean square of the velocity variation to the average velocity) is also investigated depending on the equation 6.14.

$$I = \frac{\grave{\nu}}{\nu_{ave}} = 0.16(Re_{D_H})^{-1/8} \tag{6.14}$$

where

$$\grave{\nu} = \sqrt{\frac{(\nu_1^2 + \nu_2^2 + \nu_3^2 + ... + \nu_n^2)}{n}} \tag{6.15}$$

The discretisation scheme in this work is first order; investigation of the effect of using either second order or QUICK demonstrated negligible differences for the solution criteria inspected. First order demonstrated acceptable accuracy when compared against the validation experimental data, and the shorter simulation times were necessary for the large number of transient numerical solutions that were solved. Geo-reconstruct scheme (represents the interface between fluids using a piecewise-linear approach and it assumes that the interface between two fluids has a linear slope within each cell, and uses this linear shape for calculation of the advection of fluid through the cell faces. It uses when the cell is near the interface between two phases. In fluent it is the most accurate and is applicable for general unstructured meshes.[184]) adopted for volume fraction.

6.5 Geometry and boundary condition

A flat plate boiler channel is chosen which is suitable for mounting on the back of a solar PV array to provide cooling of the concentrated solar energy surface during operation. In practice the size would be 30cm square, but we take a smaller channel within this larger design, and only the lower section is heated in order to separate the effect of boiling and flow downstream. The geometry used is shown in Figure 6.1, in which a half section with symmetry plane x-z is modelled.

Fluid flows in the horizontal direction. The boundary condition at the inlet is a constant velocity and the outlet is outflow, which is obeyed in fully-developed flows where the diffusion flux for all flow variables in the exit direction is zero as used previously in similar cases e.g. ([196, 145]). A constant wall temperature is assumed for the heated lower wall and the two other walls (one of the sides and the top) are adiabatic. The gravity direction is vertically downward and there are no significant gradients in the flow direction. A symmetric boundary is seen in the front view (on the y=0 plane) (other side wall) shown in Figure 6.1.

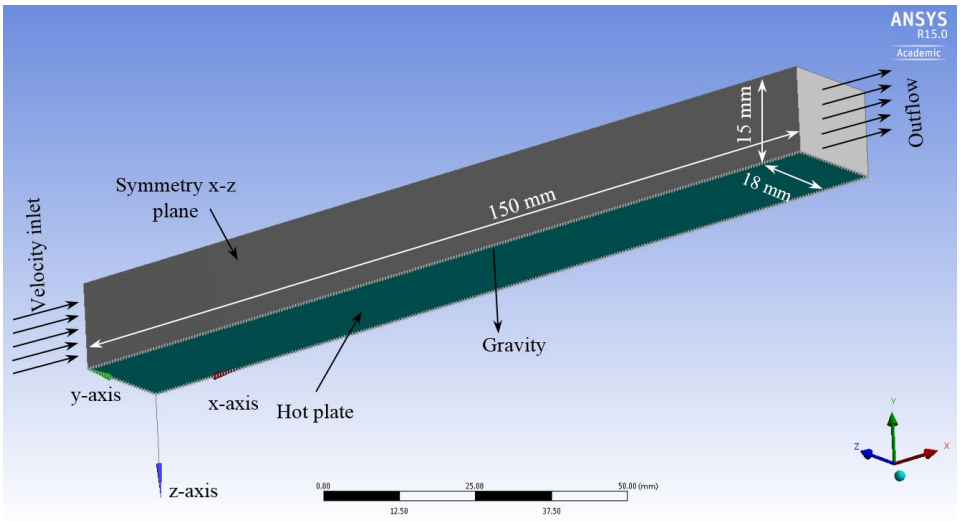


Figure 6.1: Geometry and the boundary conditions of the symmetric boiler used to boil the solution acetone/$ZnBr_2$ with graphene nanoparticles.

A no-slip condition is applied for liquid and vapour phase velocity on the channel surface. The total simulation time depends on the flow rate (time needed for fluid to pass from the inlet section till the outlet section) for which a time step size of 0.005 seconds is used (takes approximately 15 hours of wall clock time). The following flow conditions are investigated which simulate a proposed experimental boiler condition, as tested in the experimental work of chapter 4:

- Inlet flow rate 2.31, 3.66, 4.27 and 7.1 ml/s;
- Hot wall temperature 411, 418, 426, 436 & 446 K;
- Mass fraction of the $ZnBr_2$ in the entering solution is 50 wt. % and
- Volume fraction of the nanoparticles is 0, 0.1, 0.2, 0.3, 0.4 and 0.5 vol. %.

The vessel pressure is at atmospheric and it is appropriate for low temperature boiling in the order of $340K$. This study does not present the simulation of the change in the vapour saturation temperature as the concentration changes. In reality, as salt concentration increases, saturation temperature increases, and there will be reduced vapour production for a particular boiler temperature as the concentration changes with proceeding evaporation (e.g. at the atmospheric, acetone will boil at T_{sat}=330K, but 50% solution boils at T_{sat}=340K). (see log P-T diagram for the solution acetone – zinc bromide plot on (see Figure 4.16 [14])). In the work presented here, saturation temperature is maintained at $309K$. The properties of each phase used in this model are in Table 6.2 the viscosity of the nanoparticles cloud is calculated via equation 5.10 & equations 5.14-5.17.

Table 6.2: properties of each phase used in the numerical analysis

	Density (kg/m^3)	Viscosity $(kg/m.s)$	Thermal conductivity $(W/m.K)$	Specific heat $(J/kg.K)$
Acetone liquid	791	0.000331	0.18	2160
Acetone vapour	0.498	8.5×10^{-6}	0.0145	4.374
$Ac/ZnBr_2$	1825	0.2633	0.145	780
Nanoparticles	5606	0.002252 (cloud)	36	40.3

6.6 Mesh independence study:

CFD simulations are computationally complecated. The size of the grid mesh has a significant influence on the outcome accuracy and the time of running of the simulation. Mesh independence investigations are achieved to find a minimum mesh density required to give an accurate results with shorter running time. And further, refining the mesh would not change the results and integrated quantities. In practice, mesh independence depends when further mesh refinement yields only small and therefore small changes in the numerical solution found.

In order to identify the minimum mesh density, mesh sensitivity analysis was performed. Different regular hexahedral (Figure 6.2 a) and hexahedral bias (higher density grids near the hot wall as shown in Figure 6.2 b) grid sizes ((x,y,z): (121, 41, 41), (151, 51, 51), (161, 61, 61) & (151, 71, 71)) were taken to choose the best mesh regarding accuracy and solution time of the simulation. The meshes were compared by the generated vapour mass flow and heat transfer coefficient on the wall using the same boundary condition (50 wt. % $ZnBr_2$ in the solution, the hot surface temperature=426 K, inlet flow rate = 3.66 ml/s, and the particles volume fraction = 0.1 vol. %). Table 6.3 shows that the results are very similar in the regular cases 2, 3 and 4 more

than the bias cases, even showing the simulation running times were the same, therefore, mesh number 2 in the regular shape was chosen because it provided a balance between simulation running times and solution accuracy.

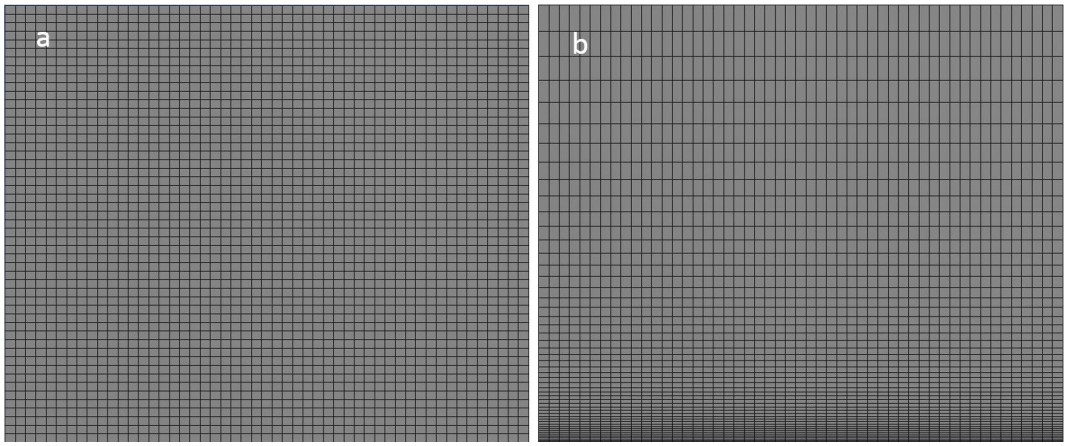


Figure 6.2: Cross-sectional view of the 151 × 51 × 51 grids, a- regular hexahedral grid b- hexahedral bias grid.

Table 6.3: Mesh independence study for the case 50 wt.% $ZnBr_2$, the hot surface temperature=426 K, inlet velocity = 3.66 ml/s, and the particles volume fraction = 0.1 vol. %.

#	Mesh (x,y,z)	$\dot{m}_{vap}$ × $10^{-6}(kg/s)$		Heat flux(W/m^2)		Simulation running time (hour)
		Regular	Bias	Regular	Bias	
1	121,41,41	6.68	6.82	8282	8281	10
2	151,51,51	6.5	6.49	8285	8286	15
3	161,61,61	6.48	6.45	8285.3	8288	22
4	151,71,71	6.47	6.43	8285.5	8289	27

6.7 Validation of mixture method applied to boiling flow

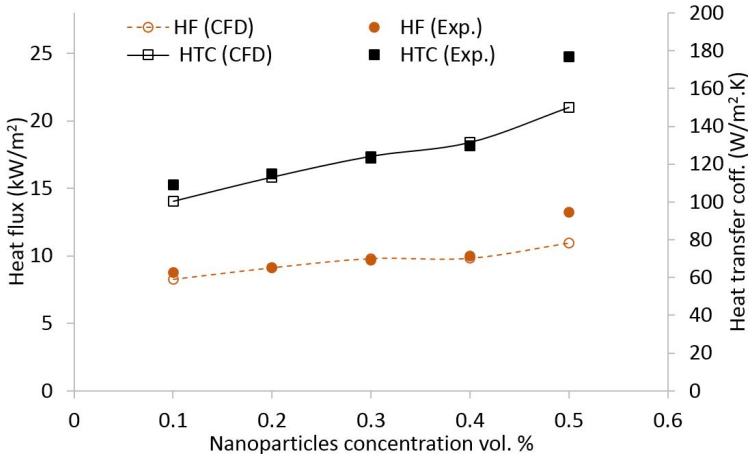
In order to validate the outcomes of the numerical simulations to be reasonable and objective, they should compare with experimental results based on quantitative parameters found under the same operating conditions such as the geometry configuration, flow rates, temperature, pressure and fluid properties.

Nanofluid model validation

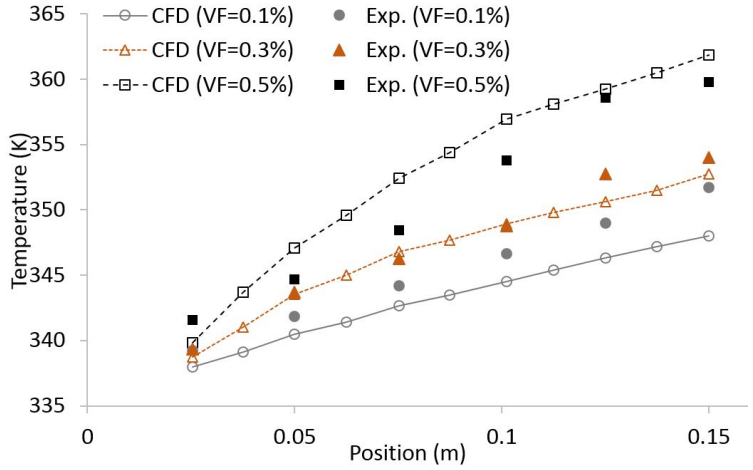
The forced boiling results from the experimental work in chapter 4 are used to validate the numerical models. Same operating condition (boiler temperature, flow rate and nanoparticles concentration) of all the cases were repeated. The comparison was achieved based on different parameters (heat flux, heat transfer coefficient, temperature of the out section and the center-line temperature) measured or calculated from experimental data for these parameters in the varying nano-particle concentration study (boiler temperature = 426 K & flow rate = 3.66 ml/s). Figure 6.3a shows that the experimental and the numerical results of the heat transfer coefficient and the heat flux have a good agreement except at the last point which is for the highest concentration of nanoparticles. The experimental results seem to show the start of an exponential growth in temperature at that point, but the numerical model shows a continuing linear trend. The temperature of the mixture on the centre-line also shows comparable results between both the experimental and the numerical as shown in Figure 6.3b. Figure 6.3c illustrates how the averaged exit temperature for the different cases shows the agreement between the experimental and the numerical.

Basefluid validation

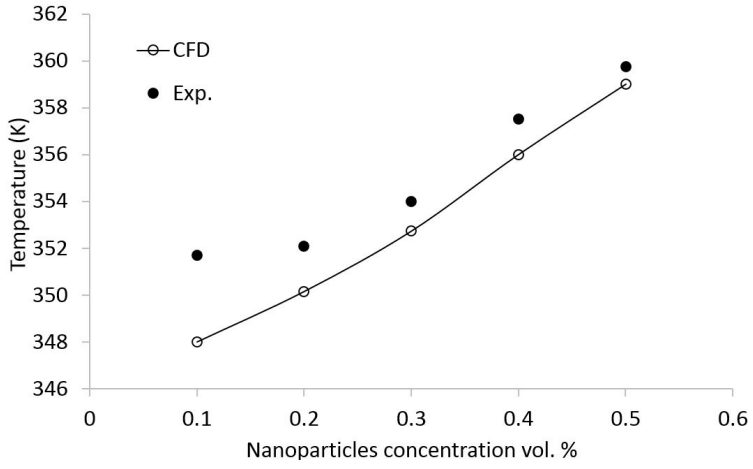
For the base fluid solution with different boiler temperatures and flow rates, the CFD results of the heat flux and the heat transfer coefficient showed good agreement with the experiment results as shown in Figure 6.4a and Figure 6.5a. There is reasonable agreement on the center-line temperature as shown in Figure 6.4b and Figure 6.5b. In all cases the heat flux and the heat transfer coefficient show better agreement than the temperatures. The heat flux depends on many parameters such as the properties of the fluid and the nanoparticles as used in both the CFD and the experimental model. But the tempera-



(a)

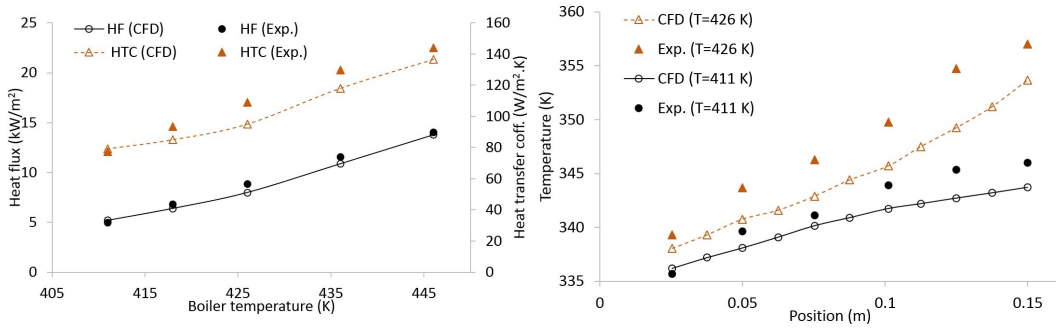


(b)



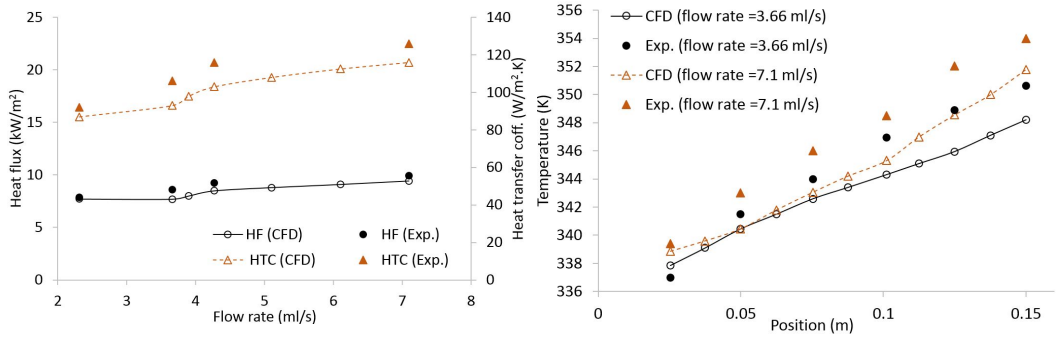
(c)

Figure 6.3: Comparison between the experimental and numerical model for varying concentration of nanoparticles, a) heat flux and heat transfer coefficient, b) centreline temperature and c) average temperature at the out section.



(a) (b)

Figure 6.4: Comparison for base fluid between the experimental and the numerical model, a) heat flux and heat transfer coefficient vs. boiler temperature and b) centreline temperature vs. axial position.



(a) (b)

Figure 6.5: Comparison for base fluid between the experimental and the numerical model, a) heat flux and heat transfer coefficient vs. flow rate and b) centreline temperature vs. axial position.

tures in the experimental side depend on the heat transferred to the solution and the position of the thermocouple from the center, which do not exactly match with pinpoint precision the numerical data point in a numerical cell with length $1mm$, height $0.3mm$ and width $0.35mm$ (see Table 6.3, grid 2). The temperature in the experiment taken by the part of the thermocouples which extend approximately $7.5mm$ in the solution (it is not exact the centerpoint of the channel), this also, causes the difference between the experiment and the numerical.

Figure 6.4b and Figure 6.5b also show the temperatures of the boiler at entrance are different between cases, this is because the temperature in the SSR varies depending on the boiler temperature and the flow rate. The temperature

of the heater was difficult to control in the experiment. For example, when the temperature was set at 426 K on the controller, the power to the boiler was activated when its temperature dropped to 424 K, then the power cut off when the temperature reached 426 K but the temperature increased till 432 K because of the high heat capacity of the boiler. The temperature of the boiler dropped down gradually, so the average temperature of the boiler was still a little over 426 K.

Generally, it was found that the model has a reasonable agreement with the experimental data. The CFD model can be used to investigate a full details of the flow characteristics in the following sections.

6.8 Quantifying the flow with the mixture model

6.8.1 Effect of nanoparticle concentrations

Figure 6.6 shows the relation between the acetone vapour mass flux produced through the boiling process and the nanoparticle concentration. It can be seen that the boiling rate is proportional to the particle volume fraction; the particles have a high thermal conductivity, therefore the thermal diffusion term $(\nabla.(k_{eff}\nabla T))$ in equation 6.3 is enhanced by the effective thermal conductivity. This makes the acetone liquid reach the saturation temperature more quickly and evaporates, consequently more vapour is generated.

The velocity (and hence mass flow rate) of the solution has an influence on the boiling rate. For example, the case of 50 wt. % $ZnBr_2$, T_h (temperature of the hot surface) equal 411 K and the concentration of the particles equal 0.5 vol. %, the mass flow rate of the vapour is $5.42 \times 10^{-6} kg/s$ (vapour volume fraction = 0.928) at flow rate 3.66 ml/s. This value increases to $6.1 \times 10^{-6} kg/s$ (vapour volume fraction = 0.939) when the flow rate change to 2.3 ml/s. The boiling rate is inversely proportional with velocity, because with lower velocity

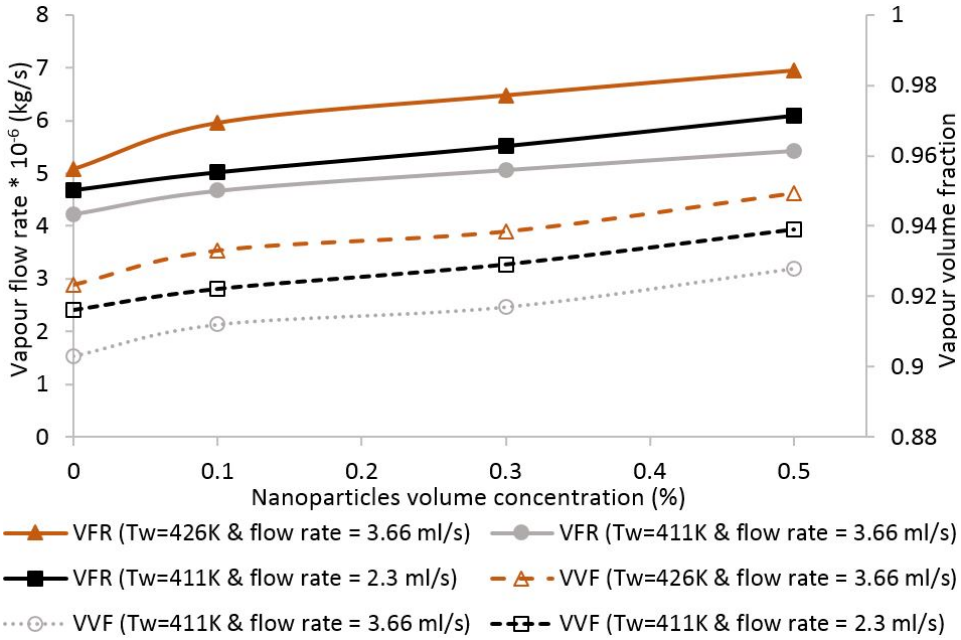


Figure 6.6: Relation between the produced acetone vapour mass flux and the nanoparticle volume fraction for different velocity and temperature and 50 wt. % $ZnBr_2$ in the solution.

the liquid has more time in contact with the hot surface which helps to generate more vapour as determined by the convective term $(\nabla . \sum_{k=1}^{n} \Phi_k \vec{\nu}_k (\rho_k E_k + P))$ in equation 6.3.

The temperature also has an influence on the phase change process, e.q. for 0.5 vol.% nanoparticles, the acetone vapour mass flux drops from $6.95 \times 10^{-6} kg/s$ (vapour volume fraction = 0.949) at 426 K (temp of the hot surface) to $5.42 \times 10^{-6} kg/s$ at $411K$ at the same velocity. Increasing the temperature gradient at the wall causes more heat transfer to the liquid, by the diffusion term in equation 6.3, which makes even the acetone located near the hot surface (not just the adjacent) undergo evaporation.

As shown in Figure 6.7, the heat flux and the heat transfer coefficient are affected by the particle volume fraction, the temperature of the hot plate and the velocity of the fluid. The heat transfer coefficient increases with increasing velocity of the fluid, due to increased turbulence, represented by the $k - \epsilon$ model, which in turn provides a more efficient mixing of the thermal energy

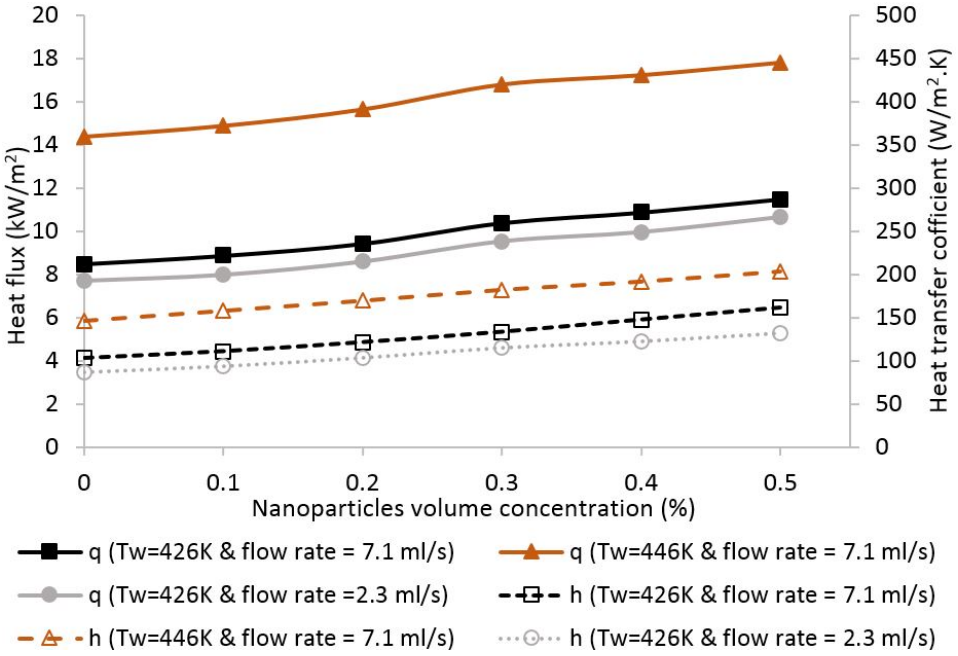


Figure 6.7: Relation between the average heat transfer coefficient and heat flux with nanoparticle volume fraction for different velocity and temperature and 50 wt. % $ZnBr_2$ in the solution.

in the fluid. It also increases with temperature of the hot surface, despite increased vapour generation, which should drop the heat transfer coefficient due to lower mixture conductivity with vapour. This is because the boiling process is in the nucleate boiling region and it doesn't reach the critical heat flux (CHF), so heat flux increases as the wall temperature increases. Figure 6.7 also shows that the heat transfer coefficient increases as the particle concentration increases because, increasing the particle loading leads to increase in the boiling rate as evidenced in Figure 6.6; hence due to the increased fluid mixing of the very low density vapour rising in the liquid there is a consequent increase in the heat transfer. This also explains the increase in the surface heat flux. For example, the surface heat transfer increases from 8.5 kW/m^2 to 11.5 kW/m^2 by increasing the particles loading from 0 to 0.5 vol. % in case of surface temperature of 426 K and flow rate of 7.1 ml/s.

The centreline temperature of the solution along the tube increases with particle concentration as shown in Figure 6.8 as a direct consequence of mixing

the highly conductive nanoparticles into the k_{eff} term in equation 6.3. The soundness of the two phase approach to modelling here, as distinct to the single phase approach and as described in ([81]) is proven in the literature. This technique depends on the nanoparticles being an independent phase in the mixture, and this effect of enhanced centreline temperature would not be seen in the single phase model.

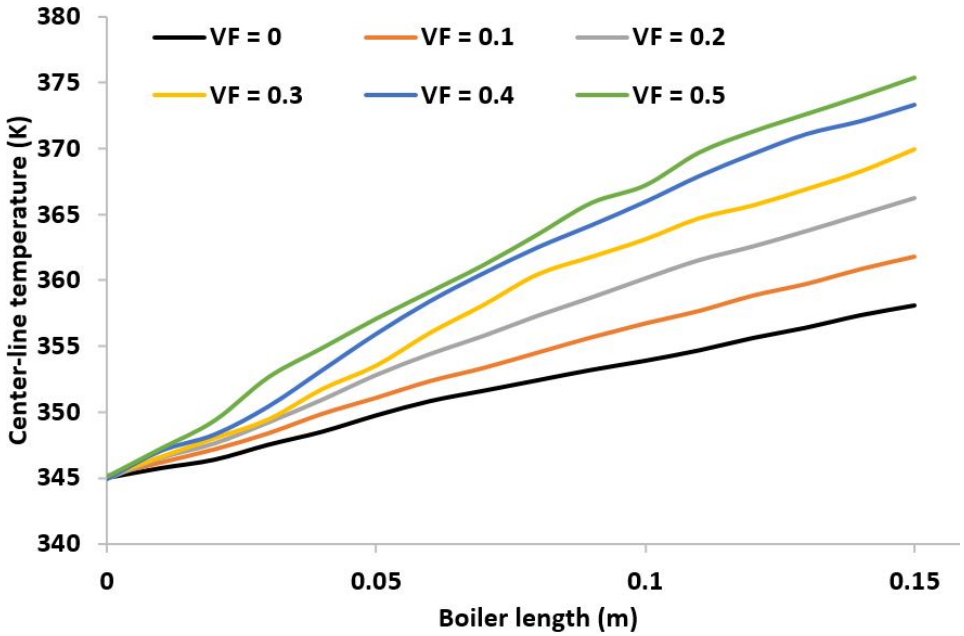


Figure 6.8: The effect of volume fraction of particles on the centreline temperature along the pipe at 50 wt. % $ZnBr_2$ concentration, $T_h = 426K$, and flow rate = $3.66ml/s$. (present in colour).

Figure 6.9 shows how the temperature out of the boiler behaves with various parameters. The temperature increases with increasing the nanoparticles concentrations; it increases also with increasing the surface temperature but drops with increasing the flow rate. The reason for the flow rate effect relates to the residence time over the hot plate; the heat transfer coefficient increases with increasing velocity due to increased Nu, but the contact time of the fluid with the hot surface is shorter and the contact time dominates regarding temperature of the fluid due to the capacity rate ($C = \dot{m}.c_p$).

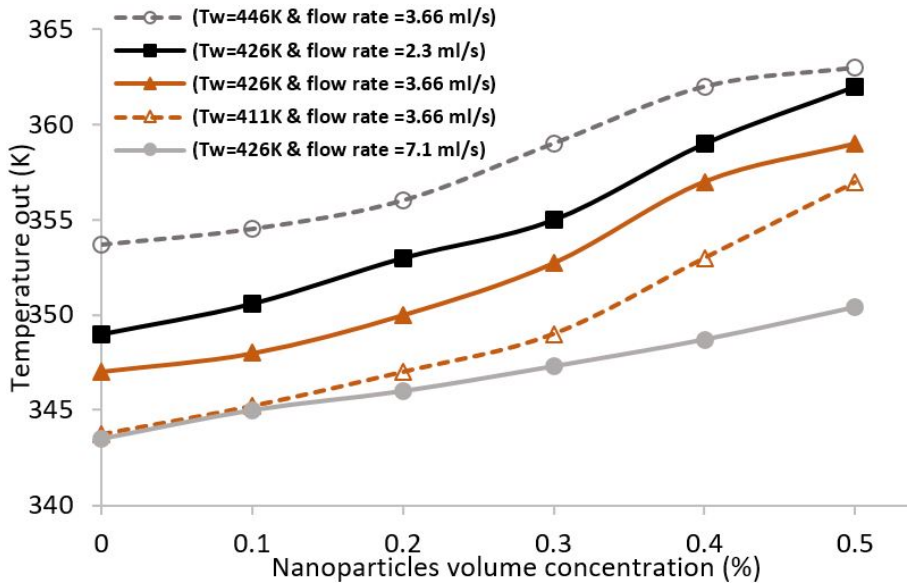


Figure 6.9: The effect of the concentration of the nanoparticles, surface temperature and the flow rate on the average outlet temperature of the mixture solution in the boiler.

Figure 6.10 shows turbulence intensity (equation 6.16 ([201])).

$$I = \frac{\sqrt{\frac{1}{3}(\bar{u}^2 + \bar{v}^2 + \bar{\omega}^2)}}{U_\infty} \tag{6.16}$$

The turbulence intensity of the nano-solution during boiling is affected by the concentration of the nanoparticles for two reasons; the first reason is with the two phase flow, the random motion of the nanoparticles (reflected in equations 6.3 & 6.7 where as the energy source is defined which will affect kinetic energy directly) which affects on the stream of the flow; the second reason is increasing the generation of vapour which rises vertically. Figure 6.10 also shows that the turbulence intensity increases with increasing surface temperature which also increase vapour generation, however it drops with increasing the flow rate, demonstrating that the dominating contribution to turbulence and therefore to convective mixing is not the liquid Nu contribution, but the gross liquid motion generated by the low density vapour rising.

Figure 6.11 shows the relation between the generated vapour volume frac-

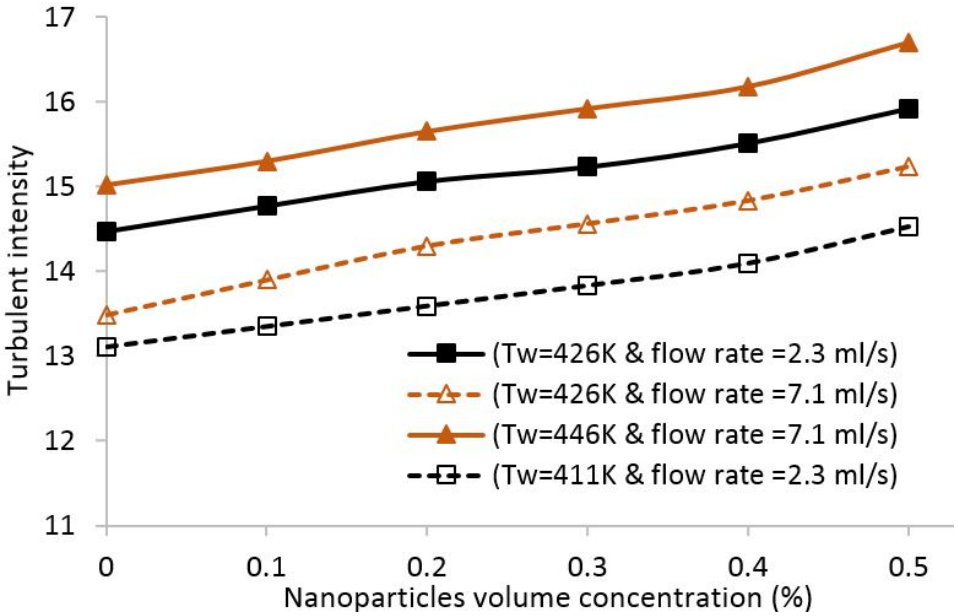


Figure 6.10: The effect of the concentration of the nanoparticles, surface temperature and the flow rate on the turbulent intensity of the mixture solution in the boiler.

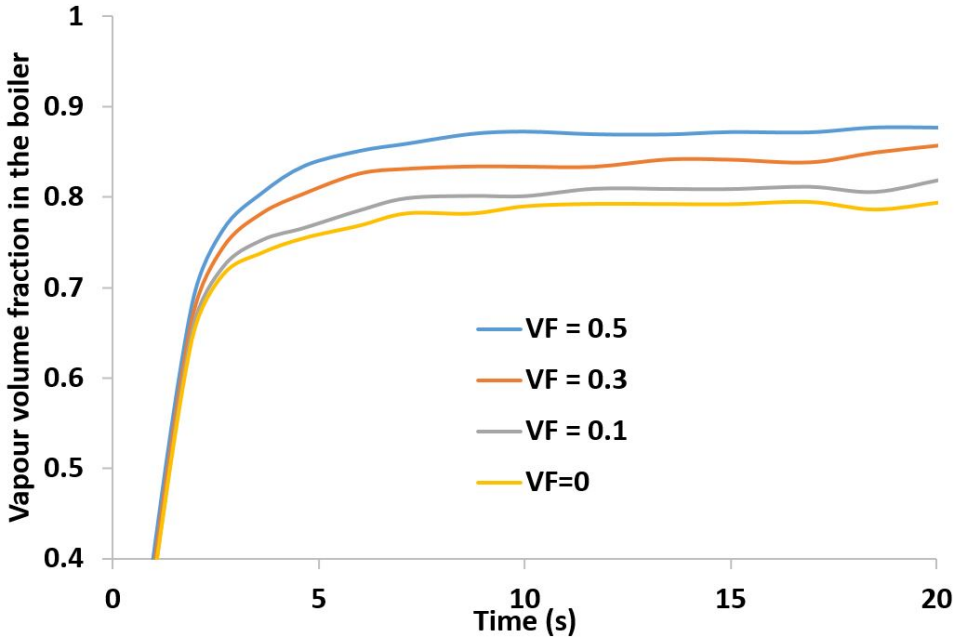


Figure 6.11: Developing of acetone vapour in the boiler with a time during the boiling of nanofluid (T_h= 426 K and flow rate = 3.66 ml/s).

tion of acetone in the domain with time. The vapour volume fraction increases with time up to 6 seconds, after which point the amount of vapour stabilizes because the boiler is open at the end with outflow exit boundary condition. Figure 6.11 also shows that the generated vapour increases as the concentration of the nanoparticles increases as stated previously.

Table 6.4: The concentration of the Graphene and $ZnBr_2$ in the liquid phase at the exit section of the boiler in different cases of Acetone-$ZnBr_2/graphene$ boiling.

	$T_h = 426K, flowrate = 3.66ml/s$			$T_h = 446$ K, $\dot{m} = 3.66ml/s$	$T_h = 426$ K, $\dot{m} = 7.1ml/s$
Graphene vol. fraction (in)	0.001	0.003	0.005	0.005	0.005
Graphene vol. fraction (out)	0.00105	0.00307	0.00513	0.00515	0.0051
$ZnBr_2$ vol. fraction (in)	0.1580	0.1580	0.1580	0.1580	0.1580
$ZnBr_2$ vol. fraction (out)	0.175	0.181	0.188	0.191	0.185
$ZnBr_2$ wt. concentration (out)	0.53	0.54	0.5514	0.556	0.565

During boiling, the concentration of components of the liquid solution changes since the concentration of liquid acetone, $ZnBr_2$ and nanoparticles change with the evaporation. This causes the volume fraction of the $ZnBr_2$ and Graphene nanoparticles in the liquid solution to increase depending on the concentration itself, the boiler temperature and the velocity. Table 6.4 presents the volume concentration of the nanoparticles and the $ZnBr_2$ in both the inlet and the outlet sections of the boiler for different temperatures of the heater and flow velocity of the solution. At $T_h = 426K$ and flow rate = 3.66 ml/s the inlet volume fraction of $ZnBr_2$ and graphene are 0.158 & 0.001 respectively, which increase at the outlet to 0.175 & 0.00105 respectively. Through increasing the vapour volume fraction, the concentration of the $ZnBr_2$ and nanoparticles in the liquid also increase, because by increasing the nanoparticles concentration, the heat transfer is enhanced which stimulates the generation of more vapour (this works as a circular actions). By comparing the results for the last three columns, it can be seen that with increasing temperature of the heater and decreasing velocity of the fluid, the concentration of both $ZnBr_2$ and graphene increase at the outlet section. In both cases the evaporation of the liquid acetone is increased.

6.8.2 Effects of the boiler temperature

Figure 6.12 shows that heat transfer increases as the boiler temperature increases. With increasing boiler temperature, more heat will transfers to the liquid at a particular time, which makes the acetone reach the boiling temperature quicker, and some acetone may evaporate at a small distance from the hot surface. This will increase the vapour volume fraction and the vapour flow rate in the boiler as illustrated in Figure 6.13.

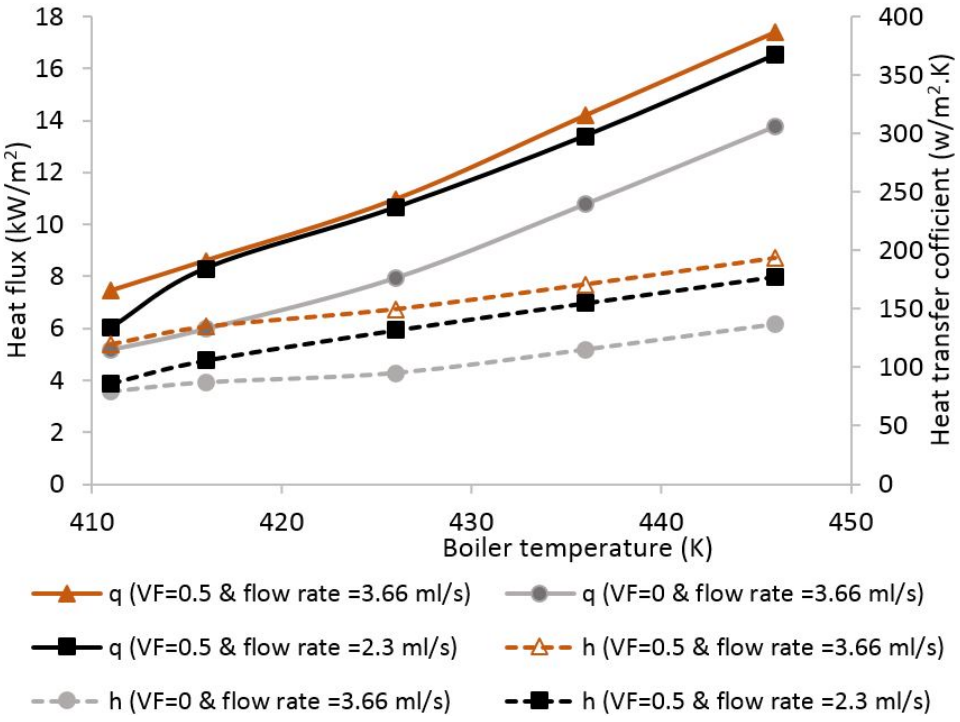


Figure 6.12: Relation between the heat flux and heat transfer coefficient and the boiler temperature for different velocity and particles concentrations with 50 wt. % $ZnBr_2$ in the solution.

Increasing the vapour in the domain will decrease the effective combined viscosity of the vapour infused liquid and increase the local velocity which directly increases the Re and consequently the turbulence intensity as shown in Figure 6.14. Because of increasing the amount of heat transfer to the solution with increasing the boiler temperature, there is an expected increase in the temperature at the out going section of the boiler (Figure 6.15). The results

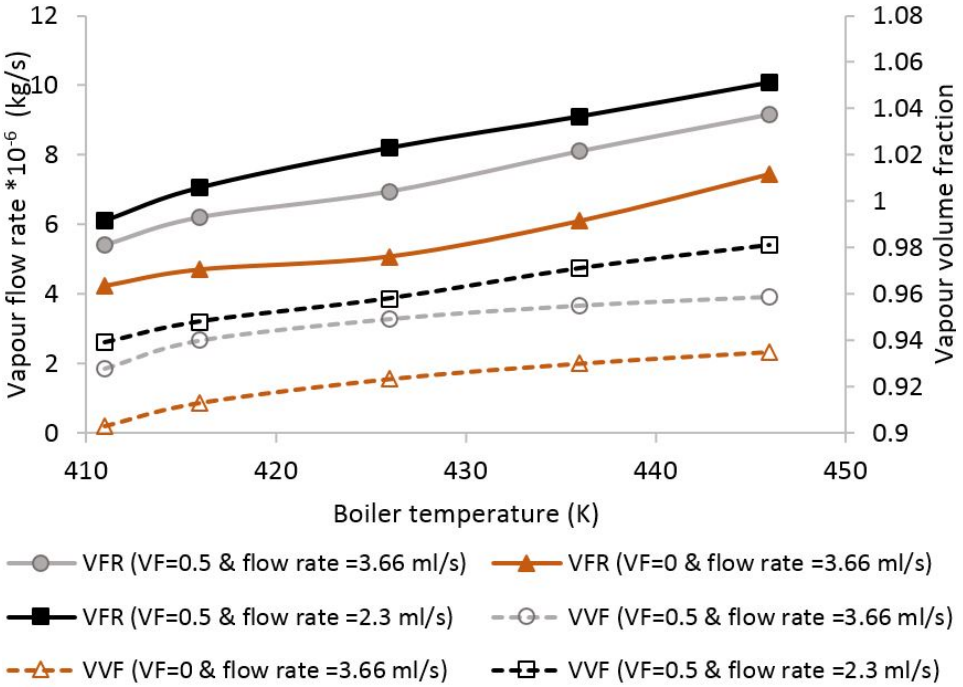


Figure 6.13: Relation between the productions of acetone vapour mass flux and vapour volume fraction and the boiler temperature for different velocity and particles concentrations with 50 wt. % $ZnBr_2$ in the solution.

and observed behaviours of studying the effects of the boiler temperature are proved experimentally as explained in the section 6.7 .

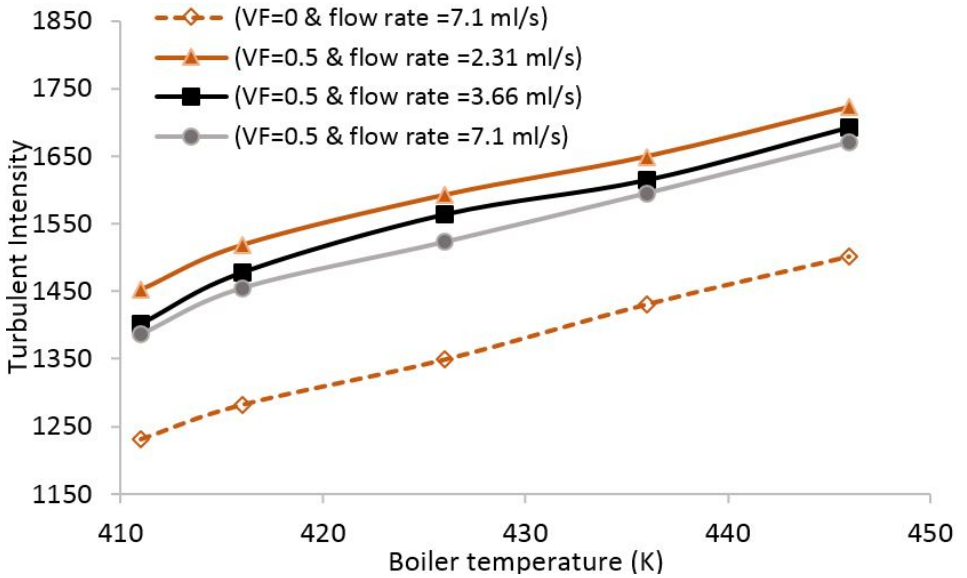


Figure 6.14: The effect of the boiler temperatures on the turbulent intensity of the mixture solution in the boiler at different particles concentration and the flow rate.

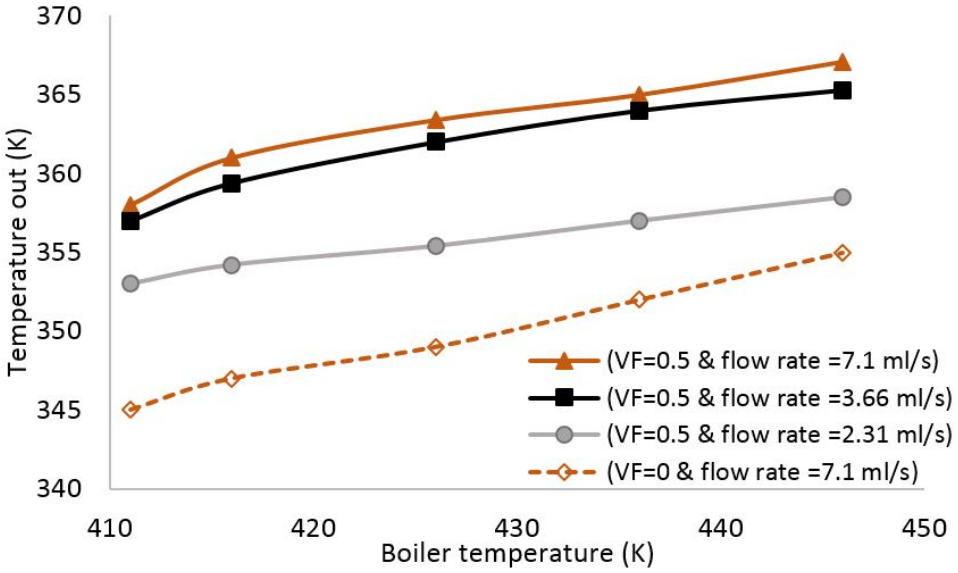


Figure 6.15: The effect of the boiler temperature on the outlet temperature of the mixture solution in the boiler with different surface temperatures and the flow rates.

6.8.3 Effects of the flow rate

The effects of the flow rate variation with various heater temperatures are shown in Figure 6.16; there is a slight increase in heat transfer, and the heat transfer coefficient corresponds to the heat flux in all the cases. This is because the wall temperature is the same for each specific case and there are a slight differences in the mean temperature caused by the flow variation. The vapour generation drops as the velocity increases because the solution has less contact time with the hot surface, as described in the previous section. This results specifically for one domain or one cycle of the solution rotation in the rig. This behaviour demonstrated by the experimental results in Figure 4.26. However, Figure 6.17 shows the generation of the vapour for passing the solution through the numerical domain from inlet to the outlet (vapour decreases with increasing the flow rate). This leads to reduction of turbulence intensity since it is proportional with vapour generation as shown in Figure 6.18

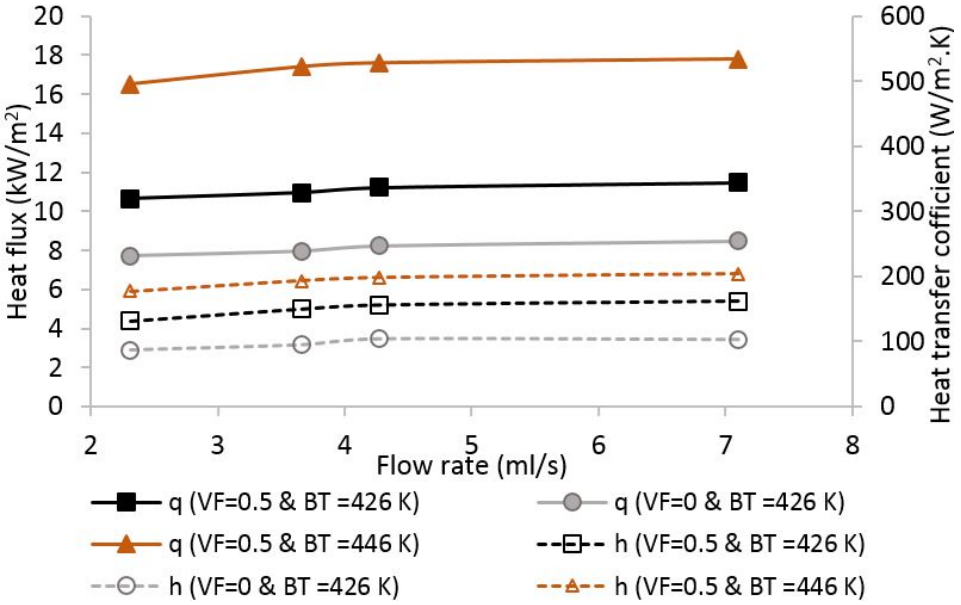


Figure 6.16: Relation of the heat flux and heat transfer coefficient with the flow rate variation for different boiler temperature and particles concentrations with 50 wt. % $ZnBr_2$ in the solution.

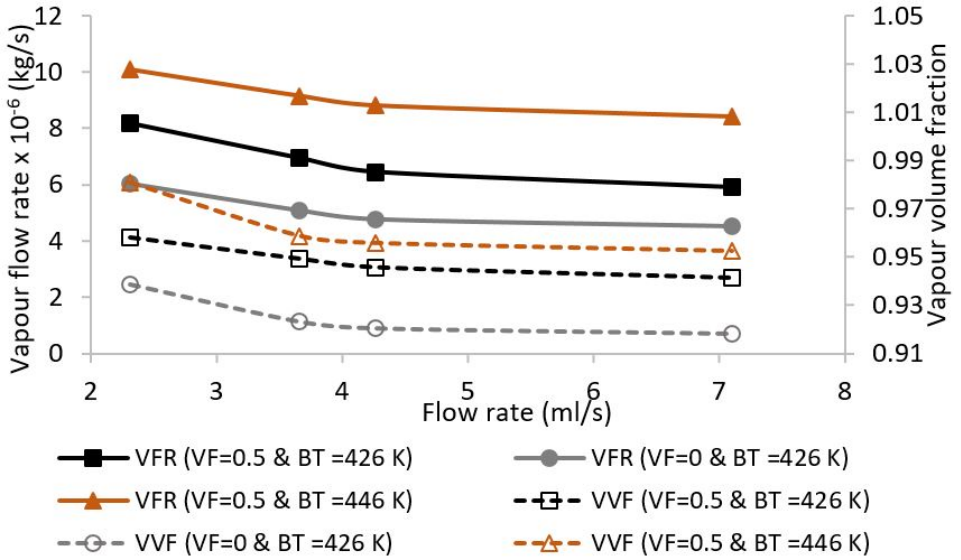


Figure 6.17: Relation of the productions of acetone vapour mass flux and vapour volume fraction with the flow rate variations for different boiler temperature and particles concentrations with 50 wt. % $ZnBr_2$ in the solution.

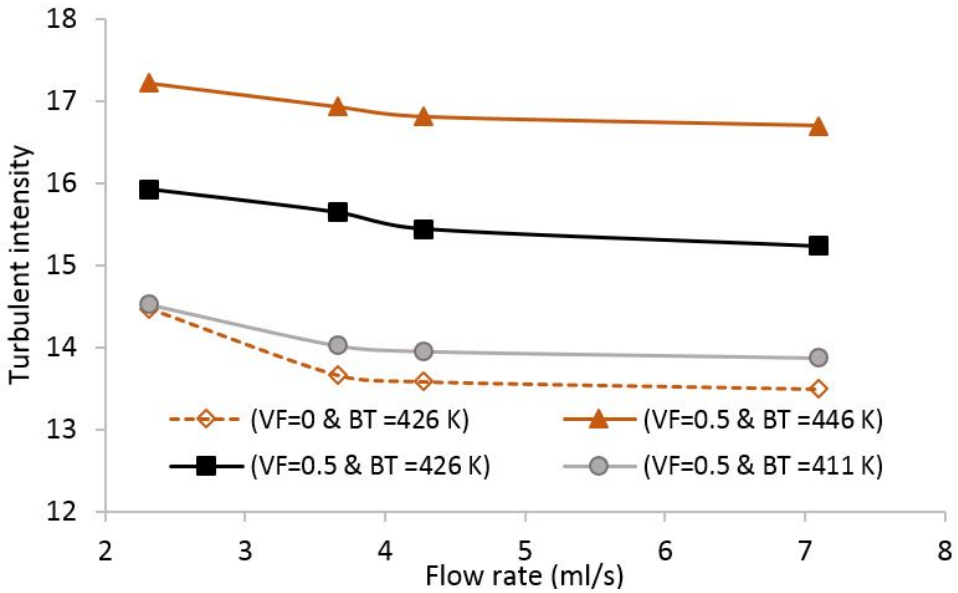


Figure 6.18: The effect of the solution flow rate on the turbulent intensity of the mixture solution in the boiler at different particles concentration and the boiler temperatures.

6.9 Visualising the flow

This flow behaviour includes three miscible phases and one immiscible phase (acetone vapour) which can be represented by the VoF model to show its behaviour. Figure 6.19 shows the development of the acetone vapour from the nanofluid solution (acetone/$ZnBr_2$ based on graphene nanoparticles) on the symmetry plane of the boiler in case of (flow rate=3.66 ml/s, T_w=426 K and Φ=0.5 Vol. %) for several time steps up to 25s. At t=0.2 s the vapour is visible and it quickly increases with time. The vapour ascends to the top surface by the first second and it gathers there. During the gathering of the vapour at the top of the channel, the vapour volume expands by further production and moves quickly (faster than the other phases) toward the exit. The amount of the vapour at the top increases gradually because the generation rate of the vapour is more than that which exits through the outflow boundary until t=8 s, and then the generation rate and the exit are approximately equal. Consequently the amount of the vapour at the top and the exit vapour rate become constant as is represented by the same quantity of the vapour in the boiler volume at 10 and 25 seconds.

The last image in Figure 6.19 shows how the vapour phase develops on several cross sections of the boiler at the 25^{th} second. Whenever the solution flows in the boiler, there are two parameters effecting boiling rate; firstly, the evaporation makes the concentration of the salt increase consequently less acetone liquid contacts the hot surface and this reduces the rate of bubble generation. Secondly, as a consequence of that, in the boiler the liquid gains more heat from the hot surface due to improved thermal contact which makes more heat transfer.

Figure 6.20 shows the concentration and the distribution of the phases in the symmetric section for different time steps in the case, flow rate=0.366

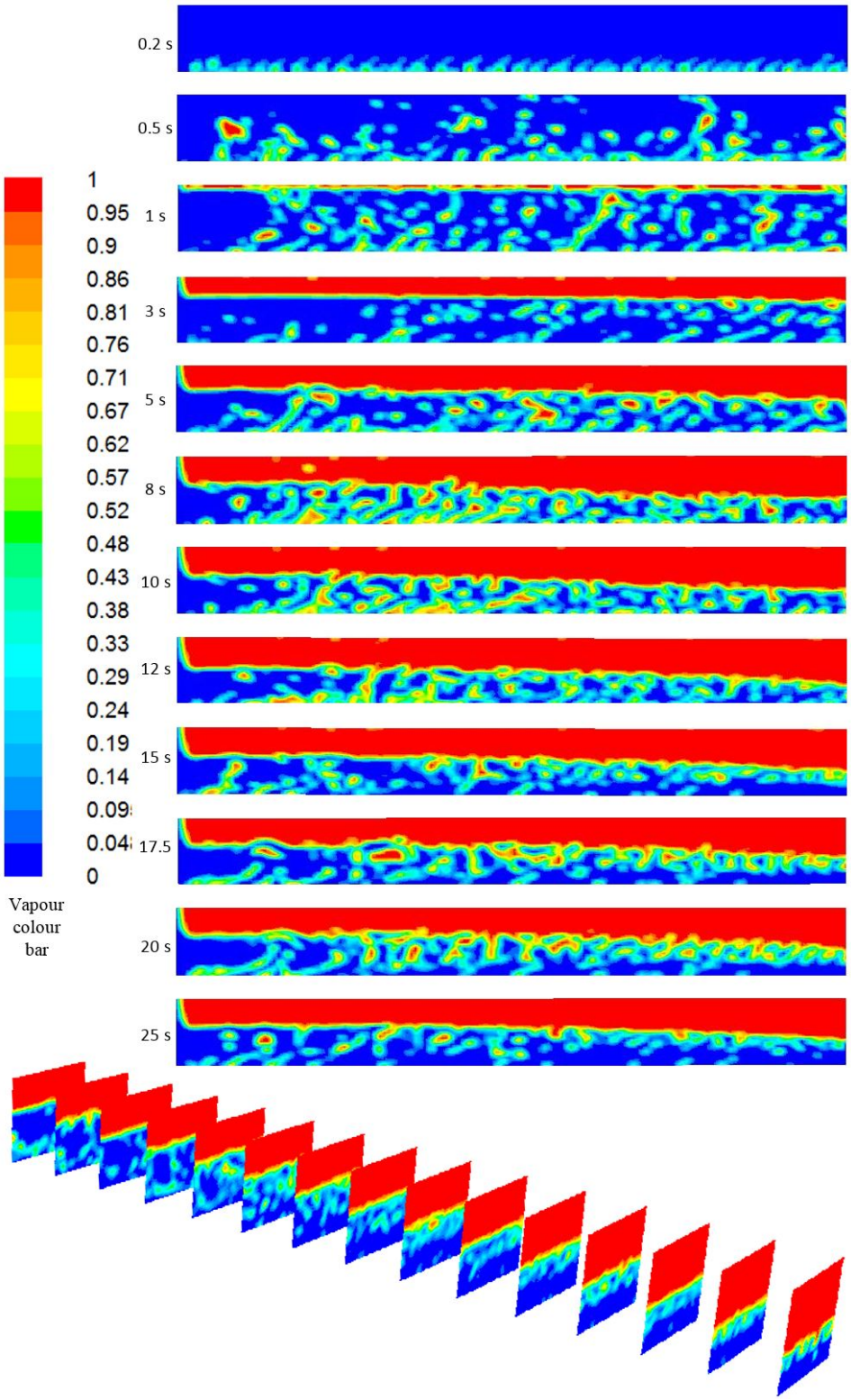


Figure 6.19: Developing of the vapour of acetone in acetone/$ZnBr_2$ based on graphene nanoparticles at the symmetric view of the rectangular boiler up to 15 second. (Flow rate=3.66 ml/s, T_w=426 K and Φ=0.5 Vol %) at the VoF method. (present in colour)

ml/s, T_w=426 K and Φ=0.5 Vol. %. In this case the process is solved with the mixture model and the contours can be used for each phase (except vapour phase) with the alternative colour bars (concentration). During the first second, the acetone vapour generates and rises, then the vapour expands faster than the liquid mixture flow toward the out section as seen in the VoF model. At any point and in any time step, the phases present are as shown in the colour bar, and the rest of the mixture is the vapour phase. For example, at the location indicated by a point in time, step 0.5s (step 1) at the top of the channel, the concentration of acetone, graphene and acetone/$ZnBr_2$ are the same as the inlet concentrations (0.57, 0.005, 0.425) with no vapour at that point. At the same position at time step 2 the volume fraction of acetone, graphene and acetone/$ZnBr_2$ are 0.44, 0.0077 and 0.325 respectively, the acetone vapour volume fraction can be calculated from the balance of the missing proportion to be 0.2273. In 20 seconds time at that point the major phase is vapour with volume fraction of 0.929. A sample of these data is presented in Table 6.5. The last image in Figure 6.20 shows the process in the boiling on the cross sections (separation distance of 1 cm between the sections) of the boiler at the 20^{th} second.

Table 6.5: Concentrations of all phases (acetone liquid, Graphene cloud, acetone/$ZnBr_2$ and acetone vapour) at the symmetric view of the rectangular boiler at the same point indicated in Figure 6.20 at different time steps, for the case (flow rate=3.66 ml/s, T_w=426 K and Φ=0.5 Vol. %) at the mixture model.

Position	Concentrations			
	Acetone/$ZnBr_2$	graphene	Acetone (Liquid)	Acetone (Vapour)
Step 1	0.57	0.005	0.425	0
Step 2	0.44	0.0077	0.325	0.2273
Step 3	0.18	0.0031	0.134	0.683
Step 4	0.04	0.00035	0.03	0.9296

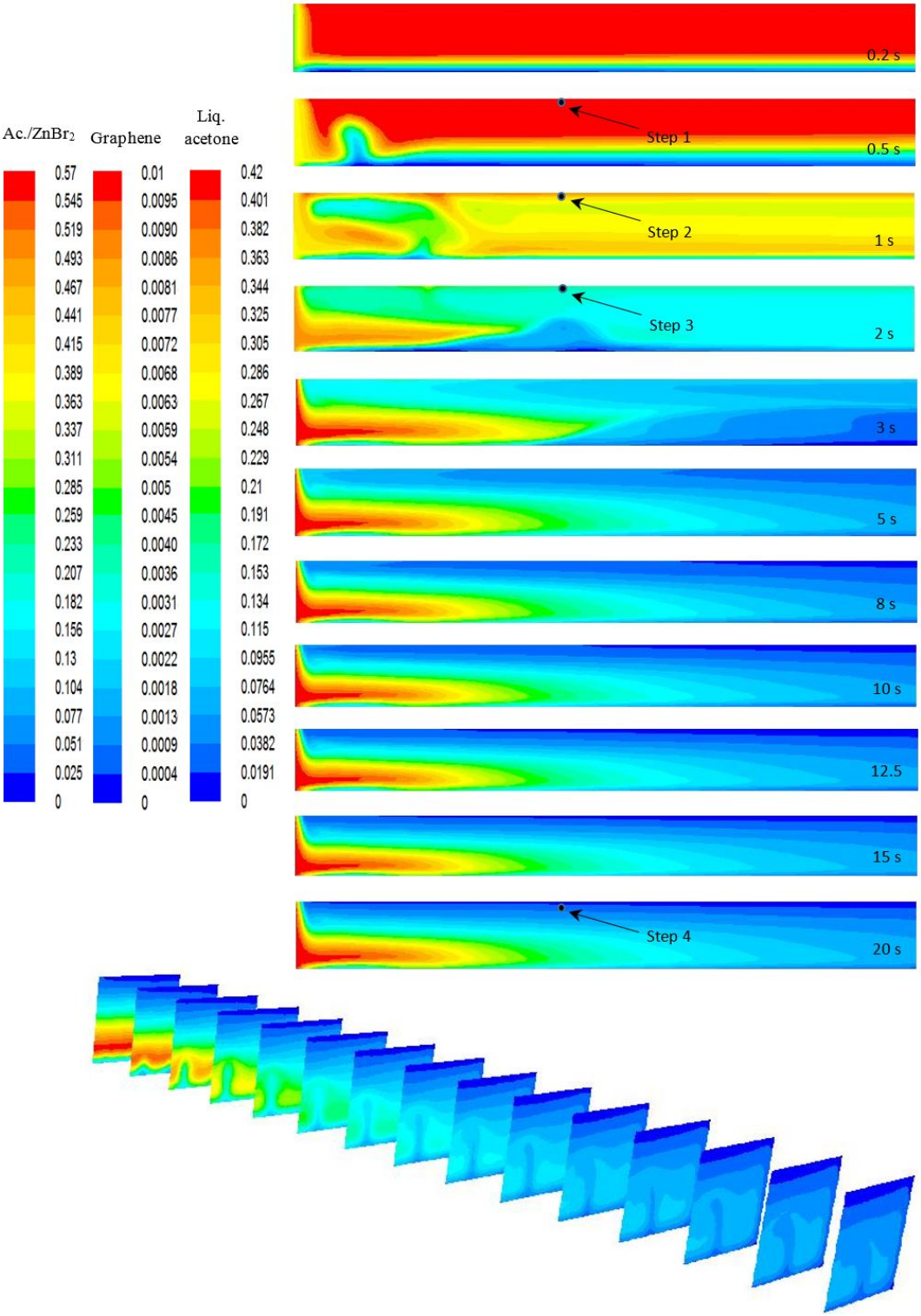


Figure 6.20: Distribution of all phases (acetone liquid, vapour, acetone/$ZnBr_2$ and graphene cloud) at the symmetric view of the rectangular boiler up to 20 seconds. In specific conditions (Flow rate=3.66 ml/s, T_w=426 K and Φ=0.5 Vol %) for the mixture model. Last image is the cross section of the boiler in different points at the 20^{th} second. (present in colour).

Figure 6.21 also illustrates those cross sections more clearly, it shows that in 1 cm cross section the original phase is in the middle section surrounded by the mixture (liquid and generated vapour), which is caused by the heater from the bottom, rising the generated vapour (appears in green) at the side and gathering the vapour and the mixture at the top. The vapour volume fraction increases towards the walls. The vapour occupies the top region of the boiler then expands to the exit. Moving away from the entrance, the vapour volume fraction increases, the original phase shrinks and mixes with the vapour phase. In the last sections of the boiler, it's clear that the major phase is vapour. Figure 6.21 also shows that there is no film boiling in all the sections of the boiler (no dark blue which refer to pure vapour in contact with the heater) which proves the process is still in the nucleate boiling region as the calculations done in the subject 4.3.2. This is because the ΔT_{sat} is relatively low and the acetone mixes with the salt, which is not evaporated and this causes some fluid to be in touch with the surface. In the mixture model the phase change appears gradually on different levels of saturated vapour; however the phase change happens rapidly without passing through saturation levels. The mixture method can predict the behaviour of the flow and the concentrations of the phases but cannot predict the development of the bubbles in the phase change (vapour phase).

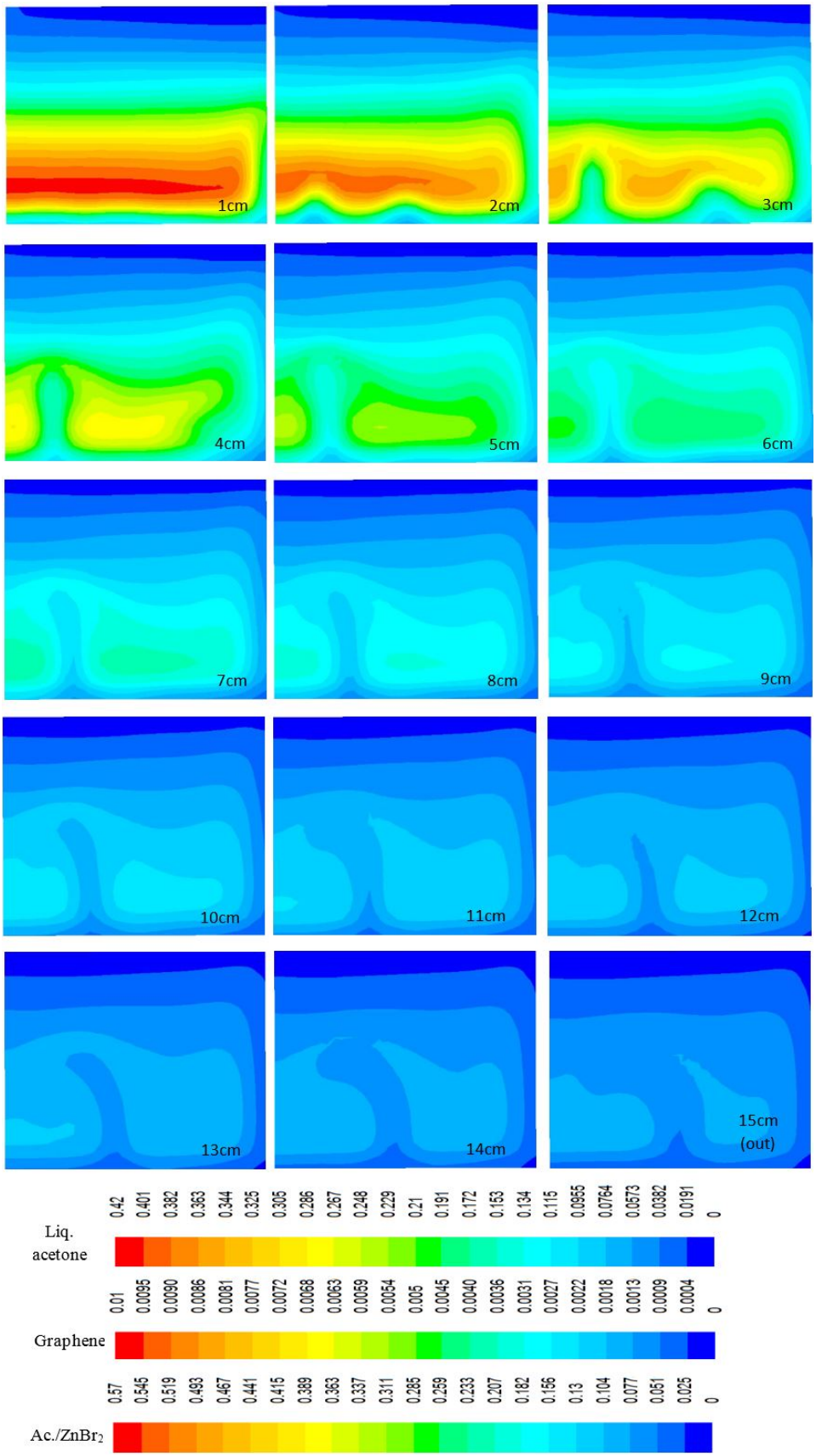


Figure 6.21: Distribution of all phases (acetone liquid, vapour, acetone/$ZnBr_2$ and graphene cloud at different cross sections of boiler at 20 seconds. (Flow rate=3.66 ml/s, T_w=426 K and Φ=0.5 Vol %) for the mixture model. (present in colour).

6.10 Summary

The mixture method compares well against literature on repeating the boiling model in a pure fluid with nano particles. This chapter proceeds to apply the method in the case of the salt solution nano-fluid and demonstrates the characteristics that should be observed in the physical situation of sub-cooled boiling in a constant cross section rectangular channel, with a heated bottom section.

The nanoparticle concentration is low, in the order of upto 0.5% by volume since this provides sufficient property enhancement, whilst allowing for a stable suspension. The results show that vapour production rate increases with nano particle concentration due to the enhanced thermal diffusion due to the nano particles causing faster heating of the nanofluid. Likewise, reducing the velocity increases vapour production (although, lower velocity will reduce the heat transfer coefficient), due to the increased residence time over the heated section. Increasing the heated surface temperature also produces greater yield of vapour in the range tested, since the regime considered is nucleate boiling prior to critical heat flux and no film boiling is observed.

Analysis of heat transfer coefficient shows it increases with wall temperature and Reynolds number. The particle population density increases in the region of the hot surface due to intense boiling which raises thermal diffusivity, further enhancing the effect, and leading to further bubble generation and this leads to increased mixing. Centreline temperature shows that velocity decrease leads to increased temperature, but only slightly since increased vapour generation at the wall reduces local thermal diffusion. Increased temperature of the hot surface leads to increased centreline temperature; increase in nano particle concentration also has an effect on increasing centreline temperature.

Overall, the mixture method shows that an effect can be seen of the nano-

particle concentration which is related to the complex flow dynamics of vapour generation and turbulence. The model allows for the effect of nano-particle concentration increase due to evaporation, and simulates its effects. The flow dynamic effects of increasing temperature and velocity are as expected, but complicated by the boiling action and the effect on thermal diffusion and convective mass transport. The model accounts for density variation in the liquid, allowing the denser concentrated solution to sink to the bottom of the channel, which raises the temperature in that region due to the intensely boiled solution closest to the hot surface, relative to the less boiled solution which rises to the upper levels since the regions of the solution with more acetone are less dense. But the contour plots reveal that the liquid constituents remain in the same proportion, such that there is no buoyant stratification other than the vapour fraction.

Turbulence intensity offers a good indication of the enhancement of mixing in the boiling flow, showing a clear enhancement of turbulent mixing with increased nanoparticle concentration. Given the complexity of the flow dynamics indicated in the other data from the models, this is a useful indicator of nanofluid effectiveness in boiling. The sensitivity of the results to ingoing turbulence intensity level variation was found to be negligible.

The VoF method is applied to show that the dynamics of bubble generation indicate the trends of behaviour observed in the mixture model, but highlights the particular regions of bubble volumetric concentration in discrete packets. The overall behaviour is seen to be very similar to the concentration profiles observed in the mixture model.

The models indicate that enhancement of the boiling process by application of the nano-particles is a complex interaction not just dependent on the enhancement due to the nanofluid effects but also the characteristics of in-

teraction between vapour and liquid constituents in the heat transfer region. The indication is that a small proportion of nanoparticles can offer a benefit on providing improved boiling at lower temperatures where the temperature potential above saturation reduces. The CFD model technique can provide capacity characteristics for ultimate design and flow configuration which result in flows producing nucleate boiling regime.

7

CONCLUSIONS AND RECOMMENDATIONS

This Chapter highlights the main conclusions form this study and the related recommendations for further work which logically follow on from it.

7.1 Conclusions

Investigation of the effects of the nanoparticles on improving heat transfer in the VARS with acetone / $ZnBr_2$ base fluid was the main aim of this work. In particular, this work reflects the heat transfer in flat PV panel (presented as the boiler in this work) to make use of low grade heat from solar PV. This study focused on the high pressure part of the VARS which includes the boiler. A novel numerical method is developed to simulate the boiling process of the working fluid (nano-salt-fluid) in the boiler, which was a symmetric rectangular duct. The preparations for execution of this process involved different actions; the working fluid of acetone / $ZnBr_2$ was prepared and converted to nanofluid with different concentration of nanoparticles. The properties of the nanofluid for all concentrations were tested experimentally (Chapter 3). The single and two phase models for the nanoparticles simulation in the CFD models are significant for the numerical results of the system. Therefore, choosing the best model to represent boiling processor required evaluation of both models (Chapter 5). Every numerical model needs validation to evaluate the

range of the applicability. To achieve that, an experimental rig of the high pressure part of VARS has been built (Chapter 4). Identical boundary conditions of flow rate, temperature and pressure of the experiments are applied in the boiling process numerical model which is the core work of this thesis (Chapter 6). The simulation show that it is unlikely VARS can be used with solar photo-voltaic (PV) waste heat because it give 80 ^oC under the vacuum condition, which cannot take the solution to the boiling state. In this work, the minimum suitable surface temperature for the boiling was found as 138 ^oC at the atmospheric pressure.

In chapter 3: A suggested novel VARS fluid consists of a binary fluid mixed with nanoparticles (ZnO and Graphene) which we call a nano-binary fluid or nano-salt-fluid. The fluid was prepared with different concentrations of nanoparticles using the two step technique of the nanofluid preparation. The purposes of this study are to investigate the improvement of the fluid properties using nanofluid. It was found that the surfactants (PVA, PVP and SDS) have no impacts on the stability of the nano-salt-fluid. However, the density of the basefluid has a significant influence on the stability. With a concentration of 65 % $ZnBr_2$ which makes the solution more dense (1550 kg/m^3) the liquid stayed stable for 48 hrs. The density of the solution increases as the concentrations of the salt increases.

Viscosity of the solution increases as the concentration of the salt or the nanoparticles increase and increasing the temperature reduces the viscosity. The nanofluid prepared shows a Newtonian behaviour over a wide range of shear rate. Improving the thermal conductivity has the most significant influence over the heat transfer process. It was found that the thermal conductivity of the pure solution rises from 0.149 - 0.159 $W/m.K$ with dropping the concentration of the salt from 65 wt.% to 40 wt.%. However, the thermal conductivity

of the nanofluid increases by 10.5 % and 4.6 % with increasing the concentration of the ZnO from 0 to 1.2 vol.% and Graphene from 0 to 0.5 vol.%, respectively. The last property investigated was heat capacity which found it drops with increasing the concentration of both the salt and the nanoparticles concentrations. It is observed that agglomeration size leads to enhanced by the concentration and the type of the nanoparticles, it was found also that the agglomeration size of ZnO is bigger than those caused by Graphene. Stability of the nanofluid is a key unreserved challenge for successful application at an operational scale.

In chapter 4: This part of work validates the numerical model of the boiling process, and proves that the system is working with the presence of nanoparticles. Different characteristics of concentrations of the graphene (0 – 0.5 vol. %), boiler temperature (411, 418, 426, 436 and 446 K) and flow rate (2.31 - 7.1 ml/s) are used to discover how each variable quantity affects the behaviour of flow boiling. The most important outcomes from this Chapter are, firstly, the Rohsenow constant of acetone $/ZnBr_2$ based graphene on smooth stainless steel is found as 0.217, depending on the Rohsenow nucleate boiling correlation over the range of power input tested (48.8 W). The stable level of the vapour pressure (happens when the evapouration rate in the boiler equal to the condensation rate) in the system increases with increasing concentration of nanoparticles, and consequently, the saturation temperature increases. The presence of nanoparticles leads to increased heat transfer coefficient, which helps to improve heat transfer during the boiling process, creating a higher vapour production rate and more concentrated exiting strong solution.

Increasing the boiler temperature will increase the vapour generation, vapour pressure and the saturation temperature. The heat transfer coefficient and the heat flux are found proportional with the boiler temperature. Also, the av-

erage boiler temperature increases with increasing the flow rate. With higher flow rate, less vapour generates meaning more liquid exists in the boiler which means the fluid can gain more heat to become warmer. The heat transfer coefficient and the heat flux also proportional with the flow rate in the system.

In chapter 5: For the multiphase flow, there are two mechanisms for modelling nanoparticles in the fluid: single and two phase flow. To evaluate which of these models can predict the heat transfer of the system more accurately, an investigation of the comparisons took place. These two approaches are applied using acetone/$ZnBr_2 - ZnO$ nanofluid inside a flat tube with laminar and turbulent mixed convection using a mixture method. From the section 5.6.2 it was found that the two phase model gives a much better prediction than the single phase model. This behaviour may cause by the Brownian motion, which effects on the thermal conductivity and the particles size, which effects on the viscosity of the fluid.

The main part of the Chapter goes onto show the effects of the nanoparticles concentration in the salt-fluid, concentration of the acetone in the solution and the Re on the heat transfer. The two phase method shows the strong effect of the nanoparticles on improving the heat transfer which provides reasonable confidence in a positive outcome in the event of using the fluid in a heat transfer situation like the absorption refrigeration cycle.

Wall shear stress increases with increasing Re and decreases with increasing acetone concentration as the viscosity of the fluid decreases; but the nanoparticles do not show a noticeable change. The behaviour of the skin or surface friction depends on the concentrations of acetone and nanoparticles as well as Re as reflected in the wall stress. The effect of increasing concentration of nanoparticles on the skin friction is significantly affected by acetone concentration and Re: the skin friction decreases with increasing concentration of

nanoparticles at 70wt. % of acetone and Re of 20000, but it increases with increasing volume fraction of the nanoparticles at 60wt. % of acetone and Re of 15000. We suggest that this may be due to particle interaction increasing in the low Re velocity gradient, where there is increased interaction time as suggested in the formulation of nano-particle cloud viscosity used.

The overall performance of the solution with the nano-particles shows promising enhancement for the heat transfer challenge of the vapour absorption refrigeration system, since an enhancement of up to 180 % of basefluid can be achieved with only 1.5 % volume fraction of ZnO particles. The concentration of the salt solution base fluid has a significant effect on the heat transfer enhancement together with the nanoparticles.

In chapter 6: This chapter is involved with the core part of this thesis. A novel numerical method of boiling nano-salt-fluid is presented using the same geometry and boundary conditions as the experiment. This method deals with four phases to allow just one component (acetone) to evaporate from the system and demonstrates the characteristics that should be observed in the physical situation of sub-cooled boiling in a constant cross section rectangular channel, with a heated bottom section.

Increasing the nanoparticles raises the production rate of the vapour because of the thermal diffusion enhancement causing faster heating of the nanofluid. Likewise, the vapour production increases with reducing the velocity, due to the increased residence time over the heated section. Increasing the boiler surface temperature produces greater yield of vapour, since the regime considered is nucleate boiling prior to critical heat flux and no film boiling is observed.

The heat transfer coefficient increases with increasing boiler temperature and flow rate. The nanoparticle population rises in the region of the hot surface due to intense boiling which raises thermal diffusivity, then more bubbles

generate. Increasing the flow rate causes a drop in temperature, but only slightly. Increasing the boiler temperature or particles loading will rise the average temperature of the solution. The turbulence intensity is increase by increasing each of the nanoparticles concentration, boiler temperature and the flow rate.

The mixture method can show the effects of the nanoparticles on the complex flow dynamics of the boiling process as well as the vapour generation. The particles concentration increases due to the evaporation and the model simulates this effect. Boiler temperature and velocity effect on the system are as expected, but it is complicated by the boiling process and nanoparticle presence.

The VOF model cannot indicate the output character of the process, but it can illustrates the dynamic bubble generation and behaviour during the boiling. VOF model is affected by variation of the density of each phase. Therefore, the densities of the inlet phases are unified to avoid sinking of the heavier phase.

Overall, the models specify that improvement of the boiling process using nano-particles is a complex collaboration. It is dependent on the enhancement due to the nanofluid effects and the characteristics of interaction between vapour and liquid constituents in the heat transfer region. The indication is that a small proportion of nanoparticles can offer a benefit on providing improved boiling at lower temperatures where the temperature potential above saturation reduces.

7.2 Recommendations

A number of avenues are opened up by this work or previous numerical or experimental work. In the following there are some recommended points for future work.

- Regarding the core of this work (numerical work):
  - Use a wider range of the boiler temperature (200 ^oC < T < 160 ^oC) and inlet velocity (7.1 $ml/s < \dot{v} < 2.3\ ml/s$) and analyse their effects.
  - Use a higher concentration of nanoparticles with different types and investigate their effects numerically.
  - Develop a new model for absorbing the vapour by the nano-salt-fluid (can include the points above) for the absorber.
  - Develop a CFD model by considering the change in the acetone saturation temperature and pressure dependant on the acetone concentration in the boiler. (In each cell, when a part of the acetone evaporates the concentration of acetone will change in that cell which affects the saturation temperature of acetone).
- Regarding the experimental side:
  - Preparing a different type of nanofluid with different metallic nanoparticles such as Cu, Fe, Al and CNT or hybird nanoparticles such as Al_2O_3 as they have high thermal conductivity.
  - Try more methods to get a stabilized solution before using it in the system by using different types of surfactant, ionizing the nanoparticles or changing the PH of the base-

fluid.

- Measure more properties such as surface tension to find how the variation in the nanoparticles concentration effect on these properties.
- Doing the experimental work with a full design (including the higher and lower pressure side of VARS), in order to include the absorber.
- Do a mathematical analysis to calculate the outcome from each component and compare them with both the numerical calculations and experimental work.
- All the experiment can be repeated under vacuum or different pressure (0-1 bar) (current work done under atmospheric pressure).

REFERENCES

[1] Pongsid Srikhirin, Satha Aphornratana, and Supachart Chungpaibulpatana. A review of absorption refrigeration technologies. *Renewable and sustainable energy reviews*, 5(4):343–372, 2001.

[2] Sarit Kumar Das, Stephen US Choi, and Hrishikesh E Patel. Heat transfer in nanofluids — A review. *Heat transfer engineering*, 27(10):3–19, 2006.

[3] Investigation into discontinuous low temperature waste heat utilisation from a renewable power plant in rural India for absorption refrigeration, author=Joel A W Hamilton. *The University of Nottingham*, 2016.

[4] Ramesh Chandra Arora. *Refrigeration and air conditioning*. PHI Learning Pvt. Ltd., 2010.

[5] Jerko Labus. *Modelling of small capacity absorption chillers driven by solar thermal energy or waste heat*. PhD thesis, Universitat Rovira i Virgili, 2011.

[6] Gayle B Jordan, R.C.P. *Refrigeration and air conditioning*. PhD thesis, 1950.

[7] J Deng, RZ Wang, and GY Han. A review of thermally activated cooling technologies for combined cooling, heating and power systems. *Progress in Energy and Combustion Science*, 37(2):172–203, 2011.

[8] T Hussain, b Rai, and V Vasudev. *Experimental study of performance comparison of air cooled and Water condenser in Ammonia vapour absorption refrigeration system*, volume 4. IJARSE, 2015.

[9] A Zacarías, M Venegas, R Ventas, and A Lecuona. Experimental assessment of

Ammonia adiabatic absorption into Ammonia–Lithium Nitrate solution using a flat fan nozzle. *Applied Thermal Engineering*, 31(16):3569–3579, 2011.

[10] Guozhen Xie, Qingping Wu, Xiaoming Fa, Lirong Zhang, and Pradeep Bansal. A novel Lithium Bromide absorption chiller with enhanced absorption pressure. *Applied Thermal Engineering*, 38:1–6, 2012.

[11] Jongsoo Jeong, Kiyoshi Saito, and Sunao Kawai. Static characteristics and efficient control of compression-and absorption-type hybrid air conditioning system. *International journal of refrigeration*, 34(3):674–685, 2011.

[12] Junye Hua, Yaping Chen, Yaodong Wang, and AP Roskilly. Thermodynamic analysis of ammonia–water power/chilling cogeneration cycle with low-grade waste heat. *Applied Thermal Engineering*, 64(1):483–490, 2014.

[13] Ratha Z Mathkor, Brian Agnew, Mohammed A Al-Weshahi, and Fathi Latrsh. Exergetic analysis of an integrated tri-generation organic rankine cycle. *Energies*, 8(8):8835–8856, 2015.

[14] Salman Ajib and Ali Karno. Thermo physical properties of Acetone–Zinc bromide for using in a low temperature driven absorption refrigeration machine. *Heat and Mass Transfer*, 45(1):61–70, 2008.

[15] J Patek and J Klomfar. A computationally effective formulation of the thermodynamic properties of $LiBr/H_2O$ solutions from 273 to 500 K over full composition range. *International Journal of Refrigeration*, 29(4):566–578, 2006.

[16] D Micallef and C Micallef. Mathematical model of a vapour absorption refrigeration unit. *International Journal of Simulation Modelling*, 9(2):86–97, 2010.

[17] SA Tassou, JS Lewis, YT Ge, A Hadawey, and I Chaer. A review of emerging technologies for food refrigeration applications. *Applied Thermal Engineering*, 30(4):263–276, 2010.

[18] Satha Aphornratana. *Theoretical and experimental investigation of a combined ejector–absorption refrigerator*. 1994.

[19] Ali Karno and Salman Ajib. Thermodynamic analysis of an absorption refrig-

eration machine with new working fluid for solar applications. *Heat and Mass Transfer*, 45(1):71–81, 2008.

[20] G Grossman, K Gommed, and D Gadoth. A computer model for simulation of absorption systems in flexible and modular form. *ASHRAE Trans.;(United States)*, 93(CONF-870620-), 1987.

[21] V Boopathi Raja and V Shanmugam. A review and new approach to minimize the cost of solar assisted absorption cooling system. *Renewable and Sustainable Energy Reviews*, 16(9):6725–6731, 2012.

[22] KR Ullah, R Saidur, HW Ping, RK Akikur, and NH Shuvo. A review of solar thermal refrigeration and cooling methods. *Renewable and Sustainable Energy Reviews*, 24:499–513, 2013.

[23] Z.Y. Xu and R.Z. Wang. Absorption refrigeration cycles: Categorized based on the cycle construction. *International Journal of Refrigeration*, 62:114 – 136, 2016.

[24] L Garousi Farshi and SM Seyed Mahmoudi. Performance comparison of the double effect Lithium Bromide / Water absorption chiller:Series, Parallel and reverse parallel,Conference: 10th International Conference on Clean Energy (ICCE-2010)At: Famagusta, N. Cyprus. 2010.

[25] GP Xu, YQ Dai, KW Tou, and CP Tso. Theoretical analysis and optimization of a double-effect series-flow-type absorption chiller. *Applied thermal engineering*, 16(12):975–987, 1996.

[26] GP Xu and YQ Dai. Theoretical analysis and optimization of a double-effect parallel-flow-type absorption chiller. *Applied thermal engineering*, 17(2):157–170, 1997.

[27] MB Arun, MP Maiya, and S Srinivasa Murthy. Equilibrium low pressure generator temperatures for double-effect series flow absorption refrigeration systems. *Applied thermal engineering*, 20(3):227–242, 2000.

[28] MB Arun, MP Maiya, and S Srinivasa Murthy. Performance comparison of double-effect parallel-flow and series flow Water–Lithium bromide absorption

systems. *Applied thermal engineering*, 21(12):1273–1279, 2001.

[29] YL Liu and RZ Wang. Performance prediction of a solar/gas driving double effect $LiBr/H_2O$ absorption system. *Renewable Energy*, 29(10):1677–1695, 2004.

[30] DS Kim and CHM Machielsen. Evaluation of air-cooled solar absorption cooling systems. In *International Sorption Heat Pump Conference, Shanghai, China.*, 2002.

[31] S Arivazhagan, R Saravanan, and S Renganarayanan. Experimental studies on HFC based two-stage half effect vapour absorption cooling system. *Applied Thermal Engineering*, 26(14):1455–1462, 2006.

[32] Berhane H Gebreslassie, Marc Medrano, and Dieter Boer. Exergy analysis of multi-effect Water–LiBr absorption systems: from half to triple effect. *Renewable energy*, 35(8):1773–1782, 2010.

[33] MR Conde-Petit. Thermophysical properties of $NH_3 + H_2O$ solutions for the industrial design of absorption refrigeration equipment. *M. Conde Engineering, Zurich, Switzerland*, 2004.

[34] Khalid A Joudi and Ali H Lafta. Simulation of a simple absorption refrigeration system. *Energy conversion and Management*, 42(13):1575–1605, 2001.

[35] DS Kim and CA Infante Ferreira. Air-cooled LiBr–Water absorption chillers for solar air conditioning in extremely hot weathers. *Energy Conversion and Management*, 50(4):1018–1025, 2009.

[36] Arzu Sencan, Kemal A Yakut, and Soteris A Kalogirou. Thermodynamic analysis of absorption systems using artificial neural network. *Renewable Energy*, 31(1):29–43, 2006.

[37] Jian Sun, Lin Fu, and Shigang Zhang. A review of working fluids of absorption cycles. *Renewable and Sustainable Energy Reviews*, 16(4):1899–1906, 2012.

[38] DR Lide. Dr 2003–2004 crc handbook of chemistry and physics. *Boca Raton, FL, itd: CRC Press,*, 2003.

[39] Zenghu Han. *Nanofluids with enhanced thermal transport properties.* PhD

thesis, 2008.

[40] Yimin Xuan and Qiang Li. Investigation on convective heat transfer and flow features of nanofluids. *Journal of Heat transfer*, 125(1):151–155, 2003.

[41] JA Eastman, SUS Choi, Sheng Li, W Yu, and LJ Thompson. Anomalously increased effective thermal conductivities of Ethylene Glycol-based nanofluids containing copper nanoparticles. *Applied physics letters*, 78(6):718–720, 2001.

[42] Shinpyo Lee and Stephen U-S Choi. Application of metallic nanoparticle suspensions in advanced cooling systems. Technical report, Argonne National Lab., IL (United States), 1996.

[43] Sarit K Das. Nanofluids—the cooling medium of the future, 2006.

[44] Xiang-Qi Wang and Arun S Mujumdar. A review on nanofluids-part II: Experiments and applications. *Brazilian Journal of Chemical Engineering*, 25(4):631–648, 2008.

[45] Subelia Senara Botha. *Synthesis and characterization of nanofluids for cooling applications*. PhD thesis, University of the Western Cape, 2006.

[46] V Sridhara, BS Gowrishankar, Snehalatha, and LN Satapathy. Nanofluids — A new promising fluid for cooling. *Transactions of the Indian Ceramic Society*, 68(1):1–17, 2009.

[47] Michael Peter Beck. *Thermal conductivity of metal Oxide nanofluids*. Georgia Institute of Technology, 2008.

[48] S Choi. Development and applications of non-Newtonian flows, Editors: DA Siginer, and HP Wang, 1995.

[49] Yimin Xuan and Wilfried Roetzel. Conceptions for heat transfer correlation of nanofluids. *International Journal of Heat and Mass Transfer*, 43(19):3701 – 3707, 2000.

[50] SUS Choi, Wenhua Yu, John R Hull, ZG Zhang, and FE Lockwood. Nanofluids for vehicle thermal management. Technical report, SAE Technical Paper, 2001.

[51] P Keblinski, SK Nayak, P Zapol, and PM Ajayan. Charge distribution and stability of charged carbon nanotubes. *Physical review letters*, 89(25):255503,

2002.

[52] Deborah Elcock et al. Potential impacts of nanotechnology on energy transmission applications and needs. Technical report, Argonne National Laboratory (ANL), 2007.

[53] Cheol Choi, HS Yoo, and JM Oh. Preparation and heat transfer properties of nanoparticle-in-transformer Oil dispersions as advanced energy-efficient coolants. *Current Applied Physics*, 8(6):710–712, 2008.

[54] MN Pantzali, AA Mouza, and SV Paras. Investigating the efficacy of nanofluids as coolants in plate heat exchangers (PHE). *Chemical Engineering Science*, 64(14):3290–3300, 2009.

[55] Joo Hyun Lee. *Convection performance of nanofluids for electronics cooling*. Stanford University, 2009.

[56] MinSheng Liu, Mark ChingCheng Lin, and ChiChuan Wang. Enhancements of thermal conductivities with Cu, CuO, and carbon nanotube nanofluids and application of MWNT/Water nanofluid on a Water chiller system. *Nanoscale research letters*, 6(1):297, 2011.

[57] R Saidur, KY Leong, and HaA Mohammad. A review on applications and challenges of nanofluids. *Renewable and sustainable energy reviews*, 15(3):1646–1668, 2011.

[58] Wei Yu and Huaqing Xie. A review on nanofluids: Preparation, stability mechanisms, and applications. *Journal of Nanomaterials*, 2012, Article ID 435873,:17, 2012.

[59] SUS Choi, ZG Zhang, Wu Yu, FE Lockwood, and EA Grulke. Anomalous thermal conductivity enhancement in nanotube suspensions. *Applied physics letters*, 79(14):2252–2254, 2001.

[60] MJl Assael, C-F Chen, I Metaxa, and WA Wakeham. Thermal conductivity of suspensions of carbon nanotubes in Water. *International Journal of Thermophysics*, 25(4):971–985, 2004.

[61] Ho Chang, Tsing-Tshih Tsung, Liang-Chia Chen, Yi-Cheng Yang, Hong-Ming

Lin, Lee-Long Han, and Chung-Kwei Lin. TiO_2 nanoparticle suspension preparation using ultrasonic vibration-assisted arc-submerged nanoparticle synthesis system (ASNSS). *Materials Transactions*, 45(3):806–811, 2004.

[62] Sidi El Becaye Maiga, Cong Tam Nguyen, Nicolas Galanis, and Gilles Roy. Heat transfer behaviours of nanofluids in a uniformly heated tube. *Superlattices and Microstructures*, 35(3):543–557, 2004.

[63] In Cheol Bang and Soon Heung Chang. Boiling heat transfer performance and phenomena of Al_2O_3/Water nano-fluids from a plain surface in a pool. *International Journal of Heat and Mass Transfer*, 48(12):2407 – 2419, 2005.

[64] HB Ma, C Wilson, B Borgmeyer, K Park, Q Yu, SUS Choi, and Murli Tirumala. Effect of nanofluid on the heat transport capability in an oscillating heat pipe. *Applied Physics Letters*, 88(14):143116, 2006.

[65] Yujin Hwang, Jae-Keun Lee, Jong-Ku Lee, Young-Man Jeong, Seong-ir Cheong, Young-Chull Ahn, and Soo H Kim. Production and dispersion stability of nanoparticles in nanofluids. *Powder Technology*, 186(2):145–153, 2008.

[66] Sayantan Mukherjee and Somjit Paria. Preparation and stability of nanofluids - A Review. *IOSR Journal of Mechanical and civil engineering*, 9(2):63–69, 2013.

[67] Xinwei Wang, Xianfan Xu, and Stephen U. S. Choi. Thermal conductivity of nanoparticle - fluid mixture. *Journal of Thermophysics and Heat Transfer*, 13(4):474–480, 1999.

[68] S Li and JA Eastman. Measuring thermal conductivity of fluids containing Oxide nanoparticles. *J. Heat Transf*, 121(2):280–289, 1999.

[69] Yimin Xuan and Qiang Li. Heat transfer enhancement of nanofluids. *International Journal of heat and fluid flow*, 21(1):58–64, 2000.

[70] SMS Murshed, KC Leong, and C Yang. Enhanced thermal conductivity of TiO_2/Water based nanofluids. *International Journal of thermal sciences*, 44(4):367–373, 2005.

[71] Jin Ki Lee, Junemo Koo, Hiki Hong, and Yong Tae Kang. The effects of

nanoparticles on absorption heat and mass transfer performance in $NH3/H2O$ binary nanofluids. *International Journal of Refrigeration*, 33(2):269–275, 2010.

[72] KS Suganthi, V Leela Vinodhan, and KS Rajan. Heat transfer performance and transport properties of ZnO–Ethylene Glycol and ZnO–Ethylene Glycol–Water nanofluid coolants. *Applied energy*, 135:548–559, 2014.

[73] WC Williams, IC Bang, E Forrest, LW Hu, and J Buongiorno. Preparation and characterization of various nanofluids. In *Proceedings of the NSTI Nanotechnology Conference and Trade Show (Nanotech'06)*, volume 2, pages 408–411, 2006.

[74] A. Ghadimi, R. Saidur, and H.S.C. Metselaar. A review of nanofluid stability properties and characterization in stationary conditions. *International Journal of Heat and Mass Transfer*, 54(17):4051 – 4068, 2011.

[75] Jaeseon Lee and Issam Mudawar. Assessment of the effectiveness of nanofluids for single-phase and two-phase heat transfer in micro-channels. *International Journal of Heat and Mass Transfer*, 50(3):452 – 463, 2007.

[76] Daxiong Wu, Haitao Zhu, Liqiu Wang, and Lumei Liu. Critical issues in nanofluids preparation, characterization and thermal conductivity. *Current Nanoscience*, 5(1):103–112, 2009.

[77] Paul C Hiemenz and Paul C Hiemenz. *Principles of colloid and surface chemistry*, volume 9. M. Dekker New York, 1986.

[78] Behrouz Takabi and Hossein Shokouhmand. Effects of Al_2O_3 – Cu/Water hybrid nanofluid on heat transfer and flow characteristics in turbulent regime. *International Journal of Modern Physics C*, 26(04):1550047, 2015.

[79] Behrouz Takabi, Amir Mirza Gheitaghy, and Pedram Tazraei. Hybrid Water-based suspension of Al_2O_3 and Cu nanoparticles on laminar convection effectiveness. *Journal of Thermophysics and Heat Transfer*, (null):523–532, 2016.

[80] Jahar Sarkar, Pradyumna Ghosh, and Arjumand Adil. A review on hybrid nanofluids: Recent research, development and applications. *Renewable and Sustainable Energy Reviews*, 43:164–177, 2015.

[81] Hayder I. Mohammed, Donald Giddings, Gavin S. Walker, and Henry Power. CFD assessment of the effect of nanoparticles on the heat transfer properties of acetone/$ZnBr_2$ solution. *Applied Thermal Engineering*, 128:264 – 273, 2018.

[82] CJ Ho, WK Liu, YS Chang, and CC Lin. Natural convection heat transfer of Alumina-Water nanofluid in vertical square enclosures: an experimental study. *International Journal of Thermal Sciences*, 49(8):1345–1353, 2010.

[83] Khalil Khanafer and Kambiz Vafai. A critical synthesis of thermo-physical characteristics of nanofluids. *International Journal of Heat and Mass Transfer*, 54(19):4410–4428, 2011.

[84] HC Brinkman. The viscosity of concentrated suspensions and solutions. *The Journal of Chemical Physics*, 20(4):571–571, 1952.

[85] GK Batchelor. The effect of Brownian motion on the bulk stress in a suspension of spherical particles. *Journal of fluid mechanics*, 83(01):97–117, 1977.

[86] SM Peyghambarzadeh, SH Hashemabadi, SM Hoseini, and M Seifi Jamnani. Experimental study of heat transfer enhancement using Water/Ethylene Glycol based nanofluids as a new coolant for car radiators. *International Communications in Heat and Mass Transfer*, 38(9):1283–1290, 2011.

[87] N Masoumi, N Sohrabi, and A Behzadmehr. A new model for calculating the effective viscosity of nanofluids. *Journal of Physics D: Applied Physics*, 42(5):055501, 2009.

[88] Vahid Delavari and Seyed Hassan Hashemabadi. CFD simulation of heat transfer enhancement of Al_2O_3/Water and Al_2O_3/Ethylene Glycol nanofluids in a car radiator. *Applied Thermal Engineering*, 73(1):380 – 390, 2014.

[89] NA Frankel and Andreas Acrivos. On the viscosity of a concentrated suspension of solid spheres. *Chemical Engineering Science*, 22(6):847–853, 1967.

[90] MJ Pastoriza-Gallego, L Lugo, D Cabaleiro, JL Legido, and MM Piñeiro. Thermophysical profile of Ethylene Glycol-based ZnO nanofluids. *The Journal of Chemical Thermodynamics*, 73:23–30, 2014.

[91] Sarit K Das, Nandy Putra, and Wilfried Roetzel. Pool boiling characteristics

of nanofluids. *International journal of heat and mass transfer*, 46(5):851–862, 2003.

[92] Bock Choon Pak and Young I Cho. Hydrodynamic and heat transfer study of dispersed fluids with submicron metallic Oxide particles. *Experimental Heat Transfer an International Journal*, 11(2):151–170, 1998.

[93] S Zhou and Rui Ni. Measurement of the specific heat capacity of Water-based Al_2O_3 nanofluid. *Applied Physics Letters*, 92(9):093123, 2008.

[94] Nandy Putra, Peter Thiesen, Wilfried Roetzel, et al. Temperature dependence of thermal conductivity enhancement for nanofluids. *J Heat Transf*, 125:567–574, 2003.

[95] Jacopo Buongiorno. Convective transport in nanofluids. *Journal of Heat Transfer*, 128(3):240–250, 2006.

[96] SMS Murshed, KC Leong, and C Yang. Determination of the effective thermal diffusivity of nanofluids by the double hot-wire technique. *Journal of Physics D: Applied Physics*, 39(24):5316, 2006.

[97] David C Venerus, Madhu S Kabadi, Sunmook Lee, and Victor Perez-Luna. Study of thermal transport in nanoparticle suspensions using forced Rayleigh scattering. *Journal of Applied Physics*, 100(9):094310, 2006.

[98] AG Nnanna. Experimental model of temperature-driven nanofluid. *Journal of Heat Transfer*, 129(6):697–704, 2007.

[99] Ying Yang, Z George Zhang, Eric A Grulke, William B Anderson, and Gefei Wu. Heat transfer properties of nanoparticle in fluid dispersions (nanofluids) in laminar flow. *International Journal of Heat and Mass Transfer*, 48(6):1107–1116, 2005.

[100] Dongsheng Wen and Yulong Ding. Formulation of nanofluids for natural convective heat transfer applications. *International Journal of Heat and Fluid Flow*, 26(6):855–864, 2005.

[101] Louis Gosselin and Alexandre K da Silva. Combined "heat transfer and power dissipation" optimization of nanofluid flows. *Applied Physics Letters*,

85(18):4160–4162, 2004.

[102] Sidi El Bécaye Maïga, Cong Tam Nguyen, Nicolas Galanis, Gilles Roy, Thierry Maré, and Mickaël Coqueux. Heat transfer enhancement in turbulent tube flow using Al_2O_3 nanoparticle suspension. *International Journal of Numerical Methods for Heat and Fluid Flow*, 16(3):275–292, 2006.

[103] G Polidori, S Fohanno, and CT Nguyen. A note on heat transfer modelling of Newtonian nanofluids in laminar free convection. *International Journal of Thermal Sciences*, 46(8):739–744, 2007.

[104] RL Hamilton and OK Crosser. Thermal conductivity of heterogeneous two-component systems. *Industrial & Engineering chemistry fundamentals*, 1(3):187–191, 1962.

[105] Seok Pil Jang and Stephen US Choi. Role of Brownian motion in the enhanced thermal conductivity of nanofluids. *Applied physics letters*, 84(21):4316–4318, 2004.

[106] Porumpathparambil Damodaran Shima and John Philip. Role of thermal conductivity of dispersed nanoparticles on heat transfer properties of nanofluid. *Industrial & Engineering Chemistry Research*, 53(2):980–988, 2014.

[107] Shawn A Putnam, David G Cahill, Paul V Braun, Zhenbin Ge, and Robert G Shimmin. Thermal conductivity of nanoparticle suspensions. *Journal of Applied Physics*, 99(8):084308, 2006.

[108] Wei Yu, Huaqing Xie, Lifei Chen, and Yang Li. Investigation of thermal conductivity and viscosity of Ethylene Glycol based ZnO nanofluid. *Thermochimica Acta*, 491(1):92–96, 2009.

[109] Huaqing Xie, Jinchang Wang, Tonggeng Xi, Yan Liu, and Fei Ai. Dependence of the thermal conductivity of nanoparticle-fluid mixture on the base fluid. *Journal of materials science letters*, 21(19):1469–1471, 2002.

[110] A Turgut, I Tavman, M Chirtoc, HP Schuchmann, C Sauter, and S Tavman. Thermal conductivity and viscosity measurements of Water-based TiO_2 nanofluids. *International Journal of Thermophysics*, 30(4):1213–1226, 2009.

[111] MJ Assael, IN Metaxa, J Arvanitidis, D Christofilos, and C Lioutas. Thermal conductivity enhancement in aqueous suspensions of carbon multi-walled and double-walled nanotubes in the presence of two different dispersants. *International Journal of Thermophysics*, 26(3):647–664, 2005.

[112] Manoj Chopkar, A. K. Das, I. Manna, and P. K. Das. Pool boiling heat transfer characteristics of ZrO_2/Water nanofluids from a flat surface in a pool. *Heat and Mass Transfer*, 44(8):999–1004, Jun 2008.

[113] Sang Hyun Kim, Sun Rock Choi, and Dongsik Kim. Thermal conductivity of metal-Oxide nanofluids: Particle size dependence and effect of laser irradiation. *Journal of Heat Transfer*, 129(3):298–307, 2007.

[114] Fei Duan. *Thermal Property Measurement of Al_2O_3/Water Nanofluids*. INTECH Open Access Publisher, 2012.

[115] Michael P Beck, Yanhui Yuan, Pramod Warrier, and Amyn S Teja. The effect of particle size on the thermal conductivity of Alumina nanofluids. *Journal of Nanoparticle Research*, 11(5):1129–1136, 2009.

[116] Huaqing Xie, Jinchang Wang, Tonggeng Xi, Yan Liu, Fei Ai, and Qingren Wu. Thermal conductivity enhancement of suspensions containing nanosized Alumina particles. *Journal of Applied Physics*, 91(7):4568–4572, 2002.

[117] Hua-qing Xie, Jin-chang Wang, Tong-geng Xi, and Yan Liu. Thermal conductivity of suspensions containing nanosized SiC particles. *International Journal of Thermophysics*, 23(2):571–580, 2002.

[118] Elena V Timofeeva, Jules L Routbort, and Dileep Singh. Particle shape effects on thermophysical properties of Alumina nanofluids. *Journal of Applied Physics*, 106(1):014304, 2009.

[119] Sezer Özerinç, Sadık Kakaç, and Almıla Güvenç Yazıcıoğlu. Enhanced thermal conductivity of nanofluids: A state of the art review. *Microfluidics and Nanofluidics*, 8(2):145–170, 2010.

[120] SMS Murshed, KC Leong, and C Yang. Investigations of thermal conductivity and viscosity of nanofluids. *International Journal of Thermal Sciences*,

47(5):560–568, 2008.

[121] Veeranna Sridhara and Lakshmi Narayan Satapathy. Al_2O_3-based nanofluids: A review. *Nanoscale research letters*, 6(1):456, 2011.

[122] Jonas Sjöberg, Qinghua Zhang, Lennart Ljung, Albert Benveniste, Bernard Delyon, Pierre-Yves Glorennec, Håkan Hjalmarsson, and Anatoli Juditsky. Nonlinear black-box modeling in system identification: A unified overview. *Automatica*, 31(12):1691–1724, 1995.

[123] JM Gordon and Kim Choon Ng. A general thermodynamic model for absorption chillers: Theory and experiment. *Heat Recovery Systems and CHP*, 15(1):73–83, 1995.

[124] Rodolfo Jesús R Silverio and José Ricardo Figueiredo. Steady state simulation of the operation of an evaporative cooled Water-Ammonia absorption scale ice maker with experimental basis. *Journal of the Brazilian Society of Mechanical Sciences and Engineering*, 28(4):413–421, 2006.

[125] Omer Kaynakli and Muhsin Kilic. Theoretical study on the effect of operating conditions on performance of absorption refrigeration system. *Energy Conversion and Management*, 48(2):599–607, 2007.

[126] Adnan Sözen and M Ali Akçayol. Modelling (using artificial neural-networks) the performance parameters of a solar driven ejector absorption cycle. *Applied Energy*, 79(3):309–325, 2004.

[127] H Jacob Manohar, R Saravanan, and S Renganarayanan. Modelling of steam fired double effect vapour absorption chiller using neural network. *Energy Conversion and Management*, 47(15):2202–2210, 2006.

[128] Bejan A. Convection heat transfer. In *John Wiley and Sons*, volume 4, page 451, 2013.

[129] Jacqueline Barber, David Brutin, and Lounes Tadrist. A review on boiling heat transfer enhancement with nanofluids. *Nanoscale Research Letters*, 6(1):280, Apr 2011.

[130] Xiande Fang, Run Wang, Weiwei Chen, Helei Zhang, and Chunxiang Ma. A

review of flow boiling heat transfer of nanofluids. *Applied Thermal Engineering*, 91:1003 – 1017, 2015.

[131] E.G.E. Saver. Air conditioning. *5Mar. 2017; Available from: https://energy.gov/energysaver/air-conditioning.*, 2017.

[132] Xiande Fang, Yafeng Chen, Helei Zhang, Weiwei Chen, Anqi Dong, and Run Wang. Heat transfer and critical heat flux of nanofluid boiling: A comprehensive review. *Renewable and Sustainable Energy Reviews*, 62:924–940, 2016.

[133] Sung Joong Kim, Thomas McKrell, Jacopo Buongiorno, and Lin-Wen Hu. Alumina nanoparticles enhance the flow boiling critical heat flux of Water at low pressure. *Journal of Heat Transfer*, 130(4):044501, 2008.

[134] Kristen Henderson, Young-Gil Park, Liping Liu, and Anthony M. Jacobi. Flow-boiling heat transfer of R-134a-based nanofluids in a horizontal tube. *International Journal of Heat and Mass Transfer*, 53(5):944 – 951, 2010.

[135] Sung Joong Kim, Tom McKrell, Jacopo Buongiorno, and Lin-wen Hu. Subcooled flow boiling heat transfer of dilute Alumina, Zinc Oxide, and diamond nanofluids at atmospheric pressure. *Nuclear Engineering and Design*, 240(5):1186–1194, 2010.

[136] Mounir Boudouh, Hasna Louahlia Gualous, and Michel De Labachelerie. Local convective boiling heat transfer and pressure drop of nanofluid in narrow rectangular channels. *Applied Thermal Engineering*, 30(17):2619 – 2631, 2010.

[137] Ho Seon Ahn, Hyungdae Kim, HangJin Jo, SoonHo Kang, WonPyo Chang, and Moo Hwan Kim. Experimental study of critical heat flux enhancement during forced convective flow boiling of nanofluid on a short heated surface. *International Journal of Multiphase Flow*, 36(5):375 – 384, 2010.

[138] E Abedini, A Behzadmehr, H Rajabnia, SMH Sarvari, and SH Mansouri. Experimental investigation and comparison of subcooled flow boiling of TiO_2 nanofluid in a vertical and horizontal tube. *Proceedings of the Institution of Mechanical Engineers, Part C: Journal of Mechanical Engineering Science*, 227(8):1742–1753, 2013.

[139] Sanjeeva Witharana. Boiling of refrigerants on enhanced surfaces and boiling of nanofluids. *Sweden: Royal Institute of Technology, Stockholm*, 2003.

[140] S. M. You, J. H. Kim, and K. H. Kim. Effect of nanoparticles on critical heat flux of Water in pool boiling heat transfer. *Applied Physics Letters*, 83(16):3374–3376, 2003.

[141] Peter Vassallo, Ranganathan Kumar, and Stephen D'Amico. Pool boiling heat transfer experiments in Silica–Water nano-fluids. *International Journal of Heat and Mass Transfer*, 47(2):407–411, 2004.

[142] DWm Zhou. Heat transfer enhancement of Copper nanofluid with acoustic cavitation. *International Journal of Heat and Mass Transfer*, 47(14):3109–3117, 2004.

[143] Dongsheng Wen and Yulong Ding. Experimental investigation into the pool boiling heat transfer of aqueous based γ-Alumina nanofluids. *Journal of Nanoparticle Research*, 7(2):265–274, Jun 2005.

[144] Hyungdae Kim, Jeongbae Kim, and Moo Hwan Kim. Effect of nanoparticles on CHF enhancement in pool boiling of nanofluids. *International Journal of Heat and Mass Transfer*, 49(25):5070 – 5074, 2006.

[145] M. Hasheminia, M. Haghshenas, S. Etemad, and S. Hashemabadi. Forced boiling of nanofluids, effects of contact angle and surface wettability. *3rd Micro and Nano Flows Conference Thessaloniki-Greece,*, pages 1 – 8, 2011.

[146] E. Abedini, A. Behzadmehr, S.M.H. Sarvari, and S.H. Mansouri. Numerical investigation of subcooled flow boiling of a nanofluid. *International Journal of Thermal Sciences*, 64:232 – 239, 2013.

[147] Sina Nabati Shoghl, Masoud Bahrami, and Mostafa Keshavarz Moraveji. Experimental investigation and CFD modeling of the dynamics of bubbles in nanofluid pool boiling. *International Communications in Heat and Mass Transfer*, 58:12 – 24, 2014.

[148] Wesley Williams, Jacopo Buongiorno, and Lin-Wen Hu. Experimental investigation of turbulent convective heat transfer and pressure loss of Alu-

mina/Water and Zirconia/Water nanoparticle colloids (nanofluids) in horizontal tubes. *Journal of Heat Transfer*, 130(4):042412, 2008.

[149] Elena V Timofeeva, Wenhua Yu, David M France, Dileep Singh, and Jules L Routbort. base fluid and temperature effects on the heat transfer characteristics of *sic* in ethylene glycol/h_2o and h_2o nanofluids. *Journal of Applied Physics*, 109(1):014914, 2011.

[150] MN Pantzali, AG Kanaris, KD Antoniadis, AA Mouza, and SV Paras. Effect of nanofluids on the performance of a miniature plate heat exchanger with modulated surface. *International Journal of Heat and Fluid Flow*, 30(4):691–699, 2009.

[151] Adi T Utomo, Ehsan B Haghighi, Ashkan IT Zavareh, Morteza Ghanbarpourgeravi, Heiko Poth, Rahmatollah Khodabandeh, Björn Palm, and Andrzej W Pacek. The effect of nanoparticles on laminar heat transfer in a horizontal tube. *International Journal of Heat and Mass Transfer*, 69:77–91, 2014.

[152] Ulzie Rea, Tom McKrell, Lin-wen Hu, and Jacopo Buongiorno. Laminar convective heat transfer and viscous pressure loss of Alumina–Water and Zirconia–Water nanofluids. *International Journal of Heat and Mass Transfer*, 52(7):2042–2048, 2009.

[153] Liang Liao and Zhen-Hua Liu. Forced convective flow drag and heat transfer characteristics of carbon nanotube suspensions in a horizontal small tube. *Heat and mass transfer*, 45(8):1129–1136, 2009.

[154] H. Demir, A.S. Dalkilic, N.A. Kürekci, W. Duangthongsuk, and S. Wongwises. Numerical investigation on the single phase forced convection heat transfer characteristics of TiO_2 nanofluids in a double-tube counter flow heat exchanger. *International Communications in Heat and Mass Transfer*, 38(2):218 – 228, 2011.

[155] Sinan Göktepe, Kunt Atalık, and Hakan Ertürk. Comparison of single and two-phase models for nanofluid convection at the entrance of a uniformly heated tube. *International Journal of Thermal Sciences*, 80:83–92, 2014.

[156] M Amoura, M Alloti, A Mouassi, and N Zeraibi. Study of heat transfer of nanofluids in a circular tube. *World Academy of Science, Engineering and Technology, International Journal of Mathematical, Computational, Physical, Electrical and Computer Engineering*, 7(9):1464–1469, 2013.

[157] Mostafa Keshavarz Moraveji, Mehdi Darabi, Seyyed Mohammad Hossein Haddad, and Reza Davarnejad. Modeling of convective heat transfer of a nanofluid in the developing region of tube flow with computational fluid dynamics. *International Communications in Heat and Mass Transfer*, 38(9):1291–1295, 2011.

[158] M. Akbari, N. Galanis, and A. Behzadmehr. Comparative analysis of single and two-phase models for CFD studies of nanofluid heat transfer. *International Journal of Thermal Sciences*, 50(8):1343 – 1354, 2011.

[159] W Yu, DM France, EV Timofeeva, D Singh, and JL Routbort. Thermophysical property-related comparison criteria for nanofluid heat transfer enhancement in turbulent flow. *Applied physics letters*, 96(21):213109, 2010.

[160] Microscopy EM Resolution supporting eloctron. Holey carbon support films for TEM, accessed at https://emresolutions.com/tem-products/support-films/holey-carbon-support-films-for-tem/ on, 21/12/2017.

[161] University of Pennsylvania / Department of Physics and Astronomy. Averaging, Errors and Uncertainty. *Labrtory Manual*, page 4.

[162] Haisheng Chen, Yulong Ding, and Chunqing Tan. Rheological behaviour of nanofluids. *New journal of physics*, 9(10):367, 2007.

[163] Tci thermal technology. Thermal conductivity analyser how it work. accessed at, http://ctherm.com/products/tci_thermal_conductivity/how_the_tci_works/mtps/ on, 23/05/2018.

[164] ASTM Standard. E1269-11, 2007,Standard Test Method for Determining Specific Heat Capacity by Differential Scanning Calorimetry. American Society for Testing and Materials. Philadelphia. 3^{rd}*edition*.

[165] MA White, C Chieh, A Anderson, and LAK Staveley. Calorimetric, spec-

troscopic, and structural studies of anhydrous Zinc bromide. *The Journal of chemical physics*, 80(3):1254–1258, 1984.

[166] Malvern Instruments. Dynamic light scattering: An introduction in 30 minutes. *Technical Note Malvern, MRK656-01*, pages 1–8, 2012.

[167] J. M. Saiz Jabardo, E. Fockink da Silva, G. Ribatski, and S. F. de Barros. Evaluation of the Rohsenow correlation through experimental pool boiling of halocarbon refrigerants on cylindrical surfaces. *Journal of the Brazilian Society of Mechanical Sciences and Engineering*, 26:218 – 230, 06 2004.

[168] Ng Kim Choon, Anutosh Chakraborty, Sai Maung Aye, and Wang Xiaolin. New pool boiling data for Water with Copper-foam metal at subatmospheric pressures: Experiments and correlation. *Applied Thermal Engineering*, 26(11):1286 – 1290, 2006.

[169] PASS. Ge druck unik 5000 configurable silicon pressure sensor.2018 [cited 2018 2nd / feb.]; available from:, 2018.

[170] Hao Peng, Guoliang Ding, Weiting Jiang, Haitao Hu, and Yifeng Gao. Measurement and correlation of frictional pressure drop of refrigerant-based nanofluid flow boiling inside a horizontal smooth tube. *International Journal of Refrigeration*, 32(7):1756 – 1764, 2009.

[171] Leyuan Yu, Aritra Sur, and Dong Liu. Flow boiling heat transfer and two-phase flow instability of nanofluids in a minichannel. *ASME. J. Heat Transfer*, 137(5), 2015.

[172] M.M. Sarafraz and F. Hormozi. Scale formation and subcooled flow boiling heat transfer of CuO–Water nanofluid inside the vertical annulus. *Experimental Thermal and Fluid Science*, 52:205 – 214, 2014.

[173] Li Xu and Jinliang Xu. Nanofluid stabilizes and enhances convective boiling heat transfer in a single microchannel. *International Journal of Heat and Mass Transfer*, 55(21):5673 – 5686, 2012.

[174] Abdurrahim Bolukbasi, Dogan Ciloglu, and Bayram Sahin. The characteristic pool boiling curves of nanofluids. *World Academy of Science, Engineering and*

Technology, (67):163 – 165, 2012.

[175] Sarit K. Das, Nandy Putra, and Wilfried Roetzel. Pool boiling of nanofluids on horizontal narrow tubes. *International Journal of Multiphase Flow*, 29(8):1237 – 1247, 2003.

[176] G. Prakash Narayan, K. B. Anoop, and Sarit K. Das. Mechanism of enhancement/deterioration of boiling heat transfer using stable nanoparticle suspensions over vertical tubes. *Journal of Applied Physics*, 102(7):074317, 2007.

[177] Adirek Suriyawong and Somchai Wongwises. Nucleate pool boiling heat transfer characteristics of TiO_2/Water nanofluids at very low concentrations. *Experimental Thermal and Fluid Science*, 34(8):992 – 999, 2010.

[178] S.M. Peyghambarzadeh, S.H. Hashemabadi, M. Naraki, and Y. Vermahmoudi. Experimental study of overall heat transfer coefficient in the application of dilute nanofluids in the car radiator. *Applied Thermal Engineering*, 52(1):8 – 16, 2013.

[179] Hamed Safikhani and Abbas Abbassi. A new dispersion model for thermal properties of nanofluids in flat tubes. *International Journal of Thermal Sciences*, 109:114 – 122, 2016.

[180] Ravikanth S. Vajjha, Debendra K. Das, and Praveen K. Namburu. Numerical study of fluid dynamic and heat transfer performance of Al_2O_3 and CuO nanofluids in the flat tubes of a radiator. *International Journal of Heat and Fluid Flow*, 31(4):613 – 621, 2010.

[181] development of new correlations for the nusselt number and the friction factor under turbulent flow of nanofluids in flat tubes.

[182] Ningbo Zhao, Jialong Yang, Hui Li, Ziyin Zhang, and Shuying Li. Numerical investigations of laminar heat transfer and flow performance of Al_2O_3/Water nanofluids in a flat tube. *International Journal of Heat and Mass Transfer*, 92:268 – 282, 2016.

[183] A. Akbarinia and A. Behzadmehr. Numerical study of laminar mixed convection of a nanofluid in horizontal curved tubes. *Applied Thermal Engineering*,

27(8):1327 – 1337, 2007.

[184] A. Fluent. Users Guide 15.0. *Ansys Inc*, UDS Theory, 9, 2014.

[185] Robert J. Moffat. Describing the uncertainties in experimental results. *Experimental Thermal and Fluid Science*, 1(1):3 – 17, 1988.

[186] H.U. Helvaci and Z.A. Khan. Heat transfer and entropy generation analysis of HFE 7000 based nanorefrigerants. *International Journal of Heat and Mass Transfer*, 104:318 – 327, 2017.

[187] V. Bianco, F. Chiacchio, O. Manca, and S. Nardini. Numerical investigation of nanofluids forced convection in circular tubes. *Applied Thermal Engineering*, 29(17):3632 – 3642, 2009.

[188] Paritosh Garg, Jorge L. Alvarado, Charles Marsh, Thomas A. Carlson, David A. Kessler, and Kalyan Annamalai. An experimental study on the effect of ultrasonication on viscosity and heat transfer performance of multi-wall carbon nanotube-based aqueous nanofluids. *International Journal of Heat and Mass Transfer*, 52(21):5090 – 5101, 2009.

[189] Mohammad Kalteh, Abbas Abbassi, Majid Saffar-Avval, and Jens Harting. Eulerian–Eulerian two-phase numerical simulation of nanofluid laminar forced convection in a microchannel. *International Journal of Heat and Fluid Flow*, 32(1):107 – 116, 2011.

[190] C.J. Ho, M.W. Chen, and Z.W. Li. Numerical simulation of natural convection of nanofluid in a square enclosure: Effects due to uncertainties of viscosity and thermal conductivity. *International Journal of Heat and Mass Transfer*, 51(17):4506 – 4516, 2008.

[191] B.E. Launder and D.B. Spalding. The numerical computation of turbulent flows. *Computer Methods in Applied Mechanics and Engineering*, 3(2):269 – 289, 1974.

[192] Hamid Nabati. Investigation on numerical modeling of Water vapour condensation from a flue gas with high COR2R content. *Energy and Power Engineering*, 3(2):181–189, 2011.

[193] M.N. Golubovic, H.D. Madhawa Hettiarachchi, W.M. Worek, and W.J. Minkowycz. Nanofluids and critical heat flux, experimental and analytical study. *Applied Thermal Engineering*, 29(7):1281 – 1288, 2009. Selected Papers from the 10th UK National Heat Transfer Conference, Edinburgh, Scotland, September 10-11, 2007.

[194] Tae Il Kim, Yong Hoon Jeong, and Soon Heung Chang. An experimental study on CHF enhancement in flow boiling using Al_2O_3 nanofluid. *International Journal of Heat and Mass Transfer*, 53(5):1015 – 1022, 2010.

[195] S. Soltani, S. Gh. Etemad, and J. Thibault. Pool boiling heat transfer of non-Newtonian nanofluids. *International Communications in Heat and Mass Transfer*, 37(1):29 – 33, 2010.

[196] Gao LiLi ; Zhang Lin ; Ma ZhiLei ; Xu Chen ; Xiao ZhangPing ; Du MingZhao. The numerical simulation of flow and boiling heat transfer of two phases in horizontal tube. *sia-Pacific Power and Energy Engineering Conference*, pages 1 – 4, 27-29March2012.

[197] Sandra C.K. De Schepper, Geraldine J. Heynderickx, and Guy B. Marin. Modeling the evaporation of a hydrocarbon feedstock in the convection section of a steam cracker. *Computers Chemical Engineering*, 33(1):122 – 132, 2009.

[198] W.H.Lee. *A Pressure iteration scheme for two-phase flow modeling*, pages 407–431. University of California, 1980.

[199] H.L. Wu, X.F. Peng, P. Ye, and Y. Eric Gong. Simulation of refrigerant flow boiling in serpentine tubes. *International Journal of Heat and Mass Transfer*, 50(5):1186 – 1195, 2007.

[200] Z. Yang, X.F. Peng, and P. Ye. Numerical and experimental investigation of two phase flow during boiling in a coiled tube. *International Journal of Heat and Mass Transfer*, 51(5):1003 – 1016, 2008.

[201] David C . Wilcox. *Turbulence Modeling for CFD*. DCW Industries, Inc. La Canada, California, 1998.

A

DATA USED TO FIND THE UNCERTAINTY

Table A.1: Collected data of the acetone / $ZnBr_2$ density (kg/m^3) as mentioned in Chapter 3.

Concentration of $ZnBr_2$	trial1	trial2	trial3	trial4	trial5	Average	St.Dv	St.er	$\triangle_{meas.}$	$\triangle_{mean}$
40%	1178	1152	1176	1168	1145	1163.8	14.66969	6.560487	16.5	7.379024
45%	1245	1239	1231	1223	1205	1228.6	15.58204	6.968500	20	8.944271
50%	1358	1361	1362	1360	1358	1359.8	1.788854	0.8	2	0.894427
55%	1429	1428	1425	1426	1423	1426.2	2.387467	1.067707	3	1.341640
60%	1546	1547	1554	1556	1546	1549.8	4.816637	2.154065	5	2.236067
65%	1665	1660	1663	1659	1662	1661.8	2.387467	1.067707	3	1.341640

Table A.2: Collected data of the acetone / $ZnBr_2 - ZnO$ density (kg/m^3) as mentioned in Chapter 3.

Concentration of ZnO	trial1	trial2	trial3	trial4	trial5	Average	St.Dv	St.er	$\triangle_{meas.}$	$\triangle_{mean}$
0	1358	1361	1362	1360	1358	1359.8	1.788854	0.8	2	0.894427
0.001	1365.3	1370.8	1364.8	1367	1372	1367.98	3.254535	1.455472	3.6	1.609968
0.003	1367	1374	1372	1369	1378	1372	4.301162	1.923538	5.5	2.459674
0.005	1376	1382	1387	1385	1385	1383	4.301162	1.923538	5.5	2.459674
0.01	1410	1404	1398	1400	1403	1403	4.582575	2.04939	6	2.683281
0.012	1423	1415	1413	1419	1415	1417	4	1.788854	5	2.236067

Table A.3: Collected data of the acetone / $ZnBr_2 - G$ density (kg/m^3) as mentioned in Chapter 3.

Concentration of Graphene	trial1	trial2	trial3	trial4	trial5	Average	St.Dv	St.er	$\triangle_{meas.}$	$\triangle_{mean}$
0	1547	1549	1551	1553	1548	1549.6	2.408318	1.077032	3	1.341640
0.0001	1551.23	1552.46	1549.15	1549.85	1547.436	1550.0252	1.928757	0.862566	2.512	1.123400
0.0005	1551.12	1549.7	1550	1551.1	1548.7	1550.125	1.021946	0.457028	1.2125	0.542246
0.001	1549.35	1549.7	1550.5	1551.44	1550.26	1550.25	0.804860	0.35994	1.045	0.467338
0.003	1548.45	1552.3	1549.6	1550.95	1552.45	1550.75	1.728076	0.772819	2	0.894427
0.005	1554.54	1553.5	1550.7	1548.6	1548.91	1551.25	2.678021	1.197647	2.97	1.328224379

Table A.4: Collected data of the acetone and acetone / $ZnBr_2$ viscosity ($mpa.s$) as mentioned in Chapter 3.

Solutions	trial1	trial2	trial3	trial4	trial5	trial6	trial7	trial8	trial9	trial10	Average	St.Dv	St.er	$\triangle_{meas.}$	$\triangle_{mean}$
Acetone	0.307	0.308	0.309	0.307	0.303	0.306	0.305	0.31	0.316	0.31	0.308	0.0035	0.0015	0.0065	0.0021
Ac./$ZnBr_2$	3.359	3.173	3.128	3.312	3.177	3.133	3.405	3.229	3.172	3.192	3.228	0.097	0.043	0.138	0.0438

Table A.5: Collected data of the acetone and acetone / $ZnBr_2$ - ZnO viscosity ($mpa.s$) as mentioned in Chapter 3.

Cons. of ZnO	trial1	trial2	trial3	trial4	trial5	trial6	trial7	trial8	trial9	trial10	Average	St.Dv	St.er	$\triangle_{meas.}$	$\triangle_{mean}$
0.0001	3.3396	3.2146(	3.1813;	3.3116(	3.231	3.206	3.3851	3.2566	3.392	3.2236	3.2743	0.0769	0.0344	0.105	0.0333
0.001	3.556	3.4203	3.3803	3.7206	3.5613	3.5346	3.748	3.613	3.689	3.6793	3.5904	0.124	0.0554	0.1841	0.0582
0.003	3.8756	3.6746	3.7046	3.965	4.1616	3.9253	4.0646	3.9736	3.959	4.134	3.9438	0.1613	0.0721	0.2435	0.077
0.005	4.01	3.8393	3.92	4.249	4.11	3.992	4.334	4.048	3.996	4.0846	4.0586	0.1471	0.0658	0.247	0.0783
0.01	4.6506	4.532	4.394	4.512	4.418	4.623	4.697	4.539	4.464	4.5033	4.53	0.0986	0.0441	0.1518	0.048
0.012	5.2943	4.8046	4.665	4.6523	4.549	4.574	5.278	4.6426	4.5046	4.969	4.7936	0.291	0.1305	0.3948	0.1248

Table A.6: Collected data of the acetone / $ZnBr_2$ thermal conductivity ($W/K.m$) as mentioned in Chapter 3.

Concentration of $ZnBr_2$	trial1	trial2	trial3	trial4	trial5	Average	St.Dv	St.er	$\triangle_{meas.}$	$\triangle_{mean}$
40%	0.158	0.157	0.157	0.163	0.16	0.159	0.00254	0.00114	0.003	0.00134
45%	0.157	0.153	0.157	0.152	0.152	0.1542	0.00258	0.00115	0.0025	0.001118
50%	0.155	0.151	0.15	0.152	0.151	0.1518	0.001923	0.00086	0.0025	0.001118
55%	0.153	0.153	0.149	0.151	0.151	0.1514	0.00167	0.000748	0.002	0.00089
60%	0.147	0.1535	0.152	0.149	0.151	0.1505	0.0025	0.00114	0.00325	0.001453
65%	0.147	0.153	0.151	0.15	0.148	0.1498	0.00238	0.00106	0.003	0.001341

Table A.7: Collected data of the acetone / $ZnBr_2 - ZnO$ thermal conductivity ($W/K.m$) as mentioned in Chapter 3.

Concentration of ZnO	trial1	trial2	trial3	trial4	trial5	Average	St.Dv	St.er	$\triangle_{meas.}$	$\triangle_{mean}$
0	0.155	0.151	0.15	0.152	0.151	0.1518	0.00192	0.00086	0.0025	0.001112
0.001	0.1514	0.149	0.154	0.153	0.1585	0.15346	0.00344	0.001539	0.00455	0.00203
0.003	0.15151	0.1564	0.15845	0.1578	0.158	0.1565	0.0029	0.0013	0.00347	0.00155
0.005	0.157	0.158	0.159	0.16	0.161	0.16	0.00166	0.00074	0.0021	0.000968
0.01	0.16053	0.16126	0.1632	0.1675	0.1649	0.1635	0.00283	0.00126	0.003485	0.001559
0.012	0.1645	0.1675	0.1709	0.1695	0.1677	0.1680	0.0024	0.001084	0.00322	0.00144

Table A.8: Collected data of the acetone / $ZnBr_2 - G$ thermal conductivity ($W/K.m$) as mentioned in Chapter 3.

Concentration of Graphene	trial1	trial2	trial3	trial4	trial5	Average	St.Dv	St.er	$\triangle_{meas.}$	$\triangle_{mean}$
0	0.147	0.1535	0.152	0.149	0.151	0.1505	0.002549	0.00114	0.00325	0.001453
0.0001	0.1501	0.149	0.1548	0.153	0.149	0.1512	0.00254	0.001138	0.0029	0.0013
0.0005	0.1548	0.1501	0.1553	0.148	0.1528	0.1522	0.00311	0.00139	0.00365	0.0016
0.001	0.15	0.1511	0.1495	0.1565	0.159	0.1532	0.0043	0.001926	0.00475	0.002124
0.003	0.1588	0.153	0.1509	0.1535	0.159	0.155	0.0036	0.00163	0.00405	0.00181
0.005	0.1612	0.1555	0.154	0.158	0.1595	0.1576	0.00292	0.0013	0.0036	0.00161

Table A.9: Collected data of the acetone / $ZnBr_2$ heat capacity ($J/g.K$) as mentioned in Chapter 3.

Concentration of $ZnBr_2$	trial1	trial2	trial3	trial4	trial5	Average	St.Dv	St.er	$\triangle_{meas.}$	$\triangle_{mean}$
40%	1.23	1.28	1.32	1.31	1.4	1.308	0.06221	0.0278	0.085	0.038
45%	1.37	1.29	1.21	1.26	1.17	1.26	0.077	0.03435	0.1	0.0447
50%	1.25	1.18	1.13	1.16	0.98	1.14	0.01	0.044	0.135	0.0603
55%	1.01	0.88	1.15	1.3	1.11	1.09	0.157	0.0702	0.21	0.0939
60%	0.97	1.107	1.101	0.94	1	1.0236	0.0764	0.03418	0.0835	0.03734
65%	0.78	0.95	0.91	1.02	0.89	0.91	0.088	0.03937	0.12	0.05367

Table A.10: Collected data of the acetone / $ZnBr_2 - G$ heat capacity ($J/g.K$) as mentioned in Chapter 3.

Concentration of Graphene	trial1	trial2	trial3	trial4	trial5	Average	St.Dv	St.er	$\triangle_{meas.}$	$\triangle_{mean}$
0	0.972	1.028	1.101	1.02	1	1.024	0.048	0.0215	0.0645	0.02884
0.0001	0.96	1.016	1.06	1.04	1.09	1.0332	0.0491	0.02196	0.065	0.02907
0.0005	1.028	1.036	0.945	1.01	1.07	1.0178	0.046	0.02	0.0625	0.028
0.001	0.98	1.0085	1.01	1.052	1.032	1.0165	0.027106272	0.0121	0.036	0.0161
0.003	1	1.006	1.0345	1.052	0.98	1.0145	0.0286	0.0128	0.036	0.0161
0.005	1.01	1.06	0.955	1.06	0.98	1.013	0.047	0.021	0.0525	0.02348

B

UDF SOURCE CODE

```
/************************************************************************
    UDF for identifying the phase change in the boiling process
************************************************************************/
    #include "udf.h"
    #include "sg_mphase.h"
    #define T_SAT 310
    #define LAT_HT 511000
    DEFINE_SOURCE(vap_src, cell, pri_th, dS, eqn)
    {
    Thread * mix_th, * sec_th;
    real m_dot_v;
    mix_th = THREAD_SUPER_THREAD(pri_th);
    sec_th = THREAD_SUB_THREAD(mix_th, 1);
    if(C_T(cell, mix_th) = T_SAT)
    {
    m_dot_v = 0.42 * C_VOF(cell, sec_th) * C_R(cell, sec_th) * fabs(C_T(cell,
sec_th) - T_SAT)/T_SAT;
    dS[eqn] = 0.;
    }
```

```
if(C_T(cell, mix_th)=T_SAT)
{
m_dot_v = -0.42 * C_VOF(cell, pri_th) * C_R(cell, pri_th) * fabs(T_SAT -
C_T(cell,pri_th))/T_SAT;
dS[eqn] = -0.42 * C_R(cell, pri_th) * fabs(C_T(cell, pri_th) - T_SAT)/T_SAT;
}
return m_dot_v ;
}
DEFINE_SOURCE(liq_src, cell, sec_th, dS, eqn)
{
Thread * mix_th, *pri_th;
real m_dot_l;
mix_th = THREAD_SUPER_THREAD(sec_th);
pri_th = THREAD_SUB_THREAD(mix_th, 0);
if(C_T(cell, mix_th) ¿= T_SAT)
{
m_dot_l = - 0.42 * C_VOF(cell, sec_th)*C_R(cell, sec_th)*fabs(C_T(cell,
sec_th) - T_SAT)/T_SAT;
dS[eqn] = - 0.42 * C_R(cell, sec_th) * fabs(C_T(cell, sec_th) - T_SAT)/T_SAT;
}
if(C_T(cell, mix_th)=T_SAT)
{
m_dot_l = 0.42 * C_VOF(cell, pri_th) * C_R(cell, pri_th) * fabs(T_SAT -
C_T(cell,pri_th))/T_SAT;
dS[eqn] = 0.;
}
return m_dot_l;
```

```
}
DEFINE_SOURCE(enrg_src, cell, mix_th, dS, eqn)
{
Thread * pri_th, * sec_th;
real m_dot;
pri_th = THREAD_SUB_THREAD(mix_th, 0);
sec_th = THREAD_SUB_THREAD(mix_th, 1);
if(C_T(cell, mix_th) ¿= T_SAT)
{
m_dot = - 0.42 * C_VOF(cell, sec_th)*C_R(cell, sec_th) * fabs(C_T(cell,
sec_th) - T_SAT)/T_SAT;
dS[eqn] = -0.42 * C_VOF(cell, sec_th) * C_R(cell, sec_th) * LAT_HT/T_SAT;
}
if(C_T(cell, mix_th) = T_SAT)
{
m_dot = 0.42 * C_VOF(cell, pri_th) * C_R(cell, pri_th) * fabs(T_SAT -
C_T(cell, pri_th))/T_SAT;
dS[eqn] = 0.42 * C_VOF(cell, pri_th) * C_R(cell, pri_th) * LAT_HT/T_SAT;
}
return LAT_HT*m_dot; }
```